Final Thesis Submission Sheet Copyright Permission Form Library and Archives Canada Licence (PhD only) McMaster University Licence

FRAGILE MAGNETISM IN XY RARE EARTH PYROCHLORES

FRAGILE MAGNETISM IN XY RARE EARTH PYROCHLORES

JONATHAN GAUDET, B.Sc., M.Sc.

A Thesis Submitted to the School of Graduate Studies
in Partial Fulfillment of the Requirements
for the Degree Doctor of Philosophy

McMaster University

DOCTOR OF PHILOSOPHY (2018)
(Physics)

McMaster University
Hamilton, Ontario

TITLE: Fragile magnetism in XY rare earth pyrochlores

AUTHOR: Jonathan Gaudet, B.Sc., M.Sc.

SUPERVISOR: Professor Bruce Gaulin

NUMBER OF PAGES: viii, 99

Lay Abstract

In this thesis, we search for new magnetic phenomena that can be obtained by decorating a lattice of corner-sharing tetrahedra with rare earth ions. In particular, we are interested in studying the magnetic properties of pyrochlore magnets built from spins that have a preference to lie perpendicular to the center of each tetrahedron, termed XY anisotropy. This ingredient is found in the rare earth pyrochlore magnets $Yb_2Ti_2O_7$ and $Er_2Ti_2O_7$. In these materials, the combination of geometrical frustration, dominant spin-orbit coupling and strong crystal-field effects give rise to several exotic magnetic states such as the quantum spin ice. The impact of disorder, dilution, hydrostatic pressure and chemical pressure on the magnetic ground states of $Yb_2Ti_2O_7$ and $Er_2Ti_2O_7$ were investigated in this thesis using inelastic neutron scattering. Our results support the notion that multiphase competition is the primary driver for spin liquid behaviour and order-by-disorder effects in these materials.

Abstract

The topic of investigation in this thesis is the pyrochlore titanates $A_2\text{Ti}_2\text{O}_7$ where A^{3+} is a magnetic rare earth ion and Ti^{4+} is non-magnetic. The pyrochlore is a cubic structure composed of two inter-penetrating networks of corner-sharing tetrahedra and is the archetypal platform for the study of magnetic frustration in three dimensions. Magnetic frustration in rare earth pyrochlores favors the stabilization of various exotic magnetic phenomena such as the classical and quantum spin liquid states. The degree of magnetic frustration in these systems depends strongly on the local spin anisotropy of the rare earth ion. In this thesis, we studied the magnetic properties of XY pyrochlore magnets where the spins have a preference to point perpendicular to the centers of the two tetrahedra they connect. XY local anisotropy is obtained in the rare earth pyrochlores $\text{Yb}_2\text{Ti}_2\text{O}_7$ and $\text{Er}_2\text{Ti}_2\text{O}_7$, which are the primary subjects of this thesis. Using elastic and inelastic neutron scattering techniques, we study the magnetic ground state of $\text{Yb}_2\text{Ti}_2\text{O}_7$ and $\text{Er}_2\text{Ti}_2\text{O}_7$ as a function of various perturbations such as disorder, dilution, hydrostatic pressure and chemical pressure. Our results on $\text{Yb}_2\text{Ti}_2\text{O}_7$ reveal a spin liquid ground state in ambient pressure. The spin liquid state of $\text{Yb}_2\text{Ti}_2\text{O}_7$ is found to be unstable upon the application of hydrostatic pressure, from which a ferromagnetic ground state is obtained. $\text{Er}_2\text{Ti}_2\text{O}_7$ is known to magnetically order into an antiferromagnetic ψ_2 state at 1.2 K. Diluting the Er^{3+} site with non-magnetic Y^{3+} ions causes a transition from the ψ_2 antiferromagnetic state found in $\text{Er}_2\text{Ti}_2\text{O}_7$ to a frozen mosaic of ψ_2 and ψ_3 at a critical dilution of $\sim$ 20%-Y. Furthermore, it will be demonstrated that $\text{Er}_2\text{Ti}_2\text{O}_7$ has a rich phase diagram in both an applied magnetic field as well as with the application of chemical pressure. The fragile magnetism in both $\text{Yb}_2\text{Ti}_2\text{O}_7$ and $\text{Er}_2\text{Ti}_2\text{O}_7$ is discussed in terms of multiphase competition that promotes spin liquid behaviour and order-by-disorder phenomena.

Acknowledgements

I'm deeply grateful to my PhD supervisor Bruce Gaulin, who is a constant source of motivation and inspiration. Bruce is an excellent mentor, who always makes time to meet with his students, even with his very busy schedule. I am particularly thankful to Bruce for introducing me to the world of neutron scattering, for teaching me effective scientific writing, for providing me with the amazing opportunity to travel around the world, and finally, for sharing many beers at the Phoenix. I sincerely hope that I will be able to continue collaborating with Bruce. I will always be appreciative to Michel Gingras for his strong recommendation to work with Bruce; I too would encourage any prospective student to work under Bruce's supervision.

None of the works presented in this thesis would be possible without the technical help of excellent scientists from McMaster University, the NIST Center for Neutron Research and the Oak Ridge National Lab. I am forever grateful to: Hanna Dabkowska, Antoni Dabkowski, Jim Garrett, Yegor Vekhov, Juscelino Leao, Alan Ye, Sergiy Gladchenko, Nick Butch, Jose Rodriguez-Rivera, Guangyong Xu, Matt Stone, Adam Aczel and Alexei Kolesnikov. I am also very grateful for the support I received from Cheryl Johnston, Rosemary McNeice, Tina Stewart and Mara Esposto.

I also want to thank my PhD colleagues from McMaster University: Edwin Kermarrec, Jerod Wagman, Connor Buhariwalla, Dalini Maharaj, Casey Marjerrison, Murray Wilson, Sean Takahashi, Yipeng Cai, Tim Munsie, Kyle Ma and James Beare. Thank you for the friendships that we developed through all these years as well as the fun atmosphere that we kept in the office.

A special thank you to my favorite collaborator, Alannah Hallas: thank you for your support, your ideas, your motivation, your passion, your amazing writing skills and also for letting me bombard you with tons of good and bad scientific ideas, even late on a Saturday night!

On a more personal note, I would like to dedicate my thesis to my family: Hugues, Johanne, Véronique, Cédric, Annabelle, Éloise, Alannah, Lucy and Casper. Merci pour les encouragements, votre affection et votre compréhension envers ma passion.

Contents

Preface

This is a stapled paper thesis. It contains six published articles. The surrounding material is meant to provide background and place the work into a broader context. All of the original research is found in the six publications.

Publication I: "*Neutron spectroscopic study of crystalline electric field excitations in stochiometric and lightly stuffed* $Yb_2Ti_2O_7$", Jonathan Gaudet, Dalini D. Maharaj, Gabriele Sala, Edwin Kermarrec, Kate A. Ross, Hanna A. Dabkowska, Alexander I. Kolesnikov, Garrett E. Granroth, and Bruce D. Gaulin. Physical Review B **92**, 134420 (2015). Reproduced from Ref. [1] with permission copyrighted by the American Physical Society.

Publication II: "*Gapless quantum excitations from an icelike splayed ferromagnetic ground state in stoichiometric* $Yb_2Ti_2O_7$", Jonathan Gaudet, Kate A. Ross, Edwin Kermarrec, Nicholas P. Butch, Georg Ehlers, Hanna A. Dabkowska, and Bruce D. Gaulin. Physical Review B **93**, 064406 (2016), editor's suggestion. Reproduced from Ref. [2] with permission copyrighted by the American Physical Society.

Publication III: "*Ground state selection under pressure in the quantum pyrochlore magnet* $Yb_2Ti_2O_7$", Edwin Kermarrec, Jonathan Gaudet, Katharina Fristch, Rustem Khasanov, Zurab Guguchia, Clemens Ritter, Kate A. Ross, Hanna A. Dabkowska, and Bruce D. Gaulin. Nature Communications **8** 14810 (2017). Reproduced from Ref. [3] with permission copyrighted by Nature Publishing Group.

Publication IV: "*Magnetic dilution and domain selection in the XY pyrochlore antiferromagnet* $Er_2Ti_2O_7$", Jonathan Gaudet, Alannah M. Hallas, Dalini D. Maharaj, Connor R.C. Buhariwalla, Edwin Kermarrec, Nicholas P. Butch, Timothy J. S. Munsie, Hanna A. Dabkowska, Graeme M. Luke, and Bruce D. Gaulin. Physical Review B **94**, 060407(R) (2016). Reproduced from Ref. [4] with permission copyrighted by the American Physical Society.

Publication V: "*Experimental evidence for field-induced emergent clock anisotropies in the XY pyrochlore* $Er_2Ti_2O_7$", Jonathan Gaudet, Alannah M. Hallas, Jacque Thibault, Nicholas P. Butch, Hanna A. Dabkowska, and Bruce D. Gaulin. Physical Review B **95**, 054407 (2017). Reproduced from Ref. [5] with permission copyrighted by the American Physical Society.

Publication VI: "*Effect of chemical pressure on the single-ion properties of the erbium pyrochlores*", Jonathan Gaudet, Alannah M. Hallas, Alexander I. Kolesnikov, and Bruce D. Gaulin. Physical Review B **97**, 024415 (2018). Reproduced from Ref. [6] with permission copyrighted by the American Physical Society.

In the course of my doctoral studies, I have benefited from fruitful collaborations with colleagues from McMaster. These collaborations resulted in several publications where I do not appear as the primary author, nor are they included in this thesis. However, these works strongly influenced the conclusions reached in this thesis and it is thus, worthwhile to enumerate these works here:

Publication VII: "*XY antiferromagnetic ground state in the effective $S = 1/2$ pyrochlore $Yb_2Ge_2O_7$*", Alannah M. Hallas, Jonathan Gaudet, Murray N. Wilson, Timothy J. Munsie, Adam A. Aczel, Matthew B. Stone, Rafael S. Freitas, Angel M. Arevalo-Lopez, J. Paul Attfield, Makoto Tachibana, Christopher R. Wiebe, Graeme M. Luke, and Bruce D. Gaulin. Physical Review B **93**, 104405 (2016). [7]

Publication VIII: "*Universal dynamic magnetism in Yb pyrochlores with disparate ground states*", Alannah M. Hallas, Jonathan Gaudet, Nicholas P. Butch, Makoto Tachibana, Rafael S. Freitas, Graeme M. Luke, Christopher R. Wiebe, and Bruce D. Gaulin . Physical Review B: Rapid Communications **93**, 100403(R) (2016). [8]

Publication IX: "*Phase competition in the Palmer-Chalker XY pyrochlore $Er_2Pt_2O_7$*", Alannah M. Hallas, Jonathan Gaudet, Nicholas P. Butch, Guangyong Xu, Makoto Tachibana, Christopher R. Wiebe, Graeme M. Luke, and Bruce D. Gaulin. Physical Review Letters **119**, 187201 (2017). [9]

Publication X: "*Experimental insights into ground state selection of quantum XY pyrochlores*", Alannah M. Hallas, Jonathan Gaudet, and Bruce D. Gaulin. Annual Reviews of Condensed Matter Physics **9**, 105 (2018). [10]

Chapter 1

Introduction

The magnetic properties of materials are strongly connected to their underlying crystalline structures. In this thesis, we take full advantage of this fact by studying the magnetism of cubic pyrochlore magnets $A_2B_2O_7$. As shown in Fig.1.1(a), both the A-site and the B-site of the pyrochlore structure form an independent network of corner-sharing tetrahedra. When one or both of the two sublattices are decorated with magnetic ions, the tetrahedral motif of the pyrochlore structure frustrates the near neighbour spin interactions and can prevent the system from selecting a conventional long-range magnetic order at low temperature. In such a case, the spin configuration of a frustrated system has an extensive degeneracy and a magnetic ground state that can potentially be described by a strongly entangled quantum mechanical wave function. The most famous example is the quantum spin liquid ground state, where the spins do not order at any temperature and remain dynamic down to $T = 0$ K. [11]

The most well-studied family of pyrochlore magnets for the topic of frustrated magnetism is the rare earth titanates $A_2\mathrm{Ti}_2\mathrm{O}_7$ [12]. In this family of pyrochlores, the B-site is occupied by non-magnetic Ti^{4+} and the A-site is occupied by a trivalent rare earth ion such as Ho^{3+}, Yb^{3+}, Er^{3+}, or Tb^{3+}. An important ingredient for describing the magnetism in these systems is their spin anisotropy. The spin anisotropy in the pyrochlore structure is defined locally which implies that the orientation of the Ising axis is different for every ion in a single tetrahedron. The local environment of the A-site in the pyrochlore lattice is shown in Fig.1.1(b). The Ising axis, also known as the local [111] axis, is defined as the direction that links the rare earth site to the centers of the two tetrahedra it connects. Pyrochlore magnets with Ising anisotropy will have their spins point into or out of the centre of each tetrahedron (red arrow in Fig.1.1(b)) and those with XY anisotropy will have their spins lying in the plane perpendicular to the local [111] axis (blue arrow in Fig.1b)). For Heisenberg spin anisotropy, the spins have no constraints and are free to point in any direction (black arrow in Fig.1b)). Each of these spin anisotropies can be obtained within the rare earth pyrochlore titanates by simply changing the rare-earth ion sitting on the A-site [13].

Theoretically, an astonishingly broad range of magnetic ground states can be stabilized on a pyrochlore lattice by mixing the different spin anisotropies with various magnetic interactions. For example, a frustrated and macroscopically degenerate 2-in 2-out spin state is stabilized for Ising spins with net ferromagnetic interactions [14], but an unfrustrated all-in all-out long-range magnetic order is obtained for Ising spins with antiferromagnetic interactions [15]. In the quest to find spin liquid behavior in real materials, it is thus natural that significant scientific attention has been devoted to investigating pyrochlore systems with Ising anisotropy and ferromagnetic interactions. The archetypical examples of such systems are the classical spin ices $\mathrm{Ho_2Ti_2O_7}$ and $\mathrm{Dy_2Ti_2O_7}$ [14, 16, 17]. It was found that the macroscopic degeneracy of the 2-in 2-out spin configuration found in these materials is exactly analogous to the case of proton disorder in water ice, hence the name spin ice [18]. The magnetic excitations in spin ice can be mapped onto diffusive magnetic charges where the positive and negative magnetic charges correspond to an excited tetrahedron with a 3-in 1-out spin configuration and a 3-out 1-in spin configuration, respectively. Both effective magnetic charges are produced by flipping a single spin within the two-in two-out manifold and the interaction with each other occurs via an emergent Coulomb interaction. [19, 20]. As such, these emergent quasi-particles mimic magnetic monopoles, a particle that is absent in the current theory of our universe.

A route towards promoting frustration as well as quantum effects in pyrochlore magnets is to investigate materials with local XY anisotropy [10]. Theoretical proposals suggest that XY anisotropy provides a key ingredient in the stabilization of various spin liquids such as the quantum spin ice state [21–28]. In addition to the emergent magnetic monopoles excitations present in the classical case, the quantum spin ice state has emergent electric monopole excitations and photon excitations that are predicted to arise at low temperatures. Furthermore, XY pyrochlore magnets can experience order-by-disorder, a phenomena where a material adopts a particular long-range magnetically ordered state due to its propensity to fluctuate [29, 30]. This type of magnetic ordering corresponds to an entropic ground state selection rather than the more conventional ground state selection via energetic arguments. Both order-by-disorder

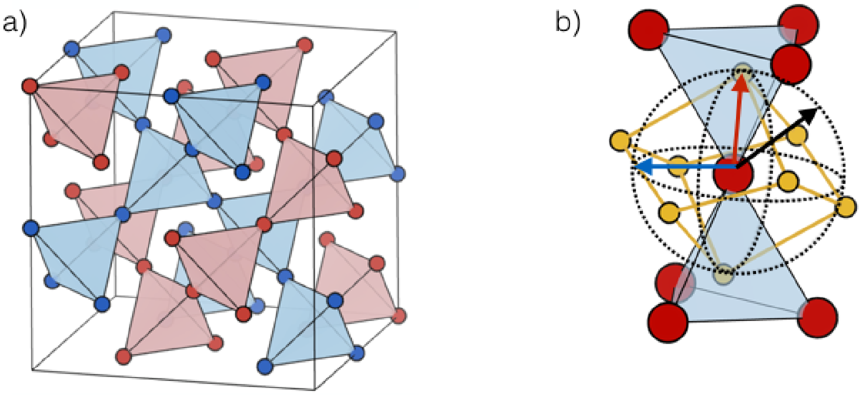

Figure 1.1: (a) The A-site and B-site basis of the cubic $Fd\bar{3}m$ pyrochlore lattice forms two independant networks of corner-sharing tetrahedra. (b) Local oxygen environment of the A-site in the pyrochlore lattice, which consists of a cube of oxygen atoms that is distorted along the local Ising axis. The different arrows (spins) shown in (b) correspond to the possible spin anisotropies of the pyrochlore lattice: local Ising anisotropy (red spin), local XY anisotropy (blue spin) and Heisenberg spins (black spin).

and quantum spin ice are magnetic phenomena that have yet to be definitively observed in any real materials, but have been discussed as relevant in the XY pyrochlores studied in this thesis: $Yb_2Ti_2O_7$ and $Er_2Ti_2O_7$.

As will be shown in Chapter 2 and 3, both $Yb_2Ti_2O_7$ and $Er_2Ti_2O_7$ have local XY anisotropy [1, 6, 13, 31–33]. $Yb_2Ti_2O_7$ displays ferromagnetic exchange [34] and its low energy spin excitations consist of a continuum of gapless excitations at low temperature [2, 35–37]. This continuum of excitations has been proposed to originate from the proximity to a quantum spin ice phase [35, 38–40]. Regarding $Er_2Ti_2O_7$, this material orders into an XY antiferromagnetic long-range state at 1.2 K with a ground state selection that is argued to originate from quantum and thermal order-by-disorder effects [41–47]. In this thesis, I will study the magnetic ground states of both $Yb_2Ti_2O_7$ and $Er_2Ti_2O_7$ under various perturbations such as chemical disorder [1, 2], hydrostatic pressure [3], magnetic dilution [4] and chemical pressure [6–10]. For all these perturbed systems, neutron scattering was used to probe their spin structures as well as their associated magnetic excitations. Our results suggest that the magnetic ground states of XY pyrochlores are unusually sensitive to many perturbations. This magnetic fragility is caused by an intrinsic multiphase competition that exists between different magnetic ground states. It is proposed that multiphase competition promotes spin liquid behavior and order-by-disorder effects in rare earth XY pyrochlores [48, 49].

The introduction begins in **Section 1.1** with a short description of the magnetism in XY rare earth pyrochlore magnets. The single-ion properties of the rare-earth ions on the pyrochlore lattice is presented as well as the relevant spin interactions. Then **Section 1.2** describes the relevant concepts of neutron scattering that are important to understanding the results and analysis found in this thesis. Chapter 2 and Chapter 3 shows the results and analysis of neutron scattering experiments performed to investigate the magnetic ground state properties of $Yb_2Ti_2O_7$ and $Er_2Ti_2O_7$, respectively.

1.1 Magnetism in rare earth XY pyrochlores

The magnetism of the pyrochlore magnets $A_2Ti_2O_7$ originates from the unpaired f electrons belonging to the rare earth ion. The single-ion properties of the rare earth ions are dominated by the Coulomb interaction between f electrons. Following Hund's rules, the Coulomb interaction is minimized by first maximizing the total spin angular momentum S and second by maximizing the total orbital angular momentum L. For the case of the Yb^{3+} ion, this leads to an electronic state with $L = 3$ and $S = 1/2$ while it leads to an electronic state with $L = 6$ and $S = 3/2$ for the Er^{3+} ions. This manifold is $(2L + 1)(2S + 1)$ degenerate, but this degeneracy is lifted by the spin-orbit coupling, the crystal electric field of the surrounding ions (CEF) and the spin-spin interactions (see Fig.1.2).

The spin-spin interactions in rare earth pyrochlores are dominated by the superexchange interaction. Due to the strong spatial localization of the f orbitals, the overlap of the $4f - O(2p) - 4f$ wave functions is weak and so too are the superexchange interactions, on the order of 1 meV [34]. The CEF is the Coulomb potential that originates from the presence of neighboring ions. For pyrochlores $A_2B_2O_7$, the CEF is dominated by the oxygen ions that have strong electro-negativity giving a magnitude in energy of about 100-150 meV [13], and it provides a much stronger energy scale than that of the exchange interactions. Finally, the spin-orbit coupling goes roughly as Z^4 where Z is the atomic number. Since rare-earth ions are heavy, the spin-orbit coupling is on the order of 0.3-3 eV [50] and dominates both the CEF and the exchange interactions. Such stratification of the energy scales in the description of rare earth pyrochlores is convenient because it allows the exchange interactions to be described as a perturbation of the CEF interaction

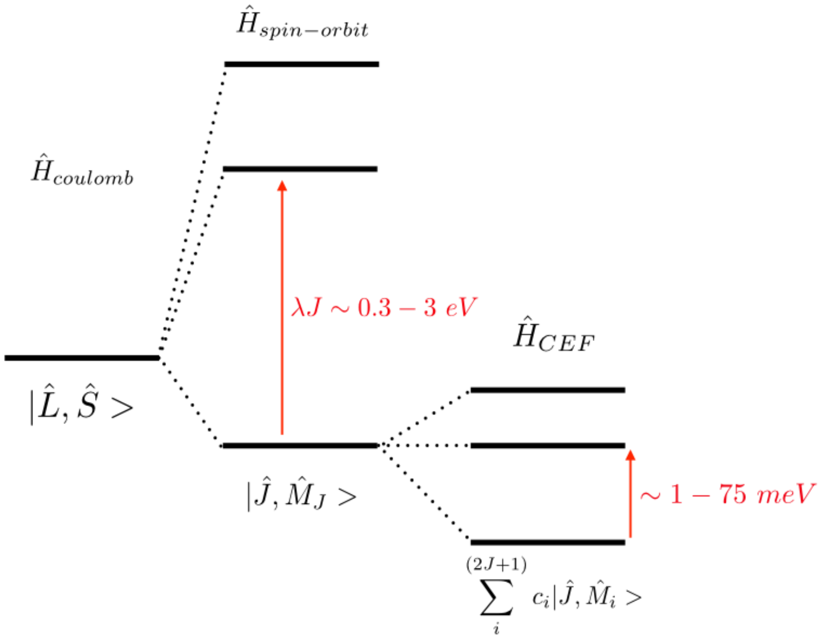

Figure 1.2: Energy scheme of the relevant interactions responsible for the single-ion properties of the rare-earth ion in the oxide pyrochlore structure. The Coulomb potential stabilizes a ground state with orbital angular momentum L and spin S. The $(2L+1)(2S+1)$ ground state manifold is split by the spin-orbit coupling that selects a ground state with quantum number J where, $\hat{J} = \hat{L} + \hat{S}$ is the total angular momentum and m_J is its projection within the local [111] axis. Finally, the degeneracy of the $(2J+1)$ ground-state spin-orbit manifold is lifted by the crystal electric field. The eigenfunctions of the CEF interaction can be written in terms of linear combinations of the $(2J+1)$ spin-orbit ground state manifold.

which in turn can be described as a perturbation of the spin-orbit coupling.

The spin-orbit interaction goes as:

$$\hat{H}_{s-o} = \lambda \hat{L} \cdot \hat{S} = \frac{\lambda}{2}[J(J+1) - L(L+1) - S(S+1)], \tag{1.1}$$

and is diagonal within the $|J, M_J\rangle$ basis where J is the quantum number of the total momentum operator $\hat{J} = \hat{L}+\hat{S}$. The spin-orbit ground states are the single-ion wave functions with $J = L+S$ if $\lambda \leq 1$ or $J = L - S$ if $\lambda > 1$. From atomic physics, it is known that λ is positive for f orbitals that are less than or equal to half-filled and that λ is negative for ions with f orbitals that are more than half-field. For both Er^{3+} and Yb^{3+}, the f orbitals are more than half-filled resulting in a ground state with J=$\frac{15}{2}$ for Er^{3+} and J=$\frac{7}{2}$ for Yb^{3+}. The spin-orbit ground state is $2J+1$

degenerate and is separated from the first spin-orbit excited states by λJ. The CEF interaction is responsible for the lifting of the $2J + 1$ degeneracy of the spin-orbit ground state. For Er^{3+} and Yb^{3+}, λJ is about 1-2 eV [50] and, consequently, the calculation of the low energy states can be performed solely using the $2J + 1$ eigenfunctions of the spin-orbit ground state. Such simplification is not possible for all rare earth ions. For example, λJ for Ce^{3+} and Sm^{3+} is about 200 meV and 365 meV, respectively [50]. As a result, a perturbative approach fails and the single ion wave functions need to be found by diagonalizing the total Hamiltonian $\hat{H} = \hat{H}_{s-o} + H_{CEF}$ within the full $|L, S\rangle$ manifold.

As briefly mentioned before, the CEF interaction originates from the electric field of the neighboring ions. The CEF potential is simply the sum of the electrostatic potential between the charges of the magnetic ion and the neighboring ions. The crystalline potential energy is then given by:

$$\hat{H}_{CEF} = \sum_{j} \sum_{j} \frac{q_j q_i}{|(\mathbf{R_j} - \mathbf{r_i})|}, \tag{1.2}$$

where q_i is the effective charge and r_i is the position of the i-th electron within the rare earth ion shell. Likewise, q_j is the effective charge and R_j is the position of the j-th neighboring ion. This potential is described in terms of the $\hat{x}$, $\hat{y}$ and $\hat{z}$ operators that determine the electrical field strength as a function of the position of the charges with respect to the magnetic ion. As the CEF interaction is a perturbation to the spin-orbit coupling, we are interested in applying the time-independent degenerate quantum perturbation theory using the ground state eigenvectors of the spin-orbit coupling. Thus, the CEF eigenfunctions and eigenvalues are obtained by diagonalizing the CEF Hamiltonian within the $|J, M_J\rangle$ basis. Such a task requires the calculation of the matrix element $\langle J, M_{J'}|\hat{H}_{CEF}|J, M_J\rangle$, which is possible using the Stevens operator formalism, $\hat{O}_n^m \equiv \hat{O}_n^m(J_x, J_y, J_z)$. This formalism consists of replacing each $\hat{x}$, $\hat{y}$ and $\hat{z}$ operator by their corresponding $\hat{J}_x$, $\hat{J}_y$ and $\hat{J}_z$ operators [51]. When doing so, the noncommutativity of $\hat{J}_x$, $\hat{J}_y$ and $\hat{J}_z$ has to be taken into account by replacing the products of $\hat{x}$, $\hat{y}$ and $\hat{z}$ with an operator that combines all possible permutations of $\hat{J}_x$, $\hat{J}_y$ and $\hat{J}_z$. For example, $\hat{x}\hat{y} = \frac{\hat{J}_x\hat{J}_y + \hat{J}_y\hat{J}_x}{2}$.

The number and choice of Stevens operators $\hat{O}_n^m$ needed to describe the electrical field for a given charge distributions depends on the point-group symmetry of the local crystalline environment [52]. For the case of the A-site in the rare-earth pyrochlores $A_2B_2\mathrm{O}_7$, the point group symmetry is D_{3d} with the following symmetry elements: a 3-fold rotation axis, an inversion center, two 2-fold rotation axes (which define the local x and y axes) and two mirror planes. The 3-fold rotation axis defines the z axis of the Hamiltonian and corresponds to the Ising or local [111] axis. The crystal electric field Hamiltonian for an ion with D_{3d} point symmetry is

$$\hat{H}_{CEF} = B_2^0\hat{O}_2^0 + B_4^0\hat{O}_4^0 + B_4^3\hat{O}_4^3 + B_6^0\hat{O}_6^0 + B_6^3\hat{O}_6^3 + B_6^6\hat{O}_6^6, \tag{1.3}$$

where the operators $\hat{O}_2^0$, $\hat{O}_4^0$, etc. are the Stevens operators [51]. The terms B_2^0, B_4^0, etc. are the crystal electric field constants that can be calculated using point-charge calculations [53] or experimentally determined using inelastic neutron scattering [54]. The latter method will be discussed in further detail in section 1.2 as well as in Publication I (chapter 2) and VI (chapter 3).

For the case of the XY rare earth pyrochlores, the ground-state of the CEF interaction is isolated from its first excited CEF level by ~70 meV in $\mathrm{Yb_2}B_2\mathrm{O_7}$ [1, 7] and ~6 meV in $\mathrm{Er_2}B_2\mathrm{O_7}$ [6]. As we are interested in the magnetic properties of these systems at very low temperature, the local g-tensor of the rare-earth ions can be well approximated by projecting the system solely within the CEF ground state. By doing so, the g-tensor components of the Zeeman coupling are given by [13]:

$$g_{\parallel} = 2g_J|\left\langle \phi_0^{\pm}\right| J_z \left|\phi_0^{\pm}\right\rangle| \;\text{ and} \tag{1.4}$$

$$g_{\perp} = g_J|\left\langle \phi_0^{+}\right| J_+ \left|\phi_0^{-}\right\rangle| = g_J|\left\langle \phi_0^{-}\right| J_- \left|\phi_0^{+}\right\rangle| \tag{1.5}$$

where $g_{\parallel}$ is the g-tensor component along the Ising direction and $g_{\perp}$ is the component of the g-tensor that is perpendicular to the Ising direction. Thus, a local Ising spin anisotropy is obtained when $g_{\parallel}$ is greater than $g_{\perp}$. Conversely, the local spin anisotropy is XY when $g_{\perp}$ is larger than $g_{\parallel}$. For both $\mathrm{Yb_2Ti_2O_7}$ and $\mathrm{Er_2Ti_2O_7}$, $g_{\perp} > g_{\parallel}$ indicating that both materials are examples of XY pyrochlore magnets [1, 6].

As the origin of the single-ion properties of the rare-earth pyrochlores have been discussed, we can now focus on the important spin-spin interactions that exist in these system. It has been shown that the super-exchange interaction is on the order of 1 meV in both $\mathrm{Yb_2}B_2\mathrm{O_7}$ and $\mathrm{Er_2}B_2\mathrm{O_7}$ and thus, the exchange interaction is important only at low temperature [34, 35, 42]. For the pyrochlore structure, the most general form of the nearest-neighbor exchange interaction

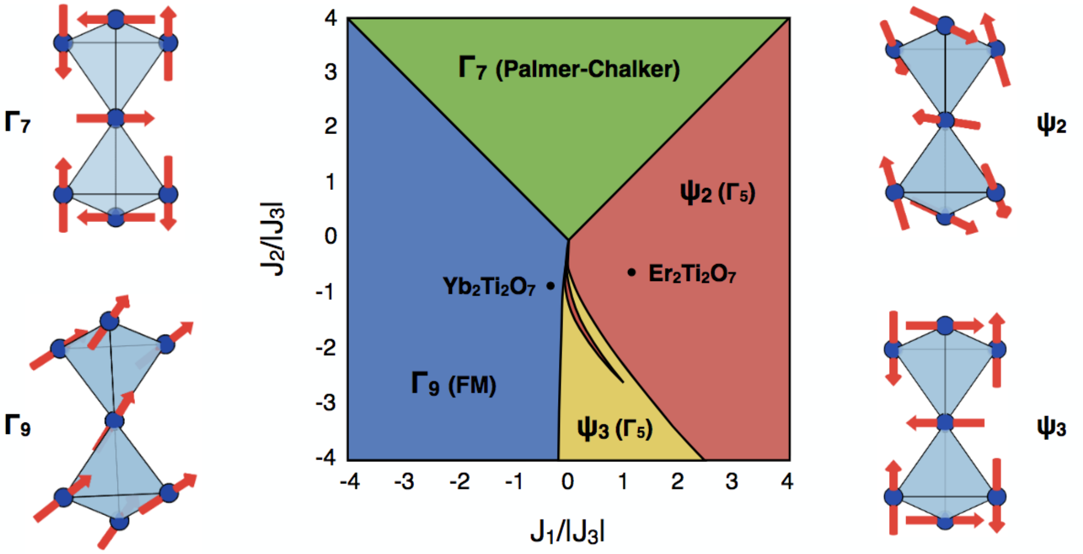

Figure 1.3: The calculated phase diagram for rare earth XY pyrochlores adapted from Ref. [49] using a classical treatment of the anisotropic exchange Hamiltonian shown in equation 1.6 with $J_4 = 0$ and $J_3 < 1$. The degeneracy of the ψ_2 and ψ_3 states within such a model is lifted by the order-by-disorder mechanism. The spin structures associated with each ordered phase are shown. The exchange parameters of $Yb_2Ti_2O_7$ and $Er_2Ti_2O_7$ obtained from inelastic neutron scattering in ref. [35] and [42] are indicated in the phase diagram. This figure has been reproduced from Ref. [10] with permission copyrighted by the Annual Review of Condensed Matter Physics.

(H_{ex}) is written as [35,49,55,56]:

$$\hat{H}_{ex} = \sum_{\langle i,j \rangle} J_{ij}^{\mu\nu} S_i^{\mu} S_j^{\nu}, \tag{1.6}$$

where the sum $\langle i,j \rangle$ goes over nearest-neighbor spins and μ, $\nu = x', y', z'$. In general, $J_{ij}^{\mu\nu}$ is a 3×3 matrix with nine different components that are reduced to four independent exchange parameters due to the symmetries of the pyrochlore lattice (J_1, J_2, J_3, J_4). With respect to the direct local bond between two spins on the same tetrahedron, the significance of the four independent exchange parameters can be interpreted as the following: J_1 is an XY term, J_2 is an Ising term, J_3 is a symmetric off-diagonal term and J_4 is an effective Dzyaloshinskii-Moriya term. By assuming the origin of our coordinate system to be the center of a tetrahedron and the positions of the four ions within the tetrahedron given by: $\mathbf{r}_0 = \frac{a}{8}(1,1,1)$, $\mathbf{r}_1 = \frac{a}{8}(1,-1,-1)$, $\mathbf{r}_2 = \frac{a}{8}(-1,1,-1)$ and $\mathbf{r}_3 = \frac{a}{8}(1,1,1)$, the exchange matrix between the ions at $\mathbf{r}_0$ and $\mathbf{r}_1$ is [49]:

$$\hat{J}_{01} = \begin{bmatrix} J_2 & J_4 & J_4 \\ -J_4 & J_1 & J_3 \\ -J_4 & J_3 & J_1 \end{bmatrix}. \tag{1.7}$$

All the other exchange matrices between the different ions of a tetrahedron can be obtained by a proper rotation of the $\hat{J}_{01}$ matrix.

In the exchange Hamiltonian written in equation 1.6, the operators $\mathbf{S_i} = (S_i^{x'}, S_i^{y'}, S_i^{z'})$ describe the magnetic moment of the rare-earth ion in a global axis frame of reference. However, since the anisotropy of the rare earth ions is defined locally, it is common to rewrite the Hamiltonian of equation 1.6 within a basis of local coordinates (x, y, z) where the z axis of each ion is defined as the local [111] or Ising axis. Then, the anisotropic exchange Hamiltonian can be written as follows [35,49]:

$$\begin{aligned} \hat{H}_{ex} = \sum_{\langle i,j \rangle} \{ & J_{zz} S_i^z S_j^z - J_{\pm}(S_i^+ S_j^- + S_i^- S_j^+) \\ & + J_{\pm\pm}[\gamma_{ij} S_i^+ S_j^+ + \gamma_{ij}^* S_i^- S_j^-] \\ & + J_{\pm\pm}[S_i^z(\zeta_{ij} S_j^+ + \zeta_{ij}^* S_j^-) + i \leftrightarrow j] \} \end{aligned} \tag{1.8}$$

with γ = -ζ^* and

$$\zeta = \begin{bmatrix} 0 & -1 & e^{i\frac{\pi}{3}} & e^{-i\frac{\pi}{3}} \\ -1 & 0 & e^{-i\frac{\pi}{3}} & e^{i\frac{\pi}{3}} \\ e^{i\frac{\pi}{3}} & e^{-i\frac{\pi}{3}} & 0 & -1 \\ e^{-i\frac{\pi}{3}} & e^{i\frac{\pi}{3}} & -1 & 0 \end{bmatrix}. \tag{1.9}$$

The relationship between the exchange parameters within the global coordinate frame (x', y', z') and the local coordinate (x, y, z) frame is given by the following [49]:

$$\begin{aligned} J_{zz} &= -\frac{1}{3}(2J_1 - J_2 + 2J_3 + 4J_4) \\ J_{\pm} &= -\frac{1}{6}(2J_1 - J_2 - J_3 - 2J_4) \\ J_{\pm\pm} &= -\frac{1}{6}(J_1 + J_2 - 2J_3 + 2J_4) \\ J_{z\pm} &= -\frac{1}{3\sqrt{2}}(J_1 + J_2 + J_3 - J_4). \end{aligned} \tag{1.10}$$

In both $Yb_2B_2O_7$ and $Er_2B_2O_7$, a well isolated ground state doublet is obtained due to strong CEF effects. Thus, the system can be projected within the CEF ground state doublet by introducing new effective pseudo-spin 1/2 operators. These pseudo-spin 1/2 operators respect the non-commutation rule for general spin operators ($[S_i^\alpha, S_i^\beta] = i\epsilon_{\alpha\beta\gamma}S_i^\gamma$) and have an anisotropy that is dictated by the local CEF. To take the CEF anisotropy into account, the dipole moment of the spin operator is written as [49]:

$$m_i^\alpha = \sum_{\beta=1}^{3} g_{local}^{\alpha\beta} S_i^\beta \tag{1.11}$$

where the g-tensor $g_{local}^{\alpha\beta}$ is diagonal within the local basis state:

$$\hat{g}_{local} = \begin{bmatrix} g_\perp & 0 & 0 \\ 0 & g_\perp & 0 \\ 0 & 0 & g_{\|} \end{bmatrix}. \tag{1.12}$$

Other spin-spin interactions in the rare earth pyrochlore magnets are important. For example, the dipolar interaction is responsible for the stabilization of the spin-ice manifold in both $Ho_2Ti_2O_7$ and $Dy_2Ti_2O_7$ [57–60]. The nearest-neighbour part of the dipolar interaction is given by:

$$\hat{H}_{dip} = D\sum_{\langle i,j\rangle}[\frac{\mathbf{S_i}\cdot\mathbf{S_j}}{|R^3_{ij}|} - 3\frac{(\mathbf{S_i}\cdot\mathbf{R_{ij}})(\mathbf{S_j}\cdot\mathbf{R_{ij}})}{|R^5_{ij}|}], \tag{1.13}$$

with $D = \frac{\mu_o\mu_B^2}{4\pi}$ and where μ_0 is the permeability of free space, μ_B is the Bohr magneton and $|R_{ij}|$ is the distance between two neighboring spins. Since its strength goes as μ^2_{eff}, the dipolar interaction for both $Yb_2B_2O_7$ ($\mu_{eff} \sim 2\mu_B$ [1, 7]) and $Er_2B_2O_7$ ($\mu_{eff} \sim 4\mu_B$ [6]) is less important than for the classical spin ices $Ho_2Ti_2O_7$ ($\mu_{eff} \sim 10\mu_B$ [54, 61]) and $Dy_2Ti_2O_7$ ($\mu_{eff} \sim 10\mu_B$ [61, 62]). Even if it is small for the XY rare earth pyrochlores ($\frac{\mu_0\mu^2_{eff}}{4\pi|R_{nn}|^3}$ ∼0.3 K), the dipolar interaction can included in the effective spin Hamiltonian of XY pyrochlores. Once projected within the pseudo-spin 1/2 basis, it has been shown that the dipolar interaction on the pyrochlore lattice can be written in the same mathematical form as the anisotropic exchange Hamiltonian shown in equation 1.8, with the following correspondence [44]:

$$\begin{bmatrix} J^{dip}_{zz} \\ J^{dip}_{\pm} \\ J^{dip}_{\pm\pm} \\ J^{dip}_{z\pm} \end{bmatrix} = \frac{D}{12}\begin{bmatrix} 20g^2_{\parallel} \\ -g^2_{\parallel} \\ 7g^2_{\perp} \\ -2\sqrt(2)g_{\parallel}g_{\perp} \end{bmatrix}. \tag{1.14}$$

This result means that because of the projection of the system within the CEF ground state doublet, the form of the spin Hamiltonian in equations 1.6 and 1.8 is accurate even with the addition of dipolar interactions. The only correction is that the dipolar term is absorbed in the definition of the effective exchange parameters. For example, the effective exchange parameter J'_{zz} is given by $J'_{zz} = J_{zz} - J^{dip}_{zz} = J_{zz} - \frac{20Dg^2_{\parallel}}{12}$.

Inelastic neutron scattering and magnetization and have been used to estimate the anisotropic exchange parameters of XY pyrochlores [9, 35, 36, 42, 63–65]. In all the XY pyrochlore magnets probed so far, the exchange parameter J_3 was always refined to be negative and J_4 refined to be small and negligible. Within such constraints, the authors of ref. [49] derived a classical phase diagram for the subspace of exchange parameters found to be relevant for rare earth XY pyrochlores. The resulting phase diagram is shown in Fig.1.3 along with the magnetic structure of the different ordered phases that are predicted to be stabilized. All these magnetic ordered phases correspond to a k=0 magnetic structure. The Γ_9 structure is a splayed ferromagnetic structure with the spins polarized along the (001) direction, but tilted along their respective local [111] axes. The tilting or splayed angle is the same for all spins in one tetrahedron, but two spins are tilting along the center of the tetrahedron and two spins are pointing away from the center of the tetrahedron. As will be discussed in Chapter 2, the magnetic structure of $Yb_2Ti_2O_7$ under pressure has been refined to belong to the Γ_9 phase with a small splayed angle ($\sim 1^\circ$) [3]. Both the Γ_7 and Γ_5 phases are XY magnetic structures where the spins are constrained to lie within the XY local plane. The Γ_7, also defined as the Palmer-Chalker phase, is obtained for isotropic exchange interactions with dominant dipolar interactions [66]. Within the family of XY pyrochlore magnets, both $Er_2Sn_2O_7$ and $Er_2Pt_2O_7$ order into the Palmer-Chalker state [9, 65]. Finally, the Γ_5 phase has two different basis vectors ψ_2 and ψ_3 which correspond to an XY pyrochlore structure where all the spins point along the local x (ψ_2) or y (ψ_3) axis. At the mean field level, the ψ_2 and ψ_3 states are degenerate [42, 43], but in the model presented in ref. [49], the degeneracy is broken by order-by-disorder effects. In such a case, the system will order into the structure with the basis vector (ψ_2 and ψ_3) that minimizes the spin wave energie and, hence, maximizes the entropy. $Er_2Ti_2O_7$, $Er_2Ge_2O_7$ and $Yb_2Ge_2O_7$ have all been refined to belong to the Γ_5 phase [7, 41, 67–69]. $Er_2Ti_2O_7$ has a ψ_2 ground state [70] and $Er_2Ge_2O_7$ is argued to order into a pure ψ_3 state [68]. The exact nature of the Γ_5 phase in $Yb_2Ge_2O_7$ is still unknown at the moment.

From the calculated phase diagram of XY pyrochlores shown in Fig.1.3 and from the experimental observation of all the predicted ordered phases in the known XY pyrochlores, it is clear that these materials live in a rich phase space with a possibility for competition between these ordered phases. This intrinsic phase competition between the Γ_9, Γ_7 and Γ_5 phases can promote spin liquid behavior, especially for materials with exchange parameters that lie near a phase boundary between two of these phases [48, 49]. Such a scenario of phase competition is proposed for $Yb_2Ti_2O_7$. As will be discussed in Chapter 1, $Yb_2Ti_2O_7$ has strong sensitivity to both disorder and hydrostatic pressure [3, 71, 72]. This observation can potentially be explained by phase competition between the ferromagnetic Γ_9 state and the antiferromagnetic Γ_5 state. A similar scenario is also proposed for the origin of the spin liquid behavior observed in $Er_2Sn_2O_7$ and $Er_2Pt_2O_7$ where phase competition between antiferromagnetic Γ_5 and Γ_9 phases has also been argued to exist [9, 63, 65]. Finally, phase competition is also responsible for promoting order-by-disorder effects in rare earth XY pyrochlore such as, potentially, the ψ_2 ground state selection in $Er_2Ti_2O_7$ and this fact will be further investigated in Chapter 2.

1.2 Neutron scattering

The neutron is a particle with physical properties that are perfectly suited to study the magnetic behavior of condensed matter systems via scattering experiments. First, the neutron has a spin, $\mu_n = -1.042 \times 10^{-3}\mu_B$, which allows a direct coupling between the neutron's spin and the spins of the unpaired electrons in a material. Second, the neutron is uncharged, which implies that there is no Coulomb interaction between the neutron and the material's electrons. Consequently, the neutron's interaction with the nucleus is relatively weak and thus, as opposed to photon scattering, the rate of magnetic scattering events is comparable to the rate of nuclear scattering events. Finally, the mass of the neutron, $m_n = 1.675 \times 10^{-27}$ kg, is such that at 293 K, the average kinetic energy of the neutron is 25.3 meV, corresponding to a wavelength of 1.798 Å. This length scale is on the order of the distance between the atoms in a material and provides the possibility of using neutrons for diffraction experiments. Furthermore, the average energy of the neutron is comparable to the energy scale of typical magnetic excitations such as spin waves and crystal field excitations. Thus, the energy gain or loss during a scattering process is a considerable fraction of the neutron incident energy which facilitates scattering experiments with good energy resolution.

The principle of neutron scattering is schematically shown in Fig.2.1 and consists of placing a sample in front of an incident neutron beam (with incident wave vector k_i and energy, $E_i = \frac{\hbar^2 k_i^2}{2m_n}$). The sample interacts with the incoming neutrons via momentum ($\mathbf{Q} = \mathbf{k}_i - \mathbf{k}_f$) and energy transfer ($\hbar\omega = E_i - E_f = \frac{\hbar^2 k_i^2}{2m_n} - \frac{\hbar^2 k_f^2}{2m_n}$), which are both conserved during the scattering event. In a neutron scattering experiment, we are interested in measuring the ratio of the number of neutrons scattered per second into the solid angle $d\Omega$ in the direction (θ, ϕ) (with respect to the direction of the incident neutron) with energy E per total incident neutron flux. This measured ratio is defined by the partial differential scattering cross-section ($\frac{d^2\sigma}{dEd\Omega}$). When multiplied by the incoming neutron flux, the cross-section σ is defined as the total number of scattered neutrons per unit of time and, hence, σ has units of area.

The calculation of $\frac{d^2\sigma}{dEd\Omega}$ requires the determination of the scattered neutron eigenstates. This task is facilitated by the fact that both the magnetic and nuclear interactions of the neutron with the sample are weak. The interaction ($\hat{V}$) of the sample can then be treated as a time-dependent perturbation of the free particle Hamiltonian. In this context, the rate of neutrons scattered from an initial state k_i to a final state k_f follows the Fermi's golden rule rules and hence, is

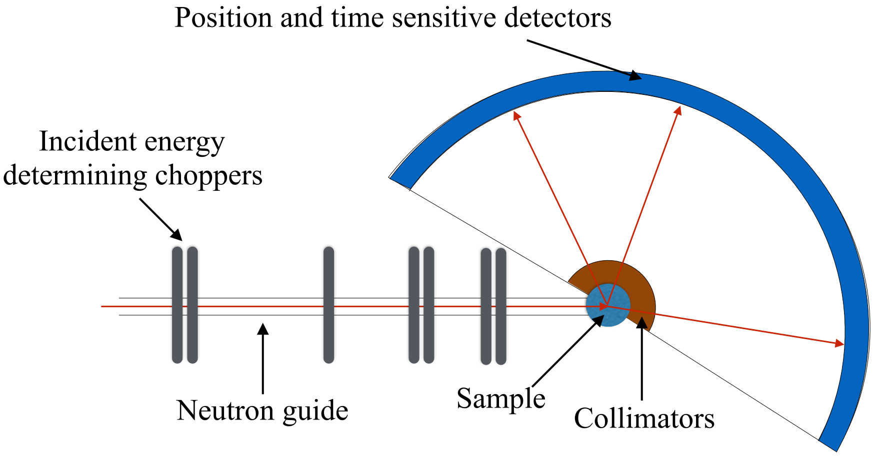

Figure 1.4: Scheme of a time-of-flight neutron spectrometer. In this example, an ensemble of seven choppers are converting a white neutron beam into a neutron beam with well-defined energy (E_i). This monochromatic neutron beam is converged to the sample space. After being scattered by the sample, the neutrons are detected by an assembly of He^3 detectors that cover a large part of 2π steradian. The momentum transfer $\mathbf{Q}$ and energy transfer $\hbar\omega$ of the scattering processes can be deduced from the time and position at which the scattered neutrons are detected.

proportional to the matrix element $|\langle \mathbf{k_f}, S^z_f, n_f|\hat{V}|\mathbf{k_i}, S^z_i, n_i\rangle|^2$. S^z_f and S^z_i are the final and initial spin state of the neutron and n_f and n_i are variables that define the final and initial states of the sample. Using this formalism, the partial differential scattering cross-section can be written as [73]:

$$\frac{d^2\sigma}{dEd\Omega} = (\frac{m_n}{2\pi\hbar^2})^2\frac{k_f}{k_i}|\langle \mathbf{k_f}, S^z_f, n_f|\hat{V}|\mathbf{k_i}, S^z_i, n_i\rangle|^2\delta(E_i - E_f - \hbar\omega) \tag{1.15}$$

where the last term is a Dirac function that ensures energy conservation and where the ratio $\frac{k_f}{k_i}$ arises because we divided the scattered neutron flux by the incident flux, which both depend on the neutron's velocity and hence, on its momentum wave vector k.

Naturally, the origin of the nuclear and magnetic interaction of the neutron with matter is different. The nuclear interaction $(\hat{V}_N)$ is only significant at short distance scales ($\sim 10^{-14}$ to 10^{-15} m) because it originates from the nuclear forces between the nucleus of an ion and the neutron. Thus, the nuclear potential can be approximated by a Dirac function and is, generally, defined as:

$$\hat{V}_N(\mathbf{r_n}, \mathbf{R_N}) = -\frac{2\pi\hbar^2}{m_n} b\delta(\mathbf{r}_n - \mathbf{R}_N), \tag{1.16}$$

where $\mathbf{r_n}$ is the position of the neutron, $\mathbf{R_N}$ is the position of the ion and b is a scattering length. The scattering length b quantifies the strength of the scattering process and is different for every nuclei. In general, the scattering length has an imaginary component that represents the absorption process of the neutron by a nuclei. Here, however, we consider only the positive and real value of the scattering length b.

The net interaction between the neutron's spin and the dipole (B_s) and orbital (B_{orb}) moment of an unpaired electron is responsible for the magnetic contribution of the scattering. The magnetic interaction ($\hat{V}_M$) between a neutron and an electron can be written as:

$$\hat{V}_M = -\boldsymbol{\mu}_\mathbf{n} \cdot (\mathbf{B_s} + \mathbf{B_{orb}}) = \frac{\mu_0}{4\pi}(\nabla \times (\frac{\boldsymbol{\mu}_\mathbf{e} \times \hat{\mathbf{R}}}{R^2}) - \frac{2\mu_B}{\hbar}\frac{\mathbf{p} \times \hat{\mathbf{R}}}{R^2}), \tag{1.17}$$

where $\hat{R}$ is a unit vector pointing along the direction between the electron position and the magnetic field at a point $\mathbf{R}$, $\mathbf{p}$ is the electron momentum and $\boldsymbol{\mu}_\mathbf{e}$ is the magnetic dipole moment of the electron.

It is now interesting to show explicit mathematical expressions of the partial differential scattering cross-section corresponding to various scattering examples relevant for the neutron analysis presented in this thesis. First, we can look at the nuclear scattering obtained from a crystal, a periodic arrangement of ions with reciprocal space vector $\boldsymbol{\tau}$. By treating each ion within the crystal as static, the scattering potential (V_T) entering equation 1.15 is the sum of V_N over all atoms within the crystal:

$$V_T(\mathbf{r}_n) = -\frac{2\pi\hbar^2}{m_n}\sum_{l=1}^{N_{cell}}\sum_{\mu=1}^{n_b} b_\mu \delta(\mathbf{r_n} - \mathbf{l} - \boldsymbol{\mu}), \tag{1.18}$$

where N_{cell} is the number of unit cells within the material and n_b is the number of atoms within one unit cell. The result obtained from inserting V_T in equation 1.15 is given by [73]:

$$\frac{d^2\sigma}{dEd\Omega} = NV_{rec}|F_N(\mathbf{Q})|^2 \sum_{\boldsymbol{\tau}} \delta(\mathbf{Q} - \boldsymbol{\tau})\delta(\hbar w) \tag{1.19}$$

where $F_N(\mathbf{Q})$ is the unit cell structure factor:

$$F_N(\mathbf{Q}) = \sum_{\mu} b_{\mu} e^{i\mathbf{Q}\cdot\mathbf{r}_{\mu}}. \tag{1.20}$$

In these equations, N is the number of atoms in the crystal, V_{rec} is the volume of the unit cell in the reciprocal space and $\delta(\hbar w)$ is a Dirac function that restricts the scattering to elastic processes only ($E_i = E_f$). The Dirac function $\delta(\mathbf{Q} - \boldsymbol{\tau})$ represents the well-known Bragg condition where non-zero intensity, or constructive interference, is possible only if the neutron momentum transfer $\mathbf{Q}$ is equal to a reciprocal space vector $\boldsymbol{\tau}$. This restriction is a necessary, but not sufficient, condition for constructive interference because the unit cell structure factor ($F_N(\mathbf{Q})$) can suppress the intensity of a particular Bragg peak. From equations 1.19 and 1.20, we can see that it is possible to use elastic neutron scattering to determine the crystal structure of any material. This is feasible because the structural Bragg peaks as a function of momentum transfer depends on the crystal symmetry of the probed material and the relative intensities of all these Bragg peaks depends on the position of the ions within the unit cell. For example, we used neutron diffraction to characterize the dimensions and exact distortion of the oxygen environment surrounding each Er^{3+} site in the different $\mathrm{Er}_2B_2\mathrm{O}_7$ compounds probed in Publication VI.

The magnetic structure determination of various XY pyrochlore magnets has also been performed in this thesis. To describe the scattering originating from a long range magnetic structure, the total interaction potential is the sum of the magnetic potential V_m (equation 1.17) over all spins sitting on a periodic lattice with reciprocal space vector $\boldsymbol{\tau}_m$. Upon inserting the net magnetic potential into equation 1.15, one can derive the following equation [73]:

$$\frac{d^2\sigma}{dE d\Omega} = \frac{\gamma r_0^2}{2\mu_B} N V_{rec} |f(|\mathbf{Q}|)|^2 \sum_{\boldsymbol{\tau}_m} \delta(\mathbf{Q} - \boldsymbol{\tau}_m) |\hat{\tau}_m \times F_M(\boldsymbol{\tau}_m) \times \hat{\tau}_m|^2 \delta(\hbar w), \tag{1.21}$$

where $F_M(\mathbf{Q})$ is the Fourier transform of the unit cell magnetization $\mathbf{M}(\mathbf{r})$:

$$F_M(\mathbf{Q}) = \int_{cell} \mathbf{M}(\mathbf{r}) e^{i\mathbf{Q}\cdot\mathbf{r}} \tag{1.22}$$

and γ is a constant equal to 1.913, r_0 is the classical radius of the electron and $f(|\mathbf{Q}|)$ is the atomic form factor. The atomic form factor is the Fourier transform of the electron spatial density of the rare earth ion. Equation 1.21 is similar to equation 1.19, but here, constructive interference is only possible for momentum transfer ($\mathbf{Q}$) that matches the magnetic reciprocal lattice vector $\boldsymbol{\tau}_m$. An important point is that the neutron is only sensitive to the components of the magnetization that are perpendicular to the momentum transfer $\mathbf{Q}$. For this reason, the term $|\hat{\tau}_m \times F_M(\boldsymbol{\tau}_m) \times \hat{\tau}_m|$ arises in equation 1.21. This sensitivity of the neutron to the moment direction was important in the analysis of the elastic scattering data in Publication V. In this publication, we studied the magnetic field induced domain re-orientation and redistribution in $\mathrm{Er_2Ti_2O_7}$. In a Γ_5 XY pyrochlore magnet such as $\mathrm{Er_2Ti_2O_7}$, the magnetic intensity of the $\mathbf{Q}$ =(220) Bragg peak oscillates as a function of the Er^{3+} spin orientation within its respective XY local plane. This oscillatory behaviour originates from the direction of the unit cell magnetization that oscillates between being fully perpendicular to $\mathbf{Q}$ (where the scattered intensity is maximal and where all the spins point along their local x or ψ_2 axis) to being fully parallel to $\mathbf{Q}$ (where the scattered intensity is zero and where all the spins point along their local y or ψ_3 axes). Finally, as shown in Chapter 2 and Chapter 3, the magnetic structures of $\mathrm{Yb_2Ti_2O_7}$ and the $\mathrm{Er_{2-\mathit{x}}Y_{\mathit{x}}Ti_2O_7}$ systems give rise to magnetic Bragg peaks that lie on top of the structural Bragg peaks at low temperature. Thus, the characterization of the nuclear contribution to the scattering is essential in order to properly separate the structural Bragg intensity from the magnetic Bragg peak intensities. The characterization of the nuclear part of the elastic scattering was performed by collecting a neutron diffraction pattern above the magnetic ordering temperature of these systems.

Inelastic neutron scattering was also performed to look for various excitations. In particular, the knowledge of the partial differential scattering cross-section of a crystal-field excitation is necessary to understand the fitting procedure of the CEF Hamiltonians for $\mathrm{Yb_2Ti_2O_7}$ and the $\mathrm{Er_2\mathit{B}_2O_7}$ pyrochlores. To derive the equation of the partial differential scattering cross-section for CEF excitations, we simply have to include equation 1.17 for a single ion into equation 1.15. As we performed inelastic neutron scattering on powder samples, a powder integration is also required and results in the following expression [73]:

$$\frac{d^2\sigma}{d\Omega dE'} = C\frac{k_f}{k_i} f^2(|Q|) \sum_{i,i'} \frac{\sum_\alpha |\langle i|J_\alpha|i'\rangle|^2 \mathrm{e}^{-\beta E_i}}{\sum_j \mathrm{e}^{-\beta E_j}} \delta(E_i - E_i' - \hbar\omega) \tag{1.23}$$

where $f^2(|Q|)$ is the atomic form factor of the rare earth ion, $\alpha = x, y, z$ and where C is a constant. Equation 1.22 indicates that the scattered intensity of a CEF transition depends directly on the matrix element $\sum_\alpha |\langle i|J_\alpha|i'\rangle|^2$ which involves the CEF state of the rare earth ion before ($|i'\rangle$) and after ($\langle i|$) the transition. This result implies that the scattered intensity of a transition between two CEF states depends directly on their compositions, which in turn depends on the CEF parameters B_n^m defined in equation 1.3. Thus, inelastic neutron scattering can be used to fit the CEF Hamiltonians of rare earth pyrochlores. This procedure consists of minimizing the chi-squared distribution of the observed and calculated scattered neutron intensities and energies of any observed CEF transitions. Analyses of this type are presented in Publication I for $Yb_2Ti_2O_7$ and in Publication VI for $Er_2Ti_2O_7$, $Er_2Ge_2O_7$, $Er_2Pt_2O_7$ and $Er_2Sn_2O_7$.

Finally, knowledge of the partial differential cross-section for phonon excitations in a crystal is important. A phonon is a quantized vibration of the crystal lattice and can be described in terms of displacement operators $\boldsymbol{\mu}^s_{k_{ph}}$, with wave vector k_{ph}, polarization vector $\mathbf{e}_s$ and energy $\hbar\omega_s$. The partial differential cross section can be derived for phonon excitations in a crystal assuming a non-static distribution of atoms. In this context, the atoms are allowed to move ($\mathbf{R}(t) = \mathbf{l} + \boldsymbol{\mu} + \boldsymbol{\mu}^s_{k_{ph}}(t)$). Acoustic phonons are in-phase displacements of the atoms within the unit cell and are present for both a Bravais ($n_b = 1$) and non-Bravais lattices ($n_b > 1$). For acoustic phonons, it can be shown that the cross section for a one-phonon emission and absorption process is written as follows [73]:

$$\frac{d^2\sigma}{d\Omega dE'} = \frac{\sigma}{8\pi M}\frac{k_f}{k_i}V_{rec}e^{-2W}\sum_s\sum_{\boldsymbol{\tau}}\frac{(\mathbf{Q}\cdot\mathbf{e}_s)^2}{\omega_s}\delta(\omega\mp\omega_s)\delta(\mathbf{Q}\mp\mathbf{q}-\boldsymbol{\tau})\langle n_s+1\rangle, \tag{1.24}$$

where σ is the cross section for a specific atom, e^{-2W} is the Debye-Waller factor and $\langle n_s + 1\rangle$ is the thermal Bose-factor. The Debye-Waller factor describes the attenuation of coherent neutron scattering caused by thermal motion of the atoms. The thermal Bose-factor characterizes the effect of temperature on the average population of phonons. The derivation of the cross-section for phonon excitations is important for Publication I and VI. Indeed, as phonon excitations are also measured in any unpolarized inelastic neutron scattering experiment, it is important to properly identify them so they can be distinguished from the magnetic excitations. As opposed to magnetic scattering, the scattering goes as $|\mathbf{Q}|^2$ and thus, the intensity of a phonon excitation should increases as a function of the momentum transfer $|\mathbf{Q}|$. As shown in equation 1.23, the $|\mathbf{Q}|$ dependence of CEF excitations follows the dependence of the magnetic form factor $f^2(|\mathbf{Q}|)$ which decreases at high $|\mathbf{Q}|$. Thus, it is typically possible to distinguish between a phonon and a magnetic excitation because they have distinct $|\mathbf{Q}|$ dependences.

Chapter 2

Fragile Magnetism in $Yb_2Ti_2O_7$

This chapter is dedicated to the ground-state properties of the rare earth pyrochlore $Yb_2Ti_2O_7$. This material piqued the interest of the frustrated magnetism community because of the exotic nature of its magnetic ground state. Experiments have revealed an unconventional continuum of gapless spin excitations at low temperature, a signature of spin liquid physics. This continuum of spin excitations was observed to condense into sharp coherent spin waves in a small applied magnetic field [74,75]. Taking advantage of the presence of sharp spin waves in the high field inelastic neutron scattering spectra of $Yb_2Ti_2O_7$, Ross *et al.* [35] fitted a spin Hamiltonian using the anisotropic exchange Hamiltonian that we defined in Equation 1.8. A mean-field development using the exchange parameters obtained from this procedure predicts that $Yb_2Ti_2O_7$ should order into a splayed ferromagnetic state at low temperature with well-behaved ferromagnetic excitations that are gapped by ∼0.2 meV [2,35]. In experiments, this conventional magnetic behavior was not found. Furthermore, the Ising exchange parameters J_{zz} was refined to be dominant, leading to proposals that the magnetic ground state of $Yb_2Ti_2O_7$ may be proximate to a quantum spin ice phase [35]. Since then, other explanations for the quantum spin liquid behavior observed in $Yb_2Ti_2O_7$ have been put forward, such as phase competition due to proximity to an antiferromagnetic Γ_5 phase [10,48,49,64] (See Figure 1.3 of the introduction) or proximity to a magnetic Coulomb liquid [76].

The nature of the magnetic ground-state of $Yb_2Ti_2O_7$ is still unknown and the mechanism responsible for the continuum of excitations at low temperature remains a mystery. A complicating factor in the quest to understand the magnetic ground state of $Yb_2Ti_2O_7$ is its extreme sensitivity to small amounts of disorder [71, 72, 78–80]. The effect of disorder on the low temperature

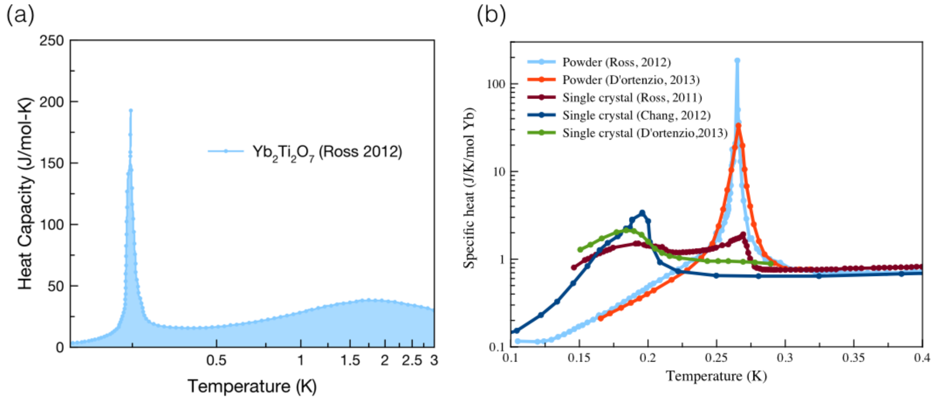

Figure 2.1: (a) Low temperature specific heat of $Yb_2Ti_2O_7$ [71] showing both the broad and anomaly centered at ∼2 K and the sharp anomaly at lower temperature, 265 mK. (b) Variability of the low temperature specific heat anomaly in $Yb_2Ti_2O_7$ for various powder and single crystal samples synthesized by different groups [71, 75–77].

magnetism of $Yb_2Ti_2O_7$ can be best appreciated by comparing the low temperature specific heat of various powder and single crystal samples synthesized by different groups. The magnetic contribution to the specific heat of $Yb_2Ti_2O_7$ consists of two features: one broad anomaly at relatively high temperature, ∼2 K [8], and another sharp anomaly at low temperature, ∼265 mK (see Fig.2.1(a)). The higher temperature broad specific heat anomaly does not exhibit any sample dependence. However, as seen in Fig. 2.1(b), both the position and shape of the low temperature specific heat anomaly vary drastically amongst different samples of $Yb_2Ti_2O_7$. This low temperature transition is the most variable in single crystal samples. The sample dependence of $Yb_2Ti_2O_7$ is also perceptible in other probes such as μSR spectroscopy and neutron scattering, where some samples of $Yb_2Ti_2O_7$ show a clear transition to a ferromagnetic ordered state [2, 40, 81–84] and some samples do not [77, 85–87]. The nature of the defects in single crystals of $Yb_2Ti_2O_7$ have been investigated by a few groups and were refined to have a small amount of cation disorder, on the level of 1-2% [71, 72, 78–80, 88]. In the pyrochlore structure, this cation disorder is termed "stuffing", which consists of replacing some Ti^{4+} atoms that resides on the B-site by an excess of Yb^{3+} ions. Other types of defects in rare earth pyrochlores have been proposed such as oxygen vacancies [89, 90]. While it is known that such defects affect the low temperature phase behavior of $Yb_2Ti_2O_7$, careful studies of this disorder and its microscopic manifestation are lacking. The three publications in this chapter seek to remedy this problem:

Publication I: "*Neutron spectroscopic study of crystalline electric field excitations in stochiometric and lightly stuffed $Yb_2Ti_2O_7$*", Jonathan Gaudet, Dalini D. Maharaj, Gabriele Sala, Edwin Kermarrec, Kate A. Ross, Hanna A. Dabkowska, Alexander I. Kolesnikov, Garret E. Granroth, and Bruce D. Gaulin. Physical Review B **92**, 134420 (2015) [1].

Publication II: "*Gapless quantum excitations from an icelike splayed ferromagnetic ground state in stoichiometric $Yb_2Ti_2O_7$*", Jonathan Gaudet, Kate A. Ross, Edwin Kermarrec, Nicholas P. Butch, Georg Ehlers, Hanna A. Dabkowska, and Bruce D. Gaulin. Physical Review B **93**, 064406 (2016) [2].

Publication III: "*Ground state selection under pressure in the quantum pyrochlore magnet $Yb_2Ti_2O_7$*", Edwin Kermarrec, Jonathan Gaudet, Katharina Fristch, Rustem Khasanov, Zurab Guguchia, Clemens Ritter, Kate A. Ross, Hanna A. Dabkowska, and Bruce D. Gaulin. Nature Communications **8**, 14810 (2017) [3].

2.1 Preface to Publication I: Single-ion properties of stoichiometric and weakly stuffed $Yb_2Ti_2O_7$.

In this work, we used forefront inelastic neutron scattering techniques to measure the CEF excitations in both a stoichiometric powder sample of $Yb_2Ti_2O_7$ as well as a crushed single crystal, with approximate composition $Yb_{2+x}Ti_{2-x}O_{7+y}$ and $x = 0.046$. This work allowed us to determine the CEF eigenvalues and eigenfunctions for Yb^{3+} in stoichiometric $Yb_2Ti_2O_7$ and also to probe the effect of stuffing on the CEF excitations of the crushed single crystal. Modeling these single-ion excitations with the proper CEF Hamiltonian for the stoichiometric powder resulted in a single-ion CEF ground state mainly composed of $|J = 7/2, m_J = \pm 1/2\rangle$. This results in XY local anisotropy and validates the quantum description for the Yb^{3+} moments in this compound. The same excitations are also observed in the stuffed powder, but with smaller lifetimes. This allow us to conclude that an extended strain field exists about each local "stuffed" site, which produces a distribution of random CEF environments. Finally, with the CEF Hamiltonian of the pure $Yb_2Ti_2O_7$ in hand, it was possible to approximate the CEF eigenfunctions of defective

Yb^{3+} sites. The eigenfunctions for defective Yb^{3+} cations siting on the B-site or siting on the A-site adjacent to an oxygen vacancy are predicted to have local Ising anisotropy, which can potentially help in disrupting the fragile magnetic order reported in some samples of $Yb_2Ti_2O_7$.

My role in this work was the analysis of the inelastic neutron scattering data. I wrote a Matlab code to refine a CEF Hamiltonian for the stoichiometric $Yb_2Ti_2O_7$ powder. Finally, I drafted the majority of the manuscript and the response to the Physical Review B referee reports. The contributions of each author are summarized below.

Author Contributions:

- *Experimental Concept*: B.D. Gaulin
- *Sample Preparation*: K.A. Ross, H.A. Dabkowska
- *Neutron Scattering Experiments*: D.D. Maharaj, E. Kermarrec, A.I. Kolesnikov, G.E. Granroth, B.D. Gaulin
- *Data Analysis*: **J. Gaudet**, G. Sala, D.D. Maharaj, B.D. Gaulin
- *Manuscript*: **J. Gaudet**, G. Sala, D.D. Maharaj, B.D. Gaulin

Neutron spectroscopic study of crystalline electric field excitations in stoichiometric and lightly stuffed $Yb_2Ti_2O_7$

J. Gaudet,[1,*] D. D. Maharaj,[1] G. Sala,[1] E. Kermarrec,[1] K. A. Ross,[2] H. A. Dabkowska,[3] A. I. Kolesnikov,[4]
G. E. Granroth,[5] and B. D. Gaulin[1,3,6]
[1]*Department of Physics and Astronomy, McMaster University, Hamilton, ON, Canada L8S 4M1*
[2]*Department of Physics, Colorado State University, Fort Collins, Colorado 80523-1875, USA*
[3]*Brockhouse Institute for Materials Research, Hamilton, ON, Canada L8S 4M1*
[4]*Chemical and Engineering Materials Division, Oak Ridge National Laboratory, Oak Ridge, Tennessee 37831, USA*
[5]*Neutron Data Analysis and Visualization Division, Oak Ridge National Laboratory, Oak Ridge, Tennessee 37831, USA*
[6]*Canadian Institute for Materials Research, 180 Dundas Street West, Toronto, Ontario, Canada M5G 1Z8*

(Received 26 July 2015; revised manuscript received 22 September 2015; published 27 October 2015)

Time-of-flight neutron spectroscopy has been used to determine the crystalline electric field (CEF) Hamiltonian, eigenvalues and eigenvectors appropriate to the $J = 7/2$ Yb^{3+} ion in the candidate quantum spin ice pyrochlore magnet $Yb_2Ti_2O_7$. The precise ground state (GS) of this exotic, geometrically frustrated magnet is known to be sensitive to weak disorder associated with the growth of single crystals from the melt. Such materials display weak "stuffing," wherein a small proportion, ≈2%, of the nonmagnetic Ti^{4+} sites are occupied by excess Yb^{3+}. We have carried out neutron spectroscopic measurements on a stoichiometric powder sample of $Yb_2Ti_2O_7$, as well as a crushed single crystal with weak stuffing and an approximate composition of $Yb_{2+x}Ti_{2-x}O_{7+y}$ with $x = 0.046$. All samples display three CEF transitions out of the GS, and the GS doublet itself is identified as primarily composed of $m_J = \pm 1/2$, as expected. However, stuffing at low temperatures in $Yb_{2+x}Ti_{2-x}O_{7+y}$ induces a similar finite CEF lifetime as is induced in stoichiometric $Yb_2Ti_2O_7$ by elevated temperature. We conclude that an extended strain field exists about each local "stuffed" site, which produces a distribution of random CEF environments in the lightly stuffed $Yb_{2+x}Ti_{2-x}O_{7+y}$, in addition to producing a small fraction of Yb ions in defective environments with grossly different CEF eigenvalues and eigenvectors.

DOI: 10.1103/PhysRevB.92.134420 PACS number(s): 75.25.−j, 75.10.Kt, 75.40.Gb, 71.70.Ch

I. INTRODUCTION

Geometrically frustrated magnetic materials are of great current interest due to the diversity of exotic ordered and disordered ground states (GSs) that they display [1]. In particular, cubic pyrochlore magnets with chemical composition $A_2B_2O_7$ have been a playground for geometric frustration as both the A^{3+} and B^{4+} sites, independently, reside on interpenetrating networks of corner-sharing tetrahedra (see Fig. 1), one of the canonical architectures for frustrated ground states in three dimensions [2]. The rare earth titanate pyrochlores have played a pivotal role in the development of the field, as Ti^{4+} at the B site is nonmagnetic, and the A site can be occupied by all trivalent rare earth ions from Sm^{3+} to Lu^{3+}. Many of these rare earth titanates therefore have a magnetic A sublattice, and the family as a whole gives rise to different combinations of magnetic anisotropies and interactions, which in turn are responsible for the diversity of exotic ground states [3].

As an example, the classical spin ice state has been the focus of much attention [4–6], and it results from a combination of local Ising anisotropy [7,8] and net ferromagnetic interactions [8] on the pyrochlore lattice, such that the Ising magnetic moments on each tetrahedron obey "ice rules" with two spins pointing into each tetrahedron and two spins pointing out, analogous to the water ice model proposed by Pauling [9]. This results in a sixfold degeneracy for a given tetrahedron, and a macroscopic degeneracy for the three-dimensional network as a whole. $Yb_2Ti_2O_7$ has attracted much recent attention [10–14] as a candidate for a quantum spin ice ground state [15,16], wherein effective $S = 1/2$ degrees of freedom decorate a pyrochlore lattice and interact via net ferromagnetic interactions [17]. The GS phase diagram and microscopic Hamiltonian appropriate to $Yb_2Ti_2O_7$ have been extensively studied [18,19]. The microscopic Hamiltonian itself has been determined by modeling spin wave dispersion and neutron intensities in the high magnetic field, low temperature state of $Yb_2Ti_2O_7$ [20]. This work convincingly showed anisotropic exchange to be the relevant form of the interactions at low temperatures.

One of the most interesting features of the GS properties of $Yb_2Ti_2O_7$ is its apparent sensitivity to small levels of defects that are present in real materials [21–23]. Stoichiometric $Yb_2Ti_2O_7$ is known to display a large and sharp anomaly in its heat capacity C_p near ∼265 mK. However, this anomaly has been observed to be sample dependent with samples displaying broader anomalies at lower temperatures depending on the exact stoichiometry of the material studied [24–28]. This phenomena is very unusual for a three-dimensional magnet, as the defect levels involved are at the limits of detectability by conventional techniques. The variation in stoichiometry, where characterized, is on the order of 1% level, far removed from percolation thresholds in three dimensions.

Polycrystalline samples of $Yb_2Ti_2O_7$ tend to display the sharpest and highest temperature C_p anomalies, likely due to the lower temperatures required for their synthesis, leading to less TiO_2 volatization. Single crystals grown by floating zone image furnace techniques typically display broad low temperature C_P anomalies, or no anomalies, and sometimes

---

[*] gaudej@mcmaster.ca

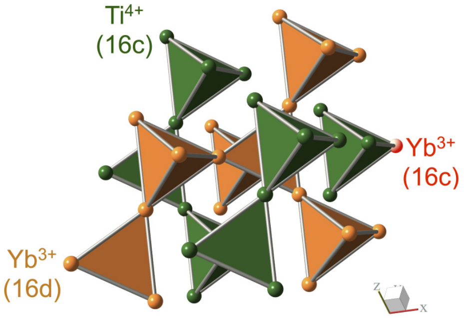

FIG. 1. (Color online) The stuffed pyrochlore structure of $Yb_2Ti_2O_7$. The pyrochlore lattice consists of interpenetrating networks of corner-sharing tetrahedra which are generated independently by the Yb^{3+} (magnetic) and Ti^{4+} (nonmagnetic) cations. The pyrochlore lattice is said to be stuffed, wherein Yb^{3+} ions, which are normally found on the 16d site (also called A site), also occupy the Ti^{4+} 16c site (B site).

show multiple peaks in C_P at low temperature. Ross *et al.* [21] undertook a detailed neutron crystallographic study of both powder and crushed single crystal $Yb_2Ti_2O_7$ samples, representative of those that displayed sharp and broad low temperature C_P signatures, respectively, and showed that the crushed single crystal sample displayed weak stuffing: a structural defect in which a slight excess of Yb occupies the Ti sublattice. Stuffing is illustrated schematically in Fig. 1, wherein Yb^{3+} ions occupy both the 16d site of the $Fd\bar{3}m$ cubic space group, as well as act as impurities on the 16c site normally occupied by Ti^{4+}. Weak stuffing was shown to occur at the 2.3% level in the crushed single crystals with composition $Yb_{2+x}Ti_{2-x}O_{7+y}$ grown by floating zone image techniques. In contrast the powder sample grown by solid state synthesis was shown to be stoichiometric.

The role of different quenched disorder has been studied in other pyrochlores and generally in the field of frustrated magnetism [29]. For example, A^{3+} site disorder in $Dy_{2-x}Tb_xTi_2O_7$ and B^{4+} site disorder in $Tb_2Ti_{2-x}Sn_xO_7$ have recently been studied in rare-earth titanate pyrochlores [30,31]. Both of these studies show evidence that the nature of the GS is very sensitive to such disorder. In light of these studies and the well-known variation in the stoichiometry of the $Yb_2Ti_2O_7$ sample, we report neutron spectroscopic measurements of the crystalline electric field (CEF) excitations in the two powder samples, the stoichiometric powder and the crushed single crystal with 2.3% stuffing previously studied by Ross *et al.* These measurements allow us to accurately determine the eigenvalues and eigenvectors appropriate to the four doublets which make up the $J = 7/2$ CEF manifold for Yb^{3+} in $Yb_2Ti_2O_7$. Measurements on both stoichiometric and lightly stuffed samples allow us to investigate the role of stuffing on the CEF levels associated with Yb^{3+} ions properly residing on the A site of the pyrochlore structure. With these benchmark measurements in hand, we calculated CEF eigenvalues and eigenvectors for the stuffed Yb^{3+} ions residing on the B site, as well as for the A site Yb^{3+} ions in the presence of oxygen vacancies [32].

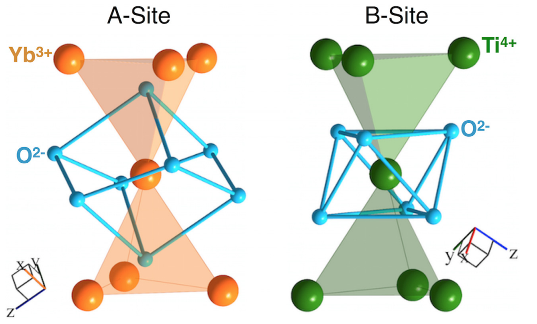

FIG. 2. (Color online) A comparison between the A-site and B-site oxygen environment in the pyrochlore structure of $Yb_2Ti_2O_7$. The left panel of the figure shows the scalenohedron environment generated by the oxygen ions at the A site where the Yb^{3+} resides. The symmetry of this structure is similar to that at the B site (right panel) where the Ti^{4+} ions are located.

II. CALCULATED CRYSTAL FIELD LEVELS FOR Yb^{3+} AT THE A SITE

Hund's rules enable the determination of the total angular momentum J of the Yb^{3+} ion. The electronic configuration of Yb^{3+} is $4f^{13}$, resulting in $J = \frac{7}{2}$ which is $2J + 1 = 8$-fold degenerate. Within the pyrochlore structure this degeneracy is lifted by the CEFs at the Yb^{3+} site due largely to the presence of the eight neighboring O^{2-} ions. As illustrated in Fig. 2 (left panel), the oxygen environment at the A site consists of a scalenohedron, which is a cube distorted along one diagonal that forms the local [111] axis. Six oxygen ions, commonly referred to as O(2), are located on a plane perpendicular to this direction, which is a threefold rotation axis. The other two oxygen ions, referred to as O(1), are located along the local [111] axis in the geometric center of the tetrahedra defined by the A-site Yb^{3+} ions. By contrast, the environment at the B site is a trigonal antiprism made of six O(2) oxygen ions surrounding the transition metal, as shown in the right panel of Fig. 2.

Following Prather's convention [33], the threefold axis should be placed along $\hat{z}$ of the reference system in order to minimize the number of CEF parameters in the Hamiltonian. Therefore, the resulting CEF Hamiltonian for Yb^{3+} on the A site can be written as

$$\mathcal{H}_{\text{CEF}} = B_2^0\hat{O}_2^0 + B_4^0\hat{O}_4^0 + B_4^3\hat{O}_4^3 + B_6^0\hat{O}_6^0 + B_6^3\hat{O}_6^3 + B_6^6\hat{O}_6^6. \tag{1}$$

Here we employ the Steven's operators $\hat{O}_n^m$ [34] and CEF parameters B_n^m to approximate the Coulomb potential generated by the crystalline electric field due to the neighboring oxygen atoms. Note that the CEF Hamiltonian contains no intersite terms such as exchange and strictly speaking would be only relevant for an isolated Yb^{3+} in $Yb_2Ti_2O_7$. However, as we will see, the CEF eigenvalues we report for $Yb_2Ti_2O_7$ are at high energies and display no dispersion, making the intersite interactions unimportant at the energy scale of the CEF transitions.

The determination of the crystal field parameters B_n^m in Eq. (1) is well suited to inelastic neutron spectroscopy. The unpolarized neutron partial differential magnetic cross section can be written within the dipole approximation as [35]

$$\frac{d^2\sigma}{d\Omega dE'} = C\frac{k_f}{k_i}F(|Q|)S(|Q|,\hbar\omega), \tag{2}$$

where Ω is the scattered solid angle, E' is the final neutron energy, $\frac{k_f}{k_i}$ is the ratio of the scattered and incident momentum of the neutron, C is a constant, and $F(|Q|)$ is the magnetic form factor. The scattering function $S(|Q|,\hbar\omega)$ gives the relative scattered intensity due to transitions between different CEF levels. At constant temperature and wave vector $|Q|$ we have

$$S(|Q|,\hbar\omega) = \sum_{i,i'} \frac{(\sum_\alpha |\langle i|J_\alpha|i'\rangle|^2)e^{-\beta E_i}}{\sum_j e^{-\beta E_j}} L(\Delta E + \hbar\omega), \tag{3}$$

where $\alpha = x,y,z$ and $L(\Delta E + \hbar\omega) = L(E_i - E_{i'} + \hbar\omega)$ is a Lorentzian function which ensures energy conservation as the neutron induces transitions between the CEF levels $i \rightarrow i'$, which possess a finite energy width or lifetime.

The procedure for fitting our inelastic neutron scattering (INS) data assumes an initial set of CEF Hamiltonian parameters. The Hamiltonian is then diagonalized to find the corresponding CEF eigenfunctions and eigenvalues. $S(|Q|,\hbar\omega)$ is then computed and directly compared with the experimental results and, finally, the CEF parameters are tuned such that the χ^2 between the calculated and measured $S(|Q|,\hbar\omega)$ is minimized.

III. EXPERIMENTAL DETAILS

Now we turn our attention to the details of the INS experiment which was conducted on two samples of $Yb_2Ti_2O_7$ of different stoichiometry. We will refer to these two samples as the stoichiometric ($x = 0$) and stuffed powder ($x = 0.046$) samples hereafter. Specific details regarding their synthesis and characterization can be found in previous work by Ross *et al.* [21]. These samples were studied utilizing the SEQUOIA direct geometry time-of-flight spectrometer [36], which is located at the Spallation Neutron Source at Oak Ridge National Laboratory. In an INS experiment the CEF excitations are manifested as dispersionless features with the strongest scattering intensity expected at low $|Q|$ positions as a result of their magnetic origin. SEQUOIA is the ideal instrument for the investigation of the CEFs since it provides low $|Q|$ coverage and a large, dynamic $(|Q|,E)$ range.

12 g of each of the stoichiometric and stuffed powder samples were loaded in an aluminum flat plate with dimensions 50 mm × 50 mm × 1 mm and sealed with indium in helium atmosphere. An empty can with the same dimensions was loaded with the two samples on a three sample changer in a closed-cycle refrigerator. Measurements have been performed over a range of temperatures from $T = 5$ to 300 K, and utilizing neutrons with incident energy $E_i = 150$ meV giving an elastic energy resolution of ±2.8 meV. The energy resolution improves with increasing energy transfer and is ∼1.4 and ∼1 meV for energy transfers of 80 and 115 meV, respectively. The corresponding chopper settings selected were $T_0 = 120$ Hz and $FC_1 = 600$ Hz. Similar measurements were conducted on the empty can for use as a background measurement.

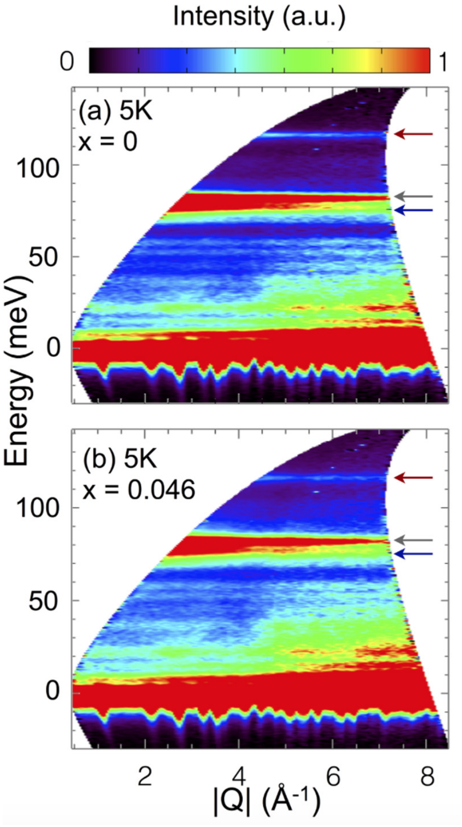

FIG. 3. (Color online) Inelastic neutron scattering spectra $S(|Q|,\hbar\omega)$ obtained for the stoichiometric powder and the stuffed powder samples at $T = 5$ K are shown in (a) and (b), respectively, with the corresponding $T = 5$ K empty can subtracted from each data set. The three horizontal arrows in blue, gray, and red highlight the three crystal field excitations which are found at 76.7, 81.8, and 116.2 meV, respectively.

IV. INELASTIC NEUTRON SCATTERING FROM CRYSTAL FIELD EXCITATIONS IN $Yb_2Ti_2O_7$

The INS spectra taken on both the stoichiometric and stuffed powder samples are shown in Fig. 3 for energies up to $E_i = 150$ meV at $T = 5$ K. An empty can data set, taken as background at the same temperature, has been subtracted from both the sample data sets. As seen in Fig. 3, we observe a set of dispersionless excitations arising from both the CEF transitions, as well as optical phonons. Below 60 meV, the intensity associated with the dispersionless excitations increases with increasing |Q|, characteristic of inelastic scattering from phonons. In contrast, the excitations at 76.7, 81.8, and 116.2 meV, highlighted with blue, gray, and red arrows, respectively, in Fig. 3 , show inelastic scattering which increases with decreasing |Q|, consistent with magnetic scattering. We therefore ascribe these three dispersionless excitations with CEF transitions from the GS doublet.

Yb^{3+} possesses 13 electrons in its almost filled $4f$ shell and, as a consequence of Kramers' theorem, its eightfold degenerate CEF levels can be maximally split into four doublets. We

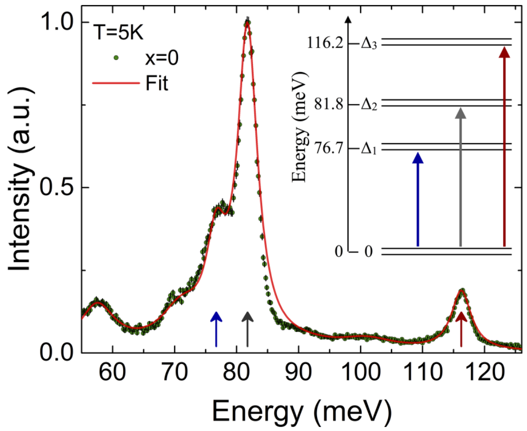

FIG. 4. (Color online) $|Q|$ integrated cut for the stoichiometric powder at $T = 5$ K. A $|Q|$ integrated cut ($|Q| = [4.5,5.25]$ Å^{-1}) obtained from the INS spectra in Fig. 3(a) for the stoichiometric powder at $T = 5$ K is shown. The arrows indicate the corresponding positions of the CEFs. The inset outlines the corresponding CEF transitions from the GS doublet.

associate the three magnetic excitations observed at $T = 5$ K in both the stoichiometric and the stuffed powder samples shown in Fig. 3, with the transitions between the CEF GS doublet and the CEF excited state doublets, as indicated in the inset of Fig. 4. These three transitions between CEF doublets account for all the CEF states within this $J = 7/2$ multiplet appropriate to Yb^{3+}. As will be described in further detail, the CEF transitions observed at low temperatures in the stoichiometric sample are sharper in energy than those in the presence of light stuffing. We shall restrict our quantitative analysis of the CEF spectra to the case of the stoichiometric powder sample. Therefore, we use the $x = 0$ data set in Fig. 3(a), and perform a $|Q|$ integrated cut ($|Q| = [4.5,5.25]$(Å^{-1}), yielding the neutron scattering intensity as a function of energy. This data set is shown in the main panel of Fig. 4, wherein the intensity at the peak of the CEF transition at 81.8 meV has been normalized to unity. The relative intensities of the CEF transitions at 76.7, 81.8, and 116.2 meV, as well as the energy of these transitions from the GS, constrain the CEF Hamiltonian.

The cut shown in Fig. 4 has been fitted to a model for the inelastic scattering [35] arising from dipole allowed transitions between the CEF GS doublet and the three excited states, using Eq. (3). The starting parameters in the CEF Hamiltonian for Yb^{3+} were those determined by Bertin *et al.* [37] for Yb$_2$Ti$_2$O$_7$ within the point charge approximation. This calculation yielded CEF transitions at ∼60, ∼70, and ∼90 meV, in contrast to those determined experimentally in Fig. 3. These starting parameters were then refined and a best fit (shown in solid red) to the $|Q|$ integrated cut in Fig. 4 was obtained. All three CEF transitions were fit using the same resolution determined energy width. In addition, relatively weak Lorentzian line shapes near 56, 70, and 100 meV phenomenologically describe the inelastic scattering from the phonons which are in near proximity to the CEFs, and improved the fit when included. As can be seen, the overall description of the INS data from the stoichiometric sample in Fig. 4 is very good.

TABLE I. A comparison of the calculated crystal field parameters (B_n^m) with those obtained by fitting INS data from the stoichiometric powder at $T = 5$ K.

B_n^m (meV)	Calculated	Fitted	Ratio
B_2^0	1.270	1.135	0.894
B_4^0	−0.0372	−0.0615	1.653
B_4^3	0.275	0.315	1.145
B_6^0	0.00025	0.0011	4.4
B_6^3	0.0023	0.037	16.087
B_6^6	0.0024	0.005	2.083

The values which were obtained for the CEF Hamiltonian parameters from the fit relevant to Yb^{3+} at the A site are given in Table I and the resulting energy eigenvalues and eigenvectors are given in Table II. The GS doublet for Yb^{3+} is comprised primarily of $m_J = \pm 1/2$ and the corresponding low temperature anisotropic g-tensor components are given by $g_\perp = 3.69 \pm 0.15$ and $g_z = 1.92 \pm 0.20$, where z corresponds to the local [111] axis. The error bars on the g values were estimated by exploring the sensitivity of the fitting procedure on the low temperature stoichiometric powder data, to different quantitative descriptions of the background phonons. Note that this determination of the g tensor is performed at zero magnetic field, in contrast to, for example, the analysis of spin wave data in high magnetic fields [20]. The g tensor is consistent with previous estimates for Yb^{3+} in Yb$_2$Ti$_2$O$_7$ [38–40], and the dominant $m_J = \pm 1/2$ character of the GS validates the effective $S = 1/2$ quantum description for the Yb^{3+} moment. In order of ascending energy, the excited state doublets correspond primarily to $m_J = \pm 7/2$, $m_J = \pm 3/2$, and $m_J = \pm 5/2$.

A. Temperature and weak stuffing dependence of the A-site CEF transitions

Inelastic neutron scattering measurements have also been carried out on both the stoichiometric and stuffed powder samples as a function of temperature, using $E_i = 150$ meV neutrons. Energy scans of the $|Q| = [4.5,5.25]$ Å^{-1} integrated inelastic scattering for the stoichiometric powder sample are shown as a function of temperature in Fig. 5. The $T = 5$ K data set is the same $x = 0$ data set shown in Fig. 4, and the peak intensity associated with the 81.8 meV CEF transition at $T = 5$ K has been normalized to unity.

We note that the maximum temperature employed in these measurements, 300 K, corresponds ≈27 meV and consequently only the GS doublet of Yb^{3+} is substantially occupied at any temperature. Qualitatively, the thermal fluctuations have three effects on the CEF neutron spectra: the CEF excitations broaden appreciably in energy; the maximum peak intensity diminishes; and the energy of the CEF excitations softens slightly. This latter effect is somewhat subtle, but it can be seen in Fig. 5 by drawing a fiducial dashed line positioned at the center of the CEF transitions at $T = 5$ K.

The energy width of the CEF excitations can be quantitatively examined by fitting the data sets as in Fig. 4, but now with

TABLE II. The CEF eigenvalues and eigenvectors for Yb^{3+} at the A site of $Yb_2Ti_2O_7$. The first column displays the CEF eigenvalues of the system, while the corresponding eigenvectors are given in each row in terms of the m_J basis.

E (meV)	$\lvert -\frac{7}{2}\rangle$	$\lvert -\frac{5}{2}\rangle$	$\lvert -\frac{3}{2}\rangle$	$\lvert -\frac{1}{2}\rangle$	$\lvert \frac{1}{2}\rangle$	$\lvert \frac{3}{2}\rangle$	$\lvert \frac{5}{2}\rangle$	$\lvert \frac{7}{2}\rangle$
0	0	0.0866	0	0	–0.9283	0	0	0.3616
0	–0.3616	0	0	–0.9283	0	0	–0.0866	0
76.706	0.9136	0	0	–0.3343	0	0	–0.2313	0
76.706	0	–0.2313	0	0	0.3343	0	0	0.9136
81.764	0	0	–1	0	0	0	0	0
81.764	0	0	0	0	0	–1	0	0
116.23	0	0.9690	0	0	0.1627	0	0	0.1858
116.23	0.1858	0	0	–0.1627	0	0	0.9690	0

a damped harmonic oscillator (DHO) line shape for the three CEF transitions, each with the same temperature dependent energy width. At the energy transfers and temperatures of interest, the DHO can be approximated by a single Lorentzian for each mode.The form of this line shape is given by

$$L(E) = \frac{1}{\pi} \frac{\left(\frac{\Gamma_{\text{obs}}}{2}\right)}{(E - \Delta E)^2 + \left(\frac{\Gamma_{\text{obs}}}{2}\right)^2}, \tag{4}$$

which is a Lorentzian function of energy with width Γ_{obs} and centered on the energy of the CEF transition ΔE. The falloff of the maximum peak intensity as a function of increasing temperature along with the concomitant broadening in the energy widths of the transitions ensures that the integrated spectral weight of this inelastic scattering is almost temperature independent, consistent with the CEF transitions being from the GS doublet of Yb^{3+} at all temperatures considered here. The common energy width or inverse lifetime of the three CEF excitations extracted from this analysis is plotted as a function of temperature in Fig. 6, where we removed the resolution contribution to the widths using the following relation:

$$\Gamma^2_{\text{intrinsic}}(T) = \Gamma^2_{\text{obs}}(T) - \Gamma^2_{\text{res}}. \tag{5}$$

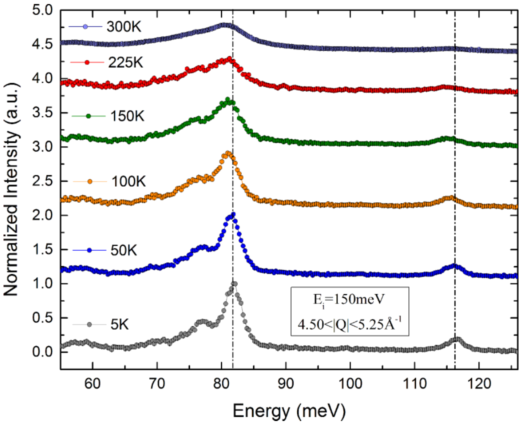

FIG. 5. (Color online) Energy cuts of the $|Q| = [4.5,5.25]$ Å^{-1} integrated inelastic scattering for the stoichiometric powder sample as a function of temperature. Energy cuts were taken with an appropriate background subtraction and all energy cuts for temperature above $T = 5$ K has been vertically translated for clarity.

Figure 6 then shows pronounced growth in the intrinsic energy width of the CEF transitions from ∼3.5 meV at $T = 5$ K to ∼9 meV at $T = 300$ K. This growth mirrors the temperature dependence of the Yb^{3+} mean squared displacements (MSDs) in stoichiometric $Yb_2Ti_2O_7$ as determined by powder neutron diffraction [21], and this is also reproduced in Fig. 6 for direct comparison. It is worth noting that we plot one of the anisotropic components of the atomic displacement parameter U_{11}, which represents the anisotropic MSD of the Yb^{3+} ions from their average positions. Although, for the specific case of the Yb^{3+} ion in the stoichiometric powder, it can be shown that U_{11} is equal to the other components of the atomic displacement, so that the MSD is effectively isotropic. The inset to Fig. 6 shows the slight softening of the CEF energies with increasing temperature. The softening is most pronounced for $T < 125$ K, and then it flattens out at higher temperature. The significance of 125 K = 11.3 meV is not completely clear, although it could be related to the temperature scale associated

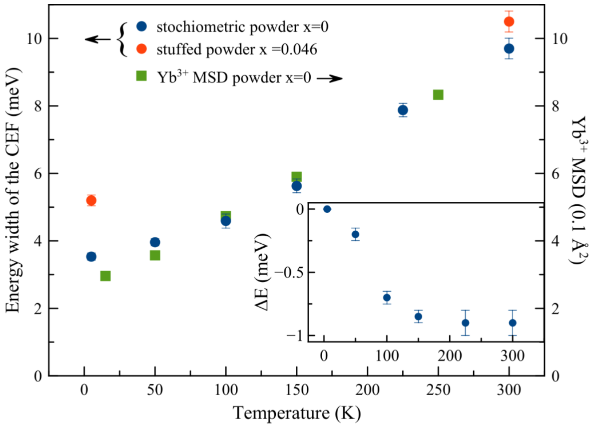

FIG. 6. (Color online) Energy width and shift of the CEF transitions as a function of temperature. The intrinsic energy width of the CEF transitions as extracted using Eq. (5). The intrinsic energy width corresponding to the stuffed powder is higher at both 5 and 300 K in comparison to the stoichiometric sample. The green dots shows the mean square displacement (MSD) of the Yb^{3+} taken from Ref. [21] and scaled in such a way that the MSDs and the energy widths of the CEF excitations in the stoichiometric powder have the same value at $T = 100$ K. The inset shows the shift in energy of the CEF transitions as a function of temperature, relative to that at $T = 5$ K.

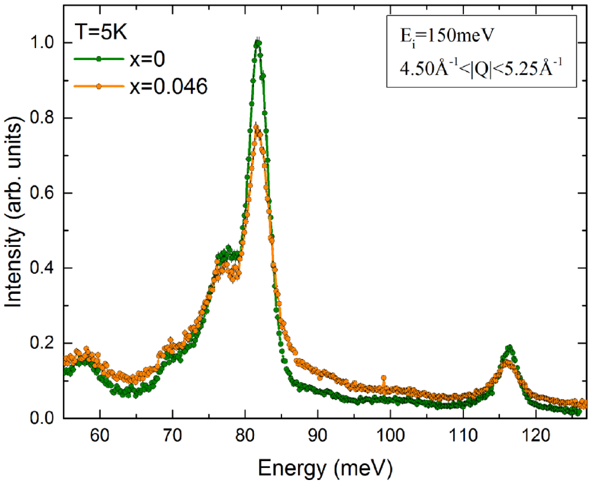

FIG. 7. (Color online) A direct comparison between the INS from CEF transitions in the stuffed powder (in orange) and the stoichiometric powder (in green) $Yb_2Ti_2O_7$ samples. Energy cuts taken at $T = 5$ K within a range $|Q| = [4.50, 5.25]$ Å^{-1} for the stuffed powder (orange) and stoichiometric powder (green) samples.

with the top of the acoustic phonon band in $Yb_2Ti_2O_7$, which is typically 10–15 meV for transition metal oxides. This effect is relatively small with a maximum observed softening of ∼0.8 meV at $T = 300$ K compared with $T = 5$ K.

The finite intrinsic energy widths of the CEF excitations in stoichiometric powder must originate from dynamics in the lattice not captured by the static structure. The strong resemblance of the temperature dependence of the Yb^{3+} MSDs to that of the CEF energy widths suggests that zero point fluctuations determine the low temperature energy widths, and the thermal population of phonons give rise to the larger widths at finite temperature. The ionic displacements associated with both zero point fluctuations and the phonons will distort the local environment at the Yb^{3+} site, giving rise to a distribution of CEF transitions energies. Displacements of harmonic phonons time average to zero, consequently the distribution of CEF transitions in the presence of the phonons is approximately centered on the zero temperature CEF transitions, and the transitions remain well defined at all temperatures.

Figure 7 shows a direct comparison of the $T = 5$ K, $|Q| = [4.50, 5.25]$ Å^{-1} integrated inelastic scattering for the stoichiometric and stuffed samples. This comparison clearly shows the CEF excitations in the lightly stuffed sample have a considerably larger energy width even at low temperatures. The INS from the stuffed powder was also fit to the same DHO line shape as was fit to the stoichiometric data, and the corresponding intrinsic energy widths at $T = 5$ and 300 K are also plotted in Fig. 6. The intrinsic energy widths of the CEF excitations in the stoichiometric and lightly stuffed samples differ by only ∼5% at $T = 300$ K; this is not surprising as the intrinsic energy widths in either sample are expected to be dominated by thermal fluctuations. However, at $T = 5$ K, the intrinsic energy width of the stuffed sample is ∼5.2 meV—approximately that displayed by the stoichiometric sample at ∼125 K.

The finite energy widths of the CEF excitations at low temperature in the lightly stuffed sample demonstrate that weak stuffing must induce a relatively large “volume of influence” about each stuffed Yb ion, that is, about each Yb ion residing on a B site. The corresponding distortion field about each stuffed site gives rise to a distribution of A-site Yb^{3+} environment, similar to those associated with phonons at finite temperature. Indeed, the stuffed B-site Yb ions would also give rise to CEF spectra completely distinct from those of Yb^{3+} in A-site environments. However, the concentration of such stuffed B-site Yb ions is known to be small, ≈2.3%, in our lightly stuffed sample and we were unable to find convincing evidence for such excitations in this study.

V. CRYSTAL FIELD CALCULATIONS FROM FIRST PRINCIPLES WITHIN THE POINT CHARGE APPROXIMATION

As discussed in Sec. II, the CEF Hamiltonian parameters can be fitted using INS data. In principle, these parameters can also be calculated from first principles within a point charge model following the procedure outlined in Refs. [41–43]. The CEF interactions are treated as a perturbation to the spin-orbit coupling and the resulting eigenfunctions of the CEF Hamiltonian are expressed as a linear combination of the $|J, m_J\rangle$ states within the $^2F_{\frac{7}{2}}$ manifold multiplets.

We have calculated the CEF Hamiltonian parameters in this manner and the ratio between these *ab initio* parameters and those extracted from fit of the INS data are shown in Table I. Note that the ionic positions were taken from the crystallographic refinement of stoichiometric $Yb_2Ti_2O_7$ [21]. As can be seen, apart from the B_6^0 and B_6^3 terms which are relatively small, all the CEF parameters agree well with those extracted from fitting the INS data. This result is remarkable given the simplicity of the point charge approximation, and it gives us confidence that we can make reasonable predictions on the strength of the CEF Hamiltonian parameters determined in this way.

The CEF eigenvectors and eigenvalues determined from the fit to the INS in the stoichiometric powder at $T = 5$ K is shown in Table II. Tables III and IV show the CEF eigenvectors and eigenvalues for Yb ions in two different impurity sites: one stuffed on the B site and one on the A site but in the presence of one O(1) oxygen vacancy. Both of these impurities are expected to be present at some small concentration in the lightly stuffed sample. In principle, O(2) vacancies can also occur, but these are higher energy defects than O(1) vacancies [32]. These CEF eigenvectors and eigenvalues have been calculated within the point charge approximation and then corrected with the same ratio of B_n^m parameters as were determined from the comparison between the INS fitted values and the calculated values in stoichiometric $Yb_2Ti_2O_7$ at low temperatures.

The differences between the fitted CEF parameters and the calculated ones originate mainly from the overlap of the $4f$ orbital of the rare earth with the $2p$ orbitals of the ligands. The corresponding effects on the B_n^m terms are difficult to estimate from first principles and are not considered here.

TABLE III. The CEF eigenvalues and eigenvectors calculated for Yb^{3+} in a depleted oxygen environment at the A site in Yb$_2$Ti$_2$O$_7$. The first column displays the CEF eigenvalues of the system, while the corresponding eigenvectors are given in each row in terms of the m_J basis. The ratio correction was applied in order to arrive at the final CEF parameters.

E (meV)	$\left\lvert -\frac{7}{2} \right\rangle$	$\left\lvert -\frac{5}{2} \right\rangle$	$\left\lvert -\frac{3}{2} \right\rangle$	$\left\lvert -\frac{1}{2} \right\rangle$	$\left\lvert \frac{1}{2} \right\rangle$	$\left\lvert \frac{3}{2} \right\rangle$	$\left\lvert \frac{5}{2} \right\rangle$	$\left\lvert \frac{7}{2} \right\rangle$
0	–0.9933	0	0	–0.1136	0	0	0.02	0
0	0	–0.02	0	0	–0.1136	0	0	0.9933
163.789	0	0.9844	0	0.0010	–0.1756	0	0.0056	0
163.789	0	0.0056	0	–0.1756	–0.0010	0	–0.9844	0
230.125	0	0	0	0	0	–1	0	0
230.125	0	0	1	0	0	0	0	0
238.306	0.1153	–0.0061	0	–0.9773	–0.0341	0	0.1743	–0.0040
238.306	–0.0040	–0.1743	0	0.0341	–0.9773	0	–0.0061	–0.1153

Instead we calculate the CEF parameters for the defective environments, and then correct these with the same B_n^m ratios which were determined in the treatment of CEFs for the stoichiometric sample. Finally, we verified that this correction did not dramatically affect the properties of the system; that is that the CEF properties within the defective environments did not qualitatively depend on this correction.

A. Crystal field calculation for Yb^{3+} at the A site in an oxygen depleted environment

We first consider an A-site Yb^{3+} in the presence of a single O(1) oxygen vacancy. This depleted environment is expected to break the symmetries of the CEF Hamiltonian. However if Prather's convention is satisfied, only the inversion operation is lost and the number of CEF parameters in our Hamiltonian is unchanged from the stoichiometric case. Note that in general a broken symmetry can dramatically affect the CEF Hamiltonian, and it may be necessary to add terms to the CEF Hamiltonian to better approximate the defective Coulomb potential.

The eigenvalues and eigenvectors calculated for A-site Yb^{3+} in the presence of a single O(1) oxygen vacancy are shown in Table III. As previously discussed, we have performed the point charge calculation and then scaled these results by the B_n^m ratios taken from the fitted and calculated CEF Hamiltonian terms determined for the stoichiometric powder.

Kramers' degeneracy still protects the Yb^{3+} ion in this defective environment and all the CEF eigenvectors appear as doublets. However, the gap between the GS and the first excited state is much larger than in the stoichiometric case. Moreover an examination of the eigenvectors in Table III shows that the GS is now a pure linear combination of $m_J = \pm 7/2$ states. These GS eigenvectors are similar to what is found in stoichiometric Dy$_2$Ti$_2$O$_7$ crystals, where the GS is comprised of a linear combination of the maximal m_J states, pure $m_J = \pm 15/2$.

With the CEF eigenfunctions in hand, we can calculate the local magnetization of the A-site Yb^{3+} in the presence of a single O(1) oxygen vacancy. This is shown in Fig. 8 where the magnetization anisotropy for Yb^{3+} moment within the defective scalenohedron is displayed. In both Figs. 8 and 9 colored spheres represent the tips of magnetization vector centered at the Yb^{3+} ion, in response to a given applied external field of $H = 1$ T with a particular [111] component and which precesses around the plane normal to [111]. Many values of the magnetization are shown simultaneously for applied fields uniformly distributed on the unit sphere. The color scale is chosen in order to match the strength of the magnetic moment from 0 μ_B (dark blue) to 4 μ_B (dark red). For the same [111] component of magnetization, the center of the spheres are sufficiently close to each other, that the final impression is that of rings (this is seen more clearly in Fig. 9). The tightness of the rings about the [111] axis implies stronger Ising-like behavior of the Yb^{3+} moment. For the case of the A-site Yb^{3+} in the presence of a single O(1) oxygen vacancy in Fig. 8, the calculated magnetic moment along the local [111] direction is 3.953 μ_B, close to the full moment of 4 μ_B. This suggests negligible precession around this easy axis and thus

TABLE IV. The CEF eigenvalues and eigenvectors calculated for Yb$_2$Ti$_2$O$_7$ at B site. The first column displays the crystal field spectrum of the system, while the corresponding eigenvectors are given in each row in terms of m_J basis. The ratio correction was applied in this case to the CEF parameters.

E (meV)	$\left\lvert -\frac{7}{2} \right\rangle$	$\left\lvert -\frac{5}{2} \right\rangle$	$\left\lvert -\frac{3}{2} \right\rangle$	$\left\lvert -\frac{1}{2} \right\rangle$	$\left\lvert \frac{1}{2} \right\rangle$	$\left\lvert \frac{3}{2} \right\rangle$	$\left\lvert \frac{5}{2} \right\rangle$	$\left\lvert \frac{7}{2} \right\rangle$
0	0	–0.2733	0	0	–0.2648	0	0	0.9248
0	0.9248	0	0	0.2648	0	0	–0.2733	0
69.991	0	–0.9558	0	0	–0.0338	0	0	–0.2921
69.991	–0.2921	0	0	0.0338	0	0	–0.9558	0
247.81	0	0	0.1238	0	0	–0.9923	0	0
247.81	0	0	–0.9923	0	0	–0.1238	0	0
318.797	0.2439	0	0	–0.9637	0	0	–0.1086	0
318.797	0	0.1086	0	0	–0.9637	0	0	–0.2439

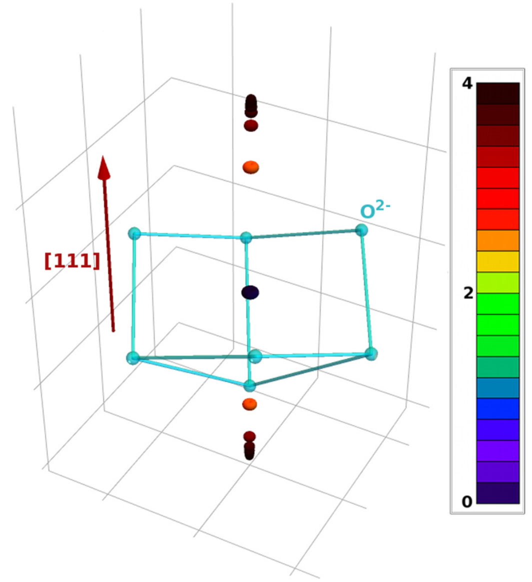

FIG. 8. (Color online) Magnetization of the A-site Yb^{3+} ion in presence of an O(1) oxygen vacancy. A colored sphere represents the tip of the magnetization vector centered at the Yb^{3+} ion in response to an applied external field of $H = 1$ T which rotates within the plane normal to [111]. Many values of the magnetization are shown simultaneously for applied fields uniformly distributed on the unit sphere. For the same [111] component of magnetization, the center of the spheres are sufficiently close to each other, that the final impression is that of rings. The tightness of the rings around the [111] axis implies stronger Ising-like behavior of the Yb^{3+} moment, in this case with a calculated magnetic moment of 3.953 μ_B along the local [111] direction.

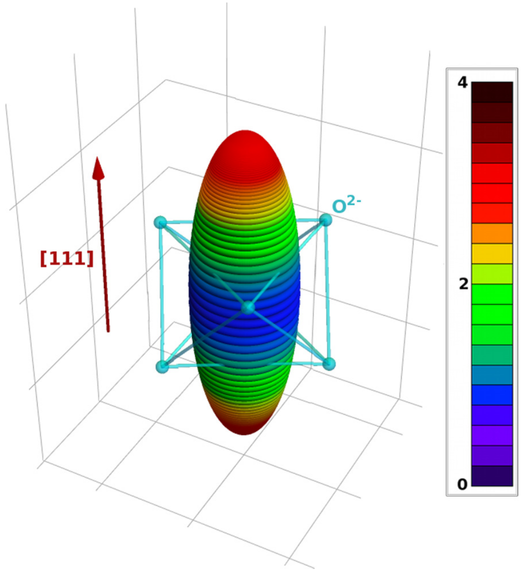

FIG. 9. (Color online) Magnetization of the "stuffed" Yb^{3+} ion at the B site of $Yb_2Ti_2O_7$. Each sphere represents the tip of the magnetization vector centered at the Yb^{3+} ion in response to an applied rotating external field of $H = 1$ T. Neighboring contiguous spheres form a ring pattern. The ellipsoidal shape of the ring pattern suggests Ising-like behavior of the rare earth moment along the local [111] direction, however the transverse extent of the ellipsoidal shape indicates a small precession around the Ising axis. The calculated magnetic moment is 3.25 μ_B.

strong Ising-like behavior. The local magnetization anisotropy for the A-site Yb^{3+} in the presence of a single O(1) oxygen vacancy is dramatically different from the stoichiometric case, where it was planar or XY-like [39,40,44], and is similar to that displayed by the prototypical spin ice magnets $Dy_2Ti_2O_7$ and $Ho_2Ti_2O_7$. This anisotropy is present even without the B_n^m ratio corrections and thus it depends only on the depleted environment.

B. Crystal field calculation for stuffed Yb^{3+} at the B site

Neutron powder diffraction measurements on the stuffed powder samples, derived from crushed single crystals, show such $Yb_2Ti_2O_7$ samples to be lightly stuffed at the 2.3% level. We therefore calculate the CEF eigenvectors and eigenvalues for stuffed Yb^{3+} at the B site. This is an interesting case to consider since the local environment at the B site is very different from that considered to this point for A site Yb^{3+}. Nonetheless, the symmetry at the B site is similar to the A site, and we can simply rotate the trigonal antiprism cage around the B site so that the local [111] direction is aligned along $\hat{z}$ and the C_2 axis along $\hat{y}$. Therefore the form of the B-site Yb^{3+} CEF Hamiltonian is identical to Eq. (1). The calculated CEF eigenvectors and eigenvalues for B-site Yb^{3+} are displayed in Table IV. Once again we have performed the point charge calculation and then scaled these results by the B_n^m ratios determined for the stoichiometric powder.

Kramers' degeneracy is again invoked and all CEF levels are again doublets, now with a gap of 105 meV between the GS and the first excited state. The eigenvectors within the GS doublet are again almost pure $m_J = \pm 7/2$ spin states, and we expect the anisotropy to be Ising-like. This is borne out by again applying a small rotating external magnetic field to probe the shape of the anisotropy of the GS magnetic moment as was done for Yb^{3+} at the A site in an oxygen depleted environment. Following the previous convention, Fig. 9 shows spheres centered along the direction in which the magnetic moment points. The color scale matches the magnetic moment size in units of μ_B. In contrast with the previous case, we can see by comparing Figs. 9 and 8 that the resulting ellipsoid is more extended normal to the local [111] direction, thus we anticipate a small precession about the easy axis with the maximum value of the magnetic moment given by $\mu = 3.25\ \mu_B$. This is similar to what was calculated for the defective scalenohedron associated with Yb^{3+} at the A site in an oxygen depleted environment (Fig. 8), but the anisotropy, characterized by the tightness of the spheres which make up the ellipsoid, is not as Ising-like as it was for that case.

It is interesting that the influence of oxygen vacancies on A-site Yb^{3+} ions and that of stuffed B-site Yb^{3+} ions have similar effects on the CEF eigenvalues and eigenvectors. Stuffing Yb^{3+} into B sites nominally occupied by Ti^{4+} will require oxygen vacancies to preserve charge neutrality, and we expect both phenomena to occur at some level in single crystals grown from the melt. The symmetry of the defective scalenohedron, especially when two O(1) are missing, is reasonably similar to the trigonal antiprism associated with stuffed Yb^{3+} at the B site, so it is perhaps not so surprising that these environments produce similar effects on the CEF eigenvalues and eigenvectors of the magnetic ions.

VI. CONCLUSIONS

Neutron scattering measurements on the stoichiometric and stuffed powder samples of the quantum spin ice candidate system $Yb_2Ti_2O_7$ have been carried out to probe the CEF eigenvalues and eigenvectors associated with the $J = 7/2$ Yb^{3+} ion in these environments. Analysis of the INS from the stoichiometric powder show the GS doublet to correspond primarily to $m_J = \pm 1/2$, with anisotropic g-tensor components given by $g_\perp = 3.69 \pm 0.15$ and $g_z = 1.92 \pm 0.20$, which therefore imply local XY anisotropy as expected. The eigenvalues and eigenvectors of the three excited state CEF doublets were all identified above a lowest CEF gap of $\sim$76.7 meV at $T = 5$ K. The energy widths, or inverse lifetimes of the CEF states, broaden with increasing temperature from $\sim$3.5 meV at low temperatures up to the highest measured temperature 300 K. This broadening mirrors the temperature dependence of the Yb^{3+} MSDs, and we associate it with the effects of zero point motion and phonons on the CEF environment around the A-site Yb^{3+} site. Interestingly, the corresponding measurements and analysis of the lightly stuffed powder sample ($x = 0.046$) of $Yb_2Ti_2O_7$ show a similar set of CEF transitions, however the energy width or inverse lifetime of the transitions are intrinsically further broadened even at $T = 5$ K. This effect is ascribed to a relatively large strain field, or "volume-of-influence," associated with each stuffed B-site Yb^{3+}.

We have also calculated the CEF eigenvectors and eigenvalues associated with Yb^{3+} in two defective environments of relevance for nonstoichiometric $Yb_2Ti_2O_7$. These are for Yb^{3+} at the A site in an oxygen depleted environment, and for stuffed Yb^{3+} at the B site. These calculations were performed within the point charge approximation and make use of a comparison of the calculated and measured eigenvalues and eigenfunctions in the stoichiometric sample to benchmark these results. Both of these defective environments give rise to related effects, wherein the GS doublet is now primarily made up of $m_J = \pm 7/2$, and the local anisotropy of the GS eigenfunctions are Ising-like, although with stronger Ising anisotropy for the oxygen depleted environment than for case of the stuffed Yb^{3+} at the B site.

These results put the nature of the CEF eigenfunctions and eigenvalues associated with Yb^{3+} in the quantum spin ice candidate system $Yb_2Ti_2O_7$ on a much firmer footing and indicate how the nature of the GS moment and anisotropy in this system can be sensitive to small amounts of disorder. The type of disorder studied in this paper is known to be relevant in many pyrochlores and most notably to influence the thermodynamics and GS properties of $Yb_2Ti_2O_7$. We hope that our systematic study of the effect of such disorder on the CEFs of $Yb_2Ti_2O_7$ will help to shed light on the role of quenched disorder in these systems.

ACKNOWLEDGMENTS

We would like to acknowledge helpful conversations with M. J. P. Gingras. We would also like to acknowledge T. E. Sherline for technical assistance with the measurements. The neutron scattering data were reduced using Mantid [45] and analyzed using the DAVE software package [46]. Research using ORNL's Spallation Neutron Source was sponsored by the Scientific User Facilities Division, Office of Basic Energy Sciences, U.S. Department of Energy. Work at McMaster University was funded by Natural Sciences and Engineering Research Council of Canada (NSERC).

[1] C. Lacroix, P. Mendels, and F. Mila, *Springer Series in Solid-State Sciences* (Springer, Heidelberg, 2011).

[2] M. Subramanian, G. Aravamudan, and G. S. Rao, Prog. Solid State Chem. **15**, 55 (1983).

[3] J. S. Gardner, M. J. P. Gingras, and J. E. Greedan, Rev. Mod. Phys. **82**, 53 (2010).

[4] S. T. Bramwell and M. J. P. Gingras, Science **294**, 1495 (2001).

[5] C. Castelnovo, R. Moessner, and S. L. Sondhi, Nature (London) **451**, 42 (2008).

[6] B. C. den Hertog and M. J. P. Gingras, Phys. Rev. Lett. **84**, 3430 (2000).

[7] S. Rosenkranz, A. P. Ramirez, A. Hayashi, R. J. Cava, R. Siddharthan, and B. S. Shastry, J. Appl. Phys. **87**, 5914 (2000).

[8] M. J. Harris, S. T. Bramwell, D. F. McMorrow, T. Zeiske, and K. W. Godfrey, Phys. Rev. Lett. **79**, 2554 (1997).

[9] L. Pauling, J. Am. Chem. Soc. **57**, 2680 (1935).

[10] Y. Yasui, M. Soda, S. Iikubo, M. Ito, M. Sato, N. Hamaguchi, T. Matsushita, N. Wada, T. Takeuchi, N. Aso *et al.*, J. Phys. Soc. Jpn. **72**, 3014 (2003).

[11] L.-J. Chang, S. Onoda, Y. Su, Y.-J. Kao, K.-D. Tsuei, Y. Yasui, K. Kakurai, and M. R. Lees, Nat. Commun. **3**, 992 (2012).

[12] J. A. Hodges, P. Bonville, A. Forget, A. Yaouanc, P. Dalmas de Réotier, G. André, M. Rams, K. Królas, C. Ritter, P. C. M. Gubbens *et al.*, Phys. Rev. Lett. **88**, 077204 (2002).

[13] K. A. Ross, J. P. C. Ruff, C. P. Adams, J. S. Gardner, H. A. Dabkowska, Y. Qiu, J. R. D. Copley, and B. D. Gaulin, Phys. Rev. Lett. **103**, 227202 (2009).

[14] K. A. Ross, L. R. Yaraskavitch, M. Laver, J. S. Gardner, J. A. Quilliam, S. Meng, J. B. Kycia, D. K. Singh, T. Proffen, H. A. Dabkowska *et al.*, Phys. Rev. B **84**, 174442 (2011).

[15] M. Hermele, M. P. A. Fisher, and L. Balents, Phys. Rev. B **69**, 064404 (2004).

[16] M. J. P. Gingras and P. A. McClarty, Rep. Prog. Phys. **77**, 056501 (2014).

[17] S. T. Bramwell, M. N. Field, M. J. Harris, and I. P. Parkin, J. Phys. Condens. Matter **12**, 483 (2000).

[18] L. Savary and L. Balents, Phys. Rev. Lett. **108**, 037202 (2012).

[19] L. Savary and L. Balents, Phys. Rev. B **87**, 205130 (2013).

[20] K. A. Ross, L. Savary, B. D. Gaulin, and L. Balents, Phys. Rev. X **1**, 021002 (2011).

[21] K. A. Ross, T. Proffen, H. A. Dabkowska, J. A. Quilliam, L. R. Yaraskavitch, J. B. Kycia, and B. D. Gaulin, Phys. Rev. B **86**, 174424 (2012).

[22] G. C. Lau, B. D. Muegge, T. M. McQueen, E. L. Duncan, and R. J. Cava, J. Solid State Chem. **179**, 3126 (2006).

[23] G. C. Lau, T. M. McQueen, Q. Huang, H. W. Zandbergen, and R. J. Cava, J. Solid State Chem. **181**, 45 (2008).

[24] H. Takatsu, H. Kadowaki, T. J. Sato, J. W. Lynn, Y. Tabata, T. Yamazaki, and K. Matsuhira, J. Phys. Condens. Matter **24**, 052201 (2012).

[25] A. Yaouanc, P. Dalmas de Réotier, Y. Chapuis, C. Marin, S. Vanishri, D. Aoki, B. Fåk, L.-P. Regnault, C. Buisson, A. Amato *et al.*, Phys. Rev. B **84**, 184403 (2011).

[26] P. D. de Reotier, V. Glazkov, C.Marin, A.Yaouanc, P. Gubbens, S.Sakarya, P. Bonville, A. Amato, C. Baines, and P. King, Physica B (Amsterdam) **374-375**, 145 (2006).

[27] H. Blote, R. Wielinga, and W. Huiskamp, Physica **43**, 549 (1969).

[28] A. Yaouanc, P. Dalmas de Réotier, C. Marin, and V. Glazkov, Phys. Rev. B **84**, 172408 (2011).

[29] A. Sen, K. Damle, and R. Moessner, Phys. Rev. Lett. **106**, 127203 (2011).

[30] X. Ke, D. V. West, R. J. Cava, and P. Schiffer, Phys. Rev. B **80**, 144426 (2009).

[31] B. D. Gaulin, E. Kermarrec, M. L. Dahlberg, M. J. Matthews, F. Bert, J. Zhang, P. Mendels, K. Fritsch, G. E. Granroth, P. Jiramongkolchai *et al.*, Phys. Rev. B **91**, 245141 (2015).

[32] G. Sala, M. J. Gutmann, D. Prabhakaran, D. Pomaranski, C. Mitchelitis, J. B. Kycia, D. G. Porter, C. Castelnovo, and J. P. Goff, Nat. Mater. **13**, 488 (2014).

[33] J. L. Prather, *Atomic Energy Levels in Crystals*, NBS Monograph 19 (National Bureau of Standards, Washington, DC, 1961).

[34] K. W. H. Stevens, Proc. Phys. Soc. London Sect. A **65**, 209 (1952).

[35] G. Squires, *Introduction to the Theory of Thermal Neutron Scattering* (Cambridge University Press, Cambridge, UK, 1978).

[36] G. E. Granroth, A. I. Kolesnikov, T. E. Sherline, J. P. Clancy, K. A. Ross, J. P. C. Ruff, B. D. Gaulin, and S. E. Nagler, J. Phys.: Conf. Ser. **251**, 012058 (2010).

[37] A. Bertin, Y. Chapuis, P. D. de Réotier, and A. Yaouanc, J. Phys. Condens. Matter **24**, 256003 (2012).

[38] H. B. Cao, A. Gukasov, I. Mirebeau, and P. Bonville, J. Phys. Condens. Matter **21**, 492202 (2009).

[39] J. A. Hodges, P. Bonville, A. Forget, M. Rams, K. Królas, and G. Dhalenne, J. Phys. Condens. Matter **13**, 9301 (2001).

[40] B. Z. Malkin, A. R. Zakirov, M. N. Popova, S. A. Klimin, E. P. Chukalina, E. Antic-Fidancev, P. Goldner, P. Aschehoug, and G. Dhalenne, Phys. Rev. B **70**, 075112 (2004).

[41] M. Hutchings, in *Solid State Physics*, edited by F. Seitz and D. Turnbull (Academic, New York, 1964), Vol. 16, pp. 227–273.

[42] U. Walter, J. Phys. Chem. Solids **45**, 401 (1984).

[43] A. J. Freeman and R. E. Watson, Phys. Rev. **127**, 2058 (1962).

[44] R. Siddharthan, B. S. Shastry, A. P. Ramirez, A. Hayashi, R. J. Cava, and S. Rosenkranz, Phys. Rev. Lett. **83**, 1854 (1999).

[45] O. Arnold, J. Bilheux, J. Borreguero, A. Buts, S. Campbell, L. Chapon, M. Doucet, N. Draper, R. Leal, M. Gigg *et al.*, Nucl. Instrum. Methods Phys. Res. Sect. A **764**, 156 (2014).

[46] R. T. Azuah, L. R. Kneller, Y. Qiu, C. M. Brown, J. R. D. Copley, R. M. Dimeo, and P. L. W. Tregenna-Piggott, J. Res. Natl. Inst. Stand. Technol. **114**, 341 (2009).

2.2 Preface to Publication II: The magnetic ground state of $Yb_2Ti_2O_7$ and its low energy spin dynamics.

The impact of low levels of stuffing on the magnetic ground state of $Yb_2Ti_2O_7$ are further investigated in this second publication. Here, we used elastic and low energy inelastic neutron scattering on the same samples as publication I. Our elastic neutron scattering experiment shows the apparition of magnetic Bragg peaks at low temperature for the stoichiometric powder of $Yb_2Ti_2O_7$. These magnetic Bragg peaks onset at a temperature that correlates well with the broad specific heat anomaly, around 2 K and are practically unresponsive to passing through the sharp specific heat anomaly at 265 mK (see Fig.2.1(a)). The magnetic structure of $Yb_2Ti_2O_7$ has been refined to a Γ_9 ferromagnetic structure with a splayed angle of ~15 °. Finally, low energy inelastic neutron scattering reveals that both the stoichiometric powder and the crushed single crystal have a continuum of excitations that do not resemble conventional spin waves. In both the stoichiometric and stuffed samples, the spin wave excitations are gapless within an energy resolution of 0.09 meV. However, the overall continuum of scattering is significantly broader in the stuffed sample. Our findings are consistent with $Yb_2Ti_2O_7$ being a dynamical ferromagnet with strong quantum fluctuations that strongly resemble a spin liquid state.

For this paper, I performed the inelastic neutron scattering experiments and analyzed the resultant data. I also refined the magnetic structure of the stoichiometric powder of $Yb_2Ti_2O_7$. Finally, I wrote part of the manuscript as well as the response to the referee reports. The contributions of each author are summarized below.

Author Contributions:

- *Experimental Concept*: K.A. Ross, B.D. Gaulin
- *Sample Preparation*: K.A. Ross, H.A. Dabkowska
- *Neutron Scattering Experiment*: K.A. Ross, E. Kermarrec, **J. Gaudet**, N.P. Butch, G. Ehlers B.D. Gaulin
- *Data Analysis*: **J. Gaudet**, K.A. Ross, E. Kermarrec, B.D. Gaulin
- *Manuscript*: **J. Gaudet**, K.A. Ross, E. Kermarrec, B.D. Gaulin

Gapless quantum excitations from an icelike splayed ferromagnetic ground state in stoichiometric $Yb_2Ti_2O_7$

J. Gaudet,[1] K. A. Ross,[2,3,*] E. Kermarrec,[1] N. P. Butch,[3] G. Ehlers,[4] H. A. Dabkowska,[5] and B. D. Gaulin[1,5,6]
[1]*Department of Physics and Astronomy, McMaster University, Hamilton, Ontario L8S 4M1, Canada*
[2]*Institute for Quantum Matter and Department of Physics and Astronomy, Johns Hopkins University, Baltimore, Maryland 21218, USA*
[3]*NIST Center for Neutron Research, National Institute of Standards and Technology, Gaithersburg, Maryland 20899, USA*
[4]*Quantum Condensed Matter Division, Oak Ridge National Laboratory, Oak Ridge, Tennessee 37831, USA*
[5]*Brockhouse Institute for Materials Research, Hamilton, Ontario L8S 4M1, Canada*
[6]*Canadian Institute for Materials Research, 180 Dundas Street West, Toronto, Ontario M5G 1Z8, Canada*
(Received 25 November 2015; published 3 February 2016)

The ground state of the quantum spin ice candidate magnet $Yb_2Ti_2O_7$ is known to be sensitive to weak disorder at the $\sim$1% level which occurs in single crystals grown from the melt. Powders produced by solid state synthesis tend to be stoichiometric and display large and sharp heat capacity anomalies at relatively high temperatures, $T_C \sim 0.26$ K. We have carried out neutron elastic and inelastic measurements on well characterized and equilibrated stoichiometric powder samples of $Yb_2Ti_2O_7$ which show resolution-limited Bragg peaks to appear at low temperatures, but whose onset correlates with temperatures much higher than T_C. The corresponding magnetic structure is best described as an icelike splayed ferromagnet. The spin dynamics in $Yb_2Ti_2O_7$ are shown to be gapless on an energy scale <0.09 meV at all temperatures and organized into a continuum of scattering with vestiges of highly overdamped ferromagnetic spin waves present. These excitations differ greatly from conventional spin waves predicted for $Yb_2Ti_2O_7$'s mean field ordered state, but appear robust to weak disorder as they are largely consistent with those displayed by nonstoichiometric crushed single crystals and single crystals, as well as by powder samples of $Yb_2Ti_2O_7$'s sister quantum magnet $Yb_2Sn_2O_7$.

DOI: 10.1103/PhysRevB.93.064406

I. INTRODUCTION

Pyrochlore magnets of the form $A_2B_2O_7$ have been of great topical interest as both the A and B sublattices independently form networks of corner-sharing tetrahedra, one of the canonical crystalline architectures supporting geometrical frustration in three dimensions [1,2]. The cubic rare earth titanates, of the form $RE_2Ti_2O_7$ have been especially relevant as many magnetic RE^{3+} ions can occupy the A site of the structure and where the nonmagnetic Ti^{4+} occupy the B site. This pyrochlore family can also be relatively easily produced in both powder and single crystal form [3–5]. One of the family members, $Yb_2Ti_2O_7$, has been particularly topical as it has been proposed as a realization of quantum spin ice [6–16]. It displays a net ferromagnetic Curie-Weiss constant of $\sim$0.6 K [17,18], and crystal field (CF) effects give rise to a CF ground state doublet at the Yb^{3+} site made up of primarily $m_J = \pm 1/2$ eigenvectors and local XY anisotropy [19–21]. $Yb_2Ti_2O_7$ is therefore a good realization of quantum $S_{\text{eff}} = 1/2$ spins decorating a network of corner-sharing tetrahedra—the pyrochlore lattice.

The microscopic spin Hamiltonian for $Yb_2Ti_2O_7$ has been estimated using neutron spectroscopic measurements of spin waves in its high field polarized state [12]. While the zero field phase of $Yb_2Ti_2O_7$ does not show well defined spin waves in single crystals, a magnetic field applied along the [1–10] direction pushes $Yb_2Ti_2O_7$ through a quantum phase transition or crossover near $\mu_0 H_C \sim 0.5$ T into a polarized phase that is characterized by resolution-limited spin waves [14]. Linear spin wave theory using anisotropic exchange produces an excellent description of the high field spin wave dispersion and intensities, and the resulting microscopic Hamiltonian has been used in high temperature series expansions which accurately describe the magnetization and heat capacity of $Yb_2Ti_2O_7$ in absolute units [22]. $Yb_2Ti_2O_7$'s spin Hamiltonian contains four symmetry-allowed near-neighbor anisotropic exchange terms, and it has been proposed that the largest of these is J_{zz}, which ferromagnetically couples together local z, or Ising components of spin [12]. These z components are aligned directly into or out of the tetrahedra, and this combination of $S_{\text{eff}} = 1/2$ spins, the spin Hamiltonian, and the pyrochlore lattice would then be responsible for the quantum spin ice phenomenology. Somewhat different phenomenology has also been discussed in which J_{zz} is less dominant [23].

While the general phase behavior for an anisotropic exchange Hamiltonian of the form which describes $Yb_2Ti_2O_7$ in zero magnetic field has exotic quantum spin liquid and Coulomb ferromagnetic mean field ground states present within it [24,25], the mean field ground state predicted on the basis of $Yb_2Ti_2O_7$'s spin Hamiltonian is a simple ferromagnet with a mean field phase transition of $T_{\text{MF}} \sim 3$ K [12]. A broad "hump" in $Yb_2Ti_2O_7$'s experimentally determined heat capacity (C_P) is observed at $\sim$2 K, roughly co-incident with the calculated T_{MF}, however there are no indications of order observed above a sharp C_P anomaly which occurs near $T_C \sim 0.26$ K in stoichiometric powders of $Yb_2Ti_2O_7$ [11,26]. Taking the sharp C_P anomaly at face value for an indication of the ferromagnetic phase transition predicted by mean field theory, this indicates that T_{MF} is suppressed by a factor of $\sim$12 by quantum fluctuations, geometrical frustration, or both. However, there are strong indications that $Yb_2Ti_2O_7$'s zero field phase below $T_C \sim 0.26$ K is far removed from

---

[*] Current address: Colorado State University, Fort Collins, Colorado 80523-1875, USA.

a conventional ferromagnet. To date there are experimental studies which support a relatively simple ferromagnetic ground state [6,8] but also studies which show extensive diffuse neutron scattering covering all of reciprocal space [10], no changes in the spin relaxation observed when cooling below the sharp C_P anomaly in μSR studies from stoichiometric samples [27], and no evidence for the conventional spin waves that are expected as the normal modes of the magnetically-ordered state in any sample [13,14,23].

An interesting feature of $Yb_2Ti_2O_7$'s exotic zero magnetic field ground state is its sensitivity to weak disorder [28,29]. The sharp C_P anomaly observed at $T_C \sim 0.26$ K in stoichiometric powder samples is observed to be broader and to occur at lower temperatures in all single crystal samples measured to date [29]. The C_P anomalies can occur as low as ~0.15 K in single crystals grown from floating zone image furnace techniques, may not obviously occur at any temperature, or may appear as multiple peaks at lower temperatures.

In the interest of understanding the microscopic structure and defects responsible for the differences between powder samples grown by solid state synthesis and single crystals grown from the melt by floating zone techniques, neutron diffraction studies were carried out on both powder and crushed single crystal (CSC) samples that were known to display different C_P behavior at low temperature [28]. The conclusions were that, while the powder sample was stoichiometric $Yb_2Ti_2O_7$, the CSC was characterized as exhibiting weak "stuffing" wherein a small proportion of excess Yb^{3+} resides on the Ti^{4+} site, and the composition of the crushed single crystal was $Yb_{2+x}Ti_{2-x}O_{7+y}$ with $x = 0.046$. Note that this defect level is close to the limit of detectability by conventional diffraction techniques. This study was greatly aided by the fact that Ti displays a negative coherent neutron scattering length, hence there is significant neutron contrast for Yb, which has a positive coherent neutron scattering length, occupying the Ti site. In and of itself, sensitivity of the ground state to such weak disorder is a remarkable result, as conventional three-dimensional ordered states are not sensitive to disorder at such a low level. For example, the phase transition to noncollinear Ψ_2 antiferromagnetic order in $Er_2Ti_2O_7$ is not sample dependent and has been studied as a function of magnetic dilution and shown to be consistent with conventional three-dimensional percolation theory [30]. A recent study of the Yb^{3+} crystal field excitations in $Yb_2Ti_2O_7$ suggests that the anisotropy of Yb^{3+} in defective environments is Ising-like, rather than XY-like in stoichiometric $Yb_2Ti_2O_7$, and this may be related to the effectiveness of disorder at this low ~1% level [21].

It is therefore important to fully characterize powder samples of $Yb_2Ti_2O_7$ which are known to be stoichiometric and to display sharp C_P anomalies at $T_C = 0.26$ K, that is to use this as a benchmark for understanding the zero field ground state of pristine $Yb_2Ti_2O_7$. In this paper, we report elastic and inelastic neutron scattering results from the same two powder samples previously studied by neutron diffraction [28] and which are known to be stoichiometric $Yb_2Ti_2O_7$ and the CSC with composition $Yb_{2+x}Ti_{2-x}O_{7-y}$ with $x = 0.046$. In addition, we report a comparison between the spin dynamics measured on a stoichiometric powder of $Yb_2Ti_2O_7$, the CSC powder, a single crystal of $Yb_2Ti_2O_7$ grown by the floating zone technique, and a powder sample of $Yb_2Ti_2O_7$'s sister pyrochlore magnet, $Yb_2Sn_2O_7$. We show that stoichiometric $Yb_2Ti_2O_7$ displays resolution-limited magnetic Bragg scattering at low temperatures, however these persist to a much higher temperature scale than $T_C = 0.26$ K. Nonetheless, looking only at the low temperature Bragg intensities, we refine a static magnetic structure which is best described as an icelike splayed ferromagnet with an ordered moment of 0.90(9) μ_B. The spin dynamics at the lowest temperatures in stoichiometric $Yb_2Ti_2O_7$ in zero field are indeed far removed from conventional spin waves. They are gapless on an energy scale <0.09 meV at all wave vectors and characterized by a continuum of scattering with a bandwidth of ~1 meV. Vestiges of very overdamped ferromagnetic spin waves can be seen in the inelastic scattering, which itself is temperature independent below $T_{MF} \sim 3$ K.

II. EXPERIMENTAL DETAILS

The powder samples employed in this study were the same samples previously studied by Ross *et al.* [28]. 10 grams of stoichiometric $Yb_2Ti_2O_7$ and eight grams of the CSC powder, $Yb_{2+x}Ti_{2-x}O_{7+y}$ with $x = 0.046$, were separately loaded in aluminum sample cans with copper lids under 10 atms of helium exchange gas. This method of loading powder samples is known to provide good thermal contact to the cold finger of the dilution refrigerator and maintains thermal conductivity below 1 K by enabling enough superfluid helium to coat the powder grains [31]. The 4 gram single crystal of $Yb_2Ti_2O_7$ (produced in a floating zone image furnace following similar procedures to those used to grow other single crystal titanate pyrochlores) was mounted on an aluminum holder.

Elastic neutron scattering measurements were carried out on the SPINS triple axis instrument at the NIST Center for Neutron Research. SPINS used pyrolytic graphite as both monochromator and analyzer, and 80' collimators before and after the sample, producing a 5.0 meV elastically scattered beam with an energy resolution of 0.25 meV. Cooled beryllium filters placed before and after the sample helped to eliminate higher harmonic contamination. The sample was first cooled to $T = 8$ K where scans of the (111), (002), (220), (113), and (222) Bragg peaks were collected. Afterwards, the sample was cooled down to 100 mK and sat at this temperature for two hours before collecting measurements at the same Bragg positions as above. Finally, the sample was warmed up to 700 mK where another scan of the same Bragg peaks was also collected.

Inelastic neutron scattering measurements were also performed on both the stoichiometric powder as well as the CSC, stuffed powder using the time-of-flight disk chopper spectrometer (DCS) at NIST [32]. For these measurements, monochromatic incident neutrons of a wavelength of 5 Å were employed, giving an energy resolution at the elastic position of 0.09 meV. Empty can measurements have been used as a background for these data. Inelastic neutron scattering measurements on the single crystal of $Yb_2Ti_2O_7$ were performed using the cold neutron chopper spectrometer (CNCS) [33] at the Spallation Neutron Source (SNS) at Oak Ridge National Laboratory. For this time-of-flight experiment, the single crystal was mounted in a dilution refrigerator and aligned with the [HHL] plane in the horizontal plane. An incident neutron energy of 3.3 meV was employed which gave an energy resolution of 0.1 meV at the elastic position. Sample rotation methods were employed wherein the single crystal sample was rotated 360° about the vertical direction in 1° steps. The background is approximated using a measurement done under the same conditions but without the sample. Magnetic and structural refinement were performed using SARAh Refine [34] and FullProf [35].

III. RESULTS AND DISCUSSION

A. Elastic neutron scattering and magnetic structure determination

Figure 1 shows elastic neutron scattering data taken on the stoichiometric powder sample of $Yb_2Ti_2O_7$ using SPINS. No magnetic Bragg peaks were observed at nuclear-disallowed positions upon cooling below T_C, and consequently we focused our attention on nuclear-allowed Bragg peaks typical of $Q = 0$ magnetic structures. Figures 1(a) and 1(b) show the (111) Bragg peak at three temperatures: $T = 0.1$ K (below T_C), $T = 0.7$ K (above T_C), and $T = 8$ K, which is above both the T_{MF} calculated for $Yb_2Ti_2O_7$ on the basis of its microscopic spin Hamiltonian, as well as above the higher temperature “hump” in its C_P near ~2 K. Figure 1(c) shows the corresponding elastic scattering at the (113) Bragg position at $T = 0.1$ K and $T = 8$ K. Elastic scattering at both wave vectors is dominated by nuclear contributions, but a weak temperature dependent magnetic contribution is identified as can be seen in Figs. 1(b) and 1(d) which show $T = 0.1$ K–$T = 0.7$ K, and $T = 0.7$ K–$T = 8$ K data sets for (111) and a $T = 0.1$–8 K data set for (113), respectively. Similar elastic scattering measurements were also carried out at the (220) Bragg position. The magnetic intensities extracted from these differences are listed in Table I, where we see that for all of the (111), (113), and (222) Bragg positions, the increase in scattering, relative to $T = 8$ K, is 3.2(4)%, 3.3(5)%, and 3.6(6)%, respectively. Relative to $T = 0.7$ K, the magnetic intensity at $T = 0.1$ K is increased by only ~1.3% at the (111) Bragg position. We also note that the differences in the elastic scattering have the same Q line shape as the original Bragg scattering, implying that the corresponding magnetic order is long range, with a correlation length exceeding 80 Å.

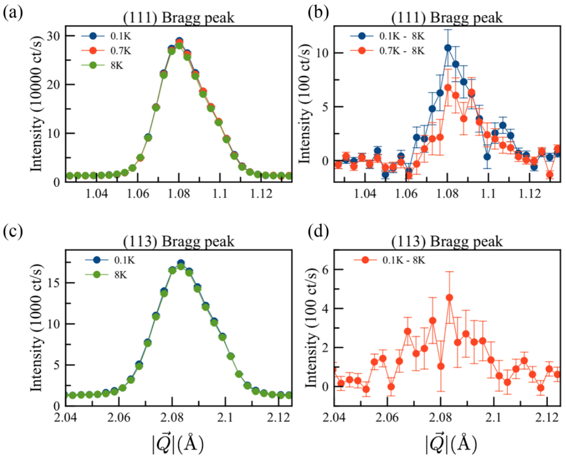

FIG. 1. The temperature dependence of the (111) and (113) Bragg peaks. Panels (a) and (c) show the elastically scattered neutron intensity as a function of the momentum transfer $|\vec{Q}|$ around the (111) and (113) Bragg peaks respectively. Panels (b) and (d) shows the subtraction between the different $|\vec{Q}|$ cuts at different temperatures. A clear, $|\vec{Q}|$-resolution-limited increase of the elastic scattering at these two Bragg peaks is observed and is representative of the data used to model the magnetic structure of stoichiometric $Yb_2Ti_2O_7$. Error bars represent one standard deviation.

Ignoring for the time being the fact that the magnetic order parameter does not go to zero above $T_C = 0.26$ K, we can nonetheless refine a magnetic structure based on the relative intensities of the differences in Bragg scattering between $T = 0.1$ K and 8 K. This difference is plotted as a function of $|Q|$ in Fig. 2(a), along with the best fit to a model for a canted or splayed ferromagnet of the form depicted in the inset of Fig. 2(b). This generalized structure has the Yb moments along a [100] direction, but also allows for a canting angle θ which can be either towards (+) or away from (−) the local [111] direction, that is the direction pointing into or out of the tetrahedron. A collinear [100] ferromagnet would correspond to a canting angle of zero, while the ordered spin ice ground state, in which all moments point directly into or out of the tetrahedra, would correspond to $\theta = 54.7°$. A negative canting angle gives an XY splayed ferromagnet. The best fit, shown as the solid line in Fig. 2(a), corresponds to a splayed icelike ferromagnetic ground state with a positive canting angle of $14 \pm 5°$ and an ordered moment (relative to 8 K) of 0.90(9) μ_B. The saturated moment determined by DC magnetization is 1.75 μ_B, which compared to the order moment we obtained gives a spin polarization of 51%. Note that, as shown in Fig. 1(b), most of the decrease in the Bragg scattering on raising the temperature occurs above 0.7 K, more than a factor of two above $T_C = 0.26$ K. Our refinements of these magnetic structures are summarized in Table I, where we have calculated the expected increases in Bragg scattering at each of (111), (113), and (222) for two different $Q = 0$ magnetic structures. The splayed XY ferromagnet, with a negative canting angle, is known to describe $Yb_2Ti_2O_7$'s sister pyrochlore magnet $Yb_2Sn_2O_7$ ($\theta \sim -10°$) [36], while the splayed spin ice structure has been reported in some studies of single crystal $Yb_2Ti_2O_7$ but with a smaller splay angle ($\theta \sim 1°$) [6,8]. Figure 2(b) shows how the goodness-of-fit parameter (χ^2) varies as a function of splay angle for this model of splayed or canted ferromagnets.

Figure 3 shows the temperature dependence of the (111) Bragg intensity from the stoichiometric powder sample of $Yb_2Ti_2O_7$, relative to $T = 0.7$ K. This data set was collected while warming from 100 mK to 700 mK with a warming rate of 1 mK/min. For reference, we overplotted the elastic scattering perviously measured near the (111) position in single crystal $Yb_2Ti_2O_7$ (note: both curves are scaled to their intensities at 100 mK, after subtracting their intensities at 700 mK). It is clear that these temperature dependencies mirror each other. We also included C_P as measured on a powder sample of $Yb_2Ti_2O_7$ with $T_C = 0.26$ K. One can see that these magnetic intensities do not resemble a conventional order parameter with $T_C = 0.26$ K. The elastic intensities are approximately constant up to ~0.35 K and then begin to decrease.

TABLE I. A Comparison of the excess intensity in the measured Bragg peaks with model calculations for possible ferromagnetic ground states. The percent excess elastic intensity for the (111), the (113), and the (222) Bragg peaks are compared with those calculated for a (100) collinear ferromagnet and a splayed ice ferromagnet [Fig. 2(b)]. The best agreement between the observed excess intensity and such a model for canted ferromagnets is achieved with the splayed ice ferromagnet and a splay angle of 14 ± 5°.The magnetic moment size at the Yb^{3+} site, based on the increase in Bragg intensity relative to 8 K, is also given for the proposed ordered states.

	% increase (111)	% increase (113)	% increase (222)	Moment size	Canting angle (θ)	χ^2
Measured	3.2(4)	3.3(5)	3.6(6)			
Collinear FM	3.2	4.5	5.6	1.1 μ_B	0°	1.09
Splayed Ice FM	3.2	3.1	4.2	0.90(9)μ_B	14° ± 5°	0.99

B. Inelastic neutron scattering and gapless spin excitations in the $Yb_2Ti_2O_7$ ground state

Inelastic neutron scattering measurements were carried out on our three $Yb_2Ti_2O_7$ samples (stoichiometric powder, lightly stuffed CSC powder, and single crystal) using time-of-flight neutron spectrometers. Measurements were carried out on the stoichiometric $Yb_2Ti_2O_7$ powder sample and the CSC lightly stuffed powder with composition $Yb_{2+x}Ti_{2-x}O_{7+y}$ $x = 0.046$ using the DCS direct geometry chopper spectrometer at NIST. The resulting $S(|\vec{Q}|,E)$ for these two samples at $T = 0.1$ K are shown in Figs. 4(a) and 4(b). The corresponding [HHL] plane-averaged data set (approximating a powder average) for single crystal $Yb_2Ti_2O_7$ at $T = 0.1$ K is shown in Fig. 4(c).

The inelastic spectral weight shown in Fig. 4 is known to be magnetic in origin from its previously determined field dependence and from its temperature dependence to be discussed shortly. We see that $S(|\vec{Q}|,E)$ in stoichiometric $Yb_2Ti_2O_7$ at $T = 0.1$ K is largely characterized by a continuum of scattering below an upper band edge of ∼1 meV, and it is gapless on an energy scale <0.09 meV at all wave vectors measured. The inelastic scattering has some weak structure to it, resembling overdamped ferromagnetic spin waves which disperse as $\hbar\omega \sim Q^2$ and whose intensity peaks at small Q.

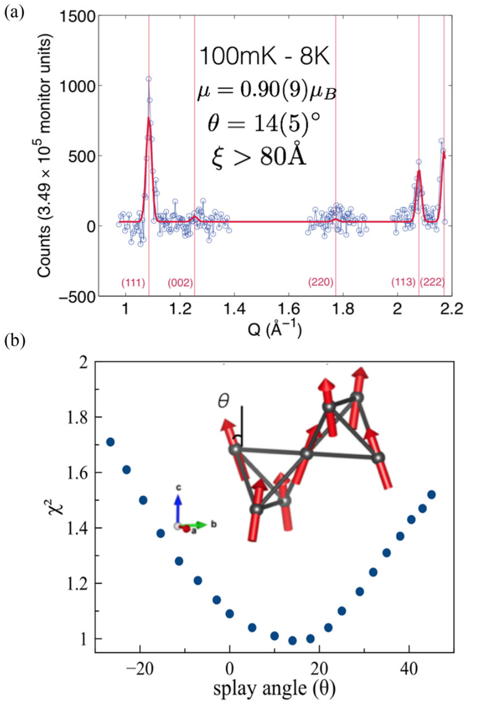

FIG. 2. Intensity of elastic magnetic scattering vs Q and the corresponding fit to the splayed ice ferromagnet. (a) the best fit of the model for a splayed ice ferromagnet to the difference of elastic neutron scattering intensity at 100 mK and 8 K (i.e., the magnetic elastic scattering) is shown. The model employed is a splayed ferromagnet (a $Q = 0$ structure with a net moment along the cubic axes) on the pyrochlore lattice, with splay angle of $\theta = 14(5)°$ and an ordered moment of 0.90(9) μ_B. Note: the error bars are not shown in this figure for clarity, but are taken into account as weights in the least squared fitting of the model. (b) The goodness-of-fit parameter χ^2 as a function of splay angle is shown. The inset to (b) shows an illustration of the best fit magnetic structure model on a pair of tetrahedra.

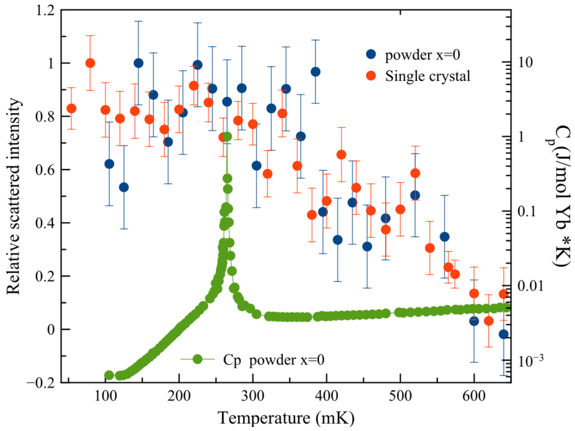

FIG. 3. The temperature dependence of the elastic scattered intensity at $|\vec{Q}| = (111)$. The scattered elastic neutron intensity, relative to $T = 700$ mK at $|\vec{Q}| = (111)$, shows similar temperature dependence for both a previously measured single crystal (data taken from Ross *et al.* [14]) and for the stoichiometric powder sample of $Yb_2Ti_2O_7$ (this paper). With increasing temperature, the elastic magnetic scattering begins to fall around $T = 0.35$ K and decreases approximately linearly above this temperature. The specific heat anomaly $T_C \sim 0.26$ K for a representative powder sample of $Yb_2Ti_2O_7$ (data taken from Ross *et al.* [28]) is shown for reference and reveals the relative insensitivity of the temperature dependence of the elastic scattering to the specific heat anomaly.

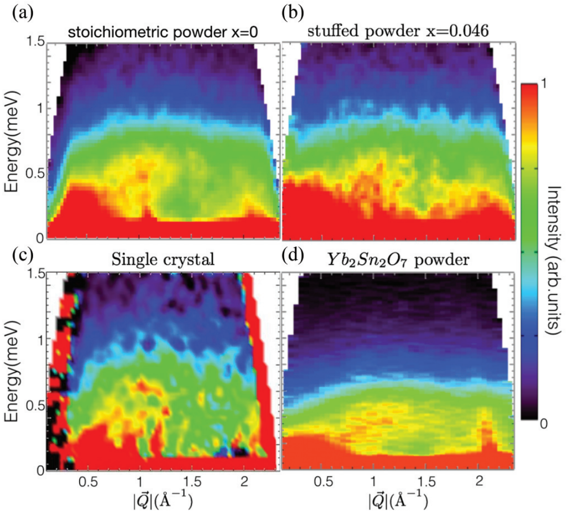

FIG. 4. $S(|\vec{Q}|,E)$ as measured for stoichiometric and weakly stuffed $Yb_2Ti_2O_7$ with comparison to $Yb_2Sn_2O_7$. (a) and (b) show $S(|\vec{Q}|,E)$ measured on the stoichiometric $Yb_2Ti_2O_7$ powder and the lightly stuffed CSC powder of $Yb_{2+x}Ti_{2-x}O_{7+y}$ with $x = 0.046$, respectively, both at $T = 0.1$ K. (c) shows the corresponding $S(|\vec{Q}|,E)$ measurement on single crystal $Yb_2Ti_2O_7$, also at $T = 0.1$ K. Panel (d) shows $S(|\vec{Q}|,E)$ measured on powder $Yb_2Sn_2O_7$ at $T = 0.1$ K, by Dun *et al.* [37]. All four data sets have had an empty can background data set subtracted from them and have had intensities scaled such that the scattering at $|\vec{Q}| = 1\,\text{Å}^{-1}$ and $E = 0.5$ meV saturates the color scale.

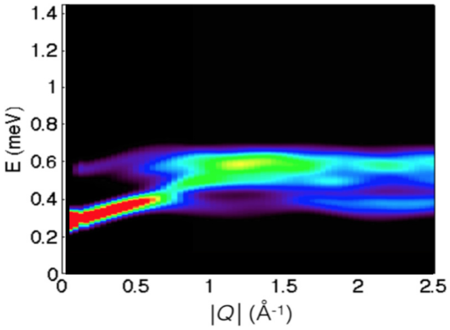

FIG. 5. Energy vs $|\vec{Q}|$ slice of the mean-field calculation of $S(|\vec{Q}|,E)$ for $Yb_2Ti_2O_7$. $S(|\vec{Q}|,E)$ has been computed using an anisotropic spin 1/2 exchange Hamiltonian with the exchange parameters determined by Ross *et al.* [12]. This calculation successfully accounts for the spin wave spectrum in the high magnetic field, polarized state at all wave vectors, but does not resemble the inelastic neutron scattering seen in Fig. 4. In particular the measured inelastic magnetic scattering is gapless at all wave vectors, while the calculated $S(|\vec{Q}|,E)$, shown here, possesses a minimum gap of ∼0.25 meV.

This continuum spin excitation spectrum is very different from that expected for spin waves within the ferromagnetically ordered state predicted by mean field theory on the basis of the anisotropic exchange Hamiltonian determined previously from the high field, polarized state. Figure 5 shows the powder average of this theoretical spin wave spectrum broadened by the instrumental resolution, and one clearly expects sharp and dispersing excitations. The predicted spin wave spectrum is gapped at all wave vectors, with a minimum gap of ∼0.25 meV at $Q = 0$. Such a gap would be easily observed with our inelastic measurements using DCS.

While the spin excitation spectrum in stoichiometric $Yb_2Ti_2O_7$ is exotic, and quite distinct from the expectations of anisotropic spin wave theory, comparison to the measured spectrum in lightly stuffed CSC $Yb_{2+x}Ti_{2-x}O_{7+y}$ with $x = 0.046$, in Fig. 4(b), and to single crystal $Yb_2Ti_2O_7$, in Fig. 4(c) which is also likely lightly stuffed, shows that is not particularly sensitive to weak disorder. The upper band edge of the continuum slightly softens in the lightly stuffed CSC sample and single crystal, and the vestiges of the overdamped ferromagnetic spin waves are not as clear compared with the stoichiometric $Yb_2Ti_2O_7$ in Fig. 4(a). However, the continuum nature of the magnetic scattering and its lack of a gap at any wave vector are common to all three samples.

These features are also common to $S(|\vec{Q}|,E)$ measured on DCS under ∼ identical conditions on a powder sample of $Yb_2Sn_2O_7$ by Dun and co-workers shown in Fig. 4(d). These measurements on $Yb_2Sn_2O_7$ were previously published [37], albeit using a high temperature subtraction, as opposed to the empty can subtraction we employ here. $Yb_2Sn_2O_7$ cannot be grown as a single crystal due to the volatility of the SnO_2 starting materials, which also likely implies some level of defects in its powders.

Energy cuts through the $S(|\vec{Q}|,E)$ data sets for stoichiometric powder $Yb_2Ti_2O_7$ and lightly stuffed CSC with approximate composition $Yb_{2+x}Ti_{2-x}O_{7+y}$ and $x = 0.046$ are shown in Fig. 6. While differences between the four data sets of Fig. 4 can be seen at $Q \leqslant 0.4\ \text{Å}^{-1}$, this low-$Q$ region corresponds to the edge of the neutron detector bank closest to the incident beam and is thus the part of the data set that is most sensitive to the precise details of the background subtraction. This low-Q region of scattering is thus avoided in the following quantitative analysis shown in the energy scans of Fig. 6. These energy scans employ different Q integrations, going from smaller Q to larger Q in Figs. 6(a)–6(d) for $Yb_2Ti_2O_7$ and Figs. 6(e)–6(h) for $Yb_{2+x}Ti_{2-x}O_{7+y}$ and $x = 0.046$. Consistent with the detailed $S(|\vec{Q}|,E)$ maps, we see that pronounced inelastic shoulders are observed at intermediate Q's, as seen in Figs. 6(b) and 6(c), and these are the vestiges of the ferromagnetic spin waves discussed earlier. Well defined ferromagnetic spin waves would show inelastic peaks which would disperse as $E \sim Q^2$. As seen in Figs. 6(f) and 6(g), the shoulders are considerably more rounded in the lightly stuffed CSC sample, indicating that the vestiges of these overdamped excitations are even further overdamped in the presence of weak disorder.

The energy cuts through $S(|\vec{Q}|,E)$ in Fig. 6, also shows the temperature evolution of this inelastic scattering from $T = 0.1$ K, well below $T_C = 0.26$ K, to $T = 8$ K, above T_{MF} and the "hump" in C_P near 2 K. This temperature dependence is very similar for both the stoichiometric $Yb_2Ti_2O_7$ and the lightly stuffed CSC powder sample, so we focus our discussion on the stoichiometric $Yb_2Ti_2O_7$ energy cuts of $S(|\vec{Q}|,E)$ shown in the top panels of Fig. 6. It is worth noting that

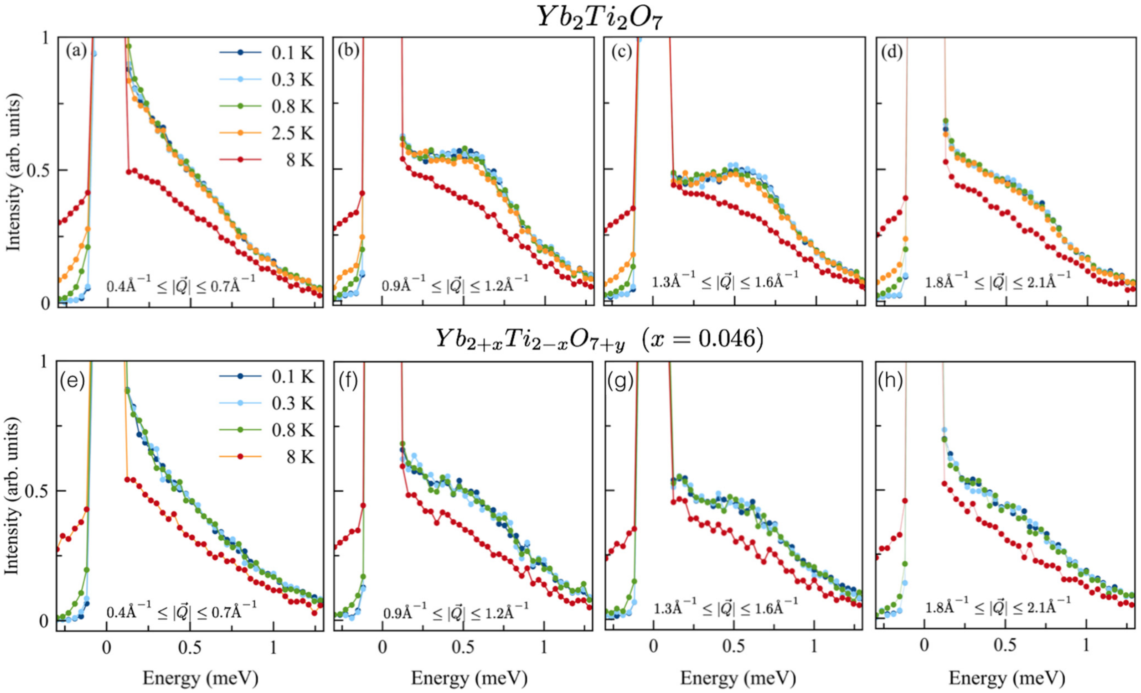

FIG. 6. Energy cuts of $S(|\vec{Q}|, E)$ for the stoichiometric powder sample of $Yb_2Ti_2O_7$ and the CSC $Yb_{2+x}Ti_{2-x}O_{7+y}$ with $x = 0.046$. Top panels: These four different panels show cuts through $S(|\vec{Q}|, E)$ of $Yb_2Ti_2O_7$, taken from Fig. 4(a), for different ranges of $|\vec{Q}|$ and at different temperatures. Four different integrations in $|\vec{Q}|$ going from smaller $|\vec{Q}|$ in (a) to larger $|\vec{Q}|$ in (d) have been applied, as indicated in the individual panels. No differences in the scattering are observed from $T = 2.5$ K down to $T = 0.1$ K. Bottom panels: Same data and $|\vec{Q}|$ integrated cuts as in (a)–(d) but for $Yb_{2+x}Ti_{2-x}O_{7+y}$ with $x = 0.046$ taken from Fig. 4(b).

the temperature evolution of $S(|\vec{Q}|, E)$ on the negative energy side shows clear evolution of the scattering from $T = 0.8$ to $T = 0.3$ K, implying that the stoichiometric $Yb_2Ti_2O_7$ was equilibrated down to at least 0.3 K. While not easily visible in Fig. 6, there is a continued decrease in the inelastic scattering near -0.1 meV from $T = 0.3$ K to 0.1 K, strongly suggesting that the system equilibrated at all temperatures measured.

The most striking feature of the temperature dependence of $S(|\vec{Q}|, E)$ in $Yb_2Ti_2O_7$ is that there is none for temperatures less than ~2.5 K. That is, the gapless, continuum form of $S(|\vec{Q}|, E)$ in stoichiometric $Yb_2Ti_2O_7$ is maintained through its large C_P anomaly at $T_C = 0.26$ K, up to 10 times this temperature. Changes in $S(|\vec{Q}|, E)$ only appear in the temperature range from 2.5 K to 8 K, consistent with a temperature evolution on the scale of the calculated $T_{\text{MF}} \sim 3$ K, or the high temperature "hump" observed in T_C near 2 K. Very similar temperature dependence of $S(|\vec{Q}|, E)$ is observed for the lightly stuffed CSC sample, as shown in the bottom panels of Fig. 6.

IV. CONCLUSIONS

New neutron scattering measurements on a stoichiometric powder sample of $Yb_2Ti_2O_7$ reveal low temperature magnetic Bragg peaks, overlapping with nuclear-allowed Bragg peaks. This elastic scattering is interpreted in terms of a long range ordered, splayed spin ice static structure with a correlation length exceeding 80 Å and an ordered moment, relative to 8 K, of 0.90(9) μ_B. However, the temperature dependence of the elastic Bragg scattering does not correlate with the $T_C = 0.26$ K expected for such powder samples. Rather, this elastic scattering begins to dissipate above ~350 mK and shows continued decrease above 700 mK.

The zero field magnetic inelastic spectrum of stoichiometric $Yb_2Ti_2O_7$ is exotic. It shows a gapless, continuum form, at $T = 0.1$ K, well below $T_C = 0.26$ K, with an upper band edge of ~1 meV. No spin gap is observed at any wave vector to an upper limit of 0.09 meV, in contrast to the expectations of anisotropic spin wave theory within the ferromagnetically ordered state predicted from the mean field model using the spin Hamiltonian derived from high field spin wave measurements. The continuum inelastic spectrum shows some weak structure, with vestiges of overdamped ferromagnetic spin waves present at small Q. The inelastic magnetic spectrum in stoichiometric $Yb_2Ti_2O_7$ shows little or no temperature dependence up to temperatures greater than 2.5 K, much larger than T_C, and on the order of $T_{\text{MF}} \sim 3$ K, and the temperature characterizing the high temperature "hump" in C_P near 2 K. The form of the magnetic inelastic scattering, its continuum nature and temperature dependence, is only slightly influenced by weak stuffing, as is known to characterize the nonstoichiometric CSC powder sample and single crystal samples that were also measured.

ACKNOWLEDGMENTS

We wish to thank Jan Kycia for collaborations and discussion related to heat capacity measurements. We thank C. Wiebe and H. Zhou for making their data available to this work. The neutron scattering data were reduced using Mantid [38] and analyzed using DAVE software package [39]. Research using ORNL's Spallation Neutron Source was sponsored by the Scientific User Facilities Division, Office of Basic Energy Sciences, U.S. Department of Energy. The NIST Center for Neutron Research is supported in part by the National Science Foundation under Agreement No. DMR-094472. Work at McMaster University was supported by the National Sciences and Engineering Research Council of Canada (NSERC).

---

[1] J. S. Gardner, M. J. P. Gingras, and J. E. Greedan, Rev. Mod. Phys. **82**, 53 (2010).

[2] M. Subramanian, G. Aravamudan, and G. S. Rao, Prog. Solid State Chem. **15**, 55 (1983).

[3] G. Balakrishnan, O. A. Petrenko, M. R. Lees, and D. M. Paul, J. Phys.: Condens. Matter **10**, L723 (1998).

[4] H. A. Dabkowska and A. B. Dabkowski, *Experimental Approach to Defects Determination* (Springer Handbook of Crystal Growth, Defects and Characterization, Berlin, 2010), pp. 367–392.

[5] D. Prabhakaran and A. T. Boothroyd, J. Cryst. Growth **318**, 1053 (2011).

[6] L.-J. Chang, S. Onoda, Y. Su, Y.-J. Kao, K.-D. Tsuei, Y. Yasui, K. Kakurai, and M. R. Lees, Nat. Commun. **3**, 992 (2012).

[7] M. J. P. Gingras and P. A. McClarty, Rep. Prog. Phys. **77**, 056501 (2014).

[8] Y. Yasui, M. Soda, S. Iikubo, M. Ito, M. Sato, N. Hamaguchi, T. Matsushita, N. Wada, T. Takeuchi, N. Aso *et al.*, J. Phys. Soc. Jpn. **72**, 3014 (2003).

[9] H. B. Cao, A. Gukasov, I. Mirebeau, and P. Bonville, J. Phys.: Condens. Matter **21**, 492202 (2009).

[10] J. S. Gardner, G. Ehlers, N. Rosov, R. W. Erwin, and C. Petrovic, Phys. Rev. B **70**, 180404 (2004).

[11] P. Dalmas De Réotier, V. Glazkov, C. Marin, A. Yaouanc, P. C. M. Gubbens, S. Sakarya, P. Bonville, A. Amato, C. Baines, and P. J. C. King, Physica B: Condensed Matter **374-375**, 145 (2006).

[12] K. A. Ross, L. Savary, B. D. Gaulin, and L. Balents, Phys. Rev. X **1**, 021002 (2011).

[13] K. A. Ross, L. R. Yaraskavitch, M. Laver, J. S. Gardner, J. A. Quilliam, S. Meng, J. B. Kycia, D. K. Singh, T. Proffen, H. A. Dabkowska *et al.*, Phys. Rev. B **84**, 174442 (2011).

[14] K. A. Ross, J. P. C. Ruff, C. P. Adams, J. S. Gardner, H. A. Dabkowska, Y. Qiu, J. R. D. Copley, and B. D. Gaulin, Phys. Rev. Lett. **103**, 227202 (2009).

[15] J. D. Thompson, P. A. McClarty, H. M. Rønnow, L. P. Regnault, A. Sorge, and M. J. P. Gingras, Phys. Rev. Lett. **106**, 187202 (2011).

[16] R. Applegate, N. R. Hayre, R. R. P. Singh, T. Lin, A. G. R. Day, and M. J. P. Gingras, Phys. Rev. Lett. **109**, 097205 (2012).

[17] S. T. Bramwell, M. N. Field, M. J. Harris, and I. P. Parkin, J. Phys.: Condens. Matter **12**, 483 (2000).

[18] J. A. Hodges, P. Bonville, A. Forget, M. Rams, K. Królas, and G. Dhalenne, J. Phys.: Condens. Matter **13**, 9301 (2001).

[19] B. Z. Malkin, A. R. Zakirov, M. N. Popova, S. A. Klimin, E. P. Chukalina, E. Antic-Fidancev, P. Goldner, P. Aschehoug, and G. Dhalenne, Phys. Rev. B **70**, 075112 (2004).

[20] A. Bertin, Y. Chapuis, P. D. de Réotier, and A. Yaouanc, J. Phys.: Condens. Matter **24**, 256003 (2012).

[21] J. Gaudet, D. D. Maharaj, G. Sala, E. Kermarrec, K. A. Ross, H. A. Dabkowska, A. I. Kolesnikov, G. E. Granroth, and B. D. Gaulin, Phys. Rev. B **92**, 134420 (2015).

[22] N. R. Hayre, K. A. Ross, R. Applegate, T. Lin, R. R. P. Singh, B. D. Gaulin, and M. J. P. Gingras, Phys. Rev. B **87**, 184423 (2013).

[23] J. Robert, E. Lhotel, G. Remenyi, S. Sahling, I. Mirebeau, C. Decorse, B. Canals, and S. Petit, Phys. Rev. B **92**, 064425 (2015).

[24] L. Savary and L. Balents, Phys. Rev. Lett. **108**, 037202 (2012).

[25] L. Savary and L. Balents, Phys. Rev. B **87**, 205130 (2013).

[26] J. A. Hodges, P. Bonville, A. Forget, A. Yaouanc, P. Dalmas de Réotier, G. André, M. Rams, K. Królas, C. Ritter, P. C. M. Gubbens *et al.*, Phys. Rev. Lett. **88**, 077204 (2002).

[27] R. M. D'Ortenzio, H. A. Dabkowska, S. R. Dunsiger, B. D. Gaulin, M. J. P. Gingras, T. Goko, J. B. Kycia, L. Liu, T. Medina, T. J. Munsie *et al.*, Phys. Rev. B **88**, 134428 (2013).

[28] K. A. Ross, T. Proffen, H. A. Dabkowska, J. A. Quilliam, L. R. Yaraskavitch, J. B. Kycia, and B. D. Gaulin, Phys. Rev. B **86**, 174424 (2012).

[29] A. Yaouanc, P. Dalmas de Réotier, C. Marin, and V. Glazkov, Phys. Rev. B **84**, 172408 (2011).

[30] J. F. Niven, M. B. Johnson, A. Bourque, P. J. Murray, D. D. James, H. A. Dabkowska, B. D. Gaulin, and M. A. White, in *Proceedings of the Royal Society of London A: Mathematical, Physical and Engineering Sciences* (The Royal Society, 2014), Vol. 470, p. 20140387.

[31] D. H. Ryan and I. P. Swainson, J. Appl. Crystallogr. **42**, 43 (2009).

[32] J. Copley and J. Cook, Chem. Phys. **292**, 477 (2003).

[33] G. Ehlers, A. A. Podlesnyak, J. L. Niedziela, E. B. Iverson, and P. E. Sokol, Rev. Sci. Instrum. **82**, 085108 (2011).

[34] A. Wills, Physica B: Condensed Matter **276**, 680 (2000).

[35] J. Rodriguez-Carvajal, in *Satellite Meeting on Powder Diffraction of the XV Congress of the IUCr* (Toulouse, France, 1990), Vol. 127.

[36] A. Yaouanc, P. Dalmas de Réotier, P. Bonville, J. A. Hodges, V. Glazkov, L. Keller, V. Sikolenko, M. Bartkowiak, A. Amato, C. Baines *et al.*, Phys. Rev. Lett. **110**, 127207 (2013).

[37] Z. L. Dun, E. S. Choi, H. D. Zhou, A. M. Hallas, H. J. Silverstein, Y. Qiu, J. R. D. Copley, J. S. Gardner, and C. R. Wiebe, Phys. Rev. B **87**, 134408 (2013).

[38] O. Arnold, J. Bilheux, J. Borreguero, A. Buts, S. Campbell, L. Chapon, M. Doucet, N. Draper, R. Leal, M. Gigg *et al.*, Nucl. Instrum. Methods Phys. Res., Sect. A **764**, 156 (2014).

[39] R. Azuah, L. Kneller, Y. Qiu, C. Brown, J. Copley, R. Dimeo, and P. Tregenna-Piggott, J. Res. Natl. Inst. Stan. Technol. **114**, 341 (2009).

2.3 Preface to Publication III: Effect of hydrostatic pressure on the magnetic ground state of $Yb_2Ti_2O_7$.

In the third and final paper of this chapter, we investigated the response of the magnetic ground state of $Yb_2Ti_2O_7$ to the application of hydrostatic pressure. Using neutron diffraction and muon spectroscopy techniques, we show that $Yb_2Ti_2O_7$ undergoes a quantum phase transition from a spin liquid state at ambient pressure to a ferromagnetic state under the application of small hydrostatic pressure. As opposed to the result in ambient pressure presented in publication II, the intensity of the ferromagnetic Bragg peaks develops coincident with the sharp specific anomaly. The magnetic structure refined in this work is also a splayed ferromagnet, but with a angle of only 1°. The discovery of magnetic order in $Yb_2Ti_2O_7$ under hydrostatic pressure is important because it demonstrates that disorder can act as a source of local pressure, which disrupts the fragile magnetic ground state of $Yb_2Ti_2O_7$.

For this study, I performed the neutron diffraction experiment under pressure and refined the magnetic structure of $Yb_2Ti_2O_7$. I also participated in the writing of the manuscript and the response to the referee reports. The contributions of each author are summarized below.

Author Contributions:

- *Experimental Concept*: E. Kermarrec, B.D. Gaulin
- *Sample Preparation*: K.A. Ross, H.A. Dabkowska
- *Neutron Scattering Experiments*: **J. Gaudet**, E. Kermarrec, K. Fristch, C. Ritters, B.D. Gaulin
- *μSR Experiment*: E. Kermarrec, R. Khasanov, Z. Guguchia, B.D. Gaulin
- *Data Analysis*: E. Kermarrec, **J. Gaudet**, B.D. Gaulin
- *Manuscript*: E. Kermarrec, **J. Gaudet**, B.D. Gaulin

nature COMMUNICATIONS

ARTICLE

Received 19 Jun 2016 | Accepted 31 Jan 2017 | Published 15 Mar 2017

DOI: 10.1038/ncomms14810

OPEN

Ground state selection under pressure in the quantum pyrochlore magnet $Yb_2Ti_2O_7$

E. Kermarrec[1,2,3], J. Gaudet[2], K. Fritsch[4], R. Khasanov[5], Z. Guguchia[5], C. Ritter[6], K.A. Ross[7], H.A. Dabkowska[8] & B.D. Gaulin[2,8,9]

A quantum spin liquid is a state of matter characterized by quantum entanglement and the absence of any broken symmetry. In condensed matter, the frustrated rare-earth pyrochlore magnets $Ho_2Ti_2O_7$ and $Dy_2Ti_2O_7$, so-called spin ices, exhibit a classical spin liquid state with fractionalized thermal excitations (magnetic monopoles). Evidence for a quantum spin ice, in which the magnetic monopoles become long range entangled and an emergent quantum electrodynamics arises, seems within reach. The magnetic properties of the quantum spin ice candidate $Yb_2Ti_2O_7$ have eluded a global understanding and even the presence or absence of static magnetic order at low temperatures is controversial. Here we show that sensitivity to pressure is the missing key to the low temperature behaviour of $Yb_2Ti_2O_7$. By combining neutron diffraction and muon spin relaxation on a stoichiometric sample under pressure, we evidence a magnetic transition from a disordered, non-magnetic, ground state to a splayed ferromagnetic ground state.

---

[1] Laboratoire de Physique des Solides, CNRS, Univ. Paris-Sud, Université Paris-Saclay, Orsay Cedex 91405, France. [2] Department of Physics and Astronomy, McMaster University, Hamilton, Ontario, Canada L8S 4M1. [3] Laboratoire National des Champs Magnétiques Intenses, CNRS, Grenoble BP 166-38042, France. [4] Helmholtz-Zentrum Berlin für Materialien und Energie, Hahn-Meitner-Platz 1, Berlin 14109, Germany. [5] Laboratory for Muon Spin Spectroscopy, Paul Scherrer Institut, Villigen PSI CH-5232, Switzerland. [6] Institut Laue Langevin, BP 156, Grenoble 38042, France. [7] Department of Physics, Colorado State University, Fort Collins, Colorado 80523-1875, USA. [8] Brockhouse Institute for Materials Research, McMaster University, Hamilton, Ontario, Canada L8S 4M1. [9] Canadian Institute for Advanced Research, 180 Dundas St. W., Toronto, Ontario, Canada M5G 1Z8. Correspondence and requests for materials should be addressed to E.K. (email: edwin.kermarrec@u-psud.fr) or to B.D.G. (email: bruce.gaulin@gmail.com).

The pyrochlore lattice, comprised of corner-sharing tetrahedra, is the archetype of magnetic frustration in three dimensions[1] (Fig. 1). Since its early study by Anderson in 1956 (ref. 2), frustrated spin Hamiltonians on the pyrochlore lattice have provided a seemingly inexhaustible source for the study of fundamental physics[3,4]. In particular, spin liquid ground states have been predicted for such a lattice decorated with Heisenberg[5,6] or XXZ[7] spins. More recently, pyrochlore magnets have been put forward as realistic vehicles for the realization of a quantum spin ice state, using the generic $S=\frac{1}{2}$ nearest-neighbour anisotropic exchange Hamiltonian[8–10]. $Yb_2Ti_2O_7$ is a promising quantum spin ice candidate as it possesses both an (effective) $S=\frac{1}{2}$ spin, thanks to the well isolated crystal field Kramers doublet ground state appropriate to Yb^{3+}[11], and strong quantum fluctuations brought by anisotropic exchange interactions and an XY g-tensor[12]. Several studies have focused on the nature of the ground state in $Yb_2Ti_2O_7$, yet a consensus has been elusive to date[13–18]. Early neutron scattering experiments ruled out the presence of conventional static order down to 90 mK in a polycrystalline sample[15], whereas other single crystal studies concluded the ground state was ferromagnetic[14,16]. The results of local probes are even more puzzling. Muon spin relaxation (μSR) measurements evidenced the presence of true static moments on the muon timescale, through the observation of both a drop of asymmetry and a decoupling of the muon spins in longitudinal applied fields[18], along with a drastic slowing down of the fluctuation rate below T_c for certain samples[13]. In contrast, μSR studies by D'Ortenzio *et al.*[17] found a non-magnetic, fluctuating ground state, in both stoichiometric polycrystalline and single crystal samples, *despite* the presence of pronounced specific heat anomalies at $T_c=265$ mK and $T_c=185$ mK, respectively. It is clear that local defects, either oxygen vacancies[19] or excess magnetic ions[20] (referred to as stuffing), vary significantly between polycrystalline powders and single crystals, and are likely responsible for such sample dependencies.

Here, by applying hydrostatic pressure to well-characterized $Yb_{2+x}Ti_{2-x}O_{7+\delta}$ samples, with $x=0$ and $x=0.046$ (ref. 20), we observe a magnetic transition in the stoichiometric, $x=0$ sample from a disordered ground state into a splayed ferromagnetic ground state. This result sheds light on the origin of the sample dependence in the ground state selection for $Yb_2Ti_2O_7$ and is consistent with the recent theoretical proposal that $Yb_2Ti_2O_7$ lies close to a phase boundary in the generic quantum spin ice Hamiltonian phase diagram[21].

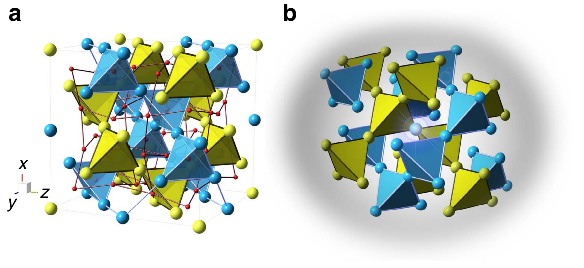

Figure 1 | Pyrochlore structure of $Yb_{2+x}Ti_{2-x}O_{7+\delta}$. Excess Yb^{3+} ion can occupy a Ti^{4+} site and create a local defect (referred to as 'stuffing'). (**a**) Representation of the ideal pyrochlore structure of $Yb_2Ti_2O_7$, with Yb in blue, Ti in yellow and O in red. Yb and Ti form corner-sharing tetrahedra lattices. (**b**) Schematic representation of the structurally distorted environment of a defect.

Results

Muon spin relaxation. μSR measurements under hydrostatic pressures as high as 25 kbar, and at temperatures as low as 0.245 K, were performed on $Yb_{2+x}Ti_{2-x}O_{7+\delta}$ samples, with $x=0$ and $x=0.046$, at the GPD beamline of PSI. The muons are implanted inside the bulk of the material, and act as local magnetic probes. The signal coming from the muons that stop inside the pressure cell was measured separately and subtracted (see Supplementary Figs 1 and 2) from the overall signal.

Figure 2a shows the temperature dependence of the μSR signal for the stoichiometric, $x=0$ sample in zero field, $R_{zf}(t)$, as a function of time t and under an applied pressure $P=19.7$ kbar. Well above $T_c=0.265$ K, at $T\geq 0.97$ K, the majority of the Yb^{3+} magnetic moments are paramagnetic and in a fast fluctuating regime, and display single-exponential relaxation. For $T\leq 0.5$ K, we observe the development of a small magnetic fraction f of the Yb^{3+} moments, which grows nonlinearly as the temperature decreases. The absence of oscillations at short time is indicative of a highly disordered magnetic state. The zero-field relaxation is well described by a Gaussian distribution of static internal fields with standard deviation Δ (see Supplementary Note 1), and the following phenomenological function:

$$R_{zf}(t)=f\left(\frac{2}{3}e^{-\Delta^2t^2/2}+\frac{1}{3}e^{-\lambda t}\right)+(1-f)e^{-\lambda t} \qquad (1)$$

In a purely static scenario, the second term (1/3-tail) should be constant. Here, a fluctuating component is nonetheless observed and we modelled this using a relaxation rate λ. The third term accounts for the paramagnetic component, and assumes the same relaxation rate λ, for simplicity. The unconventional shape of the zero-field longitudinal relaxation was discussed in detail in refs 13,22. In contrast, the evolution of the relaxation in temperature of the $x=0$ sample under zero applied pressure, shown in Fig. 2b, shows little or no magnetic fraction ($f\simeq 6\%$) at any temperature above our base $T=0.245$ K, in agreement with D'Ortenzio *et al.*[17] previously reported μSR studies. Using equation (1) we extract the magnetic fraction for each pressure and temperature, and collect the results in Fig. 2c. The development of the magnetic fraction with temperature is clearly pressure dependent, and turns on strongly at low temperatures, below $T_c=0.265$ K, for our minimum pressure of 1.2 kbar. For each pressure, one can define a critical temperature T_c, such that for $T\leq T_c$, 50% of the magnetic moments are frozen. The corresponding $P-T$ phase diagram is shown in Fig. 3. Clearly, the phase transition extrapolated from finite pressure measurements to zero pressure agrees well with the sharp C_p anomaly at $T_c=0.265$ K, appropriate to the $x=0$ sample. However the zero-pressure state for the $x=0$ sample at 0.245 K, below T_c, is disordered, indicating that the ground state of the stoichiometric, $x=0$ sample, is a spin liquid.

We now turn to the $x=0.046$ sample. The zero-field relaxation at $T=0.245$ K under zero and an applied pressure $P=24.1$ kbar are shown in Fig. 2d. Strikingly, no frozen magnetic fraction is observed upon the application of a pressure as high as $P=24.1$ kbar. Instead, we observe an increase of the relaxation for this $x=0.046$ sample, demonstrating its sensitivity to pressure. The temperature dependence of the relaxation is reported in Fig. 2e,f. One can speculate that a transition to a fully ordered state, as it is observed for the $x=0$ sample, would require higher pressures or lower temperatures, consistent with the lower $T_c=0.185$ K of the $x=0.046$ sample.

μSR studies on other samples have reported a drastic slowing down of spin fluctuations[13], or static order[18], under zero applied pressure for temperatures below 0.25 K. In the light of our results, even relatively low (applied or chemical) pressure can destroy the

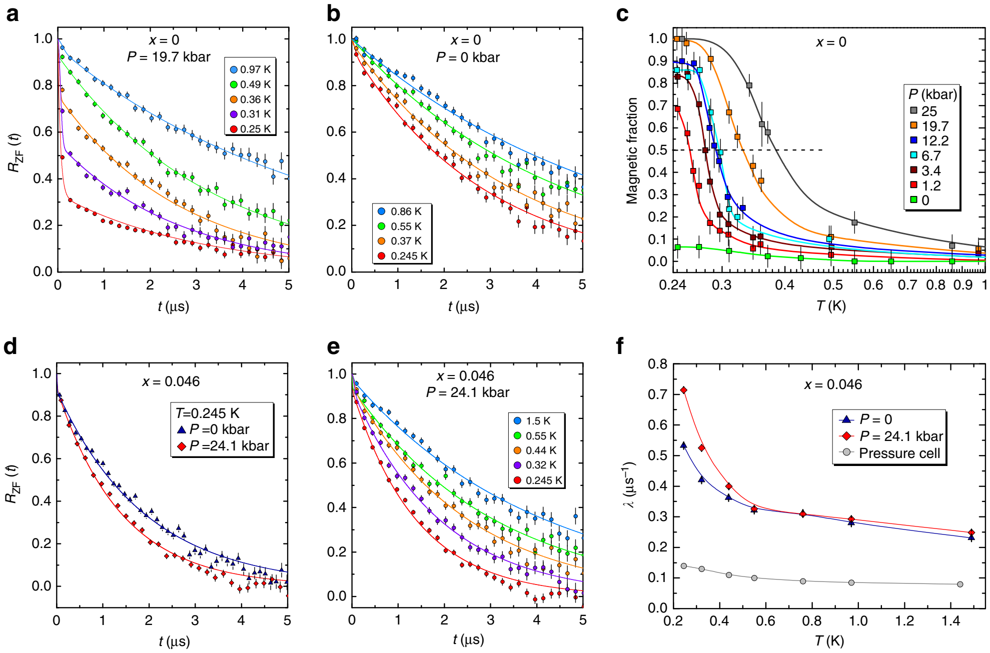

Figure 2 | Temperature evolution of the μSR relaxation in $Yb_{2+x}Ti_{2-x}O_{7+\delta}$ under pressure. (**a**–**c**) Refer to the $x = 0$ and (**d**–**f**) refer to the $x = 0.046$ sample. (**a**) The drastic increase of relaxation observed upon decreasing temperature in the $x = 0$ sample indicates a spin freezing under an applied pressure $P = 19.7$ kbar, which is absent under zero pressure (**b**) and for the $x = 0.046$ sample (**d**). (**c**) The temperature evolution of the magnetic fraction is reported for various pressures. The black horizontal dashed line represents a volume magnetic fraction of 50%, used as a criterion to define T_c. (**e**,**f**) For the $x = 0.046$ sample, only a moderate increase of the spin dynamics is observed under applied pressure. The error bars of the μSR relaxation data are of statistical origin and correspond to the square root of the total number of detected positrons resulting from muon decays. Error bars of the relaxation rate λ represent standard deviation of the fit parameters. Error bars of the magnetic fraction represent standard deviation of the fit parameters, with a minimal value of 0.05 corresponding to the typical error on the total asymmetry for μSR under pressure.

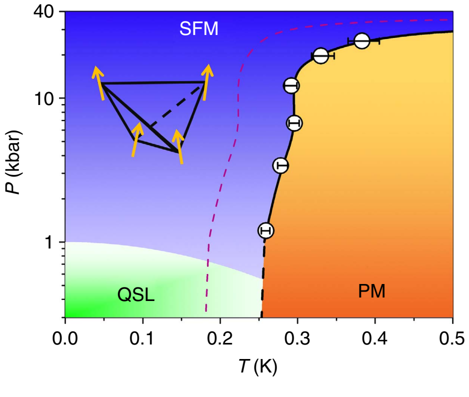

Figure 3 | Pressure-temperature phase diagram of $Yb_{2+x}Ti_{2-x}O_{7+\delta}$. The vertical axis displays the pressure P in logarithmic scale and the horizontal axis the temperature T. Empty black circles define the transition line between the collective paramagnetic (PM, orange) and the splayed ferromagnetic (SFM, blue) regions relative to the $x = 0$ sample. The transition temperature is defined such that for $T \leq T_c$ 50% of the magnetic moments are frozen (see Fig. 2c). Error bars allow T_c to be defined between 40 and 60% of the magnetic fraction. The green region highlights the presence of a disordered, non-magnetic phase (QSL) found at $P = 0$. Black thick line is a guide to the eye. Dashed purple line is the hypothetical transition line for $x = 0.046$.

disordered spin liquid state and induce magnetic order. A low level of defects in the different samples is a natural explanation to the contradictory μSR results. Such disorder, at the ∼2% level, is difficult to characterize, but it is largely absent in polycrystalline samples, synthesized at lower temperatures by solid state methods.

Neutron diffraction. Armed with the knowledge of the $P-T$ phase diagram in Fig. 3, we sought to determine the nature of the pressure-induced magnetic order in $Yb_{2+x}Ti_{2-x}O_{7+\delta}$ samples, with $x = 0$, by performing neutron diffraction on the stoichiometric powder sample at the D20 high-flux diffractometer of the ILL. The detection of small magnetic moments under pressure using neutron diffraction is challenging due to the significant background signal of the pressure cell itself. Figure 4a shows the neutron diffraction data for the maximum hydrostatic pressure of the cell, $P = 11(2)$ kbar, and temperatures from 400 to 100 mK, from which a background measured at 800 mK was subtracted. We clearly observe the development of magnetic Bragg intensities at the (111), (311), (222) and (004) positions upon cooling below 400 mK. This is firm evidence for the existence of long-range magnetic order in $Yb_{2+x}Ti_{2-x}O_{7+\delta}$ samples, with $x = 0$, under an applied pressure $P = 11(2)$ kbar. The refinement of the neutron diffraction data gives us the temperature dependence of the ordered moment, shown in Fig. 4b. The contrast with previous experiments under zero pressure is striking. First, the saturated moment $\mu = 0.33(5)\ \mu_B$ is

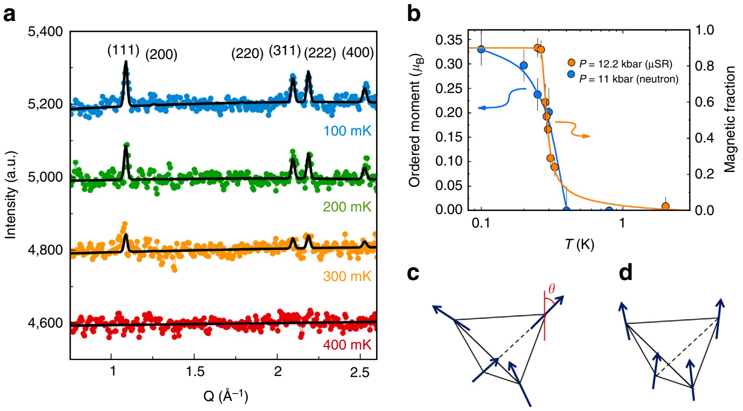

Figure 4 | Neutron diffraction measurements of $Yb_2Ti_2O_7$ under applied pressure. (**a**) Diffraction data sets from 400 to 100 mK after the 800 mK data set has been subtracted. Error bars are not shown for clarity. (**b**) Ordered moment versus temperature determined by neutron diffraction for $P = 11(2)$ kbar (blue, left axis) and magnetic fraction determined by μSR for $P = 12.2$ kbar (orange, right axis). Error bars of the ordered moment represent s.d. of the refinement. Schematic spin structure of the ice-like splayed ferromagnet with $\theta = 14°$ for $P = 0$ (**c**) and $\theta = 5°$ for $P = 11$ kbar (**d**), where θ is the splay angle between the [001] direction and the magnetic moment, tilted towards the local [111] directions of the tetrahedron.

much smaller than that $\mu \sim 1\ \mu_B$ reported previously for different $Yb_2Ti_2O_7$ samples[16], although similar to the ordered moment in the Γ_5 ordered state of $Yb_2Ge_2O_7$ (ref. 23). Second, the ordered moment vanishes cleanly above $T_c \sim 0.4$ K, with no anomalous magnetic Bragg intensity well above T_c (refs 24,25). The previously reported order parameter at $P = 0$ of our $x = 0$ polycrystalline sample is anomalous[24]; it shows no change across T_c and only falls off at much higher temperatures. Consistency with our $P = 0$ μSR results on the same sample requires that this Bragg-like scattering is dynamic on slow time scales. That notwithstanding, the magnetic structure previously refined on the basis of a very high temperature (~ 8 K) background subtraction gave a splayed ice-like ferromagnetic structure[24], with the moments on a tetrahedron lying mainly in the [100] direction with a positive splay angle $\theta = 14(5)°$, such that the moments tilt towards the local [111] direction (Fig. 4c). The components perpendicular to the local [111] axis obey the 2-in/2-out ice rule on a single tetrahedron. A different type of splayed ferromagnet, with the perpendicular components satisfying the all-in/all-out structure, has also been reported recently[26], in addition to a nearly collinear ferromagnet ($\theta \sim 0°$)[16], for other samples. The magnetic structure associated with the true Bragg scattering we refine here in the stoichiometric $x = 0$ sample under $P = 11(2)$ kbar is also a splayed ice-like structure, but with a much reduced splay angle $\theta = 5(4)°$, such that it is close to a collinear [100] ferromagnet (Fig. 4d).

Discussion

These results bring a fresh perspective on the long standing debate about the presence or absence of static magnetic order in the quantum pyrochlore magnet $Yb_{2+x}Ti_{2-x}O_{7+\delta}$. The acute sensitivity to local (through the Yb^{3+} stuffing) or applied pressure is surprising. However, a corollary of our new $P-T$ phase diagram is that non-stoichiometric samples with non-zero chemical pressure can easily display an ambient applied pressure phase transition to a splayed ferromagnetic state at T_c. Yet, this interpretation remains challenged by the fact that our $x = 0.046$ sample does not show evidence for magnetic order at ambient pressure, and by previous reported observations of a magnetic transition in polycrystalline, likely $x \sim 0$, sample even under zero pressure[13,18]. This may indicate that the non-magnetic low-temperature region of the phase diagram is extremely narrow, existing only for a certain range of x, whose absolute values are still to be determined. This would actually be reminiscent of the recent findings on the $Tb_{2+x}Ti_{2-x}O_{7+\delta}$ pyrochlore magnet, which has been shown to display an ordered phase that is extremely sensitive to disorder, appearing only for $0 < x < 0.01$ (refs 27–29).

Furthermore, the present work illustrates the relevance of applying hydrostatic pressure to tune the magnetic properties of frustrated pyrochlore compounds, a path that was followed by pioneering work on the other spin liquid candidate $Tb_2Ti_2O_7$ (ref. 30). In case of $Yb_2Ti_2O_7$, we found that the pressure tunes the delicate balance between the anisotropic exchanges of the quantum spin ice Hamiltonian, and selects a splayed ferromagnetic ground state away from the degenerate antiferromagnetic ground states manifold. This scenario confirms recent theoretical proposals that $Yb_2Ti_2O_7$ lies close to phase boundaries derived from the generic $S_{\mathrm{eff}} = \frac{1}{2}$ quantum spin ice Hamiltonian[21], and provides the missing key to understand its exotic magnetic properties. Particularly appealing is the prediction that accidental degeneracies in the vicinity of these phase boundaries can lead to the emergence of a quantum spin liquid[31]. This would offer a natural explanation for a non-magnetic, disordered state under zero pressure in stoichiometric $Yb_2Ti_2O_7$ and recent observations of a continuum of gapless quantum excitations[24,32] at low temperatures.

Methods

Sample preparation. The $Yb_{2+x}Ti_{2-x}O_{7+\delta}$ samples with $x = 0$ and $x = 0.046$ were prepared at the Brockhouse Institute for Materials Research, McMaster University. The $x = 0$ powder sample was obtained through conventional solid-state reaction between pressed powders of Yb_2O_3 and TiO_2 sintered at 1,200 °C in air. The $x = 0.046$ powder sample was obtained by crushing a single crystal grown by the floating zone method in 4 atm of O_2 with a growth rate of 5 mm h^{-1}. More details on the details of the synthesis and the characterization can be found in ref. 25.

Muon spin relaxation. μSR measurements were carried out at the GPD instrument of the Paul Scherrer Institut, Switzerland. About 1 g of each powder sample was mixed with ~ 3 mm^3 of a pressure medium (Daphne 7373 oil) and placed inside the sample channel of a double-wall pressure cell. Two different cells were used, labelled as (1) and (2) (see Supplementary Note 1), and are described in more details in ref. 33. The muon momentum was adjusted in order to obtain an optimal fraction of the muons stopping in the sample, with optimal values found at $P = 106$ and $P = 107$ MeV c^{-1}. The relaxation of both cells were measured without any sample down to 0.245 K. The applied pressure was determined by measuring the superconducting transition temperature of a small piece of pure indium inserted in the sample channel[33].

Neutron diffraction. The neutron diffraction experiment was conducted at the D20 beamline, a high intensity two axis diffractometer, at the Institut Laue-Langevin, using a neutron wavelength $\lambda = 2.4$ Å. A mass of 1.5 g of $Yb_2Ti_2O_7$ powder sample and a small amount of NaCl powder, which serves as a pressure calibration, were both mounted in a high pressure clamp cell and inserted in a ^3He–^4He dilution fridge. Fluorinert was used as a pressure transmitter. A minimum of 12 h of data was collected at each temperature. The diffraction pattern obtained for $T = 800$ mK is shown in Supplementary Fig. 3. Structural refinements for both NaCl and $Yb_2Ti_2O_7$ and magnetic refinements for $Yb_2Ti_2O_7$ have been performed using the Fullprof program suite[34].

Data availability. The data sets generated during and/or analysed during the current study are available from the corresponding author on reasonable request.

References

1. Lacroix, C., Mendels, P. & Mila, F. *Introduction to Frustrated Magnetism* (Springer, 2011).
2. Anderson, P. W. Ordering and antiferromagnetism in ferrites. *Phys. Rev.* **102,** 1008 (1956).
3. Bramwell, S. T. & Gingras, M. J. P. Spin ice state in frustrated magnetic pyrochlore materials. *Science* **294,** 1495–1501 (2001).
4. Fennell, T. *et al.* Magnetic Coulomb phase in the spin ice $Ho_2Ti_2O_2$. *Science* **326,** 415–417 (2009).
5. Moessner, R. & Chalker, J. T. Properties of a classical spin liquid: the Heisenberg pyrochlore antiferromagnet. *Phys. Rev. Lett.* **80,** 2929–2932 (1998).
6. Canals, B. & Lacroix, C. Pyrochlore antiferromagnet: a three-dimensional quantum spin liquid. *Phys. Rev. Lett.* **80,** 2933–2936 (1998).
7. Hermele, M., Fisher, M. P. A. & Balents, L. Pyrochlore photons: the U(1) spin liquid in a $S=\frac{1}{2}$ three-dimensional frustrated magnet. *Phys. Rev. B* **69,** 064404 (2004).
8. Savary, L. & Balents, L. Coulombic quantum liquids in spin-1/2 pyrochlores. *Phys. Rev. Lett.* **108,** 037202 (2012).
9. Benton, O., Sikora, O. & Shannon, N. Seeing the light: experimental signatures of emergent electromagnetism in a quantum spin ice. *Phys. Rev. B* **86,** 075154 (2004).
10. Gingras, M. J. P. & McClarty, P. A. Quantum spin ice: a search for gapless quantum spin liquids in pyrochlore magnets. *Rep. Prog. Phys* **77,** 056501 (2014).
11. Gaudet, J. *et al.* Neutron spectroscopic study of crystalline electric field excitations in stoichiometric and lightly stuffed $Yb_2Ti_2O_7$. *Phys. Rev. B* **92,** 134420 (2015).
12. Ross, K., Savary, L., Gaulin, B. D. & Balents, L. Quantum excitations in quantum spin ice. *Phys. Rev. X* **1,** 021002 (2011).
13. Hodges, J. A. *et al.* First-order transition in the spin dynamics of geometrically frustrated $Yb_2Ti_2O_7$. *Phys. Rev. Lett.* **88,** 077204 (2002).
14. Yasui, Y. *et al.* Ferromagnetic transition of pyrochlore compound $Yb_2Ti_2O_7$. *J. Phys. Soc. Jpn* **72,** 3014–3015 (2003).
15. Gardner, J. S., Ehlers, G., Rosov, N., Erwin, R. W. & Petrovic, C. Spin-spin correlations in $Yb_2Ti_2O_7$: a polarized neutron scattering study. *Phys. Rev. B* **70,** 180404 (2004).
16. Chang, L.-J. *et al.* Higgs transition from a magnetic Coulomb liquid to a ferromagnet in $Yb_2Ti_2O_7$. *Nat. Commun.* **3,** 992 (2012).
17. D'Ortenzio, R. M. *et al.* Unconventional magnetic ground state in $Yb_2Ti_2O_7$. *Phys. Rev. B* **88,** 134428 (2013).
18. Chang, L.-J. *et al.* Static magnetic moments revealed by muon spin relaxation and thermodynamic measurements in the quantum spin ice $Yb_2Ti_2O_7$. *Phys. Rev. B* **89,** 184416 (2014).
19. Sala, G. *et al.* Vacancy defects and monopole dynamics in oxygen-deficient pyrochlores. *Nat. Mater.* **13,** 488–493 (2014).
20. Ross, K. A. *et al.* Lightly stuffed pyrochlore structure of single-crystalline $Yb_2Ti_2O_7$ grown by the optical floating zone technique. *Phys. Rev. B* **86,** 174424 (2012).
21. Jaubert, L. D. C. *et al.* Are multiphase competition and order by disorder the keys to understanding $Yb_2Ti_2O_7$. *Phys. Rev. Lett.* **115,** 267208 (2015).
22. Yaouanc, A., Maisuradze, A. & Dalmas de Réotier, P. Influence of short-range spin correlations on the µSR polarization functions in the slow dynamic limit: application to the quantum spin-liquid system $Yb_2Ti_2O_7$. *Phys. Rev. B* **87,** 134405 (2013).
23. Hallas, A. M. *et al.* XY antiferromagnetic ground state in the effective $S = 1/2$ pyrochlore $Yb_2Ge_2O_7$. *Phys. Rev. B* **93,** 104405 (2016).
24. Gaudet, J. *et al.* Gapless quantum excitations from an icelike splayed ferromagnetic ground state in stoichiometric $Yb_2Ti_2O_7$. *Phys. Rev. B* **93,** 064406 (2016).
25. Ross, K. A. *et al.* Dimensional evolution of spin correlations in the magnetic pyrochlore $Yb_2Ti_2O_7$. *Phys. Rev. B* **84,** 174442 (2011).
26. Yaouanc, A., Dalmas de Réotier, P., Keller, L., Roessli, B. & Forget, A. A novel type of splayed ferromagnetic order observed in $Yb_2Ti_2O_7$. *J. Phys. Condens. Matter* **28,** 426002 (2016).
27. Taniguchi, T. *et al.* Long-range order and spin-liquid states of polycrystalline $Tb_{2+x}Ti_{2x}O_{7+y}$. *Phys. Rev. B* **87,** 060408(R) (2013).
28. Kermarrec, E. *et al.* Gapped and gapless short-range-ordered magnetic states with (1/2, 1/2, 1/2) wave vectors in the pyrochlore magnet $Tb_{2+x}Ti_{2x}O_{7+\delta}$. *Phys. Rev. B* **92,** 245114 (2015).
29. Takatsu, H. *et al.* Quadrupole order in the frustrated pyrochlore $Tb_{2+x}Ti_{2x}O_{7+y}$. *Phys. Rev. Lett.* **116,** 217201 (2016).
30. Mirebeau, I. *et al.* Pressure-induced crystallization of a spin liquid. *Nature* **420,** 54–57 (2002).
31. Yan, H., Benton, O., Jaubert, L. D. C. & Shannon, N. Living on the edge: ground-state selection in quantum spin-ice pyrochlores. Preprint at https://arxiv.org/abs/1311.3501 (2013).
32. Robert, J. *et al.* Spin dynamics in the presence of competing ferromagnetic and antiferromagnetic correlations in $Yb_2Ti_2O_7$. *Phys. Rev. B* **92,** 064425 (2015).
33. Khasanov, R. *et al.* High pressure research using muons at the Paul Scherrer Institute. *High Press. Res.* **36,** 140–166 (2016).
34. Rodriguez-Carvajal, J. Recent advances in magnetic structure determination by neutron powder diffraction. *Physica B* **192,** 55–69 (1993).

Acknowledgements

Work at McMaster University was supported by NSERC of Canada. This work is based on experiments performed at SµS, Paul Scherrer Institute, Villigen, Switzerland and at the Institut Laue-Langevin, Grenoble, France. This project has received funding from the European Union's Seventh Framework Programme for research, technological development and demonstration under the NMI3-II Grant number 283883. E.K. acknowledges useful discussions with P. Mendels, F. Bert, S. Petit, L. D. C. Jaubert and C. Decorse.

Authors contributions

E.K., J.G. and B.D.G. wrote the manuscript. E.K., J.G., K.F. and B.D.G. performed the neutron diffraction experiment. E.K. and B.D.G. performed the µSR experiment. K.A.R. and H.A.D. synthesized and characterized the samples. C.R. designed and performed the neutron scattering experiment. Z.G. and R.K. designed and performed the µSR experiment. All the co-authors discussed the results and improved the manuscript.

Additional information

Supplementary Information accompanies this paper at http://www.nature.com/naturecommunications

Competing interests: The authors declare no competing financial interests.

Reprints and permission information is available online at http://npg.nature.com/reprintsandpermissions/

How to cite this article: Kermarrec, E. *et al.* Ground state selection under pressure in the quantum pyrochlore magnet $Yb_2Ti_2O_7$. *Nat. Commun.* **8,** 14810 doi: 10.1038/ncomms14810 (2017).

Supplementary Note 1 background subtraction for μSR measurements

The relaxation of both cells was measured without any sample from 2 K down to 0.245 K. The relaxation of each cell (R_{cell}) was fitted separately and subsequently subtracted from the whole signal (pressure cell + sample) in order to extract the relaxation due to the sample only (R_{sample}). The total signal in zero field $R_{\text{zf}}(t)$ is fitted to the following general function:

$$A_{\text{tot}}R_{\text{zf}}(t) = A_{\text{tot}}\left[f_{\text{cell}}R_{\text{cell}}(t) + (1 - f_{\text{cell}})R_{\text{sample}}(t)\right] \tag{1}$$

The total asymmetry A_{tot} is determined by a weak transverse-field measurement above the magnetic transition. At low temperature, the polarization relative to the sample can be easily distinguished from the pressure cell signal due to the difference of relaxation, and we estimate $f_{\text{cell}} = 0.545$, a typical value for experiments using such double-wall cells. This fraction was then held fixed for all subsequent fits. We detail below the measurements of the relaxation of each pressure cell, $R_{\text{cell}}(t)$.

Supplementary Fig. 1a) shows the relaxation obtained for the pressure cell (1) only, at 2 K and 0.245 K. These relaxations could be well fitted to a dynamical Kubo-Toyabe (DKT) function:

$$R^{(1)}_{\text{cell}}(t) = (1 - B)\text{DKT}(\nu, \sigma, \Gamma, t) + B \tag{2}$$

with $\nu = 0$ (zero-field), σ the width of the Gaussian distribution, Γ the hopping rate and the background value $B = 0.035$. σ and Γ are found to smoothly evolve from 2 K ($\sigma = 0.361(2)$ μs^{-1}, $\Gamma = 0.20(2)$ μs^{-1}) to 0.245 K ($\sigma = 0.500(4)$ μs^{-1}, $\Gamma = 0.63(3)$ μs^{-1}) and we thus used interpolated values for the subtraction at intermediate measured temperatures assuming an exponential variation with temperature. Supplementary Fig. 1b) shows a typical measurement with the loaded pressure cell at $P = 19.7$ kbar, i.e. with muons stopping inside the pressure cell and the sample and Supplementary Fig. 1c) shows the result of the subtraction at 0.245 K fitted to the following phenomenological function:

$$R_{\text{sample}}(t) = f\left(\frac{2}{3}e^{-\Delta^2 t^2/2} + \frac{1}{3}e^{-\lambda t}\right) + (1-f)e^{-\lambda t} \tag{3}$$

with f the volume magnetic fraction, Δ the Gaussian width of the static field distribution, and λ the paramagnetic relaxation rate used for both the 1/3-tail and the paramagnetic component, for simplicity. The departure from the traditional static or dynamic Gaussian Kubo-Toyabe function was already observed and studied in details in Supplementary Ref.[2–4].

Supplementary Fig. 2a) shows the relaxation obtained for the pressure cell (2) only, at 1.8 K and 0.245 K. These relaxations could be well fitted to a single exponential form:

$$R^{(2)}_{\text{cell}}(t) = e^{-\lambda_c t} \tag{4}$$

with λ_c the exponential relaxation rate. λ_c was found to smoothly evolve from 1.8 K ($\lambda_c = 0.077$ μs^{-1}) to 0.245 K ($\lambda_c = 0.134$ μs^{-1}) and we thus used interpolated values for the subtraction at intermediate measured temperatures assuming an exponential variation with temperature. Supplementary Fig. 2b) shows a typical measurement with the loaded pressure cell at $P = 25$ kbar, i.e. with muons stopping inside the pressure cell and the sample and Supplementary Fig. 2c) shows the result of the subtraction at 0.245 K fitted to the phenomenological function (equation (3) in Supplementary Note 1).

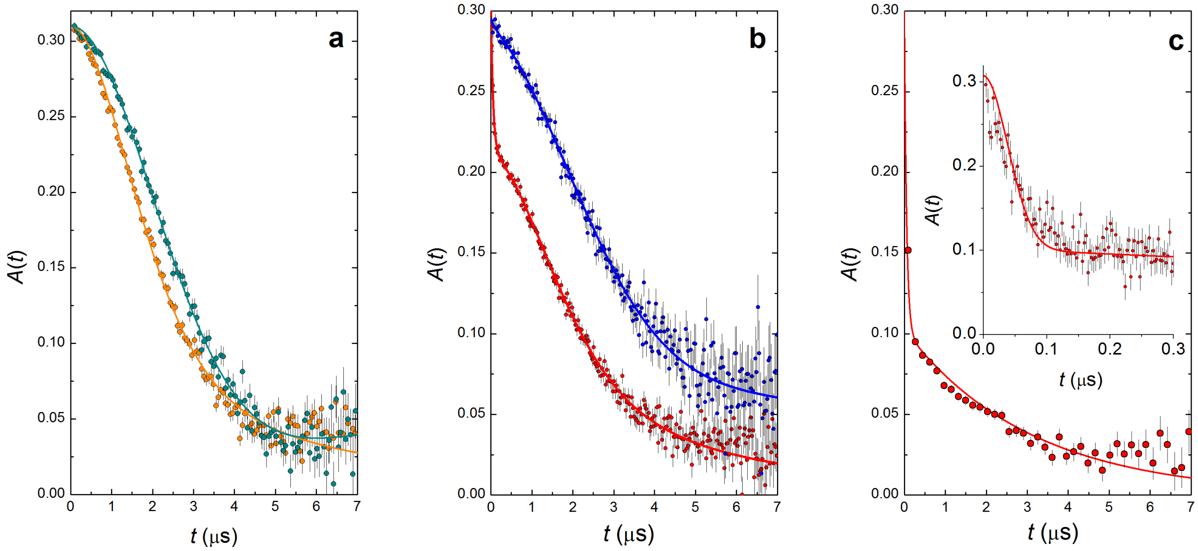

Supplementary figure 1: **Background subtraction for the pressure cell (1)**. $A(t) = A_{\mathrm{tot}}R_{\mathrm{zf}}(t)$ is the measured asymmetry as a function of time t. a) Relaxation of the pressure cell (1) only $[f_{\mathrm{cell}} = 1]$, measured at 0.245 K (orange) and 2 K (dark cyan). Lines are fits to the equation (2) in Supplementary Note 1. b) Relaxation measured above (1.5 K) and below (0.245 K) the magnetic transition under an applied pressure $P = 19.7$ kbar for a loaded pressure cell $[f_{\mathrm{cell}} = 0.545]$. Lines are fit to to the equations (1), (2) and (3) in Supplementary Note 1. c) Relaxation relative to the sample only after subtraction of the pressure cell signal, measured at 0.245 K. Line is a fit to the equation (3) in Supplementary Note 1. Inset: Zoom at short times. The error bars of the μSR relaxation data are of statistical origin and correspond to the square root of the total number of detected positrons resulting from muon decays.

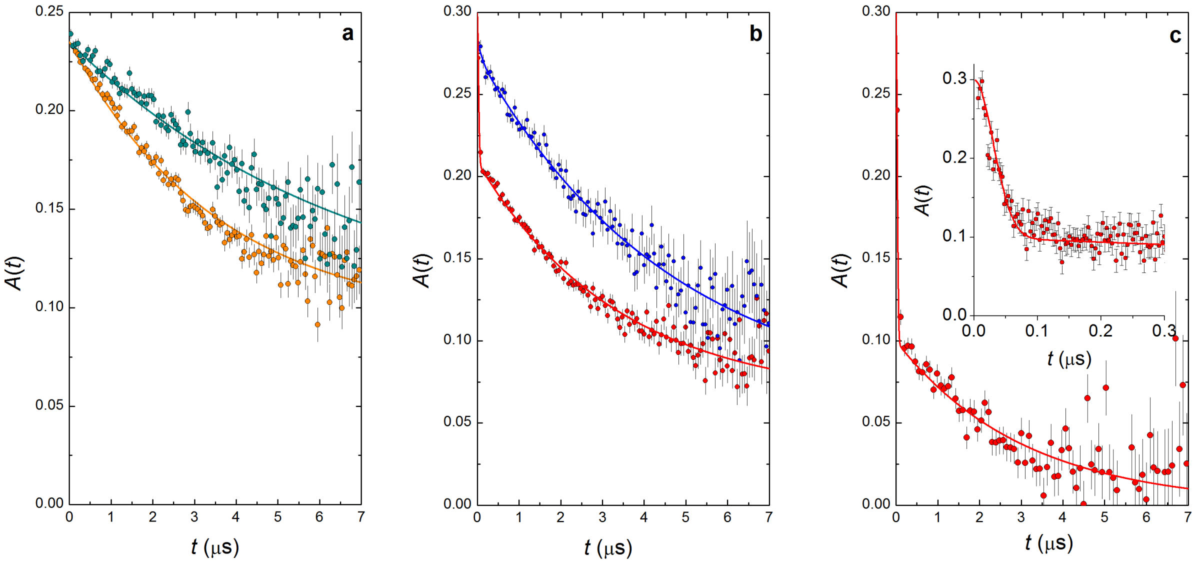

Supplementary figure 2: **Background subtraction for the pressure cell (2)**. $A(t) = A_{\mathrm{tot}}R_{\mathrm{zf}}(t)$ is the measured asymmetry as a function of time t. a) Relaxation of the pressure cell (2) only $[f_{\mathrm{cell}} = 1]$, measured at 0.245 K (orange) and 1.8 K (dark cyan). Lines are fits to the equation (4) in Supplementary Note 1. b) Relaxation measured above (0.86 K, blue) and below (0.245 K, red) the magnetic transition under an applied pressure $P = 25$ kbar for a loaded pressure cell $[f_{\mathrm{cell}} = 0.545]$. Lines are fit to the equations (1),(4) and (3) in Supplementary Note 1. c) Relaxation relative to the sample only after subtraction of the pressure cell signal, measured at 0.245 K. Line is a fit to the equation (3) in Supplementary Note 1. Inset: Zoom at short times. The error bars of the μSR relaxation data are of statistical origin and correspond to the square root of the total number of detected positrons resulting from muon decays.

Supplementary Note 2 neutron diffraction

A typical diffraction pattern obtained for $T = 0.800$ K is shown in Supplementary Fig. 3 for which the assignment of some of the structural Bragg peaks of $Yb_2Ti_2O_7$ and the NaCl are indicated. Contributions to the scattering coming from the cryostat as well as the pressure cell create a substantial background, especially in the region of Q going from 1.25 Å^{-1} to 1.75 Å^{-1}, and this region is thus excluded from all refinements. The resulting lattice parameter for NaCl is 5.54 Å. Using a calibration table for the lattice parameter of NaCl as a function of the applied pressure[5], we deduced the pressure in the cell to reach 11±2 kbar. The structural refinement of $Yb_2Ti_2O_7$ at $T = 0.800$ K was assumed to be of nuclear origin only and is consistent with a slightly smaller lattice parameter as well as a lower axial distortion of the eight oxygens surrounding the Yb^{3+} atoms than at ambient pressure. However, the large value of our uncertainty precludes any quantitative analysis.

In addition to $T = 0.800$ K, the diffraction pattern of $Yb_2Ti_2O_7$ has also been collected for T =0.100, 0.200, 0.250, 0.300 and 0.400 K. Fig. 4a) of the main text shows the resulting magnetic diffraction pattern at low temperature where the 0.800 K data set has been subtracted as a background. For T =0.100 K, we observed a clean subtraction of the background signal but an excess of scattering is seen at the (111), (113), (222) and (004) Bragg peaks position of $Yb_2Ti_2O_7$. This purely magnetic scattering was refined using a fixed scale factor which had been determined by the purely nuclear refinement of the paramagnetic 800 mK dataset. As every magnetic Bragg peak is located on a nuclear allowed position of $Yb_2Ti_2O_7$, we assumed a k =0 magnetic structure.

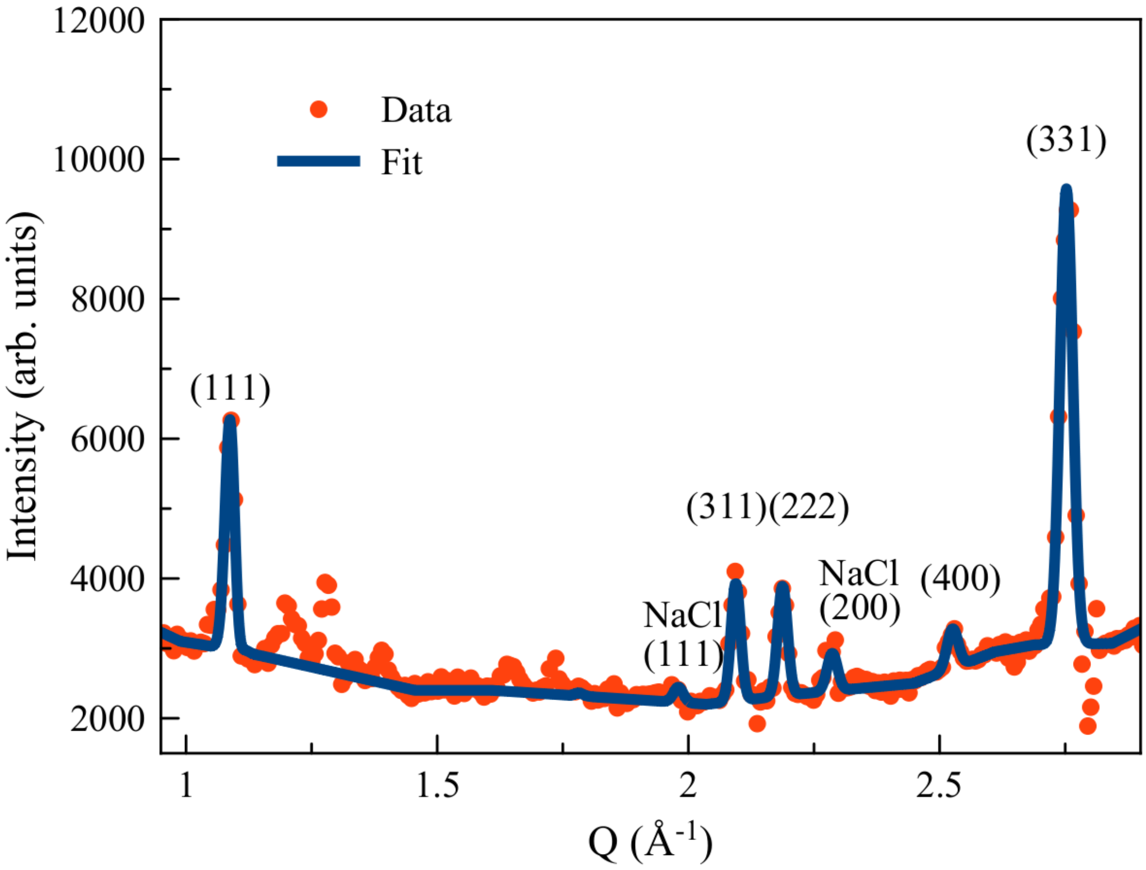

Supplementary figure 3: **Structural refinement of the neutron diffraction pattern.** Diffraction pattern measured at $T = 0.800$ K (red points) and structural refinement for both the $Yb_2Ti_2O_7$ and the NaCl phases (blue line). The region of Q from 1.125 $Å^{-1}$ to 1.75 $Å^{-1}$ is polluted from spurious contributions coming from the cryostat and the pressure cell, and thus excluded from the refinement. The refined value of the lattice parameter of NaCl is used to determine the applied pressure of 11±2 kbar.

The possible irreducible representation for the $16d$ site of the $Fd\overline{3}m$ pyrochlore lattice are Γ_3, Γ_5, Γ_7 and Γ_9. The Γ_9 representation manifold gives the best agreement with our data and the resulting magnetic moment is 0.33(5) μ_B at $T = 0.100$ K. The refined spin structure consists of all spins pointing almost fully along the [100] direction but slightly tilted towards the [111] local direction by $5 \pm 4°$. Finally, the same refinement has been performed for all other measured temperatures and a decrease of the resulting magnetic moment is observed up to 0.400 K for which no extra scattering is observed (Fig. 4b) of the main text).

Supplementary references

1. Khasanov, R., *et al.* High pressure research using muons at the Paul Scherrer Institute. *High Pressure Research* **36**, 140-166 (2016).
2. Hodges, J. A. *et al.* First-order transition in the spin dynamics of geometrically frustrated $Yb_2Ti_2O_7$. *Phys. Rev. Lett.* **88,** 077204 (2002).
3. Yaouanc, A., Maisuradze, A. & Dalmas de Réotier, P. Influence of short-range spin correlations on the µSR polarization functions in the slow dynamic limit: application to the quantum spin-liquid system $Yb_2Ti_2O_7$. *Phys. Rev. B* **87,** 134405 (2013).
4. Maisuradze, A., *et al.* Anomalously slow spin dynamics and short-range correlations in the quantum spin ice systems $Yb_2Ti_2O_7$ and $Yb_2Sn_2O_7$. *Phys. Rev. B* **92**, 094424 (2015).
5. Decker, D. L. Equation of state of NaCl and its use as a pressure gauge in high-pressure research. *J. Appl. Phys.* **36**, 157 (1965).

6. Rodriguez-Carvajal, J. Recent advances in magnetic structure determination by neutron powder diffraction. *Physica B : Condensed Matter* **192**, 55 (1993).

Chapter 3

Fragile Magnetism in $Er_2Ti_2O_7$

The second portion of this thesis addresses the ground-state selection of $Er_2Ti_2O_7$ under various perturbations such as magnetic dilution, magnetic field and chemical pressure. $Er_2Ti_2O_7$ is an XY pyrochlore that orders below 1.2 K into a non-linear, non-coplanar ψ_2 antiferromagnetic state, which belongs to the Γ_5 representation manifold (see Fig.1.3 in section 1.1) [41, 70]. To investigate the ψ_2 ground state selection in $Er_2Ti_2O_7$, Savary et al. [42] fitted a spin Hamiltonian for this compound using inelastic neutron scattering data. The resulting spin Hamiltonian for $Er_2Ti_2O_7$ has a Γ_5 ground state, but the ψ_2 and the ψ_3 states are degenerate at the mean-field level. However, it was found that the spin wave excitations from the ψ_2 state cost less energy than the ones created from the ψ_3 state. Hence, it was concluded that $Er_2Ti_2O_7$'s ψ_2 ground state is selected to minimize the total free energy by maximizing the fluctuation entropy. Thus, $Er_2Ti_2O_7$ was proposed as a definitive example of a magnetic system where the ground-state selection occurs via an order-by-disorder mechanism [41–43].

The key ingredients for order-by-disorder in $Er_2Ti_2O_7$ are the high symmetry of the pyrochlore lattice and the stabilization of a well-isolated CEF doublet with local XY anisotropy. In $Er_2Ti_2O_7$, the first two excited CEF states are separated from its ground state by 6.3 and 7.3 meV [6, 41]. Therefore, one would expect that the CEF ground state doublet could be accurately treated as well-isolated for temperatures much below 60 K. However, it was shown that the ground state selection of $Er_2Ti_2O_7$ might still be influenced by the proximity of these low lying CEF excited states [91–93]. Although thermal excitations between crystal fields levels do indeed become negligible at low temperature, higher order perturbation theory reveals that virtual crystal field transitions are still allowed due to multipolar interactions. These virtual crystal field processes also promote the ψ_2 state over the ψ_3 state in $Er_2Ti_2O_7$ [92, 93]. Thus, it is not clear if the order-by-disorder mechanism of $Er_2Ti_2O_7$ is dominant in its ground state selection: virtual crystal field transitions, an energetic selection mechanism, can also open a gap between ψ_2 and ψ_3 state. Hence, the importance of order-by-disorder effects in $Er_2Ti_2O_7$ remains an open question.

Recently, theoretical works have sough to uncover the real nature of the ground-state selection mechanism in $Er_2Ti_2O_7$ by studying the stability of the ψ_2 state towards different perturbations such as magnetic dilution [94,95] and chemical pressure [49]. The experimental works presented in this chapter address these theoretical predictions and confirm that the magnetic ground state of $Er_2Ti_2O_7$ is indeed fragile towards these perturbations. The following publications are presented in this chapter:

Publication IV: "*Magnetic dilution and domain selection in the XY pyrochlore antiferromagnet $Er_2Ti_2O_7$*", Jonathan Gaudet, Alannah M. Hallas, Dalini D. Maharaj, Connor R.C. Buhariwalla, Edwin Kermarrec, Nicholas P. Butch, Timothy J. S. Munsie, Hanna A. Dabkowska, Graeme M. Luke, and Bruce D. Gaulin. Physical Review B **94**, 060407(R) (2016) [4].

Publication V: "*Experimental evidence for field-induced emergent clock anisotropies in the XY pyrochlore $Er_2Ti_2O_7$*", Jonathan Gaudet, Alannah M. Hallas, Jacque Thibault, Nicholas P. Butch, Hanna A. Dabkowska, and Bruce D. Gaulin. Physical Review B **95**, 054407 (2017) [5].

Publication VI: "*Effect of Chemical Pressure on the Single-Ion Properties of the Erbium Pyrochlores*", Jonathan Gaudet, Alannah M. Hallas, Alexander I. Kolesnikov, and Bruce D. Gaulin. Physical Review B **97**, 024415 (2018) [6]

3.1 Preface to Publication IV: Tuning the ground state of $Er_2Ti_2O_7$ with magnetic dilution.

This study was prompted by two theoretical works that studied the effect of magnetic dilution in XY pyrochlores. Both of these studies predicted that if order-by-disorder is the primary mechanism responsible for $Er_2Ti_2O_7$'s ψ_2 ground state, then removing a small fraction of the magnetic moments ($\sim$ 10%) should induce a transition to the ψ_3 state [94, 95]. To investigate these theoretical predictions, we grew three single crystals of $Er_{2-x}Y_xTi_2O_7$ with $x = 0$ (pure), 0.2 (10%-Y) and 0.4 (20%-Y) where the magnetic ion Er^{3+} is substituted by a non-magnetic ion, Y^{3+}. We performed sophisticated elastic and inelastic neutron scattering experiments on these three single crystals. We discovered that dilution from pure $Er_2Ti_2O_7$ up to 10%-Y leaves the ψ_2 ground state unaffected. However, the 20%-Y sample undergoes a phase transition to a frozen mosaic of $\psi_2$and ψ_3 states. Our results confirm the predicted fragility of the ψ_2 state in $Er_2Ti_2O_7$ towards dilution, but the exact magnetic structure found in our study is different than theoretically predicted. This indicates that while Y-substitution does indeed lead to magnetic dilution, it may also introduce non-trivial disorder absent from the theoretical works.

For this paper, I grew the three single crystals of $Er_{2-x}Y_xTi_2O_7$ using the optical floating zone technique. I conducted the inelastic neutron scattering experiments and analyzed the resulting data. Finally, I wrote the manuscript and the response to the referee reports. The contributions of each author are summarized below.

Author Contributions:

- *Experimental Concept*: **J. Gaudet**, B.D. Gaulin
- *Sample Preparation*: **J. Gaudet**, C.R.C. Buhariwalla, H.A. Dabkowska
- *Susceptibility Measurements*: T.J. Munsie, A.M. Hallas, G.M. Luke
- *Neutron Scattering Experiments*: **J. Gaudet**, D.D. Maharaj, N.P. Butch, B.D. Gaulin
- *Data Analysis*: **J. Gaudet**, A.M. Hallas, B.D. Gaulin
- *Manuscript*: **J. Gaudet**, A.M. Hallas, B.D. Gaulin

Magnetic dilution and domain selection in the XY pyrochlore antiferromagnet $Er_2Ti_2O_7$

J. Gaudet,[1] A. M. Hallas,[1] D. D. Maharaj,[1] C. R. C. Buhariwalla,[1] E. Kermarrec,[1] N. P. Butch,[2] T. J. S. Munsie,[1]
H. A. Dabkowska,[3] G. M. Luke,[1,4] and B. D. Gaulin[1,3,4]
[1] *Department of Physics and Astronomy, McMaster University, Hamilton, Ontario L8S 4M1, Canada*
[2] *NIST Centre for Neutron Research, Gaithersburg, Maryland, USA*
[3] *Brockhouse Institute for Materials Research, Hamilton, Ontario L8S 4M1, Canada*
[4] *Canadian Institute for Advanced Research, 180 Dundas Street West, Toronto, Ontario M5G 1Z8, Canada*

(Received 23 March 2016; revised manuscript received 23 July 2016; published 15 August 2016)

Below $T_N = 1.1$ K, the XY pyrochlore $Er_2Ti_2O_7$ orders into a $k = 0$ noncollinear, antiferromagnetic structure referred to as the ψ_2 state. The magnetic order in $Er_2Ti_2O_7$ is known to obey conventional three-dimensional (3D) percolation in the presence of magnetic dilution, and in that sense is robust to disorder. Recently, however, two theoretical studies have predicted that the ψ_2 structure should be unstable to the formation of a related ψ_3 magnetic structure in the presence of magnetic vacancies. To investigate these theories, we have carried out systematic elastic and inelastic neutron scattering studies of three single crystals of $Er_{2-x}Y_xTi_2O_7$ with $x = 0$ (pure), 0.2 (10% Y) and 0.4 (20% Y), where magnetic Er^{3+} is substituted by nonmagnetic Y^{3+}. We find that the ψ_2 ground state of pure $Er_2Ti_2O_7$ is significantly affected by magnetic dilution. The characteristic domain selection associated with the ψ_2 state, and the corresponding energy gap separating ψ_2 from ψ_3, vanish for Y^{3+} substitutions between 10% Y and 20% Y, far removed from the three-dimensional percolation threshold of ~60% Y. The resulting ground state for $Er_2Ti_2O_7$ with magnetic dilutions from 20% Y up to the percolation threshold is naturally interpreted as a frozen mosaic of ψ_2 and ψ_3 domains.

DOI: 10.1103/PhysRevB.94.060407

The network of corner-sharing tetrahedra that make up the pyrochlore lattice is one of the canonical architectures for geometrical frustration in three dimensions [1]. In the pyrochlore magnets with chemical composition $A_2B_2O_7$, each of the A^{3+} and B^{4+} sublattices independently form such a network and can be decorated by many ions. The rare-earth titanate family, $R_2Ti_2O_7$, which features a single magnetic R^{3+} site and nonmagnetic Ti^{4+} on the B site, has been of specific interest. This family displays a great variety of exotic magnetic ground states, including classical [2–4] and quantum spin ice [5–8], as well as spin liquid states [9–11]. Such exotic states arise from different combinations of magnetic anisotropies with differing exchange and dipolar interactions, depending on the nature of the R^{3+} magnetic ion.

Much current interest is focused on the XY antiferromagnetic pyrochlore $Er_2Ti_2O_7$, which displays an antiferromagnetic Curie-Weiss susceptibility with $\theta_{CW} = -22$ K [12]. Crystal field effects on Er^{3+} in this environment give rise to a g tensor with XY anisotropy [13–15]. In contrast to the exotic ground states displayed by other members of the $R_2Ti_2O_7$ family, $Er_2Ti_2O_7$ has a rather conventional $k = 0$, Γ_5 antiferromagnetic ground state below $T_N = 1.1$ K [12,16–19]. Γ_5 is made up of two basis vectors, referred to as ψ_2 and ψ_3, and sophisticated magnetic crystallography was used to identify the ordered structure in $Er_2Ti_2O_7$ as ψ_2 [16]. The microscopic spin Hamiltonian for $Er_2Ti_2O_7$ was determined through measurements of the spin wave dispersions within its field polarized state [20,21]. This work, among others [12,22,23], has provided an explanation for the selection of ψ_2 within the Γ_5 manifold in terms of a quantum order-by-disorder mechanism. The order-by-disorder scenario has been further strengthened by works showing that thermal fluctuations also select ψ_2 over ψ_3 [24–27]. A spin wave gap of 0.053 ± 0.006 meV has been successfully measured in $Er_2Ti_2O_7$, consistent with the order-by-disorder mechanism [28]. Recently, there has been a proposal that the selection of the ψ_2 ordered state could also occur via higher multipolar interactions, originating from virtual crystal field transitions [21,29].

The phase transition to the ψ_2 antiferromagnetic ordered state in $Er_2Ti_2O_7$ is unusual among the $R_2Ti_2O_7$ family by virtue of how conventional it is. In contrast to $Yb_2Ti_2O_7$ [30–32] and $Tb_2Ti_2O_7$ [33,34], there appears to be no sample dependence to its low-temperature phase diagram. Also, systematic studies of magnetic dilution at the rare-earth site in $Er_2Ti_2O_7$ are consistent with three dimensional (3D) percolation theory [35]. It was therefore surprising that two recent, independent theoretical works predicted that, upon magnetic dilution, the ψ_2 ground state selection in $Er_2Ti_2O_7$ should be unstable to the selection of its ψ_3 partner within the Γ_5 manifold [36,37].

Such a possible ψ_2 to ψ_3 phase transition upon magnetic dilution in $Er_2Ti_2O_7$ has yet to be explored experimentally and is the topic of this paper. The phase transition between ψ_2 and ψ_3 in $Er_2Ti_2O_7$ is predicted to occur near a critical dilution of ~7% [36,37]. As Y^{3+} is nonmagnetic and comparable in size to Er^{3+}, it is an ideal ion to employ for magnetic dilution studies. Hence, we have grown single-crystal samples of $Er_{2-x}Y_xTi_2O_7$ with $x = 0$ (pure), 0.2 (10% Y) and 0.4 (20% Y) to investigate a possible change in the magnetic ground state. We performed time-of-flight inelastic neutron scattering measurements on these three single crystals at various temperatures and magnetic fields. Our results show that the signature for ψ_2 long-range magnetic order disappears upon dilution. Instead, we observe a softening of the zero-field, low-energy excitations at the (220) ordering wave vector, consistent with a closing of the spin gap. At a relatively high level of magnetic dilution, on the order of 20% Y, the system cannot globally select the ψ_2 state over ψ_3, and we suggest that it forms a frozen mosaic of both ψ_2 and ψ_3 domains.

TABLE I. Summary of the dc susceptibility measurements performed on each of the $Er_{2-x}Y_xTi_2O_7$ samples with 0%, 10%, and 20% yttrium. The full data are shown in the Supplemental Material.

	T_N(K)	θ_{CW}(K)	μ_{eff}/Er^{3+}
$Er_2Ti_2O_7$(0% Y)	1.1(1)	−18.0(2)	9.555(4) μ_B
$Er_{1.8}Y_{0.2}Ti_2O_7$(10% Y)	1.04(5)	−17.2(3)	8.965(7) μ_B
$Er_{1.6}Y_{0.4}Ti_2O_7$(20% Y)	0.74(8)	−17.7(3)	8.523(6) μ_B

The three $Er_{2-x}Y_xTi_2O_7$ samples were characterized by dc magnetic susceptibility, and these results are summarized in Table I. In each case, the transition to the ordered phase is marked by a cusp and a bifurcation of the field-cooled and zero-field-cooled susceptibilities, as shown in the Supplemental Material [38]. Both the Néel temperature and the paramagnetic moment per formula unit systematically decrease as a function of the magnetic dilution. The Curie-Weiss temperature (θ_{CW}) does not vary appreciably in these three materials, ranging from −17.2(3) K to −18.0(2) K.

We performed time-of-flight elastic and inelastic neutron scattering on these three single crystals using the Disc Chopper Spectrometer at the NIST Center for Neutron Research [39]. Measurements were performed in a dilution refrigerator in both zero magnetic field and with an applied magnetic field along the $[1,-1,0]$ direction, perpendicular to the (HHL) scattering plane. For each of the three samples, magnetic Bragg peaks form below their respective Néel transitions (see Table I). The relative intensities of the magnetic Bragg reflections in the 10% Y and 20% Y crystals are unchanged from pure $Er_2Ti_2O_7$. That is to say, all three order into the Γ_5 irreducible representation, which is dominated by an intense magnetic Bragg reflection at (220). In large magnetic fields, all three enter a field-polarized state, characterized by an intense (111) magnetic Bragg reflection and the disappearance of the (220) magnetic reflection [40,41].

The Γ_5 irreducible representation is composed of two basis vectors, ψ_2 and ψ_3, which are indistinguishable in an unpolarized elastic neutron scattering experiment. However, the distinction between ψ_2 and ψ_3 ground-state selection can be resolved by considering the magnetic field dependence of the (220) magnetic Bragg peak. Both ψ_2 and ψ_3 display six distinct domains that are degenerate in zero field. This degeneracy is lifted by the application of a small magnetic field along the $[1,-1,0]$ direction [20,42,43]. For ψ_2, the two domains selected in a magnetic field are the ones that maximize the (220) magnetic Bragg peak, resulting in a twofold increase of its intensity. Domain selection in a [1–10] field for the ψ_3 state is less clear. Two scenarios are proposed; one selecting two domains which reduce the intensity of (220) [20,42] while in the other scenario, four domains are selected that result in a factor of 1.5 increase for (220) [43,44]. We note these domain effects occur in small $[1,-1,0]$ fields, significantly below the onset of the field-polarized state. The effects of the canting angle on the (220) Bragg peak intensity have been well characterized for $Er_2Ti_2O_7$ [40,41,45] and little effect is seen on its intensity between 0.1 and 1 T. Hence, we used a field of 0.5 T to investigate domain effects, which is sufficiently large to overcome pinning of domains by disorder in a small field.

We first consider the elastic scattering from the three crystals at the (220) Bragg position in zero field, 0.5 T, and 3 T, as shown in Fig. 1. The intensities have been normalized using the Bragg intensity at $H = 3$T, which corresponds to the polarized state where the scattered intensity at (220) is purely structural. As the field is increased to 0.5 T, we observe a marked increase in the peak intensity for the pure sample as well as for the 10% Y–doped sample, but not for the 20% Y–diluted crystal. More striking is the evolution of the shape of the (220) Bragg peak with magnetic dilution. In zero field, the undoped sample exhibits a resolution-limited Bragg peak with a small amount of diffuse scattering extending out along [HH0] [Fig. 1(a)]. Upon dilution, the relative contribution of the resolution-limited Bragg scattering weakens with a corresponding increase in the diffuse scattering, such that the line shape of the 20% Y sample is dominated by a Lorentzian form in both zero field and at 0.5 T [Fig. 1(c)].

To determine the origin of the diffuse scattering around (220), we look to the full inelastic neutron spectra in Fig. 2. These data are shown along three reciprocal space directions for each of the three samples in four different magnetic fields applied along the $[1,-1,0]$ direction. In zero field (top row of Fig. 2), the spin waves of the three samples are qualitatively similar, consisting of one flat branch near 0.4 meV and quasi-Goldstone modes which soften at (111) and (220). A

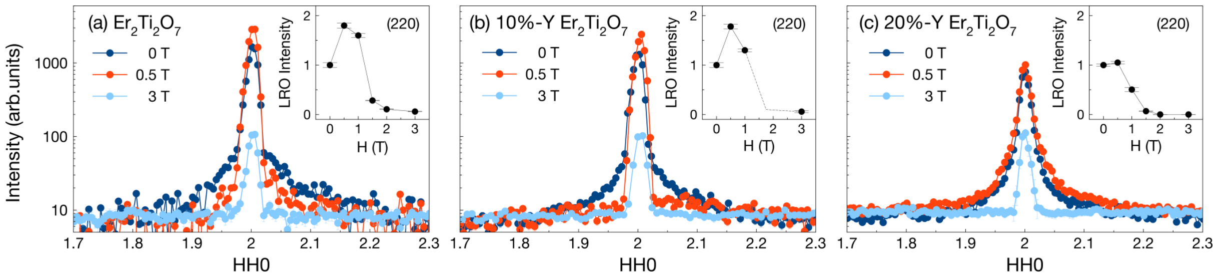

FIG. 1. Magnetic Bragg peak intensity for $Q = (220)$ as a function of field for the pure, 10% Y and 20% Y diluted samples of $Er_{2-x}Y_xTi_2O_7$. The elastic scattering was isolated by integrating from −0.2 to 0.2 in the [00L] direction and from −0.1 to 0.1 meV in energy transfer. The insets show the integrated intensity of the long-range ordered component of the scattering for each of the three samples. Examples of the fits used to obtain these intensities are shown in Fig. 1 of the Supplemental Material [38]. The dashed line in the inset of (b) indicates the expected behavior for the 10% Y sample at 1.75 T.

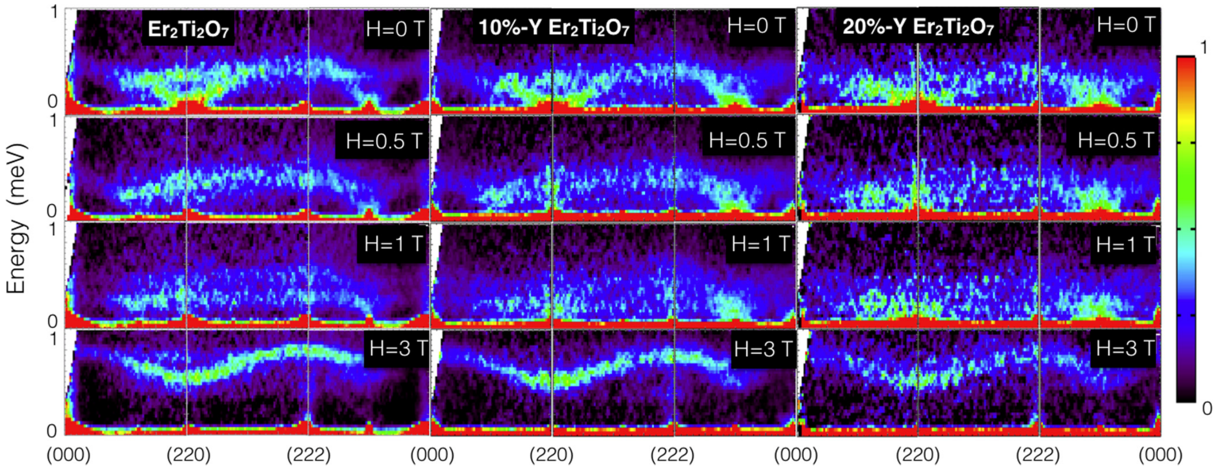

FIG. 2. Spin wave spectra along three different directions in the HHL plane: [HH0], [22L], and [HHH], all at $T = 0.1$ K. The spectra are shown for each of the three samples in zero magnetic field and with magnetic fields of 0.5, 1, and 3 T applied along the [1-10] direction. The contour plots along the [HH0], [22L], and [HHH] directions are obtained by integrating the 3D data set, $S(\vec{Q},E)$, over $-0.2 \leqslant$ [00L] $\leqslant 0.2$, $1.8 \leqslant$ [HH0] $\leqslant 2.2$ and $0.2 \leqslant$ [HH-2H] $\leqslant 0.2$, respectively.

previous high-resolution inelastic neutron scattering study of the pure sample determined that the quasi-Goldstone modes are gapped by 0.053 ± 0.006 meV [28]. As the energy resolution associated with the present inelastic measurements is 0.09 meV, elastic cuts of the form shown in Fig. 1 necessarily integrate over some of the spectral weight of these quasi-Goldstone modes. Thus, for the pure sample, this low-energy inelastic scattering is the origin of the diffuse scattering observed in our cuts over (220) in Fig. 1. However for the 10% Y and especially the 20% Y samples, our data suggest that the spin gap is reduced from 0.053 meV, allowing for additional quasielastic and elastic magnetic scattering, characteristic of a frozen mosaic of ψ_2 and ψ_3 domains.

In order to understand the contributions to the scattering in the cuts of Fig. 1, we fit each elastic data set to the sum of a Gaussian and a Lorentzian line shape, quantifying the magnetic long-range order (LRO) and the dynamic, quasielastic, or frozen spin contributions, respectively. An example of such a fit for each sample is shown in the Supplemental Material [38]. The resulting fits show that the relative contribution of the diffuse, Lorentzian line shape grows as a function of doping and accounts for ~75% of the Q-integrated scattering near (220) in the 20% Y sample at $T = 0.1$ K and zero field. We therefore suggest that with increasing magnetic dilution, x, the spin excitations near (220) in $Er_{2-x}Y_xTi_2O_7$ soften to lower energies and freeze. This is likely the result of a collapsing spin gap, a direct measure of the selection of ψ_2 over ψ_3.

We can now isolate the LRO component of the elastic scattering and study its field dependence at $T = 0.1$ K. Once again, we use the fits to the scattering around (220), wherein a resolution-limited Gaussian line shape represents the LRO and a broadened Lorentzian represents the dynamic, quasielastic, and frozen spin response captured by our finite energy resolution. The LRO integrated intensity at (220) is shown as a function of a $[1,-1,0]$ magnetic field for each sample in the insets of Fig. 1. Comparing the LRO intensity at zero field and 0.5 T, we observe a twofold increase for both the pure and 10% Y samples, while the LRO is unchanged for the 20% Y sample. This indicates, via the domain selection scenario described above, that the pure and 10% Y samples order into ψ_2, but the 20% Y sample does not. Furthermore, these results are inconsistent with the detailed theoretical predictions that low levels (~7%) of magnetic dilution should induce a transition from ψ_2 to ψ_3 [36,37].

A striking feature of Fig. 1, is the almost complete absence of diffuse scattering around (220) at $H = 0.5$ T for both the pure and 10% Y samples, but not the 20% Y sample. Examination of the detailed spin wave spectra in Fig. 2 shows that a 0.5 T field gaps the quasi-Goldstone mode at (220) in the pure and 10% Y samples (second row of Fig. 2). Meanwhile, quasielastic scattering persists around (220) in the 20% Y sample to fields greater than 1 T. To quantify this effect, we integrated a small portion of reciprocal space around (220) and plotted the energy dependence of this scattering in zero field and 0.5 T for all three samples (Fig. 3). It is clear that the quasielastic scattering from the quasi-Goldstone modes in the pure and 10% Y samples are gapped by ~0.3 meV in a 0.5 T field. However, for the 20% Y sample, the zero-field excitations soften and the application of a 0.5 T magnetic field makes little difference to the low-energy spectral weight near (220). Both of these observations are consistent with the absence of a spin-wave gap and the associated domain selection in a magnetic field in the 20% Y sample.

We propose the schematic phase diagram shown in Fig. 4 to describe the magnetic state in magnetically diluted $Er_{2-x}Y_xTi_2O_7$. The phase transition and ψ_2 ground-state selection are already well established in the pure material [12,16], along with the concomitant opening of a 0.053 ± 0.006 meV spin wave gap at $T_N = 1.1$ K [28]. Heat-capacity measurements as a function of magnetic dilution are consistent with conventional 3D percolation theory [46], and a percola-

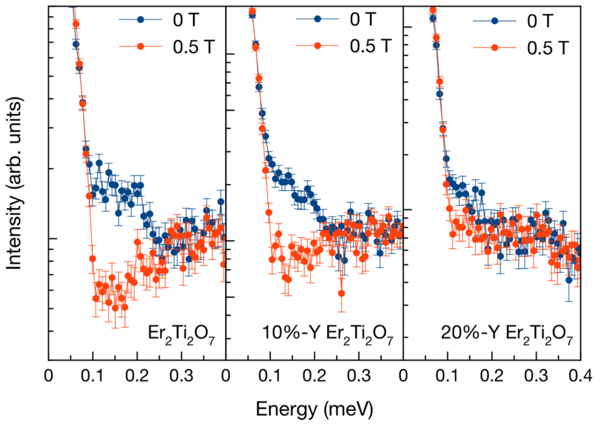

FIG. 3. Inelastic intensity as a function of energy at the (220) Bragg position for the pure, 10% Y and 20% Y diluted samples of $Er_{2-x}Y_xTi_2O_7$. These plots are obtained by integrating the 3D data sets $S(\vec{Q},E)$ at $T = 0.1$ K over $1.6 \leqslant$ [HH0] $\leqslant 2.4$ and $-0.5 \leqslant$ [00L] $\leqslant 0.5$.

tion threshold near 60% Y has also been established [35]. The present measurements on magnetically diluted single-crystal samples shows that ψ_2 domain selection is observed at low temperatures for the 10% Y sample but not for the 20% Y sample. This strongly suggests the presence of a phase boundary that mirrors the collapse of the spin gap as a function of dilution, indicated by the dashed line in Fig. 4(a). Weak dilution to the left of the dashed line produces a stable set of ψ_2 domains [Fig. 4(b)], at least above our minimum $T = 0.1$ K. However, to the right of the dashed line, the spin gap collapses and there is no mechanism for selection of ψ_2 over ψ_3. A ground state characterized by a linear combination of ψ_2 and ψ_3 forming the full U(1) manifold is consistent with our data. However, in light of the theoretical study of Refs. [36,37], it is then natural to think of the diluted system forming a frozen mosaic of ψ_2 and ψ_3 domains, with the ψ_3 domains [Fig. 4(c)] pinned by locally high concentrations of the quenched vacancies [Fig. 4(d)]. It is interesting to note that a similar mixed ψ_2 and ψ_3 state is also observed in $NaCaCo_2F_7$ but believed to originate from bond disorder [47].

We find that the ψ_2 ordered state in $Er_2Ti_2O_7$ displays remarkable fragility induced by the presence of magnetic vacancies. Measurements as a function of temperature in our most magnetically dilute sample, 20% Y provide no evidence for an additional phase transition between $T_N = 0.74(8)$ K and our base temperature of 0.1 K, as shown in Fig. 3 of the Supplemental Material [38]. Nonetheless, we do identify a change in phase behavior between ψ_2 and a ground state characterized by no selection of ψ_2 over ψ_3, likely a frozen mosaic of the two, all at dilution concentrations far below the 3D percolation threshold. Clearly, the preceding theoretical work correctly identified the sensitivity of the ψ_2 ground-state selection to the presence of this form of quenched disorder, if not the detailed manifestation of the disorder on the phase behavior. As such, we hope our characterization of the spin statics and dynamics in single-crystal $Er_{2-x}Y_xTi_2O_7$, and low-temperature phase behavior as a function of dilution, will motivate a complete understanding of these exotic, and fragile, ordered states.

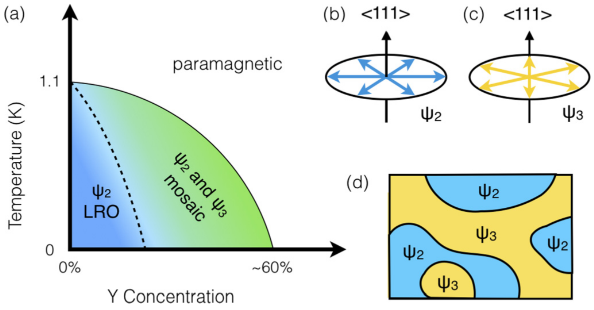

FIG. 4. (a) The schematic temperature-dilution phase diagram for $Er_{2-x}Y_xTi_2O_7$. A dilution between 10% Y and 20% Y marks a crossover from a pure ψ_2 state into a frozen mosaic of ψ_2 and ψ_3 domains. The six discrete domains allowed by (b) ψ_2 and (c) ψ_3 within the XY plane. (d) Schematic illustration of the state at moderate dilution showing the mosaic of ψ_2 and ψ_3 domains.

We wish to acknowledge useful conversations with Leon Balents, Kate Ross, Mike Zhitomirsky, Michel Gingras, and Jeff Rau. We would also like to thank Juscelino Leao for his assistance with the sample environment. This work was supported by the Natural Sciences and Engineering Research Council of Canada and the Canada Foundation for Innovation. Work at the NIST Center for Neutron Research is supported in part by the National Science Foundation under Agreement No. DMR-0944772.

---

[1] J. S. Gardner, M. J. P. Gingras, and J. E. Greedan, Rev. Mod. Phys. **82**, 53 (2010).
[2] M. J. Harris, S. T. Bramwell, D. F. McMorrow, T. H. Zeiske, and K. W. Godfrey, Phys. Rev. Lett. **79**, 2554 (1997).
[3] A. P. Ramirez, A. Hayashi, R. J. Cava, R. Siddharthan, and B. S. Shastry, Nature (London) **399**, 333 (1999).
[4] C. Castelnovo, R. Moessner, and S. L. Sondhi, Nature (London) **451**, 42 (2008).
[5] K. A. Ross, L. Savary, B. D. Gaulin, and L. Balents, Phys. Rev. X **1**, 021002 (2011).
[6] M. J. P. Gingras and P. A. McClarty, Rep. Prog. Phys. **77**, 056501 (2014).
[7] R. Applegate, N. R. Hayre, R. R. P. Singh, T. Lin, A. G. R. Day, and M. J. P. Gingras, Phys. Rev. Lett. **109**, 097205 (2012).
[8] S. B. Lee, S. Onoda, and L. Balents, Phys. Rev. B **86**, 104412 (2012).
[9] J. S. Gardner, S. R. Dunsiger, B. D. Gaulin, M. J. P. Gingras, J. E. Greedan, R. F. Kiefl, M. D. Lumsden, W. A. MacFarlane, N. P. Raju, J. E. Sonier, I. Swainson, and Z. Tun, Phys. Rev. Lett. **82**, 1012 (1999).

[10] H. Takatsu, H. Kadowaki, T. J. Sato, J. W. Lynn, Y. Tabata, T. Yamazaki, and K. Matsuhira, J. Phys. Condens. Matter **24**, 052201 (2011).

[11] M. J. P. Gingras, B. C. den Hertog, M. Faucher, J. S. Gardner, S. R. Dunsiger, L. J. Chang, B. D. Gaulin, N. P. Raju, and J. E. Greedan, Phys. Rev. B **62**, 6496 (2000).

[12] J. D. M. Champion, M. J. Harris, P. C. W. Holdsworth, A. S. Wills, G. Balakrishnan, S. T. Bramwell, E. Čižmár, T. Fennell, J. S. Gardner, J. Lago, D. F. McMorrow, M. Orendáč, A. Orendáčová, D. M. Paul, R. I. Smith, M. T. F. Telling, and A. Wildes, Phys. Rev. B **68**, 020401 (2003).

[13] H. Cao, A. Gukasov, I. Mirebeau, P. Bonville, C. Decorse, and G. Dhalenne, Phys. Rev. Lett. **103**, 056402 (2009).

[14] P. Bonville, S. Petit, I. Mirebeau, J. Robert, E. Lhotel, and C. Paulsen, J. Phys. Condens. Matter **25**, 275601 (2013).

[15] A. Bertin, Y. Chapuis, P. D. de Réotier, and A. Yaouanc, J. Phys. Condens. Matter **24**, 256003 (2012).

[16] A. Poole, A. S. Wills, and E. Lelievre-Berna, J. Phys. Condens. Matter **19**, 452201 (2007).

[17] J. Lago, T. Lancaster, S. J. Blundell, S. T. Bramwell, F. L. Pratt, M. Shirai, and C. Baines, J. Phys. Condens. Matter **17**, 979 (2005).

[18] P. Dalmas de Réotier, A. Yaouanc, Y. Chapuis, S. H. Curnoe, B. Grenier, E. Ressouche, C. Marin, J. Lago, C. Baines, and S. R. Giblin, Phys. Rev. B **86**, 104424 (2012).

[19] H. W. J. Blöte, R. F. Wielinga, and W. J. Huiskamp, Phys. (Amsterdam, Neth.) **43**, 549 (1969).

[20] L. Savary, K. A. Ross, B. D. Gaulin, J. P. C. Ruff, and L. Balents, Phys. Rev. Lett. **109**, 167201 (2012).

[21] S. Petit, J. Robert, S. Guitteny, P. Bonville, C. Decorse, J. Ollivier, H. Mutka, M. J. P. Gingras, and I. Mirebeau, Phys. Rev. B **90**, 060410 (2014).

[22] M. E. Zhitomirsky, M. V. Gvozdikova, P. C. W. Holdsworth, and R. Moessner, Phys. Rev. Lett. **109**, 077204 (2012).

[23] A. W. C. Wong, Z. Hao, and M. J. P. Gingras, Phys. Rev. B **88**, 144402 (2013).

[24] J. Oitmaa, R. R. P. Singh, B. Javanparast, A. G. R. Day, B. V. Bagheri, and M. J. P. Gingras, Phys. Rev. B **88**, 220404 (2013).

[25] M. E. Zhitomirsky, P. C. W. Holdsworth, and R. Moessner, Phys. Rev. B **89**, 140403 (2014).

[26] B. Javanparast, A. G. R. Day, Z. Hao, and M. J. P. Gingras, Phys. Rev. B **91**, 174424 (2015).

[27] P. A. McClarty, P. Stasiak, and M. J. P. Gingras, Phys. Rev. B **89**, 024425 (2014).

[28] K. A. Ross, Y. Qiu, J. R. D. Copley, H. A. Dabkowska, and B. D. Gaulin, Phys. Rev. Lett. **112**, 057201 (2014).

[29] J. G. Rau, S. Petit, and M. J. P. Gingras, Phys. Rev. B **93**, 184408 (2016).

[30] K. A. Ross, T. Proffen, H. A. Dabkowska, J. A. Quilliam, L. R. Yaraskavitch, J. B. Kycia, and B. D. Gaulin, Phys. Rev. B **86**, 174424 (2012).

[31] J. Gaudet, D. D. Maharaj, G. Sala, E. Kermarrec, K. A. Ross, H. A. Dabkowska, A. I. Kolesnikov, G. E. Granroth, and B. D. Gaulin, Phys. Rev. B **92**, 134420 (2015).

[32] A. Yaouanc, P. Dalmas de Réotier, C. Marin, and V. Glazkov, Phys. Rev. B **84**, 172408 (2011).

[33] T. Taniguchi, H. Kadowaki, H. Takatsu, B. Fåk, J. Ollivier, T. Yamazaki, T. J. Sato, H. Yoshizawa, Y. Shimura, T. Sakakibara, T. Hong, K. Goto, L. R. Yaraskavitch, and J. B. Kycia, Phys. Rev. B **87**, 060408 (2013).

[34] E. Kermarrec, D. D. Maharaj, J. Gaudet, K. Fritsch, D. Pomaranski, J. B. Kycia, Y. Qiu, J. R. D. Copley, M. M. P. Couchman, A. O. R. Morningstar, H. A. Dabkowska, and B. D. Gaulin, Phys. Rev. B **92**, 245114 (2015).

[35] J. F. Niven, M. B. Johnson, A. Bourque, P. J. Murray, D. D. James, H. A. Dabkowska, B. D. Gaulin, and M. A. White, Proc. R. Soc. London, Ser. A **470**, 20140387 (2014).

[36] V. S. Maryasin and M. E. Zhitomirsky, Phys. Rev. B **90**, 094412 (2014).

[37] A. Andreanov and P. A. McClarty, Phys. Rev. B **91**, 064401 (2015).

[38] The full susceptibility data and additional details on fitting of the magnetic Bragg peaks are shown in the Supplemental Material at http://link.aps.org/supplemental/10.1103/PhysRevB.94.060407.

[39] J. R. D. Copley and J. C. Cook, Chem. Phys. **292**, 477 (2003).

[40] J. P. C. Ruff, J. P. Clancy, A. Bourque, M. A. White, M. Ramazanoglu, J. S. Gardner, Y. Qiu, J. R. D. Copley, M. B. Johnson, H. A. Dabkowska *et al.*, Phys. Rev. Lett. **101**, 147205 (2008).

[41] P. A. McClarty, S. H. Curnoe, and M. J. P. Gingras, J. Phys.: Confer. Ser. **145**, 012032 (2009).

[42] Z. L. Dun, X. Li, R. S. Freitas, E. Arrighi, C. R. D. Cruz, M. Lee, E. S. Choi, H. B. Cao, H. J. Silverstein, C. R. Wiebe *et al.*, Phys. Rev. B **92**, 140407 (2015).

[43] V. S. Maryasin, M. E. Zhitomirsky, and R. Moessner, Phys. Rev. B **93**, 100406(R) (2016).

[44] M. E. Zhitomirsky (private communication).

[45] H. B. Cao, I. Mirebeau, A. Gukasov, P. Bonville, and C. Decorse, Phys. Rev. B **82**, 104431 (2010).

[46] B. D. Gaulin and J. S. Gardner, in *Frustrated Spin Systems* (World Scientific, Singapore, 2004), p. 457.

[47] K. A. Ross, J. W. Krizan, J. A. Rodriguez-Rivera, R. J. Cava, and C. L. Broholm, Phys. Rev. B **93**, 014433 (2016).

SUPPLEMENTAL MATERIAL: Magnetic dilution and domain selection in the XY pyrochlore antiferromagnet $Er_2Ti_2O_7$

J. Gaudet,[1] A. M. Hallas,[1] D. D. Maharaj,[1] C. R. C. Buhariwalla,[1] E. Kermarrec,[1]
N. P. Butch,[2] T. J. S. Munsie,[1] H. A. Dabkowska,[3] G. M. Luke,[1,4] and B. D. Gaulin[1,3,4]

[1] *Department of Physics and Astronomy, McMaster University, Hamilton, ON L8S 4M1, Canada*
[2] *NIST Centre for Neutron Research, Gaithersburg Maryland USA*
[3] *Brockhouse Institute for Materials Research, Hamilton, ON L8S 4M1, Canada*
[4] *Canadian Institute for Advanced Research, 180 Dundas Street West, Toronto, Ontario M5G 1Z8, Canada*

(Dated: July 22, 2016)

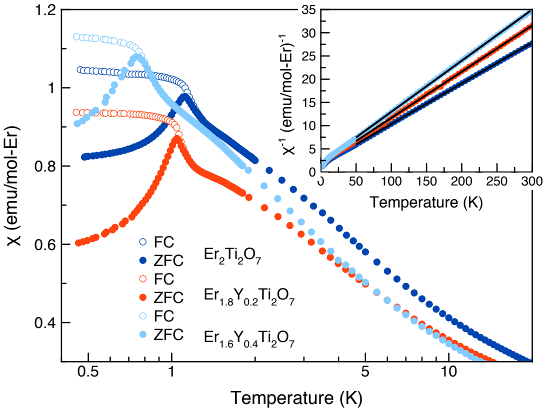

FIG. 1. Magnetic susceptibility data obtained for $Er_{2-x}Y_xTi_2O_7$ with x =0 (pure), 0.2 (10%-Y) and 0.4 (20%-Y). Powder samples from crushed single crystals used in the neutron scattering measurements were employed. For each sample, both the zero field cooled (ZFC - closed symbols) and the field cooled (FC - open symbols) susceptibility are shown. The inset shows the Curie-Weiss fits performed for each sample.

MAGNETIC SUSCEPTIBILITY

Single crystals of $Er_{2-x}Y_xTi_2O_7$ with $x = 0$ (pure), 0.2 (10%-Y) and 0.4 (20%-Y) were grown at McMaster University using a two-mirror floating zone image furnace. The growth procedure closely resembled the one used in Ref. [1–3]. The single crystal of $Er_2Ti_2O_7$ used for this study is the same as the one studied by previous neutron scattering work [4–6]. The susceptibility measurements were performed using a Quantum Design MPMS magnetometer equipped with a ^{3}He insert and the results are shown in Fig. 1.

Magnetic susceptibility measurements were performed on a small portion of the crushed single crystal of undoped $Er_2Ti_2O_7$ and on crushed single crystal of the 10%-Y and 20 %-Y samples. The dc susceptibility was measured on warming using both a field cooled and a zero field cooled protocol with an external field of 0.01 T. In each case, the transition to long range magnetic order is marked by a cusp in the susceptibility as well as a bifurcation of the field cooled and zero field cooled susceptibilities. As the cusp and the bifurcation in the susceptibility do not occur concomitantly, we define T_N as the cusp maxima, and the difference between the two as the error bar. The undoped $Er_2Ti_2O_7$ orders at $T_N = 1.1(1)$ K, consistent with previous studies [7]. The effect of diluting magnetic Er^{3+} with non-magnetic Y^{3+} is to suppress the magnetic ordering transition to lower temperature. The 10%-Y and 20%-Y samples have Néel temperatures of $T_N = 1.04(5)$ K and $T_N = 0.74(8)$ K, respectively. This suppression of T_N is consistent with previous studies of yttrium-dilution in $Er_2Ti_2O_7$ [1].

At high temperatures, Curie-Weiss behavior is observed in both undoped and yttrium-doped $Er_2Ti_2O_7$. Curie-Weiss fits were performed for each sample between 50 K and 300 K, and the results of these fits are summarized in Table I of the main manuscript. The Curie-Weiss temperature (θ_{CW}) does not change appreciably in these three materials, ranging from $-17.2(3)$ K to $-18.0(2)$ K. The paramagnetic moment extracted from the high-temperature Curie-Weiss fits, $9.555(4)\mu_B$ for Er^{3+} as well as prior bulk magnetization studies [8]. However, the paramagnetic moment per Er^{3+} systematically decreases with yttrium doping, likely a consequence of differences in the high energy crystal electric field schemes in these three materials. We note, however, that our inelastic scattering study revealed no low-lying crystal electric field levels in either the 10%-Y or 20%-Y samples up to 3 meV.

LONG RANGE ORDERED AND DIFFUSE CONTRIBUTIONS TO THE (220) BRAGG PEAK IN $Er_{2-x}Y_xTi_2O_7$

To extract the long-range order as well as the dynamic, quasi-elastic and frozen contributions to the (220) magnetic Bragg peak, we performed an integration of the neutron scattering data set of -0.2 to 0.2 in the [00L] direction and -0.1 to 0.1 meV in energy transfer. The results of such integration for the three single crystals are shown in Fig. 2 for $T = 0.1$ K and zero applied field. Each

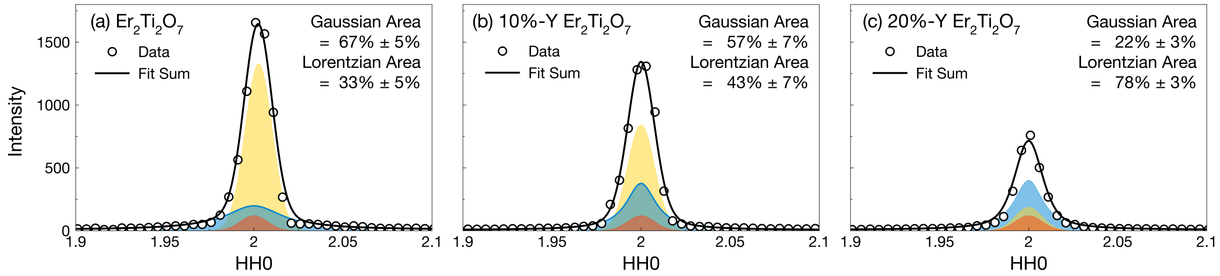

FIG. 2. Typical fits of the (220) magnetic Bragg peak performed in this work for $Er_{2-x}Y_xTi_2O_7$ with $x = 0$ (pure), 0.2 (10%-Y) and 0.4 (20%-Y)) at $T = 0.1$ K in zero field. The yellow areas represent the elastic, resolution-limited (Gaussian) magnetic contribution to the scattering and the blue area represents the dynamic, quasi-elastic or frozen (Lorentzian) contributions to the scattering. The red area shows the structural scattering obtained via a fit of the 3T data set. The black lines shows the resulting fit which are obtained by the addition of the three curves (blue,yellow and red).

Bragg peak has been fit to a Gaussian function to account for the long-range order (blue shaded region in Fig. 2) and a Lorentzian function for the dynamic, quasi-elastic and frozen contributions to the scattering (yellow shaded region in Fig. 2). The width of the Gaussian function was fixed by the width of a strictly nuclear reflection in the 3T data set. An additional Gaussian contribution to the scattering was accounted for by the 3T data set itself, representing the nuclear contribution (red shaded region in Fig. 2) and kept fix for the low field data sets. Finally, the width of the Lorentzian function was allowed to refine freely. The results for all samples show that the relative contribution of the Lorentzian scattering over the Gaussian (long-range order) contributions is strongly enhanced as a function of doping. As discussed in the main manuscript, this indicates that upon dilution, the spins do not order in the discrete states belonging to ψ_2 but instead freeze into a mosaic of ψ_2 and ψ_3 domains, whose characteristic size is approximated by the inverse of the Q-width of the Lorentzian component to the scattering, which gives 35 ± 7 Å.

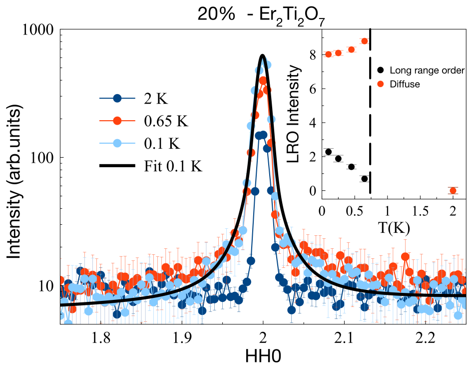

FIG. 3. Elastic cut showing the (220) magnetic Bragg peak for varying temperature in $Er_{2-x}Y_xTi_2O_7$ with x=0.4 (20%-Y) in zero applied field. The black line represents the resulting fit for the $T = 0.1$ K data set. The inset panel shows the temperature dependence of the Gaussian, long range ordered, and Lorentzian contributions to the (220) scattering, where the dashed line marks the Néel transition temperature, $T_N = 0.74(8)$ K.

TEMPERATURE DEPENDENCE OF THE (220) BRAGG PEAK FOR 20%-Y $Er_2Ti_2O_7$.

The temperature dependence of the (220) magnetic Bragg peak in $Er_{2-x}Y_xTi_2O_7$ with $x = 0.4$ (20%-Y) has also been explored to investigate a possible phase transition between ψ_2 and ψ_3 states at temperatures between the base temperature of our neutron experiment ($T = 0.1$ K) and the Néel temperature ($T = 0.74(8)$ K) of this sample. Fig. 3 shows elastic cuts around the (220) Bragg position obtained by an integration of −0.2 to 0.2 in the [00L] direction and −0.1 to 0.1 meV in energy transfer. The same procedure followed in the previous section was again employed to fit the (220) magnetic Bragg peak at every temperature collected in our neutron experiment in zero applied field. In this figure, the structural contribution of the long-range order scattering at (220) has been removed using intensity obtained from the paramagnetic, $T = 2$ K data set. The temperature dependence of the Lorentzian and the long-range order scattering are shown in the inset of Fig. 3. The long-range order contribution shows typical order parameter behavior, correlated with T_N and no anomaly is observed below that temperature. In contrast, the Lorentzian scattering has little temperature dependence but is enhanced near T_N, consistent with critical scattering near a continuous phase transition.

[1] J. F. Niven, M. B. Johnson, A. Bourque, P. J. Murray, D. D. James, H. A. Dabkowska, B. D. Gaulin, and M. A. White, in *Proc. R. Soc. A*, Vol. 470 (The Royal Society,

2014) p. 20140387.

[2] G. Balakrishnan, O. Petrenko, M. R. Lees, and D. M. Paul, J. Phys. Condens. Matter **10**, L723 (1998).

[3] C. Bryan, C. A. Whitman, M. B. Johnson, J. F. Niven, P. Murray, A. Bourque, H. A. Dabkowska, B. D. Gaulin, and M. A. White, Phys. Rev. B **86**, 054303 (2012).

[4] J. P. C. Ruff, J. P. Clancy, A. Bourque, M. A. White, M. Ramazanoglu, J. S. Gardner, Y. Qiu, J. R. D. Copley, M. B. Johnson, H. A. Dabkowska, *et al.*, Phys. Rev. Lett. **101**, 147205 (2008).

[5] L. Savary, K. A. Ross, B. D. Gaulin, J. P. C. Ruff, and L. Balents, Phys. Rev. Lett. **109**, 167201 (2012).

[6] K. A. Ross, Y. Qiu, J. R. D. Copley, H. A. Dabkowska, and B. D. Gaulin, Phys. Rev. Lett. **112**, 057201 (2014).

[7] J. D. M. Champion, M. J. Harris, P. C. W. Holdsworth, A. S. Wills, G. Balakrishnan, S. T. Bramwell, E. Čižmár, T. Fennell, J. S. Gardner, J. Lago, D. F. McMorrow, M. Orendáč, A. Orendáčová, D. M. Paul, R. I. Smith, M. T. F. Telling, and A. Wildes, Phys. Rev. B **68**, 020401 (2003).

[8] S. Bramwell, M. Field, M. Harris, and I. Parkin, Journal of Physics: Condensed Matter **12**, 483 (2000).

3.2 Preface to Publication V: Emergent Zeeman clock anisotropies in $Er_2Ti_2O_7$.

Putting aside the issue of the exact ground state selection mechanism, in this work we took advantage of the fact the $Er_2Ti_2O_7$ is a rare example of a discrete Z_6 symmetry breaking. The ψ_2 ground state of $Er_2Ti_2O_7$ is composed of six equally distributed domains that are related to one another by a 60° rotation of the spins within the XY plane. While the Z_6 discrete symmetry breaking, found in the case of Ising anisotropy, is relatively ubiquitous, higher order discrete symmetry breaking systems are scarce. However, theoretically, the behavior of a Z_6 symmetry breaking system is predicted to be rich under the application of a magnetic field along various high symmetry directions, giving rise to a multitude of domain reorientations and redistributions [96]. The full manifold of field-induced states has a 12-fold symmetry that can be mapped onto a conventional analog clock. The effective Zeeman terms were found to be well described using such clock terms. We performed inelastic neutron scattering studies on $Er_2Ti_2O_7$ with a magnetic field applied along the [001], [110], and [111] high symmetry crystallographic directions. In a [001] field a transition from ψ_2 to ψ_3 is both predicted and observed. Meanwhile for a [110] field, only a domain redistribution is expected, and indeed observed. However, in striking contrast to the good agreement found for [100] and [110], our experimental results in a [111] field do not conform with the theoretical predictions. This discrepancy may arise due to the presence of an out-of-plane Zeeman coupling, absent from the theoretical model. Finally, a quantitative analysis of the [001] domain transition in $Er_2Ti_2O_7$ is consistent with order-by-disorder being the dominant ground state selection mechanism.

In this paper, I conceived and performed the inelastic neutron scattering experiments. I also analyzed the data and wrote the manuscript as well as the response to the referee reports. The contributions of each author are summarized below.

Author Contributions:

- *Experimental Concept*: **J. Gaudet**, B.D. Gaulin
- *Sample Preparation*: J. Thibault, H.A. Dabkowska
- *Neutron Scattering Experiment*: **J. Gaudet**, A.M. Hallas, N.P. Butch, B.D. Gaulin
- *Data Analysis*: **J. Gaudet**, A.M. Hallas, B.D. Gaulin
- *Manuscript*: **J. Gaudet**, A.M. Hallas, B.D. Gaulin

Experimental evidence for field-induced emergent clock anisotropies in the XY pyrochlore $Er_2Ti_2O_7$

J. Gaudet,[1,*] A. M. Hallas,[1] J. Thibault,[1] N. P. Butch,[2] H. A. Dabkowska,[3] and B. D. Gaulin[1,3,4]
[1]Department of Physics and Astronomy, McMaster University, Hamilton, Ontario L8S 4M1, Canada
[2]NIST Center for Neutron Research, National Institute of Standards and Technology, Gaithersburg, Maryland 20899, USA
[3]Brockhouse Institute for Materials Research, Hamilton, Ontario L8S 4M1 Canada
[4]Canadian Institute for Materials Research, 180 Dundas Street West, Toronto, Ontario M5G 1Z8, Canada

(Received 3 October 2016; revised manuscript received 18 December 2016; published 6 February 2017)

The XY pyrochlore antiferromagnet $Er_2Ti_2O_7$ exhibits a rare case of Z_6 discrete symmetry breaking in its ψ_2 magnetic ground state. Despite being well-studied theoretically, systems with high discrete symmetry breakings are uncommon in nature. Thus, $Er_2Ti_2O_7$ provides an experimental playground for the study of broken Z_n symmetry, for $n > 2$. A recent theoretical work examined the effect of a magnetic field on a pyrochlore lattice with broken Z_6 symmetry and applied it to $Er_2Ti_2O_7$. This study predicted multiple domain transitions depending on the crystallographic orientation of the magnetic field, inducing rich and controllable magnetothermodynamic behavior. In this work, we present neutron scattering measurements on $Er_2Ti_2O_7$ with a magnetic field applied along the [001] and [111] directions and provide experimental observation of these exotic domain transitions. In a [001] field, we observe a ψ_2 to ψ_3 transition at a critical field of 0.18 ± 0.05 T. We are thus able to extend the concept of the spin-flop transition, which has long been observed in Ising systems, to higher discrete Z_n symmetries. In a [111] field, we observe a series of domain-based phase transitions for fields of 0.15 ± 0.03 T and 0.40 ± 0.03 T. We show that these field-induced transitions are consistent with the emergence of twofold, threefold, and possibly sixfold Zeeman terms. Considering all the possible ψ_2 and ψ_3 domains, these Zeeman terms can be mapped onto an analog clock—exemplifying a literal clock anisotropy. Lastly, our quantitative analysis of the [001] domain transition in $Er_2Ti_2O_7$ is consistent with order-by-disorder as the dominant ground state selection mechanism.

DOI: 10.1103/PhysRevB.95.054407

I. INTRODUCTION

The pyrochlore lattice is a face centered cubic structure with a basis of corner-sharing tetrahedra. In the case of the pyrochlore $Er_2Ti_2O_7$, the spins residing on this network of tetrahedra are known to have a $k = 0$, Γ_5 magnetic structure, for which all the spins lie in the plane perpendicular to the local $\langle 111 \rangle$ axis [1]. A representation of this Γ_5 structure is shown in Fig. 1(a) with its associated basis vectors ψ_2 and ψ_3. The linear combination of these two basis vectors can generate any spin orientation spanning the local XY plane, which is the entire U(1) manifold. An appropriate model Hamiltonian that includes anisotropic exchange and dipolar interactions, with experimentally determined exchange parameters for $Er_2Ti_2O_7$, has its energy minimized by the U(1) manifold, which is degenerate at the mean field level [2,3]. However, in the real material, this degeneracy is lifted when the Er^{3+} moments order antiferromagnetically into a pure ψ_2 state below $T_N = 1.2$ K [4]. The mechanism responsible for this degeneracy breaking in $Er_2Ti_2O_7$ has attracted much attention, as it could be the first demonstration of ground state selection via order-by-disorder [5,6]. Indeed, it is widely believed that instead of ordering via energetic selection, thermal and quantum fluctuations drive this system to an entropically favorable magnetically ordered state [1–3,7–9]. This scenario is not yet definitive, however, as a competing theory has been proposed that might explain the ground-state selection via energetic selection [10–12]. Regardless, $Er_2Ti_2O_7$ remains the most promising candidate for ground state selection via the order-by-disorder mechanism.

Another interesting aspect of the phase transition in $Er_2Ti_2O_7$ is that it represents a rare case of higher order discrete symmetry breaking. Indeed, time inversion and rotational symmetry allow six distinct spin orientations within the ψ_2 state, i.e., a Z_6 symmetry breaking. The Ising model, with Z_2 symmetry breaking, is known to capture the salient physics of many magnetic materials and a wealth of other physical systems [13,14]. Although many theoretical models for systems with higher Z_n symmetry breaking have been proposed, there are in fact few experimental realizations [15,16]. Thus, $Er_2Ti_2O_7$ provides a rare and possibly unique opportunity to investigate the properties of such discrete symmetry breaking. Recently, Maryasin *et al.* [17] developed a theory for the effect of a magnetic field on the properties of a Z_6 pyrochlore magnet and predicted rich and exotic domain effects to occur in $Er_2Ti_2O_7$ due to the emergence of twofold, threefold, and sixfold anisotropic Zeeman terms. The degeneracy as well as the local XY angle of the states minimized by each of these Zeeman terms can be mapped out in analogy to a conventional clock, where the twelve hours of the clock are represented by the six ψ_2 and the six ψ_3 states [Figs. 1(b) and 1(c)].

In this paper, we use time-of-flight neutron scattering on $Er_2Ti_2O_7$ with a magnetic field applied along high symmetry cubic directions to provide experimental evidence of these predicted domain effects. We find a host of low field domain selections and reorientations, which henceforth we will collectively refer to as “domain transitions,” not to be confused with a change of representation manifold [U(1) or Γ_5], which would be a thermodynamic phase transition. Indeed, we find that for a field applied along the [001] direction, $Er_2Ti_2O_7$

---

[*] gaudej@mcmaster.ca

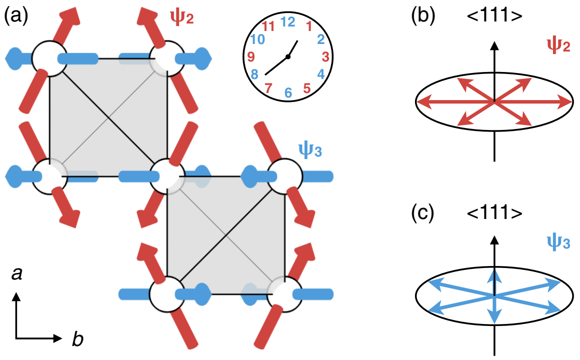

FIG. 1. (a) The $k = 0$, Γ_5 magnetic structure on the pyrochlore ($Fd\bar{3}m$) lattice, which is constructed by the ψ_2 (red) and ψ_3 (blue) basis vectors. Within the local XY plane, six specific spin orientations are allowed by (b) ψ_2 and six interleaving angles are allowed by (c) ψ_3. The ensemble of the full ψ_2 and ψ_3 states mimic a literal clock and can be used to represent the different anisotropic Zeeman terms via the selection of different hours (angles) on the clock.

exhibits a clear ψ_2 to ψ_3 transition at a critical field of 0.18 ± 0.05 T. This domain transition can be seen as the Z_n generalization of the spin-flop transition that occurs in Ising Z_2 systems. Our neutron scattering results also indicate possible domain transitions at 0.15 ± 0.03 T and 0.40 ± 0.03 T in a [111] magnetic field. We provide a complete description of the domains transitions that occur in $Er_2Ti_2O_7$ and show that our observations are consistent with the predicted emergent Zeeman twofold, threefold, and possibly sixfold clock terms.

II. EXPERIMENTAL DETAILS

A large single crystal of $Er_2Ti_2O_7$ was grown in a floating zone image furnace in 3 atm. of air and with a growth rate of 7 mm h^{-1}. This method of crystal growth is well established for the rare earth titanate pyrochlores [18–20]. This crystal was cut into two 2–3 gram segments, which were respectively aligned in the (H,K,0) and the (K+H,K-H, -2K) scattering planes using x-ray Laue diffraction. Time-of-flight neutron scattering measurements were performed using the Disc Chopper Spectrometer (DCS) at the NIST Center for Neutron Research [21]. An incident wavelength of 5 Å was employed, giving a maximum energy transfer of ∼ 2 meV and an energy resolution of 0.09 meV. All uncertainties correspond to one standard deviation. A magnetic field was applied perpendicular to the scattering plane. Thus, for the sample aligned in the (H,K,0) scattering plane, the field is applied along the [001] direction. For the sample aligned in the (K+H,K-H, -2K) scattering plane, the field is applied along the [111] direction. For both alignments, the (220) or (2-20) Bragg peak was observed only within the central bank of our detectors providing a 2° upper limit on the possible misalignment of our magnetic field. Scans with a total sample rotation of 35° with 0.25° steps were performed, centered on the (220) or (2-20) Bragg peak [these positions are symmetrically equivalent and will henceforth be referred to as (220)]. Lastly, for completeness, we also present previously published measurements of $Er_2Ti_2O_7$ aligned in the (H,H,L) scattering plane, with a magnetic field applied along the [1-10] direction. This earlier experiment was performed on the same spectrometer (DCS at NIST) but with a different single crystal; the full experimental details can be found in Ref. [22].

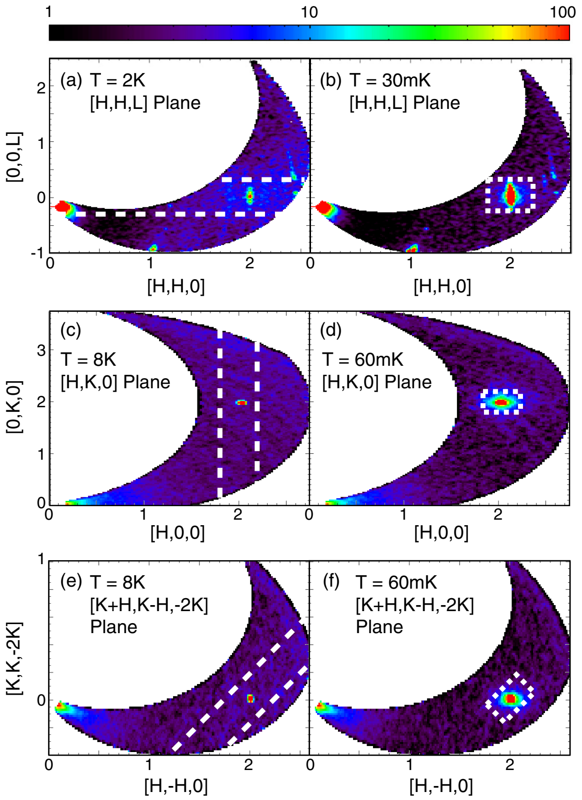

FIG. 2. The elastic scattering of $Er_2Ti_2O_7$ above and below the Neel ordering transition for crystals aligned in the (a,b) (H,H,L) plane, (c,d) (H,K,0) plane, and (e,f) (K+H,K-H, -2K) plane. At high temperature, the intensity of the (220) Bragg peak is purely structural, while at low temperature a magnetic Bragg peak also forms on the (220) position. Each of these data sets has been integrated in energy from −0.1 to 0.1 meV, which is approximately the resolution of elastic scattering in this experiment. Within the magnetically ordered state, this integration picks up a component of the magnetic inelastic scattering, giving the appearance of a significantly broadened peak. The dashed white lines indicate the areas of integration described in the text.

Typical elastic scattering maps of $Er_2Ti_2O_7$ for each of the three sample orientations above ($T = 8$ K or 2 K) and below ($T = 60$ mK or 30 mK) the Neel ordering transition are shown in Fig. 2. At high temperature, we observe a resolution limited Bragg peak that is purely structural in origin. At low temperature, passing into the magnetically ordered state, additional magnetic Bragg and diffuse scattering can be observed at the (220) position for all sample orientations. In the subsequent analysis, elastic cuts have been extracted for

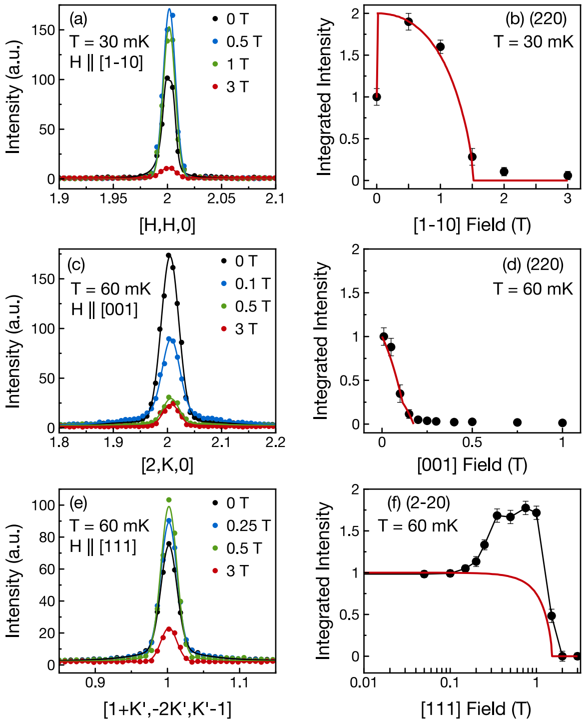

FIG. 3. Representative selection of elastic cuts over the (220) Bragg peak in varying magnetic field strength, for fields applied along (a) the [1-10] direction, (c) the [001] direction, and (e) the [111] direction. The solid lines in these panels are the fits to the Bragg peak, which were used to extract the integrated intensity. The resultant field dependence of the magnetic elastic intensity at (220) with the field applied along the (b) [1-10], (d) [001], and (f) [111] direction, revealing multiple low field domain transitions in $Er_2Ti_2O_7$. The red curves in these panels correspond to the theoretically predicted domain transitions [17]. Note that the (2-20) Bragg position is symmetrically equivalent to (220), as it is referred to in the main text.

each data set with varying magnetic field, as indicated by the white dashed lines in Figs. 2(a), 2(c), and 2(e). Those cuts have been obtained by integrating the respective data sets in energy from −0.1 to 0.1 meV with an additional integration (i) from −0.3 to 0.3 in the [0,0,L] direction for the [1-10] sample, (ii) from 1.8 to 2.2 in the [H00] direction for the [001] sample, and (iii) from 0.8 to 1.2 in the [H′,0,-H′] direction for the [111] sample [Figs. 3(a), 3(c) and 3(e)]. The inelastic spectra, which are shown for each field direction in Fig. 4, are extracted by using the same directional integrations, but without the integration in energy. Integrations of the total inelastic signal about (220) are presented in Fig. 5, where the area of integration corresponds to the white dashed boxes in Figs. 2(b), 2(d), and 2(f). Those spectra are obtained using the same directional integrations as above, but with an additional integration (i) from 1.7 to 2.3 in [H,H,0] for the [1-10] sample, (ii) from 1.8 to 2.2 in [0K0] for the [001] sample, and (iii) from 0.8 to 1.2 in [K′,-2K′, K′] for the [111] sample.

III. RESULTS

A. Magnetic field dependence of the elastic scattering at (220)

Neutron scattering spectra of $Er_2Ti_2O_7$ were collected at very low temperature, below 100 mK, with a magnetic field ranging from 0 T to 3 T applied along three crystallographic directions: [1-10], [001], and [111]. As can be seen by comparing the high temperature data sets [Figs. 2(a), 2(c), and 2(e)] with the low temperature data sets [Figs. 2(b), 2(d), and 2(f)], there is considerable magnetic diffuse scattering at low temperature for all field directions. This diffuse scattering is far broader than a resolution limited Bragg peak typical of long range order. The origin of this diffuse scattering is an intense quasi-Goldstone mode, which softens towards (220) [2,11,22]. The quasi-Goldstone-mode excitations have been previously measured in detail and are known to be gapped by 0.053 ± 0.006 meV [11,23]. As the energy resolution of this experiment is 0.09 meV, we inevitably integrate over a portion of this low energy inelastic scattering when extracting the elastic component. Thus, the diffuse scattering observed in Figs. 2(b), 2(d), and 2(f) originates from a partial integration of the quasi-Goldstone-mode magnetic excitations.

To investigate the field dependence of the elastic scattering, we performed integrations along the (220) Bragg peak for each data set at low temperature, with varying field strength and direction. A representative selection of these elastic scattering cuts are shown in Figs. 3(a), 3(c) and 3(e). At low temperature, there is a significant increase in the intensity of the resolution-limited Bragg scattering, due to the long range magnetic order, and also, a diffuse contribution originating from the inelastic scattering as discussed above. These two contributions to the scattering at the magnetic Bragg position necessitate a two component fit [24]. These fits were performed with a Gaussian function, to account for the resolution limited elastic Bragg scattering, and a Lorentzian function, which captures the inelastic contribution to the scattering. The Q width of the elastic Gaussian peak was fixed to the value determined from fitting the high temperature data set, for which the scattering at (220) is purely structural. The width of the Lorentzian function was allowed to freely vary. A sloping background was also used to account for the instrumental background. The solid lines seen in Figs. 3(a), 3(c), and 3(e) are examples of typical fits obtained from following this procedure, giving excellent agreement with the measured data. The resulting integrated intensity for the elastic (Gaussian) component as a function of the [1-10], [001], and [111] applied magnetic field are shown in Figs. 3(b), 3(d), and 3(f), respectively. The field dependence of the Lorentzian part of the scattering is presented in the Appendix for all field directions.

The elastic scattering dependence of the (220) magnetic Bragg peak in a [1-10] field is shown in Fig. 3(b). At low field, we observe an abrupt doubling of the intensity at (220). Above 0.5 T, the elastic scattering smoothly diminishes as a function of field and reaches zero intensity by 1.5 T. This smooth diminution of the (220) elastic scattering at high field corresponds to the transition towards the field polarized state [17,22,25–27]. For the [001] field direction, the magnetic elastic intensity at (220) falls off precipitously under the application of a small field [Fig. 3(d)]. Indeed, the elastic magnetic scattering at (220) reaches zero intensity in a field

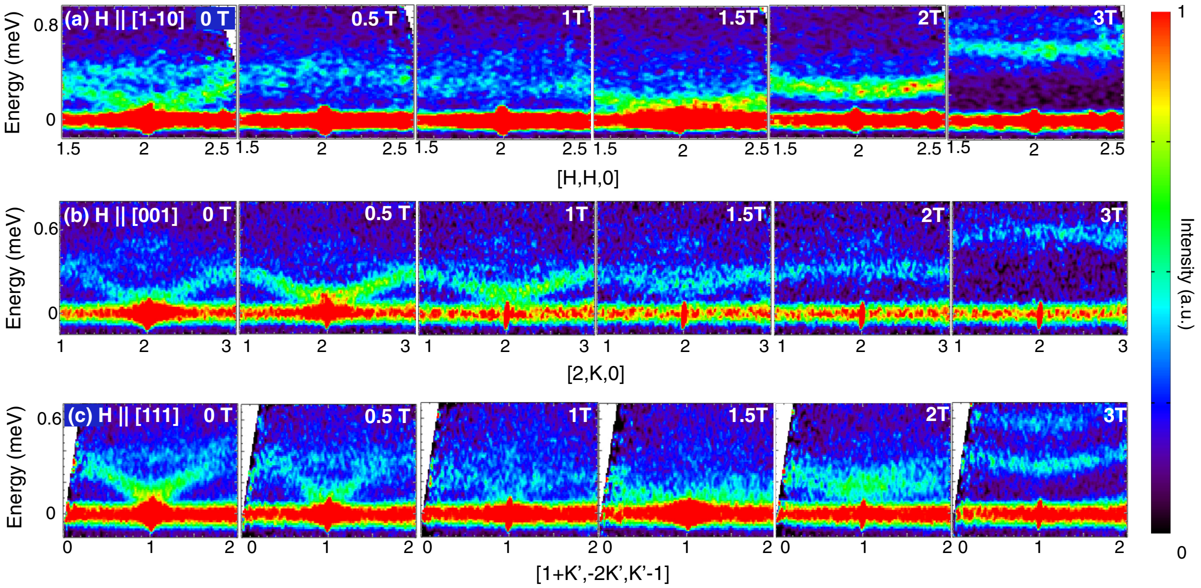

FIG. 4. Magnetic field dependence of the inelastic neutron scattering spectrum of $Er_2Ti_2O_7$ centered on the (220) Bragg position. These energy spectra are plotted along (a) the [H,H,0] direction for a [1-10] field, (b) the [2,K,0] direction for a [001] field, and (c) the [1+K′,-2K′,K′-1] direction for a [111] field. For the [1-10] field orientation, there is an immediate diminution of the quasi Goldstone-mode excitations at 0.5 T. For the [001] field orientation, the quasi-Goldstone mode excitations at (220) are intensified by the application of a field up to 1 T. In a [111] field, the quasi-Goldstone mode excitations have their intensity continuously decreased for fields ranging from 0.15 to 1 T. Above 1.5 T, the response of the spin wave spectra is due to the transition towards the field polarized state for all field orientations.

as small as 0.2 T. As the field is further increased, up to 3 T, the intensity remains zero. Finally, for the [111] field, the elastic scattering at (220) is unaffected up to 0.15 T [Fig. 3(f)]. Between 0.15 T and 0.4 T, the elastic scattering abruptly increases, reaching an intensity that is 1.75 times larger than the zero field value. The intensity then remains constant from 0.4 T to 1 T. Above 1 T, the intensity decreases, ultimately reaching zero intensity for fields larger than 1.5 T. This decrease of the elastic scattering at (220) above 1.5 T, as before, is concomitant with the phase transition towards the field polarized state [25,26].

B. Magnetic field dependence of the inelastic scattering at (220)

Now, turning our attention to the inelastic scattering, we can first look at Fig. 4, which shows the spin wave spectra of $Er_2Ti_2O_7$ as a function of [1-10], [001], and [111] field. Integrations as a function of energy centered on the (220) Bragg peak for each field direction are also shown in Fig. 5. The spin wave spectra at 0 T is dominated by low energy quasi-Goldstone-mode excitations centered on (220). These low energy excitations have a linear dispersion and are maximally intense approaching the (220) Bragg position. Accordingly, in the 0 T energy cuts of Fig. 5, the integration over the quasi-Goldstone-mode excitations produces the first inelastic feature, centered just below 0.2 meV. At slightly higher energy, 0.35 meV, we also observe weaker flat modes. The structure of the spin wave spectra in an applied field are further analyzed in, first, the low field regime and second, in the high field regime crossing into the field polarized state. The critical field of the transition to the field polarized state depends on the field orientation and is known, from bulk measurements, to be 1.5–1.7 T [25,26].

The application of a small [1-10] field results in a complete diminishment of the low energy scattering at 0.5 T, indicating the removal of the quasi-Goldstone-mode excitations at (220) [Figs. 4(a) and 5(a)]. However, the opposite scenario is observed upon the application of a weak [001] field. Indeed, an immediate increase in the scattering of the quasi-Goldstone-mode excitations is observed. This enhancement of the scattering can be seen by comparing the 0 T and 0.5 T data sets in Figs. 4(b) and 5(b). For the [111] field direction, the quasi-Goldstone-mode excitations show no field dependence up to 0.15 T [Figs. 4(c) and 5(c)]. Above 0.15 T, we observe a suppression of the quasi-Goldstone-modes excitations, but without their complete removal, as in the case of a [1-10] field. In fact, while continuously decreasing up to 1 T, the intensity of these excitations remains finite in a [111] field.

Lastly, we can examine the changes in the spin wave spectra upon transitioning into the field polarized state, which is known to occur at 1.5–1.7 T [25,26]. The evolution of the spin wave spectra when passing into the field polarized state gives similar behavior for [1-10] and [111] fields. Figures 4(a) and 4(c) show that the spectral weight for these two field orientations softens towards the elastic line in a 1.5 T field. Upon further increasing the magnetic field to 3 T, this quasielastic scattering moves to higher energies and forms weakly-dispersing spin wave modes. A qualitatively different behavior is observed in

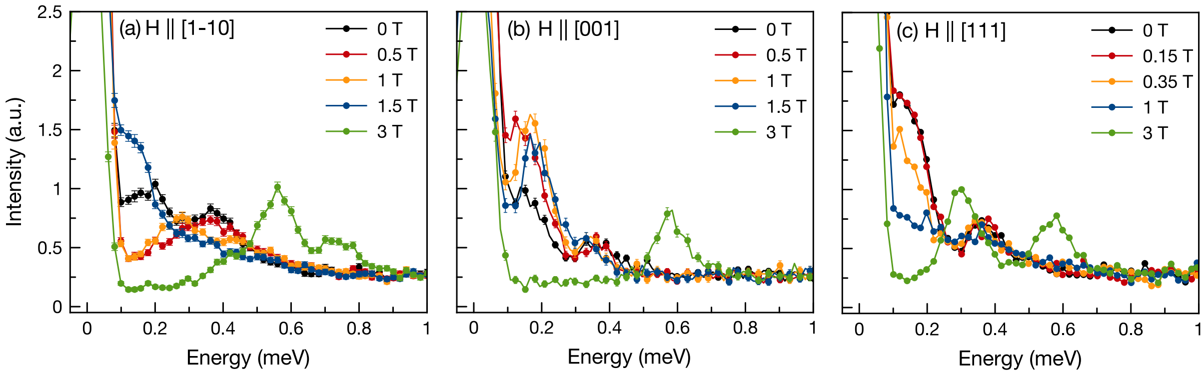

FIG. 5. The inelastic intensity centered on (220) as a function of energy for varying (a) [1-10] magnetic fields, (b) [001] magnetic fields, and (c) [111] magnetic fields. In a [1-10] field, the low energy scattering is completely suppressed upon the application of a 0.5 T field. In a [001] field, the inelastic intensity at low energies strongly increases for fields as small as 0.1 T. Further increasing the field shifts the spectral weight to higher energies. In a [111] field, the inelastic spectra is unaffected by fields up to 0.15 T. At larger [111] fields, the intensity at low energies continuously decreases. The integrations performed in Q are given in the experimental methods section.

the case of a [001] field. Approaching the polarized state for a [001] field, coherent low energy excitations are still observed, but with an increasing spin wave gap at (220). In Fig. 5(b), the opening of the spin wave gap is demonstrated by the shifting of the low energy feature upwards in energy. Upon the application of a [001] field greater than 1.5 T, the dispersion of the low energy quasi-Goldstone-mode excitations smoothly evolves to a nondispersive mode, as seen at 3 T.

IV. DISCUSSION

The magnetic ground state of $Er_2Ti_2O_7$ in zero magnetic field is well established and corresponds to an equiprobable distribution of the six ψ_2 domains within Γ_5 [4]. The elastic neutron scattering profile of this magnetic structure is characterized, in part, by an intense (220) magnetic Bragg peak [1,10,22]. Once a weak magnetic field is applied along any direction, the degeneracy of the six ψ_2 domains is lifted. However, it is important to re-emphasize that this does not correspond to a thermodynamic phase transition or a change of representation manifold. Rather, the spins remain constrained to the U(1) plane (Γ_5 manifold), as has been previously shown by heat capacity [22,26], magnetization [25], and neutron scattering [22,27]. Depending on the field orientation, this degeneracy breaking results in an increase or decrease of the (220) Bragg peak intensity due to domain effects. To understand these intensity changes, it is important to understand that the scattered intensity at (220) follows an $I \propto \cos^2(\theta)$ relationship, where θ is the local XY angle (Fig. 6). As neutron scattering is only sensitive to the component of the magnetization perpendicular to the direction of the scattering vector, a variation in the scattered intensity is observed due to the different orientations of the moments in each domain. Thus, by using the results of the calculation in Fig. 6 and the fact that the magnetic state at 0 T is well known (six ψ_2 states), it is possible to deduce the distribution of the domains that occurs in a magnetic field by measuring the relative change of the (220) elastic intensity.

A. Domain selection in a [1-10] magnetic field

Before discussing the [001] and [111] field evolution of the (220) Bragg peak, we briefly review the well-established domain effects for a field applied along the [1-10] direction. For this field orientation, an increase of the scattering at (220) is observed for fields above 0.1 T [Fig. 3(b)] [1,22]. The origin of this intensity gain is well understood: The application of a [1-10] field on $Er_2Ti_2O_7$ in its ψ_2 magnetic ground state induces a twofold clock term that favors the ψ_2 states with XY angles of 0 and π [2,17]. These two angles are highlighted by the dashed black circles in Fig. 6(a) and are the ones that maximize the scattered intensity of the (220) magnetic Bragg peak. These two angles give a factor two intensity increase to (220) from the average value for the six zero field ψ_2 states. These two domains selected by the Zeeman-clock term for a [1-10] field are also selected by the sixfold anisotropic term at 0 T. No further domain transitions are observed or predicted at low field. Beyond that, at high field, a continuous transition towards the field polarized state is observed at 1.5 T which is indicated by the smooth diminution of the (220) intensity [Fig. 3(b)]. This diminution of the (220) intensity occurs due to canting effects that become non-negligible approaching the field polarized state. This canting effect introduces a nonzero spin component away from the XY local plane. Several studies have modeled this behavior [10,22,27], but we reproduced via the red line in Fig. 3(b) the results using the method found in Maryasin *et al.* [17], which captures well the experimental data.

B. Domain selection and reorientation in a [001] magnetic field

As was the case for a [1-10] field, it has been predicted that in a [001] field, the Zeeman coupling will give rise to a twofold clock term [17]. The states that are selected in a [001] field are rotated by $\pi/2$ with respect to the states favored by a [1-10] field. Thus, the Zeeman energy is fully minimized by the ψ_3 states with XY local angles of $\pi/2$ and $3\pi/2$. However, at very low fields, where the Zeeman energy is much smaller

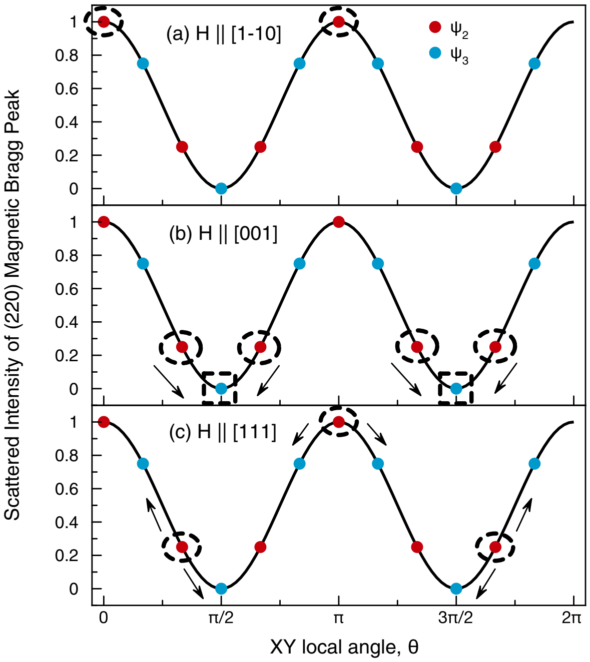

FIG. 6. The scattered intensity at the (220) Bragg position in $Er_2Ti_2O_7$ as a function of the angle, θ, in the XY local plane. The red dots represent the six ψ_2 domains and the blue dots represent the six ψ_3 domains. In (a) the two ψ_2 domains circled in black are the ones selected when a magnetic field of order 0.1 T is applied along the [1-10] direction. In (b) the four domains circled in black are the four ψ_2 states immediately selected in a [001] field. These states then cant towards the two ψ_3 states indicated by the black squares, which are selected by a 0.18 ± 0.05 T [001] magnetic field. In (c) the three ψ_2 domains circled in black are the ones selected for magnetic fields up to 0.15 T applied along the [111] direction. At higher fields, these domains are predicted to split by an angle, θ, as indicated by the arrows. Our measurement in a [111] field measured the (2-20) Bragg peak, which is symmetrically equivalent to (220).

than the sixfold ψ_2 clock term that dominates at 0 T, it is not possible to select these two ψ_3 domains. Instead, the system compromises by selecting the nearest ψ_2 domains, those with XY local angles of $2\pi/6$, $4\pi/6$, $8\pi/6$, and $10\pi/6$ [see black dashed circles in Fig. 6(b)]. Compared to 0 T, this new domain distribution should decrease the (220) intensity by a factor of two. Experimentally, referring back to Fig. 3(d), we do indeed observe a clear decrease of the scattering at low field.

The application of a field along [001] is inherently more interesting than a [1-10] field, as no ψ_2 state can fully minimize the Zeeman energy. Thus, there is competition between the emergent twofold Zeeman term and the 0 T sixfold clock term. At higher fields, as the Zeeman energy begins to overwhelm the 0 T sixfold clock term, there will be a continuous rotation of the spins towards a pure ψ_3 state made up of $\pi/2$ and $3\pi/2$ domains, where the (220) intensity should decrease to zero. In our experiment, the intensity of (220) continuously and drastically decreases to reach zero intensity by 0.2 T [Fig. 3(b)]. We associate this dramatic intensity loss with the above-described ψ_2 to ψ_3 transition, which is an XY spin-flop transition. As opposed to the ψ_2 state, all the spins within the ψ_3 states point perpendicular to the [001] direction [see Fig. 1(a)]. This result generalizes the well known concept of spin-flop transitions seen in the Ising system (Z_2) to systems with discrete symmetry breaking Z_n with $n > 2$.

The domain transition in a [001] field also opens an interesting line of inquiry, as the critical field for the ψ_2 to ψ_3 transition occurs when the Zeeman energy equals the energy of the 0 T sixfold clock term. Thus, we are able to provide an independent measurement of the 0 T sixfold clock term in $Er_2Ti_2O_7$, which is of course relevant to the zero field ground state selection, be it order-by-disorder and/or energetic selection involving virtual crystal field processes. Using analytical equations from Ref. [17], which account for the field dependence of the XY local angle upon the application of a [001] field, it is possible to model the decrease of the elastic scattering, the result of which is shown by the red line in Fig. 3(d). This fit is optimized as a function of the critical field, and the value we obtained is 0.18 ± 0.05 T. Calculations using only the quantum order-by-disorder term have predicted a critical field of 0.2 T [17], which is in excellent agreement with our experimental value. Naively, such a result can be interpreted as the ψ_2 selection in $Er_2Ti_2O_7$ being largely dominated by order-by-disorder effects, with virtual crystal-field excitations contributing relatively little to the ψ_2 selection. However, the critical field for the ψ_2 to ψ_3 spin-flop transition can only be indirectly modeled, introducing a degree of uncertainty. Further analysis, perhaps via numerical methods, may allow a more accurate comparison between the strength of the 0 T order-by-disorder sixfold clock term and the experimental data. Nonetheless, in principle, our measurement of the 0 T sixfold clock term should provide important information that would allow the ground state selection in $Er_2Ti_2O_7$ to be definitively understood.

C. Domain selection and reorientation in a [111] magnetic field

The Zeeman coupling for a field along the [111] direction is predicted to induce a combination of threefold and sixfold clock terms and, hence, the domain behavior of $Er_2Ti_2O_7$ in a [111] field is expected to be rich [17]. The threefold clock term selects the ψ_2 states with angles corresponding to $\pm\pi/3$ and π. However, the sixfold clock term is not the same as the one that selects the 0 T ψ_2 states. Instead, this [111] sixfold Zeeman clock term selects states which are rotated with respect to both the ψ_2 and ψ_3 states. This term then competes with both the threefold Zeeman clock term and also against the 0 T sixfold clock term that favors the ψ_2 states.

At low field, it is predicted that the domain selection behavior should be dominated by the combination of both the threefold Zeeman clock term and the 0 T sixfold clock term. First, at very low fields, the three domains with an angle of $\pm\pi/3$ and π should be selected [see black circles in Fig. 6(c)], which would result in no change in the (220) intensity. Experimentally, we refer back to our measurement shown in Fig. 3(f), which shows that the elastic scattering is constant up to 0.15 T. This is then consistent with the theoretical prediction that the three indicated ψ_2 states are selected for small [111] fields. Moreover, our data is in good agreement with the theoretical prediction that a weak [111] field induces an emergent threefold clock term.

Upon further increasing the [111] field, it is predicted that $Er_2Ti_2O_7$ should experience two additional domain transitions prior to entering its classical field polarized state. The origin of these transitions is the emergent sixfold Zeeman clock term. The first of these transitions is theoretically predicted to occur at $H_{c1} = 0.16$ T and results in the formation of six new domains. These six new domains are related to the previously selected $\pm\pi/3$ and π domains, but with a splitting angle of $\pm\theta$ [see black arrows in Fig. 6(c)]. This splitting angle θ is predicted to have the same value for all domains and should increase as a function of the applied field. At still higher fields, $H_{c2} = 0.4$ T, a second transition decreases the splitting angle back to zero, returning the system to a state with $\pm\pi/3$ and π domains. These transitions would be difficult to verify using unpolarized neutron scattering, as the domain splitting by an angle θ would have zero net effect on the intensity of (220). Thus, for a [111] field, the (220) Bragg peak is predicted to have no changes to its intensity up until the transition to the field polarized state. The predicted (220) behavior calculated by Maryasin *et al.* [17] is indicated by the red line in Fig. 3(f), and it is apparent that our experimental observations are not fully consistent with the predicted scenario, as the intensity of (220) is observed to substantially vary above 0.15 ± 0.03 T. We note, however, the predicted critical fields for these transitions, $H_{c1} = 0.16$ T and $H_{c2} = 0.4$ T do appear to be meaningful in $Er_2Ti_2O_7$: The first, H_{c1}, corresponds with the observed increase in elastic intensity at (220) by a factor of 1.75 and the second, H_{c2}, corresponds quite well with the field at which the intensity flattens, 0.4 ± 0.03 T.

To account for the observed intensity gain of (220) above 0.15 T, we propose a scenario of nonequiprobable domain distribution or inequivalent splitting angles [Fig. 6(c)]. Such scenarios would explain the increase in the elastic scattering at (220) but would require an additional Zeeman clock term that would favor the π domain over the $\pm\pi/3$ domains. In the theoretical work of Maryasin *et al.*, no such term is predicted for a perfectly aligned sample [17]. One possible origin of such a Zeeman clock term is a slight misalignment of the field along the [111] direction. While we can place an upper bound of 2° on the error in our alignment, it is worth noting that very small misalignments in a [111] field are known to be enhanced by demagnetization effects in spin ice [28]. However, in contrast to the spin ice case, $Er_2Ti_2O_7$ is an antiferromagnet where such demagnetization effects are naively expected to be far less important. Another possible origin of additional Zeeman terms is out-of-plane coupling, which wasn't included in the model of Maryasin *et al.*. Thus, the precise domain distributions and orientations occurring for fields between 0.15 and 0.4 T in a [111] field remain an open question at present.

D. Effect of domain selection on the quasi-Goldstone-mode excitations

Finally, it is interesting to comment on the low field behavior of the quasi-Goldstone-mode excitations centered on (220). In a small [1-10] field, as we discussed in Sec. III B., the quasi-Goldstone-mode excitations disappear at this particular ordering wave vector. This is best observed by comparing the inelastic spectra of 0 T and 0.5 T in Fig. 4(a) and Fig. 5(a). The disappearance of the quasi-Goldstone-mode excitations is concomitant with the increase of the elastic scattering at (220) [Fig. 3(b)]. The exact opposite behavior is observed for a field along the [001] direction, where we observe that the quasi Goldstone-mode excitations increase for small fields [Fig. 4(b) and Fig. 5(b)], while the elastic scattering [Fig. 3(d)] decreases for the same field range. Thus, there is a clear tradeoff between the intensities of the elastic scattering and the quasi-Goldstone-mode scattering at the (220) magnetic Bragg peak while transitioning into states with different XY local angles. To understand this observation, we suggest that the intensity of the quasi-Goldstone mode at (220) goes like $I \propto \sin^2(\theta)$. This can be understood by first pointing out that for magnetic neutron scattering, it is the component of the moment perpendicular to Q that couples to the neutron [i.e., in this case perpendicular to (220)]. The domains for which the (220) elastic scattering is maximized have their spin directions maximally perpendicular to the (220) direction, and vice versa. However, for low fields, the spins remain constrained to lie within the local XY plane. Thus, in the case of a [1-10] field, where the spins are maximally perpendicular to the scattering vector, the quasi-Goldstone-mode excitations must necessarily have their intensity reduced, as the spins will become more parallel to Q and will become less visible to neutron scattering. The opposite is true for a [001] field, where the spins are maximally parallel to the scattering vector and must excite into a more perpendicular orientation. The effects of a field on the scattered intensity of the quasi-Goldstone mode are thus, another direct signature of the domain effects. Moreover, the field dependence of the inelastic and elastic scattering in $Er_2Ti_2O_7$ are consistent with each other.

V. CONCLUSIONS

We have performed comprehensive time-of-flight neutron scattering measurements on single crystals of $Er_2Ti_2O_7$ with a magnetic field applied along the [001] and [111] directions. For fields smaller than 1 T, the field induced effects can be attributed to domain selection. The zero field state of $Er_2Ti_2O_7$ assumes the ψ_2 antiferromagnetic structure, which is composed of six equally probable domains. For small fields applied along the [001] direction, we observe a dramatic decrease of the (220) magnetic Bragg peak intensity, which agrees very well with the predicted transition from the six ψ_2 domains to two ψ_3 domains. For the [111] field direction, we observe that the elastic scattering at (220) is independent of field for low fields, consistent with an emergent threefold Zeeman clock term. Further increasing the field results in a large enhancement of the (220) Bragg peak intensity, inconsistent with the predicted domain selection scenario and hinting at an even richer phase behavior. Lastly, our experiment provides a measure of the zero field sixfold clock term strength, 0.18 ± 0.05 T. This result should prove useful in establishing a complete understanding of the mechanism of ground state selection in $Er_2Ti_2O_7$.

The work presented here experimentally confirms the rich and exotic magnetothermodynamic behavior predicted to exist in the XY pyrochlore antiferromagnet $Er_2Ti_2O_7$, or any other pyrochlore magnet ordering into the Γ_5 manifold.

We demonstrate that, depending on the field direction, a combination of two-, three-, and possibly sixfold Zeeman clock terms emerge and compete with the sixfold clock term present in zero field. We anticipate this work will help determine the ground state selection and field effects in other topical Γ_5 pyrochlores, such as $NaCaCo_2F_7$ [29], $Er_2Ge_2O_7$ [30], and $Yb_2Ge_2O_7$ [30,31].

Note added in proof. A related experimental study of $Er_2Ti_2O_7$ recently appeared as a preprint [32].

ACKNOWLEDGMENTS

We thank M. Zhitomirsky and R. Moessner for very useful discussions and for providing us the theoretical curves of the field dependence of the (220) Bragg peak intensity shown in Figs. 3(d) and 3(f). We also wish to thank Yegor Vekhov for his technical support with the dilution fridge used in the neutron experiment. The neutron scattering data were reduced and analyzed using DAVE software package [33]. The NIST Center for Neutron Research is supported in part by the National Science Foundation under Agreement No. DMR-094472. Work at McMaster University was supported by the Natural Sciences and Engineering Research Council (NSERC) of Canada. J.G. and A.M.H. gratefully acknowledge support from NSERC's Canada Graduate Scholarships.

APPENDIX: FIELD EFFECTS ON THE LORENTZIAN CONTRIBUTION OF THE (220) MAGNETIC BRAGG PEAK

As discussed in the paper, elastic cuts of the (220) magnetic Bragg peak have been carefully modeled with a two component fit for all field strengths and orientations. An example of one such fit is shown in Fig. 7(a) for the [111] sample at 0 T. The Gaussian component of the scattering originates from the nuclear and magnetic long-range order, and its field dependence is thoroughly discussed in the paper. The second component of the scattering at (220) is captured by a Lorentzian function and accounts for the inelastic part of the scattering due to the partial integration over the quasi-Goldstone-mode excitations. The Lorentzian contribution of the scattering is somewhat interesting as it provides information on the very low energy inelastic field dependence. The field evolution of the integrated intensity of the Lorentzian component is shown for all field directions in Figs. 7(b)–7(d).

For the [1-10] field direction, the Lorentzian part of the scattering reaches zero intensity for a field of 0.5 T [Fig. 7(b)]. This decrease of scattering is consistent with the complete removal of the quasi-Goldstone-mode excitations [Fig. 4(a)]. The Lorentzian contribution of the scattering maintains zero intensity up to 1.5 T, at which point a clear and abrupt increase is observed. This originates from the softening of the spin wave excitations towards the elastic line [Fig. 4(a) and Fig. 5(a)] and, thus, are picked up by our integration over the elastic channel. Above 1.5 T, no Lorentzian contribution of the scattering is observed in a [1-10] field.

For the [001] field direction, the Lorentzian contribution increases dramatically at 0.1 T, due to the enhancement of the scattering from the quasi-Goldstone-mode excitations [Fig. 7(c)]. Indeed, as seen in Fig. 4(b) and Fig. 5(b), the quasi-Goldstone-mode excitations are clearly enhanced upon application of fields up to 0.5 T. Referring once again to Fig. 7(c), we can see that above 0.1 T, the inelastic (Lorentzian) contribution steadily decreases, reaching zero intensity for fields above 0.75 T. This effect can also be explained by examining the energy cuts of Fig. 5(b). Comparing the data sets between 0.1 T and 1 T, we see that the inelastic intensity shifts to progressively higher energies with increasing field. As we are integrating over our elastic resolution in Fig. 7(c), from −0.1 to 0.1 meV, this integration picks up less of the inelastic contribution at higher fields as the intensity moves out of our elastic window. This shifting of the inelastic intensity to higher energies signals that the spin wave gap of the quasi-Goldstone mode is growing from 0.1 T up to 1 T. Above 1 T, the Lorentzian part of the scattering completely disappears as the (220) magnetic Bragg peak has zero intensity in the field polarized state.

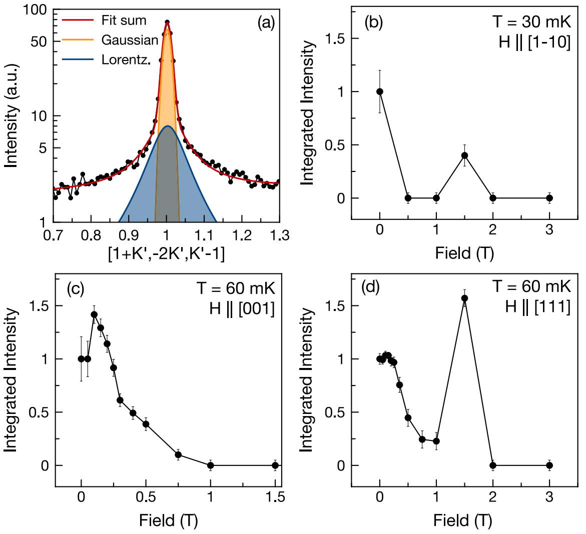

FIG. 7. (a) A typical fit of the scattering at the (220) Bragg peak position using both a Gaussian function and a Lorentzian function, to capture the elastic and inelastic contributions to the scattering, respectively. The field dependence of the Lorentzian contribution of the scattering for a (b) [1-10] magnetic field, (c) [001] magnetic field, and (d) [111] magnetic field. The field dependence of the Lorentzian contribution tracks the intensity of the low energy quasi-Goldstone-mode excitations.

Lastly, we turn our attention to the field evolution of the Lorentzian component in a [111] field which is shown in Fig. 7(d). Similar to the low field dependence of the elastic scattering [Fig. 3(f)], we observe that the inelastic intensity is flat up to 0.15 T. Above 0.15 T, the intensity falls off abruptly up to 1 T. This decrease of scattering is consistent with the reduced intensity of the quasi-Goldstone-mode excitations [Fig. 4(c) and Fig. 5(c)]. As was the case for the [1-10] field, for 1.5 T, we observe a large enhancement of the Lorentzian intensity. This originates from the softening of the spin wave excitations towards the elastic line. This feature is best observed by looking at the 1.5 T energy slice shown in Fig. 4(c). Above 1.5 T, the spin wave excitations are pushed to higher energy, and the Lorentzian contribution of the scattering remains at zero intensity.

[1] J. D. M. Champion, M. J. Harris, P. C. W. Holdsworth, A. S. Wills, G. Balakrishnan, S. T. Bramwell, E. Čižmár, T. Fennell, J. S. Gardner, J. Lago *et al.*, Phys. Rev. B **68**, 020401 (2003).

[2] L. Savary, K. A. Ross, B. D. Gaulin, J. P. C. Ruff, and L. Balents, Phys. Rev. Lett. **109**, 167201 (2012).

[3] M. E. Zhitomirsky, M. V. Gvozdikova, P. C. W. Holdsworth, and R. Moessner, Phys. Rev. Lett. **109**, 077204 (2012).

[4] A. Poole, A. S. Wills, and E. Lelievre-Berna, J. Phys.: Condens. Matter **19**, 452201 (2007).

[5] J. Villain, R. Bidaux, J.-P. Carton, and R. Conte, J. Phys. **41**, 1263 (1980).

[6] E. F. Shender, Zh. Eksp. Teor. Fiz. **83**, 326 (1982).

[7] A. W. C. Wong, Z. Hao, and M. J. P. Gingras, Phys. Rev. B **88**, 144402 (2013).

[8] J. Oitmaa, R. R. P. Singh, B. Javanparast, A. G. R. Day, B. V. Bagheri, and M. J. P. Gingras, Phys. Rev. B **88**, 220404 (2013).

[9] B. Javanparast, A. G. R. Day, Z. Hao, and M. J. P. Gingras, Phys. Rev. B **91**, 174424 (2015).

[10] P. A. McClarty, S. H. Curnoe, and M. J. P. Gingras, J. Phys.: Conf. Ser. **145**, 012032 (2009).

[11] S. Petit, J. Robert, S. Guitteny, P. Bonville, C. Decorse, J. Ollivier, H. Mutka, M. J. P. Gingras, and I. Mirebeau, Phys. Rev. B **90**, 060410 (2014).

[12] J. G. Rau, S. Petit, and M. J. P. Gingras, Phys. Rev. B **93**, 184408 (2016).

[13] P. M. Chaikin and T. C. Lubensky, *Principles of Condensed Matter Physics*, Vol. 1 (Cambridge University Press, Cambridge, UK, 2000).

[14] E. Schneidman, M. J. Berry, R. Segev, and W. Bialek, Nature (London) **440**, 1007 (2006).

[15] F.-Y. Wu, Rev. Mod. Phys. **54**, 235 (1982).

[16] R. B. Potts, in *Mathematical Proceedings of the Cambridge Philosophical Society* (Cambridge University Press, Cambridge, UK, 1952), Vol. 48, pp. 106–109.

[17] V. S. Maryasin, M. E. Zhitomirsky, and R. Moessner, Phys. Rev. B **93**, 100406 (2016).

[18] Q. Li, L. Xu, C. Fan, F. Zhang, Y. Lv, B. Ni, Z. Zhao, and X. Sun, J. Cryst. Growth **377**, 96 (2013).

[19] G. Balakrishnan, O. Petrenko, M. R. Lees, and D. M. Paul, J. Phys.: Condens. Matter **10**, L723 (1998).

[20] H. A. Dabkowska and A. B. Dabkowski, in *Springer Handbook of Crystal Growth* (Springer, Heidelberg, Germany, 2010), pp. 367–391.

[21] J. R. D. Copley and J. C. Cook, Chem. Phys. **292**, 477 (2003).

[22] J. P. C. Ruff, J. P. Clancy, A. Bourque, M. A. White, M. Ramazanoglu, J. S. Gardner, Y. Qiu, J. R. D. Copley, M. B. Johnson, H. A. Dabkowska *et al.*, Phys. Rev. Lett. **101**, 147205 (2008).

[23] K. A. Ross, Y. Qiu, J. R. D. Copley, H. A. Dabkowska, and B. D. Gaulin, Phys. Rev. Lett. **112**, 057201 (2014).

[24] J. Gaudet, A. M. Hallas, D. D. Maharaj, C. R. C. Buhariwalla, E. Kermarrec, N. P. Butch, T. J. S. Munsie, H. A. Dabkowska, G. M. Luke, and B. D. Gaulin, Phys. Rev. B **94**, 060407 (2016).

[25] P. Bonville, S. Petit, I. Mirebeau, J. Robert, E. Lhotel, and C. Paulsen, J. Phys.: Condens. Matter **25**, 275601 (2013).

[26] S. S. Sosin, L. A. Prozorova, M. R. Lees, G. Balakrishnan, and O. A. Petrenko, Phys. Rev. B **82**, 094428 (2010).

[27] H. B. Cao, I. Mirebeau, A. Gukasov, P. Bonville, and C. Decorse, Phys. Rev. B **82**, 104431 (2010).

[28] D. J. P. Morris, D. A. Tennant, S. A. Grigera, B. Klemke, C. Castelnovo, R. Moessner, C. Czternasty, M. Meissner, K. C. Rule, J.-U. Hoffmann *et al.*, Science **326**, 411 (2009).

[29] K. A. Ross, J. W. Krizan, J. A. Rodriguez-Rivera, R. J. Cava, and C. L. Broholm, Phys. Rev. B **93**, 014433 (2016).

[30] Z. L. Dun, X. Li, R. S. Freitas, E. Arrighi, C. R. D. Cruz, M. Lee, E. S. Choi, H. B. Cao, H. J. Silverstein, C. R. Wiebe *et al.*, Phys. Rev. B **92**, 140407 (2015).

[31] A. M. Hallas, J. Gaudet, M. N. Wilson, T. J. Munsie, A. A. Aczel, M. B. Stone, R. S. Freitas, A. M. Arevalo-Lopez, J. P. Attfield, M. Tachibana *et al.*, Phys. Rev. B **93**, 104405 (2016).

[32] E. Lhotel, J. Robert, E. Ressouche, F. Damay, I. Mirebeau, J. Ollivier, H. Mutka, P. Dalmas de Réotier, A. Yaouanc, C. Marin, C. Decorse, and S. Petit, arXiv:1701.07220 [cond-mat.str-el] (2009).

[33] R. Azuah, L. Kneller, Y. Qiu, C. Brown, J. Copley, R. Dimeo, and P. Tregenna-Piggott, J. Res. Natl. Inst. Stan. Technol. **114**, 341 (2009).

3.3 Preface to Publication VI: Effect of chemical pressure on the single-ion properties of $Er_2Ti_2O_7$.

In the final paper of this thesis, we turn our attention to the effect of chemical pressure on the single-ion properties of $Er_2Ti_2O_7$. As briefly mentioned in Section 1.1, XY pyrochlores are known to live in a rich phase space where four ordered states are predicted to compete and influence each other. This phase diagram of XY pyrochlores has been explored via chemical pressure, which consists of replacing the non-magnetic *B*-site cations by smaller or larger non-magnetic ions. For the erbium pyrochlores, in addition to $Er_2Ti_2O_7$, it is possible to synthesize polycrystalline samples of $Er_2Ge_2O_7$, $Er_2Sn_2O_7$ and $Er_2Pt_2O_7$ [10]. $Er_2Ge_2O_7$ is known to order into a Γ_5 phase [68] and has been argued to belongs to the ψ_3 state as opposed to the ψ_2 state found in $Er_2Ti_2O_7$ [70]. For $Er_2Sn_2O_7$ and $Er_2Pt_2O_7$, it was found that both materials order into the Γ_7 phase [9, 65]. The multiple ordered states found in the erbium family of pyrochlores is thus consistent with the rich phase diagram shown in Fig.1.3 [49]. In this paper, we investigated the evolution of the single-ion properties of $Er_2Ti_2O_7$ upon replacing Ti^{4+} by Sn^{4+}, Pt^{4+} and Ge^{4+}. This allows us to quantify the key ingredients that stabilize the different ordered states found in this family. We found that all four members have XY local anisotropy, but with significant variation in its magnitude. Curiously, the magnitude of the XY local anisotropy correlates strongly with their ordered states. Indeed, $Er_2Ti_2O_7$ and $Er_2Ge_2O_7$ have weak XY anisotropy ($\frac{g_\perp}{g_\parallel} < 4$) and both order into the Γ_5 manifold, while $Er_2Sn_2O_7$ and $Er_2Pt_2O_7$ have strong XY anisotropy ($\frac{g_\perp}{g_\parallel} > 25$) and both order into the Γ_7 manifold.

In this paper, I designed and performed the inelastic neutron scattering experiments. I analyzed and modeled the data using the same Matlab code as in Publication I. I also wrote the manuscript as well as the response to the referee reports. The contributions of each author are summarized below.

Author Contributions:

- *Experimental Concept*: **J. Gaudet**, A.M. Hallas, B.D. Gaulin
- *Sample Preparation*: A.M. Hallas
- *Neutron Scattering Experiment*: **J. Gaudet**, A.M. Hallas, A.I. Kolesnikov, B.D. Gaulin
- *Data Analysis*: **J. Gaudet**, A.M. Hallas, B.D. Gaulin
- *Manuscript*: **J. Gaudet**, A.M. Hallas, B.D. Gaulin

Effect of chemical pressure on the crystal electric field states of erbium pyrochlore magnets

J. Gaudet,[1] A. M. Hallas,[1,*] A. I. Kolesnikov,[2] and B. D. Gaulin[1,3,4]
[1]Department of Physics and Astronomy, McMaster University, Hamilton, Ontario L8S 4M1, Canada
[2]Chemical and Engineering Materials Division, Oak Ridge National Laboratory, Oak Ridge, Tennessee 37831, USA
[3]Canadian Institute for Advanced Research, 661 University Ave., Toronto, Ontario, M5G 1M1, Canada
[4]Brockhouse Institute for Materials Research, Hamilton, Ontario L8S 4M1 Canada

(Received 25 July 2017; revised manuscript received 29 November 2017; published 17 January 2018)

We have carried out a systematic study of the crystal electric field excitations in the family of cubic pyrochlores $Er_2B_2O_7$ with $B =$ Ge, Ti, Pt, and Sn, using neutron spectroscopy. All members of this family are magnetic insulators based on $4f^{11}$ Er^{3+} and nonmagnetic B^{4+}. At sufficiently low temperatures, long-range antiferromagnetic order is observed in each of these $Er_2B_2O_7$ pyrochlores. The different ionic sizes associated with different nonmagnetic B^{4+} cations correspond to positive or negative chemical pressure, depending on the relative contraction or expansion of the crystal lattice, which gives rise to different local environments at the Er^{3+} site. Our results show that the g-tensor components are XY-like for all four members of the $Er_2B_2O_7$ series. However, the XY anisotropy is much stronger for $Er_2Pt_2O_7$ and $Er_2Sn_2O_7$ ($g_\perp/g_z > 25$) than for $Er_2Ge_2O_7$ and $Er_2Ti_2O_7$ ($g_\perp/g_z < 4$). The variation in the nature of the XY anisotropy in these systems correlates strongly with their ground states as $Er_2Ge_2O_7$ and $Er_2Ti_2O_7$ order into Γ_5 magnetic structures, whereas $Er_2Pt_2O_7$ and $Er_2Sn_2O_7$ order in the Γ_7 Palmer-Chalker structure.

DOI: 10.1103/PhysRevB.97.024415

I. INTRODUCTION

The cubic pyrochlore lattice is adopted by many magnetic materials with chemical composition $A_2B_2O_7$. This lattice is prone to magnetic frustration due to its architecture that consists of two interpenetrating networks of corner-sharing tetrahedra on which both the A^{3+} and the B^{4+} ions independently reside [1]. A peculiar attribute of the pyrochlore lattice is that the Ising axis and XY plane both are defined explicitly in a local, rather than global, coordinate frame. Ising spins on the pyrochlore lattice are constrained to point along the axis that connects the vertex of the tetrahedra to its center, termed the local $\langle 111 \rangle$ direction. Correspondingly, spins with XY anisotropy are constrained to lie in the plane perpendicular to the local $\langle 111 \rangle$ direction. Among the rare-earth pyrochlores, XY anisotropy is obtained when the A sublattice is occupied by either Er^{3+} or Yb^{3+}.

XY pyrochlores have the potential to exhibit a range of exotic magnetic phenomena [2]. Theoretical studies have shown that XY pyrochlores can stabilize various spin liquid states including the much sought-after quantum spin ice state. The quantum spin ice state is a $U(1)$ quantum spin liquid with magnetic excitations that can be mapped onto diffusive magnetic monopoles, such as in a classical spin ice but with emergent electric monopoles and photon excitations [3]. It has been proposed that quantum spin ice physics may lie at the origin of the continuum of low-energy spin excitations observed in $Yb_2Ti_2O_7$ [4]. Another interesting aspect of XY pyrochlore magnetism is the observation that order by disorder can affect their ground-state (g.s.) selection. Order by disorder is the phenomenology whereby a particular magnetic structure is selected due to its propensity to fluctuate, an entropic selection rather than a conventional energetic selection [5,6]. Order by disorder is known to favor the magnetic ground state observed in $Er_2Ti_2O_7$ [7–11] but appears to act in conjunction with an energetic selection mechanism that originates from virtual crystal field processes [12–14]. The effect of quenched disorder on the magnetism of XY pyrochlores has also been of significant interest and in many cases is found to have a profound impact on the low-temperature magnetism [15–21].

Underpinning the remarkable physics of the XY pyrochlores is the highly anisotropic nature of their exchange interactions. Classical calculations using an anisotropic exchange Hamiltonian have shown that several different ordered magnetic ground states exist within a narrow subspace of exchange parameters that are relevant to known XY pyrochlore magnets. This has led to theoretical proposals that competition between phases could account for many of their observed magnetic properties [22,23]. Experimentally, evidence for phase competition indeed is found within the $Er_2B_2O_7$ family of XY pyrochlores. Both $Er_2Ti_2O_7$ and $Er_2Ge_2O_7$ order into the $k = 0$ Γ_5 manifold at $T_N = 1.2$ and 1.4 K, respectively [7,24] but in a pure ψ_2 state for the former [25] and likely a pure ψ_3 state for the latter [24]. Meanwhile, both $Er_2Pt_2O_7$ and $Er_2Sn_2O_7$ order into the $k = 0$ Γ_7 manifold with significantly lower ordering temperatures at $T_N = 0.3$ and 0.1 K, respectively [26,27]. This state, the so-called Palmer-Chalker state, is stabilized for XY dipolar magnets with weak and isotropic exchange interactions [28]. The experimentally determined anisotropic exchange couplings for these two Γ_7 magnets place them in close proximity to the classical phase boundary with Γ_5

---

[*] Present address: Rice Center for Quantum Materials, Houston, TX 77005-1827, USA.

[26,27,29]. The magnetic structures observed within the family of erbium pyrochlores where only the nonmagnetic B-site ion is varied are all ones that exist in the computed anisotropic exchange phase diagram [23]. It is therefore interesting to uncover the microscopic origin of the changing magnetic ground states across this family that results from changing the nonmagnetic B-site cation. To carry out such a detailed study, a key starting point is the precise determination of the spin anisotropy that originates from single-ion physics.

In this paper, we study the single-ion properties of the four erbium pyrochlores within this family $Er_2Ge_2O_7$, $Er_2Ti_2O_7$, $Er_2Pt_2O_7$, and $Er_2Sn_2O_7$. We measure their crystal electric field excitations using neutron spectroscopic techniques. The analysis of these measurements allows us to determine the full crystal electric field (CEF) Hamiltonian for each member of this family. We find that the Er^{3+} moments in all four members possess XY-like anisotropy, but the strength of this anisotropy varies significantly across the family. We then show that the degree of XY anisotropy of the Er^{3+} moments correlates strongly with the precise magnetic ground state that is selected.

II. CRYSTAL FIELD CALCULATION

The magnetism in the $Er_2B_2O_7$ pyrochlores originates from the Er^{3+} ions that possess a [Xe]$4f^{11}$ electronic configuration. Using Hund's rules, the total angular momentum of the spin-orbit ground state is $J = \frac{15}{2}$ with $L = 6$ and $S = \frac{3}{2}$. This spin-orbit ground state is $2J + 1 = 16$-fold degenerate in the absence of the crystal electric field. The neighboring ions, primarily the O^{2-} that surround the Er^{3+} ions, generate the CEF, which acts on an energy scale of approximately 100 meV. Note that for Er^{3+} the first-excited spin-orbit manifold is separated from the spin-orbit ground state by $\lambda J \approx 2.5$ eV [30]. Thus, for the Er^{3+} pyrochlores, we need not consider the higher-J multiplets in our CEF analysis. This is in contrast to systems with Ce^{3+} or Pr^{3+}, where λJ is an order of magnitude smaller and the inclusion of higher-order multiplets is necessary to obtaining an accurate description of their CEF schemes [31].

The form of the CEF Hamiltonian depends on the point-group symmetry at the Er^{3+} site, which has twofold and threefold rotation axes as well as an inversion symmetry with respect to the local $\langle 111 \rangle$ axis. These symmetry operations result in a D_{3d} point-group symmetry. Using the Steven's operator formalism, the CEF Hamiltonian for the D_{3d} point-group symmetry can be written as follows [32–35]:

$$\begin{aligned}\mathcal{H}_{\mathrm{CEF}} &= A_2^0\alpha_J\langle r^2\rangle\hat{O}_2^0 + A_4^0\beta_J\langle r^4\rangle\hat{O}_4^0\\ &\quad + A_4^3\beta_J\langle r^4\rangle\hat{O}_4^3 + A_6^0\gamma_J\langle r^6\rangle\hat{O}_6^0\\ &\quad + A_6^3\gamma_J\langle r^6\rangle\hat{O}_6^3 + A_6^6\gamma_J\langle r^6\rangle\hat{O}_6^6. \end{aligned} \tag{1}$$

The $\hat{O}_n^m$ are Steven's operators that are written in terms of J_+, J_-, and J_z operators [36]. The α_J, β_J, and γ_J are reduced matrix elements that have been calculated previously in Ref. [36]. The values for $\langle r^n \rangle$ are listed in Ref. [37] and consist of the expected value of the nth power of distance between a nucleus and the $4f$-electron shell. The 16 states of the spin-orbit ground state are split by the CEF into eight doublets, and these are protected from further degeneracy breaking by Kramers theorem. The CEF energy eigenvalues and eigenfunctions associated with these eight doublets are controlled by the crystal field parameters A_n^m, and these can be probed directly with inelastic neutron spectroscopy. The partial differential cross section for magnetic neutron scattering can be written as follows [38]:

$$\frac{d^2\sigma}{d\Omega\, dE'} = C\frac{k_f}{k_i}F^2(|Q|)S(|Q|,\hbar\omega), \tag{2}$$

where Ω is the scattered solid angle, E' is the final neutron energy, $\frac{k_f}{k_i}$ is the ratio of the scattered and incident momentum of the neutron, C is a constant, and $F(|Q|)$ is the magnetic form factor. The scattering function $S(|Q|,\hbar\omega)$ for a CEF transition is given by

$$S(|Q|,\hbar\omega) = \sum_{i,i'}\frac{\sum_\alpha |\langle i|J_\alpha|i'\rangle|^2 e^{-\beta E_i}}{\sum_j e^{-\beta E_j}}L(\Delta E + \hbar\omega), \tag{3}$$

where $\alpha = x, y, z$ and $L(\Delta E + \hbar\omega) = L(E_i - E_{i'} + \hbar\omega)$ is a Lorentzian function that ensures energy conservation as the neutron induces transitions between the CEF levels $i \to i'$, which possess a finite-energy width or lifetime.

In order to determine the CEF parameters A_n^m, we start with a particular set of A_n^m and diagonalize the CEF Hamiltonian to obtain a set of initial energy eigenvalues and eigenfunctions. In this paper, we used the A_n^m obtained for $Er_2Ti_2O_7$ from Ref. [39] as our starting CEF parameters. A least-squares refinement of the A_n^m values then is performed to minimize the difference between the calculated and the observed CEF spectra. This refinement considers both the energies of the transitions as well as their relative intensities.

III. EXPERIMENTAL DETAILS

The four erbium pyrochlore magnets were all studied in powder form. Large 10-g samples of both $Er_2Ti_2O_7$ and $Er_2Sn_2O_7$ were prepared via conventional solid-state synthesis [40]. $Er_2Ge_2O_7$ and $Er_2Pt_2O_7$ were prepared using a belt-type high-pressure apparatus, yielding 2.8- and 1.1-g samples, respectively. The details of the high-pressure synthetic method employed are given in Ref. [41] for $Er_2Ge_2O_7$ and in Ref. [42] for $Er_2Pt_2O_7$.

Powder neutron diffraction was carried out on each of the four samples using the time-of-flight diffractometer POWGEN at the Spallation Neutron Source at Oak Ridge National Laboratory [43]. The samples were sealed in vanadium cans in the presence of a helium atmosphere and were each measured for 1 h at 10 K. These measurements were performed with a median wavelength of $\lambda = 1.066$ Å. This configuration allows for momentum transfers between $1.2\ \text{Å}^{-1} < Q < 22.8\ \text{Å}^{-1}$. Rietveld refinements of the data were carried out using the FULLPROF [44] software suite.

The inelastic neutron-scattering measurements were performed using the direct geometry time-of-flight chopper spectrometer SEQUOIA at the Spallation Neutron Source [45]. Each sample was measured at two temperatures (5 and 100 K) and three incident neutron energies (25, 90, and 150 meV). For all incident neutron energies, the fine Fermi chopper was used to achieve the maximum energy

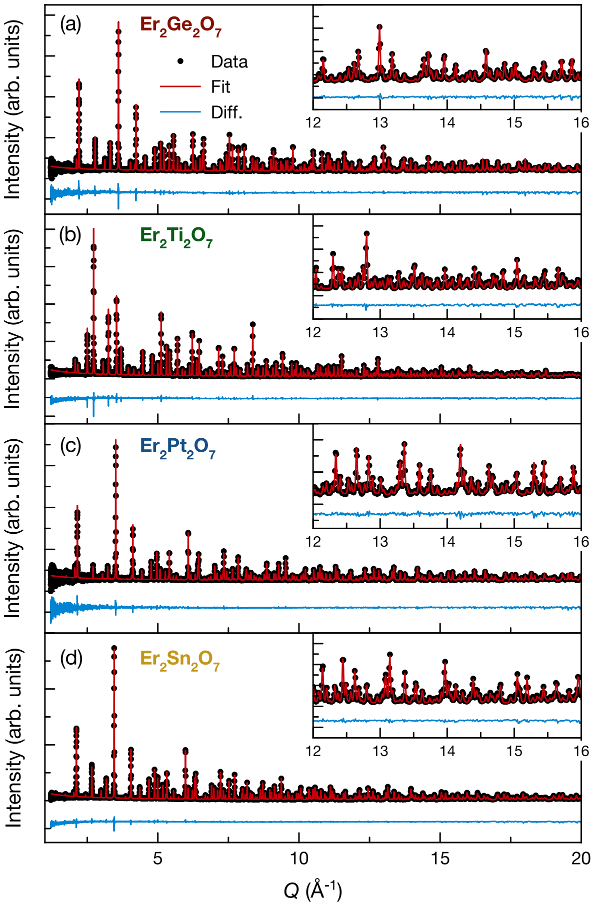

FIG. 1. Rietveld refinements of the time-of-flight neutron powder-diffraction patterns for each of the erbium pyrochlore magnets $Er_2B_2O_7$, B = (a) Ge, (b) Ti, (c) Pt, and (d) Sn. The data sets were collected at 10 K using Bank 2 of the POWGEN diffractometer ($\lambda_{\text{center}} = 1.066$ Å). The data were refined against the $Fd\bar{3}m$ space group, and the goodness-of-fit parameters for each sample are given in Table I. The insets show an expanded view of a high-Q region from 12 to 16 Å^{-1}.

resolution, corresponding to 1–2% of the neutron's initial energy E_i. The resultant energy resolution at the elastic line is $\Delta E = 0.45$ meV for $E_i = 25$ meV, $\Delta E = 1.5$ meV for $E_i = 90$ meV, and $\Delta E = 2.8$ meV for $E_i = 150$ meV. The energy resolution improves as a function of energy transfer and at 80% E_i reaches a value that is approximately one-third of the elastic resolution. The samples were packed in aluminum cans in annular geometry and sealed with indium in the presence of a helium atmosphere. An identical empty can also was measured, and this served as a background where all the data presented have had the empty can data set subtracted from them. The inelastic neutron-scattering data were reduced using MANTID [46] and were analyzed using DAVE [47].

IV. RESULTS AND ANALYSIS

A. Structural refinement by powder neutron diffraction

In order to characterize the structural properties of each of the four erbium pyrochlore magnets, we performed time-of-flight powder neutron diffraction. The data were analyzed by Rietveld refinement using the $Fd\bar{3}m$ space group as shown in Fig. 1. The fitted parameters resulting from these refinements are summarized in Table I. The largest structural differences going across this series arise from the substitution of the nonmagnetic B site. Indeed the cubic lattice parameter a is observed to vary linearly with the ionic radius of the B-site cation. Thus, $Er_2Ge_2O_7$, which has the smallest B-site cation, has a lattice parameter of $a = 9.87(5)$ Å, whereas $Er_2Sn_2O_7$ with the largest B site has a lattice parameter of $a = 10.30(1)$ Å. Across the whole series, the lattice parameter varies by 4%. It is interesting to note that the two middle members, $Er_2Ti_2O_7$ and $Er_2Pt_2O_7$, have the most similar B-site radii and correspondingly, the most similar lattice parameters, varying by only 0.7%. $Er_2Pt_2O_7$, however, is a unique member of this family due to the fact that platinum, unlike the other nonmagnetic B-site ions, does not have a closed electron shell configuration. Platinum in its 4+ oxidation state has a [Xe]$5d^6$ electron configuration, which is nonmagnetic due to the filled t_{2g} levels and sizable gap to the empty e_g levels.

In the cubic pyrochlore structure, erbium sits at the 16d Wyckoff position and is surrounded by a distorted cube of oxygen anions. This distortion acts along the local $\langle 111 \rangle$ direction, compressing the cube along the body diagonal. Thus, there are two equivalent Er-O1 bonds and six equivalent Er-O2 bonds. The degree of this distortion is characterized by the O1 x coordinate, which is the only adjustable parameter in the pyrochlore structure. An oxygen environment taking up a perfect cube would have $x = 0.375$, and the distortion grows

TABLE I. Summary of fitted structural parameters for the erbium pyrochlore magnets as determined by Rietveld refinement of their powder neutron-diffraction patterns measured at 10 K. The variance in the cubic lattice parameter a is controlled largely by the radius of the B-site cation. The only adjustable atomic coordinate within the pyrochlore ($Fd\bar{3}m$) structure is the x position of the apical oxygens (O1). The four entries of the final columns give the goodness-of-fit parameters for the Rietveld refinements, which are shown in Fig. 1.

	B (Å)	a (Å)	O1 x	Er-O1 (Å)	Er-O2 (Å)	$\frac{\text{Er-O2}}{\text{Er-O1}}$(%)	R_p (%)	R_{wp} (%)	R_{exp} (%)	χ^2
$Er_2Ge_2O_7$	0.67	9.87(5)	0.327	2.442	2.136	0.875	5.4	4.0	1.6	6.5
$Er_2Ti_2O_7$	0.745	10.05(3)	0.330	2.463	2.176	0.883	7.7	6.8	1.7	15.8
$Er_2Pt_2O_7$	0.765	10.13(2)	0.340	2.416	2.193	0.908	4.6	2.8	1.6	3.0
$Er_2Sn_2O_7$	0.83	10.30(1)	0.338	2.470	2.230	0.903	8.0	7.2	1.9	14.6

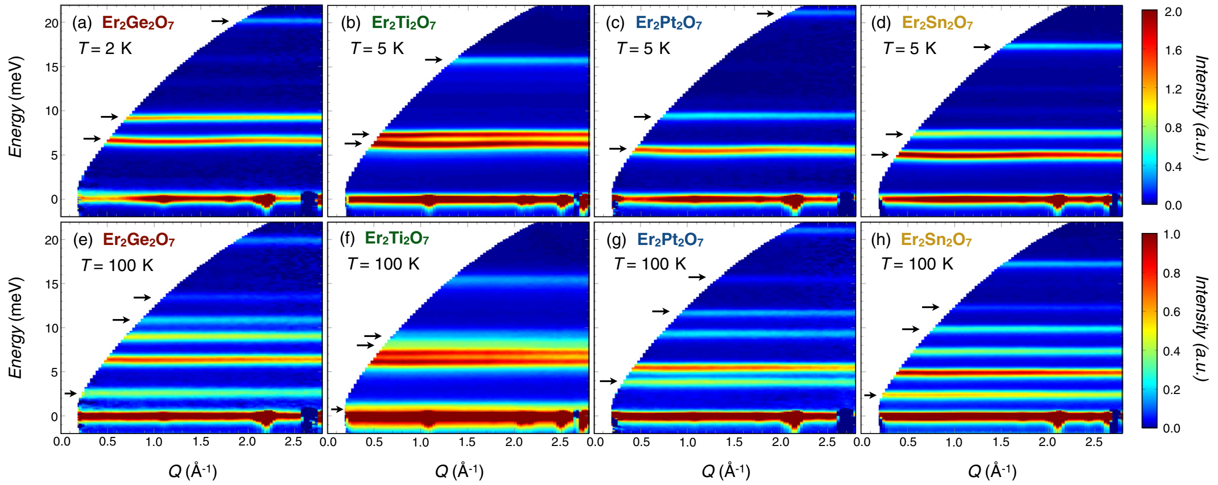

FIG. 2. Inelastic neutron-scattering measurements with an incident energy of $E_i = 25$ meV for the $Er_2B_2O_7$ pyrochlores, $B =$ (a) and (e) Ge, (b) and (f) Ti, (c) and (g) Pt, and (d) and (h) Sn. The top row shows the spectra at a base temperature (2 or 5 K) for each sample. In each case, three ground-state crystal electric field excitations are identified at the positions indicated by the arrows. The bottom row shows the spectra at 100 K, which is high enough to thermally populate transitions from the first and second-excited-state levels. The excited-state transitions at 100 K are indicated by the arrows. An empty can measurement has been subtracted from all data sets.

with the deviation from this value. The distortion from an ideal cubic environment can alternatively be parametrized by the ratio of the Er-O1 and Er-O2 bond lengths as tabulated in Table I. The most distorted erbium oxygen environment occurs in $Er_2Ge_2O_7$, and the least distorted environment occurs in $Er_2Pt_2O_7$. Aside from $Er_2Pt_2O_7$, this distortion scales linearly with lattice parameter. Lastly, it is worth mentioning that the erbium oxygen bond distances are generally the shortest in $Er_2Ge_2O_7$ ($\langle$Er-O$\rangle = 2.21$ Å) and the largest in $Er_2Sn_2O_7$ ($\langle$Er-O$\rangle = 2.29$ Å).

B. Determination of the crystal field Hamiltonian with inelastic neutron scattering

The CEF spectra of the four erbium pyrochlore magnets were measured with inelastic neutron scattering. Data sets employing incident energies of 25 and 150 meV were collected at $T = 2$ or 5 K for all samples and are shown in the upper panels of Figs. 2 and 3. As CEF excitations are single-ion properties, they largely lack dispersion and decrease in intensity as a function of momentum transfer ($|\vec{Q}|$) following the magnetic form factor of Er^{3+}. From these criteria, it is

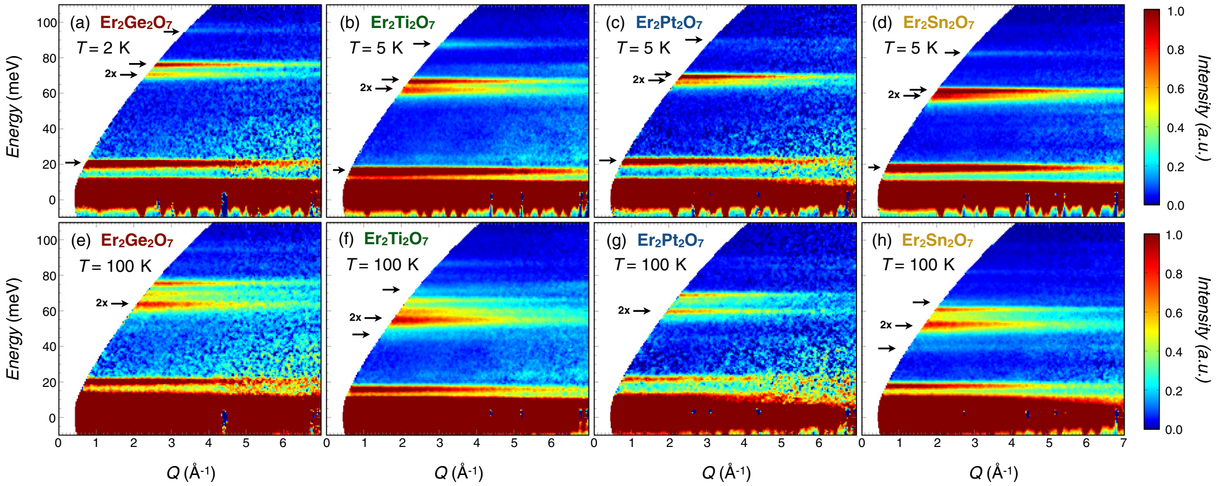

FIG. 3. Inelastic neutron-scattering measurements with an incident energy of $E_i = 150$ meV for the $Er_2B_2O_7$ pyrochlores, $B =$ (a) and (e) Ge, (b) and (f) Ti, (c) and (g) Pt, and (d) and (h) Sn. The top row shows the spectra at a base temperature (2 or 5 K) for each sample. In each case, four higher-energy ground-state crystal electric field excitations are identified at the positions indicated by the arrows in addition to the transition at ~ 20 meV, which also was seen in the $E_i = 25$-meV data set. The bottom row shows the spectra at 100 K, which is high enough to thermally populate transitions from the first- and second-excited-state levels. The excited-state transitions at 100 K are indicated by the arrows. An empty can measurement has been subtracted from all data sets.

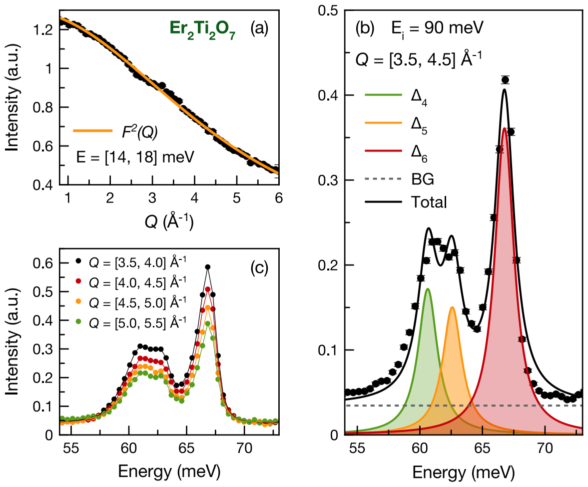

FIG. 4. (a) The $|\vec{Q}|$ dependence of the 15.7-meV CEF excitation of $Er_2Ti_2O_7$ is well captured by the single-ion magnetic form factor of Er^{3+}. The same $|\vec{Q}|$ dependence is observed for all the CEF excitations resolved in this paper. (b) The neutron-scattering intensity as a function of energy transfer for $Er_2Ti_2O_7$, revealing the presence of three CEF excitations over the energy range shown. An example of a fit to the CEF spectra is shown. The fit captures the integrated intensity for all three CEF excitations and was used to optimize the CEF Hamiltonian. (c) The $|\vec{Q}|$ dependence associated with the Er^{3+} magnetic form factor can also be seen by performing energy cuts of the data with integrations over different $|\vec{Q}|$ ranges.

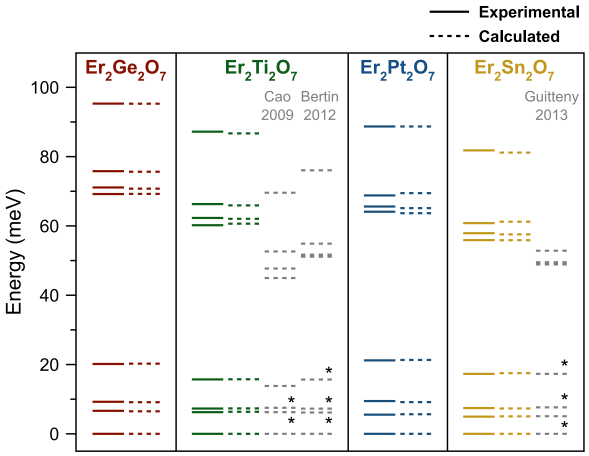

FIG. 5. Comparison between the experimentally resolved CEF energy schemes of the four erbium pyrochlore magnets and those calculated using the CEF Hamiltonians given in Table II. The calculated CEF spectra for $Er_2Ti_2O_7$ [39,48] and $Er_2Sn_2O_7$ [29] derived from previous studies also are compared to our experimental data and are given by the gray dashed lines where asterisks mark the levels that were fit.

clear that the $E_i = 25$-meV data sets at base temperatures in Figs. 2(a)–2(d) each show three CEF excitations as indicated by the black arrows. For example, $Er_2Ti_2O_7$ has CEF excitations at 6.3, 7.3, and 15.7 meV. An example of the $|\vec{Q}|$ dependence of the CEF scattering is shown in Fig. 4(a) for the 15.7-meV excitation in $Er_2Ti_2O_7$ where the solid line corresponds to the magnetic form factor of Er^{3+}. All other CEF transitions observed in this paper follow a similar $|\vec{Q}|$ dependence. As will be discussed later, it is interesting to note that the lack of dispersion of the low-energy CEF excitations is not complete. Weak dispersion in the lowest-energy levels develops at low temperatures as a consequence of exchange coupling between the Er^{3+} moments.

For each of the erbium pyrochlores studied in this paper, the energy of the first CEF excitation is ~6 meV above the ground state. As these measurements were performed at $T = 2$ or 5 K, this first-excited state cannot be significantly thermally populated, and thus all observed CEF excitations necessarily originate from the CEF ground state. As previously discussed, the lowest-energy manifold for Er^{3+} with $J = 15/2$ is composed of eight doublets, one of which is the ground state. Thus, to resolve the full CEF manifold requires the identification of a total of seven transitions. Turning our attention to the base temperature $E_i = 150$-meV data sets shown in Figs. 3(a)–3(d), three additional CEF transitions clearly are observed for all samples as indicated by the black arrows. For example, $Er_2Ti_2O_7$ has CEF transitions at 61.0, 66.3, and 87.2 meV. From our analysis thus far, we can account for three CEF levels below 20 meV and three additional CEF levels between 50 and 100 meV.

As seven transitions are required to fully determine the energy scheme of the CEF manifold, there is a final CEF excitation that is not immediately resolved in the $E_i = 25$- and $E_i = 150$-meV data sets. However, inelastic neutron-scattering spectra collected with an incident energy of 90 meV allow us to resolve the missing CEF level. For $Er_2Ti_2O_7$, the level centered near 61.0 meV as shown in Fig. 4(b) is, in fact, two closely spaced CEF transitions that were unresolvable using higher incident energy with corresponding lower-energy resolution. Figure 4(c) shows the decreasing intensity of these two peaks as a function of momentum transfer, confirming that both features are magnetic in origin and, thus, CEF excitations. The corresponding CEF level in each of the Er pyrochlore magnets is split by a similar amount. With this final CEF transition now accounted for, the entire CEF manifold is known and is presented in Fig. 5 for the four samples probed in this paper.

Our experimentally deduced CEF scheme can be compared to the CEF Hamiltonians previously derived for $Er_2Ti_2O_7$ [39,48] and $Er_2Sn_2O_7$ [29]. Using the parametrization from these previous works we have computed the CEF energy schemes, which also are presented by the dashed gray lines in Fig. 5. By comparing with our new results, it is clear that the previous CEF Hamiltonians do not reproduce well the high-energy CEF levels. Thus, a new refinement of the CEF Hamiltonians was performed for $Er_2Ti_2O_7$ and $Er_2Sn_2O_7$ as well as for $Er_2Ge_2O_7$ and $Er_2Pt_2O_7$ for which no previous CEF Hamiltonian has been derived. In this paper, it is now possible to rigorously constrain the CEF Hamiltonian because the full spin-orbit ground-state manifold has been determined experimentally. This is in contrast to previous works that only considered the low-energy excited states. To execute the fitting procedure, integrations of the scattered intensity as a

TABLE II. The refined CEF parameters A_n^m obtained for all four erbium pyrochlore magnets studied in this paper.

(All in meV)	A_2^0	A_4^0	A_4^3	A_6^0	A_6^3	A_6^6
$Er_2Ge_2O_7$	39.3	36.2	275	1.23	−19.10	26.6
$Er_2Ti_2O_7$	37.5	33.5	282	1.25	−17.15	21.6
$Er_2Pt_2O_7$	49.0	31.2	262	1.10	−19.15	24.6
$Er_2Sn_2O_7$	50.8	28.4	266	1.10	−17.15	20.9

function of energy transfer between $Q = 2.3$ and 2.8 Å^{-1} for the $E_i = 25$-meV data set and $Q = 3.6$ to 4.6 Å^{-1} for the $E_i = 150$-meV data set have been extracted from the base temperature contour maps of Figs. 2 and 3. The energy of each CEF level was determined by fitting the transition with a Lorentzian function for which the area represents the relative scattered intensity of the particular CEF transition. The relative intensities of the CEF transitions measured with 25, 90, and 150 meV were normalized to each other using the third-excited CEF state which appeared in all data sets (for example, the CEF at 20.2 meV for $Er_2Ge_2O_7$). In this manner, the CEF Hamiltonian was constrained using the energies of all transitions and their relative scattered intensities, giving a total of 13 constraints for each of the four erbium pyrochlore magnets studied.

Using the extracted experimental constraints, the CEF Hamiltonian was first diagonalized using the CEF parameters of Bertin *et al.* derived for $Er_2Ti_2O_7$ [39]. A broad scan of the CEF parameters around this particular solution was performed to minimize the χ^2 value between the calculated and the experimental CEF schemes, which considers both the energies of the transitions as well as their relative intensities. Very good agreement was obtained for all samples using the appropriate CEF parameters presented in Table II. The results of this optimization procedure are presented in Table III where the computed energies and intensities are compared to the experimental values. The resulting χ^2 of our calculation is equal to 1.3, 2.6, 2.3, and 3.2 for $Er_2Ge_2O_7$, $Er_2Ti_2O_7$, $Er_2Pt_2O_7$, and $Er_2Sn_2O_7$, respectively. To better appreciate the results of the fitting procedure, the entire neutron-scattering spectra were computed between 0 and 120 meV using the CEF parameters of Table II with the addition of a sloping background to account for the phonon contribution. The resulting theoretical calculation is compared to the data in Fig. 6 for the four erbium pyrochlore samples. Excellent agreement between the calculated and the measured scattering spectra is observed with no significant differences, validating the goodness of the fits.

To further scrutinize the quality of our CEF Hamiltonian parameters, inelastic neutron-scattering spectra were collected at a temperature of 100 K using both $E_i = 25$ and $E_i = 150$ meV, which is shown in the bottom panels of Figs. 2 and 3. The increase in temperature from 5 to 100 K produces new CEF excitations that originate from the increasing thermal population of the first- and second-excited CEF states. The new (relative to low-temperature) low-energy CEF excitations are indicated by the black arrows in the bottom panels of Fig. 2. For example, new transitions are observed at 1.1, 8.4, and 9.5 meV in $Er_2Ti_2O_7$ at 100 K. These originate from transitions between the first- and the second-excited CEF states, the first- and the third-excited CEF states, and the second- and the third-excited CEF states. For the 100 K high-energy spectra shown in Fig. 3, multiple new CEF excitations are observed between 40 and 100 meV. These also correspond to transitions from the first- and second-excited CEF states to higher-energy CEF states. The prominent new CEF transitions are indicated by black arrows in the bottom panels of Fig. 3.

Using Eq. (2), we can compute the predicted inelastic-scattering spectra at 100 K using the CEF parameters derived from our base temperature fits, given in Table II. The resulting

TABLE III. Tables giving the experimental and calculated values of the seven CEF excited-state energies as well as the relative scattered intensities. The relative scattered intensity has been normalized by the intensity of the transition between the CEF ground state and the first-excited state.

	$Er_2Ge_2O_7$					$Er_2Ti_2O_7$			
	E_{exp} (meV)	E_{calc} (meV)	I_{exp} (a.u.)	I_{calc} (a.u.)		E_{exp} (meV)	E_{calc} (meV)	I_{exp} (a.u.)	I_{calc} (a.u.)
1	6.6(1)	6.5	1	1	1	6.3(1)	6.4	1	1
2	9.3(1)	9.1	0.65(5)	0.57	2	7.3(1)	7.3	0.75(5)	0.88
3	20.2(1)	20.3	0.20(3)	0.24	3	15.7(1)	15.7	0.20(5)	0.3
4	69.2(3)	69.2	0.04(3)	0.04	4	60.2(3)	60.6	0.04(2)	0.07
5	71.1(3)	70.8	0.04(3)	0.04	5	62.3(3)	62.0	0.04(2)	0.05
6	75.8(3)	75.6	0.10(2)	0.14	6	66.3(3)	65.9	0.09(2)	0.13
7	95.3(4)	95.3	0.015(5)	0.03	7	87.2(4)	86.7	0.01(1)	0.04

	$Er_2Pt_2O_7$					$Er_2Sn_2O_7$			
	E_{exp} (meV)	E_{calc} (meV)	I_{exp} (a.u.)	I_{calc} (a.u.)		E_{exp} (meV)	E_{calc} (meV)	I_{exp} (a.u.)	I_{calc} (a.u.)
1	5.5(1)	5.7	1	1	1	5.0	5.0	1	1
2	9.5(1)	9.1	0.29(5)	0.33	2	7.4(1)	7.3	0.36(5)	0.43
3	21.2(1)	21.3	0.21(5)	0.28	3	17.3(1)	17.5	0.24(5)	0.3
4	64.1(3)	63.7	0.04(2)	0.03	4	55.9(3)	55.8	0.04(2)	0.04
5	65.6(3)	65.1	0.06(2)	0.06	5	57.9(3)	57.5	0.06(2)	0.07
6	68.8(3)	69.5	0.12(2)	0.16	6	66.8(3)	61.2	0.10(2)	0.2
7	88.7(4)	88.7	0.01(1)	0.02	7	81.8(4)	81.1	0.02(1)	0.02

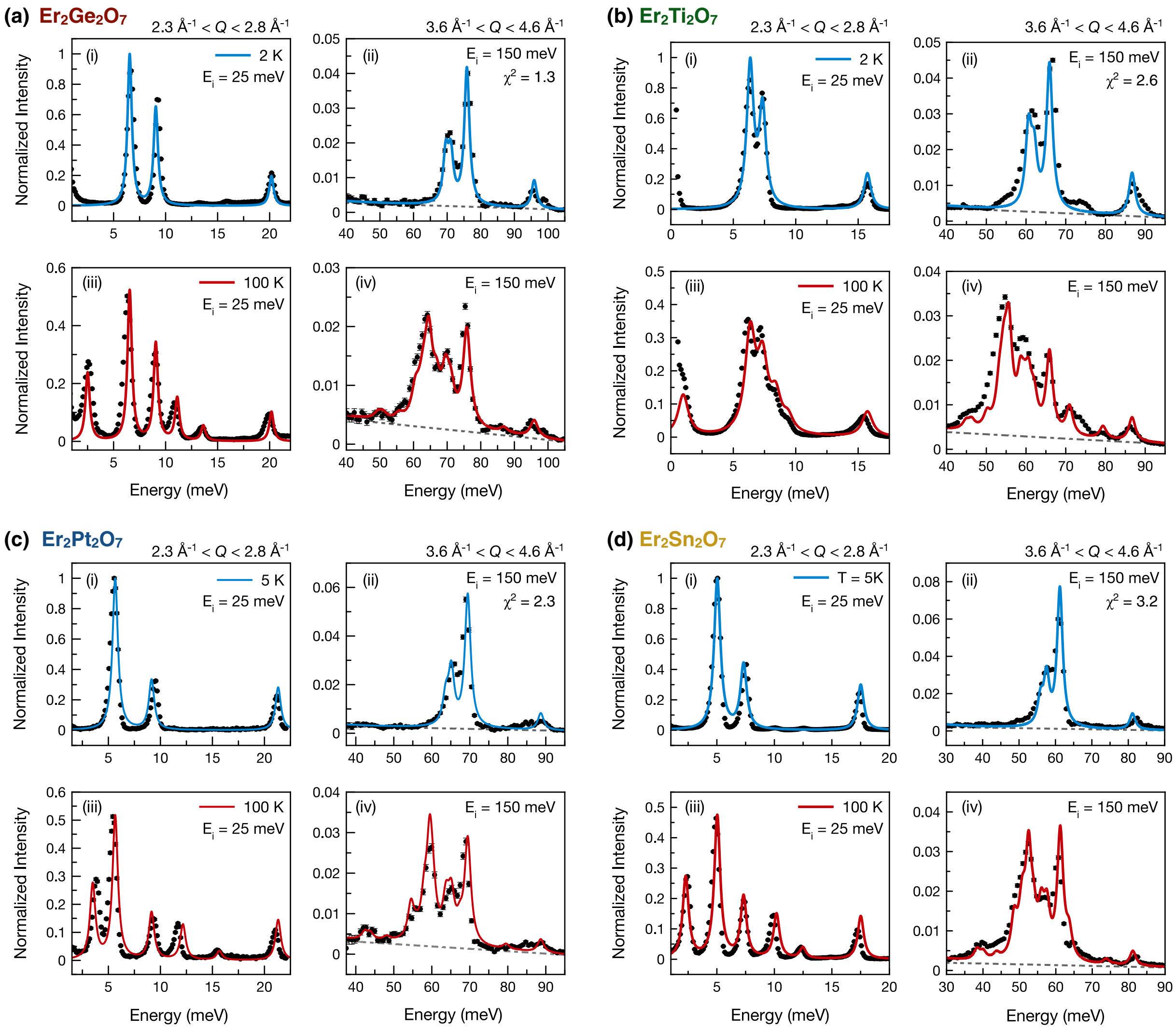

FIG. 6. Inelastic neutron spectra for (a) $Er_2Ge_2O_7$, (b) $Er_2Ti_2O_7$, (c) $Er_2Pt_2O_7$, and (d) $Er_2Sn_2O_7$ showing the scattering intensity as a function of energy transfer at base temperature [(i) $E_i = 25$ meV and (ii) $E_i = 150$ meV] and 100 K [(iii) $E_i = 25$ meV and (iv) $E_i = 150$ meV]. These data sets are extrated from the contour maps of Figs. 2 and 3 with the indicated integration in momentum transfer $|\vec{Q}|$. The calculated CEF spectra, using the CEF Hamiltonian parameters shown in Table II, are plotted by the blue ($T = 2$ and 5 K) and red ($T = 100$ K) lines.

calculations can be compared with the experimental data by performing cuts in energy integrated over the same range in $|\vec{Q}|$ as previously performed on the base temperature data sets. A sloping background has been added to the calculation to account for the increased phonon contribution. The comparison between the theoretical curves and the experimental data at 100 K are shown in Fig. 6 for all four samples. The computed spectra are entirely consistent with the experimental data, demonstrating that our CEF Hamiltonian fits are well constrained and further validating the quality of the fit. Note that by comparing the 2- and 100-K experimental spectra, slight negative energy shifts of the CEF transitions originating from the CEF ground state are observed upon raising the temperature. Such softening of the CEF excitations also has been observed in other rare-earth pyrochlore systems [49], and this is due to lattice expansion that occurs on raising the temperature, which in turn reduces the strength of the electric field at the Er^{3+} position.

As briefly alluded to earlier, our neutron-scattering results reveal that the lowest-energy CEF excitations in the erbium pyrochlores do not have a perfectly flat dispersion. To illustrate this effect, an enhanced view on the lowest-energy CEF excitations of $Er_2Ti_2O_7$ measured with $E_i = 25$ meV is shown in Fig. 7(a). This reveals weak dispersion for the CEF excitation at 6.25 meV and possibly for the CEF excitation at 7.3 meV. When the temperature is increased to $T = 100$ K, this dispersion disappears as shown in Fig. 7(b). To quantify the dispersion, we performed integrations along different $|\vec{Q}|$ values with a width of 0.1 Å^{-1}. For every integration, we determined the positions of the low-energy CEF excitations by fitting their line shapes

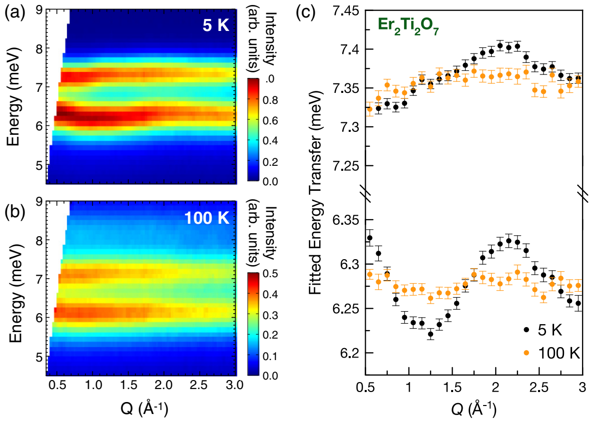

FIG. 7. An enhanced view of the lowest-energy crystal electric field levels in $Er_2Ti_2O_7$ at (a) 5 K and (b) 100 K, revealing weak dispersion. (c) The maximum fitted intensity of these two CEF excitations as a function of $|\vec{Q}|$ at both 5 and 100 K.

to a Gaussian function. The fitted centers of the Gaussian are plotted as a function of $|\vec{Q}|$ in Fig. 7(c) for both 5 and 100 K. At 5 K, the 6.25-meV CEF excitation has a minimum in energy at $|\vec{Q}| \sim 1.1$ Å^{-1}, which corresponds to the range of $|\vec{Q}|$ where the (111) magnetic Bragg peak develops below $T_N = 1.2$ K in $Er_2Ti_2O_7$. The bandwidth of the dispersion of the 6.25-meV CEF excitation is 0.10(5) meV at 5 K and perhaps slightly less for the CEF excitation near 7.3 meV. Weak dispersion also is observed for the first- and second-excited CEF levels of the three other erbium pyrochlores probed in this paper. The shape of the dispersion as well as its suppression at high temperatures are similar throughout the family. The origin of this weak dispersion is likely exchange interactions that lead to enhanced intersite correlations at low temperatures. Similar effects are observed in terbium pyrochlores for which the lowest-lying CEF excitations, located near 1 meV, display intense dispersion relative to their mean energy [50,51].

V. DISCUSSION

With their CEF Hamiltonians in hand, it is interesting to analyze the evolution of the single-ion properties going across the erbium pyrochlore series. The composition of the CEF ground-state doublet and the associated g-tensor components for each of the $Er_2B_2O_7$ materials are shown in Table IV. Across the family, the compositions of the ground-state doublets are qualitatively similar and consist of a mixture of $J_z = |\pm\frac{13}{2}\rangle, |\pm\frac{7}{2}\rangle, |\pm\frac{1}{2}\rangle, |\mp\frac{5}{2}\rangle, |\mp\frac{11}{2}\rangle$. In each case, the ground-state doublet has local XY-like anisotropy because the g tensor perpendicular to the local $\langle 111\rangle$ ($g_\perp$) is larger than the parallel (g_z) component. However, the strength of the local XY anisotropy is an order of magnitude smaller for $Er_2Ge_2O_7$ and $Er_2Ti_2O_7$ than it is for $Er_2Pt_2O_7$ and $Er_2Sn_2O_7$. This result suggests that the change in the g-tensor anisotropy going across the family could underly the stabilization of different magnetically ordered states. Indeed, both $Er_2Ge_2O_7$ and $Er_2Ti_2O_7$ order into the $k = 0$ Γ_5 manifold [24,25] and possess relatively weak XY anisotropy. In contrast, both $Er_2Pt_2O_7$ and $Er_2Sn_2O_7$ order into the $k = 0$ Γ_7 manifold [26,27] and possess strong XY anisotropy.

To examine such a hypothesis, we can refer to the anisotropic exchange phase diagram of Ref. [52], where the four exchange couplings are labeled J_{zz}, $J_\pm$, $J_{\pm\pm}$, and $J_{z\pm}$. The classical phase boundary between the Γ_5 and the Γ_7 states occurs at a critical ratio of $\frac{J_{\pm\pm}}{J_\pm} = 2$. Above this value, the predicted ground state is Γ_7, and below this value, the predicted ground state is Γ_5 [52]. Interestingly, both $J_{\pm\pm}$ and $J_\pm$ are proportional to $g_\perp^2$ [29], and thus, the ratio of $\frac{J_{\pm\pm}}{J_\pm}$ should not, strictly speaking, depend on the g-tensor anisotropy. This would then suggest that the transition in the magnetic ground state across the erbium pyrochlore family is driven by changes in the details of the orbital overlap and not the single-ion properties. Related to this point, it is interesting to note that the oxygen environment derived from our powder neutron analysis reveals a more cubic environment for $Er_2Pt_2O_7$ and $Er_2Sn_2O_7$ as compared to $Er_2Ge_2O_7$ and $Er_2Ti_2O_7$. This may indicate a more isotropic exchange interaction for the two former materials, consistent with recent estimates of their exchange parameters [26,27,29]. Nonetheless, the two members of the erbium pyrochlore family that order into the Palmer-Chalker state also show extreme XY anisotropy, very small g_z, suppressed T_N, and a more cubic local environment around the Er^{3+} site as compared with the two members that order into Γ_5 states.

This study of the erbium pyrochlores has resolved all possible CEF excitations within the lowest-energy J multiplet, an analysis that has not been achieved for any other titanate pyrochlore besides $Yb_2Ti_2O_7$ [49], which has only three excited levels. Furthermore, as Er^{3+} is a Kramers ion, the assignment of each CEF level as a doublet is unambiguous, in contrast to non-Kramers $Tb_2Ti_2O_7$ and $Ho_2Ti_2O_7$. It is therefore informative to use a scaling argument to approximate the CEF schemes for other pyrochlore magnets based on our comprehensive results. As the titanates are the best studied family of insulating

TABLE IV. The composition of the CEF ground-state doublet for the four erbium pyrochlore magnets studied in this paper. The calculated components of the g tensor perpendicular ($g_\perp$) and parallel (g_z) to the local $\langle 111\rangle$ axis also are shown along with their ratio $g_\perp/g_z$ and the calculated moment (μ_{cef}). The experimentally determined magnetic g.s. and its associated magnetic moment (μ_{ord}) obtained via powder neutron diffraction also are given for each erbium pyrochlore.

	$\lvert\pm 13/2\rangle$	$\lvert\pm 7/2\rangle$	$\lvert\pm 1/2\rangle$	$\lvert\mp 5/2\rangle$	$\lvert\mp 11/2\rangle$	$g_\perp$	g_z	$g_\perp/g_z$	μ_{cef} (μ_B)	μ_{ord} (μ_B)	T_N (K)	g.s.
$Er_2Ge_2O_7$	0.395	0.338	−0.521	−0.176	0.653	7.0(6)	2.1(4)	3.3	3.6	3.23(6)	1.4	Γ_5 [24]
$Er_2Ti_2O_7$	0.389	0.257	−0.491	−0.082	0.732	6.3(5)	3.9(5)	1.6	3.7	3.25(9)	1.2	Γ_5 [25]
$Er_2Pt_2O_7$	0.381	0.439	−0.563	−0.280	0.516	7.7(6)	0.30(7)	28	3.9	3.4(2)	0.3	Γ_7 [26]
$Er_2Sn_2O_7$	0.541	0.244	−0.578	−0.413	0.379	7.6(7)	0.14(5)	54	3.8	3.1	0.1	Γ_7 [27]

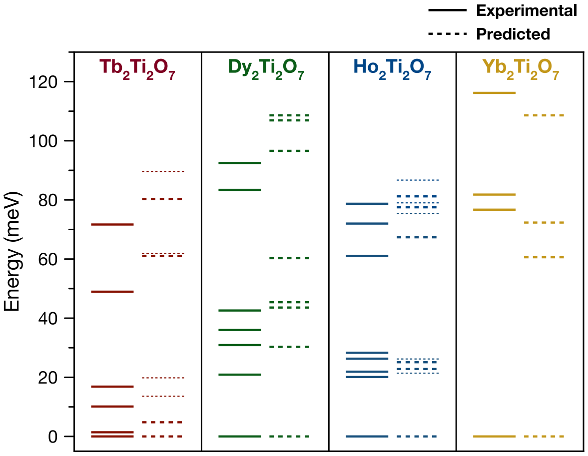

FIG. 8. Calculated CEF schemes for the rare-earth titanates $A_2Ti_2O_7$ (A = Tb, Dy, Ho, and Yb) obtained using scaling arguments from our fitted parameters for $Er_2Ti_2O_7$. The calculated levels are indicated by the dashed lines where, for $Tb_2Ti_2O_7$ and $Ho_2Ti_2O_7$, the singlet levels are denoted by a lighter dashed line. The experimentally determined CEF energies, reproduced from Refs. [49,54,55], are given by the solid lines.

rare-earth pyrochlores, we have focused on approximating the CEF schemes for $A_2Ti_2O_7$ (A = Tb, Dy, Ho, and Yb) starting from the parameters obtained for $Er_2Ti_2O_7$. The scaling argument that connects the CEF parameters $A_n^m(R)$ between different rare-earth-based pyrochlores is given by the following [32]:

$$A_n^m(R') = \frac{a^{n+1}(R)}{a^{n+1}(R')} A_n^m(R), \tag{4}$$

where the cubic lattice parameters $a(R)$ have been taken from Ref. [53]. The resulting CEF Hamiltonian approximation is given in Fig. 8 where it is compared with the measured schemes from Refs. [49,54,55]. The CEF schemes obtained from this procedure have good qualitative agreement with the experimental data but are quantitatively inaccurate, which should not be surprising for several reasons. First, this analysis assumes that the oxygen environment surrounding each rare-earth ion has the same O1 x parameter and that the oxygen cage simply scales with the lattice parameter. However, it is known that the distortion of the oxygen cage depends on the A-site ion [56], which directly impacts the CEF energy scheme. Second, the shielding factor, which influences the overall scale of the CEF splitting, also depends on the A-site ion. This second point explains most of the discrepancy between our calculation and the experimental data. The correct form of the CEF scheme is observed for all the calculated spectra, but the overall energy range is either too high (for A = Tb, Dy, and Ho) or too low (for A = Yb). In the cases where the scaling is too large, the cation in question lies to the left of erbium on the periodic table, and the opposite is true when the scaling is too small. The best agreement is obtained for $Ho_2Ti_2O_7$ where Er and Ho are next-door neighbors in the periodic table. These observations suggest that the shielding factor decreases on going from smaller (heavier) to bigger (lighter) rare-earth ions.

Even if a quantitative discrepancy exists between the real and the calculated CEF schemes, the scaling procedure can still be useful in terms of providing a starting point for analyzing the CEF scheme of any pyrochlore oxide. For example, it has been observed that the low-energy CEF scheme for $Tb_2Ti_2O_7$ consists of four distinct magnetic excitations at approximatively 1, 10, 14, and 16 meV [55,57,58]. However, no CEF Hamiltonian has been able to capture such a CEF energy scheme while remaining consistent with the high-energy levels. Rather, one excited CEF doublet at 1 meV and two excited CEF singlets at 10 and 16 meV have been refined [55,58]. To resolve this issue, it has been proposed that spin-phonon coupling is the origin of the extra inelastic feature observed at 14 meV [55]. Our CEF approximation for $Tb_2Ti_2O_7$, based on the scaling arguments above, also reveals only one excited CEF doublet at 4 meV and two excited CEF singlets at 12 and 20 meV. Thus, our scaling calculation further validates the spin-phonon origin of the enigmatic fourth excitation observed below 20 meV in $Tb_2Ti_2O_7$.

VI. CONCLUSION

We have carried out inelastic neutron-scattering measurements on four members of the erbium pyrochlore family: $Er_2B_2O_7$ (B = Ge, Ti, Pt, and Sn). These measurements allow us to identify the entire set of CEF excitations belonging to the lowest-energy J multiplet for all four compounds. On the basis of these measurements, a CEF Hamiltonian was refined. These results give local XY-like anisotropy for the g tensors of all four erbium pyrochlore magnets. However, large differences in the degree of XY anisotropy were observed with $Er_2Ge_2O_7$ and $Er_2Ti_2O_7$ displaying relatively more isotropic g tensors as compared to $Er_2Pt_2O_7$ and $Er_2Sn_2O_7$, which display extreme XY anisotropy with very low values of g_z. This variation in the relative XY anisotropy correlates strongly with the magnetic ground-state selection as $Er_2Ti_2O_7$ and $Er_2Ge_2O_7$ order into the Γ_5 antiferromagnetic structures, where asEr$_2$Pt$_2$O$_7$ and $Er_2Sn_2O_7$ order into the Γ_7 Palmer-Chalker structures. Finally, our paper represents a very detailed analysis of the single-ion properties of these erbium pyrochlores, a key ingredient for a detailed characterization of their spin Hamiltonians, and crucial for a clear understanding of the exotic magnetism observed in the XY pyrochlore magnets.

ACKNOWLEDGMENTS

We acknowledge useful conversations with K. A. Ross and J. G. Rau. We thank M. Tachibana, H. Sakurai, and H. A. Dabkowska for assistance in preparing the samples measured in this paper. We thank Dr. A. Huq and Dr. M. Kirkham of ORNL for collecting the neutron-diffraction data. J.G. and A.M.H. acknowledge support from the Canada Graduate Scholarship Program. This research used resources at the Spallation Neutron Source, a DOE Office of Science User Facility operated by the Oak Ridge National Laboratory (ORNL). This work was supported by the Natural Sciences and Engineering Research Council of Canada (NSERC).

[1] J. S. Gardner, M. J. P. Gingras, and J. E. Greedan, Rev. Mod. Phys. **82**, 53 (2010).
[2] A. M. Hallas, J. Gaudet, and B. D. Gaulin, Annu. Rev. Condens. Matter Phys. **9**, 105 (2018).
[3] M. J. P. Gingras and P. A. McClarty, Rep. Prog. Phys. **77**, 056501 (2014).
[4] K. A. Ross, L. Savary, B. D. Gaulin, and L. Balents, Phys. Rev. X **1**, 021002 (2011).
[5] J. Villain, R. Bidaux, J.-P. Carton, and R. Conte, J. Phys. **41**, 1263 (1980).
[6] C. L. Henley, Phys. Rev. Lett. **62**, 2056 (1989).
[7] J. D. M. Champion, M. J. Harris, P. C. W. Holdsworth, A. S. Wills, G. Balakrishnan, S. T. Bramwell, E. Čižmár, T. Fennell, J. S. Gardner, J. Lago, D. F. McMorrow, M. Orendáč, A. Orendáčová, D. M. Paul, R. I. Smith, M. T. F. Telling, and A. Wildes, Phys. Rev. B **68**, 020401 (2003).
[8] L. Savary, K. A. Ross, B. D. Gaulin, J. P. C. Ruff, and L. Balents, Phys. Rev. Lett. **109**, 167201 (2012).
[9] M. E. Zhitomirsky, M. V. Gvozdikova, P. C. W. Holdsworth, and R. Moessner, Phys. Rev. Lett. **109**, 077204 (2012).
[10] J. Oitmaa, R. R. P. Singh, B. Javanparast, A. G. R. Day, B. V. Bagheri, and M. J. P. Gingras, Phys. Rev. B **88**, 220404(R) (2013).
[11] M. E. Zhitomirsky, P. C. W. Holdsworth, and R. Moessner, Phys. Rev. B **89**, 140403(R) (2014).
[12] P. A. McClarty, S. H. Curnoe, and M. J. P. Gingras, J. Phys. Conf. Ser. **145**, 012032 (2009).
[13] S. Petit, J. Robert, S. Guitteny, P. Bonville, C. Decorse, J. Ollivier, H. Mutka, M. J. P. Gingras, and I. Mirebeau, Phys. Rev. B **90**, 060410 (2014).
[14] J. G. Rau, S. Petit, and M. J. P. Gingras, Phys. Rev. B **93**, 184408 (2016).
[15] V. S. Maryasin and M. E. Zhitomirsky, Phys. Rev. B **90**, 094412 (2014).
[16] A. Andreanov and P. A. McClarty, Phys. Rev. B **91**, 064401 (2015).
[17] J. Gaudet, A. M. Hallas, D. D. Maharaj, C. R. C. Buhariwalla, E. Kermarrec, N. P. Butch, T. J. S. Munsie, H. A. Dabkowska, G. M. Luke, and B. D. Gaulin, Phys. Rev. B **94**, 060407(R) (2016).
[18] K. A. Ross, J. W. Krizan, J. A. Rodriguez-Rivera, R. J. Cava, and C. L. Broholm, Phys. Rev. B **93**, 014433 (2016).
[19] K. E. Arpino, B. A. Trump, A. O. Scheie, T. M. McQueen, and S. M. Koohpayeh, Phys. Rev. B **95**, 094407 (2017).
[20] R. Sarkar, J. W. Krizan, F. Brückner, E. C. Andrade, S. Rachel, M. Vojta, R. J. Cava, and H.-H. Klauss, Phys. Rev. B **96**, 235117 (2017).
[21] E. C. Andrade, J. A. Hoyos, S. Rachel, and M. Vojta, arXiv:1710.06658.
[22] L. D. C. Jaubert, O. Benton, J. G. Rau, J. Oitmaa, R. R. P. Singh, N. Shannon, and M. J. P. Gingras, Phys. Rev. Lett. **115**, 267208 (2015).
[23] H. Yan, O. Benton, L. Jaubert, and N. Shannon, Phys. Rev. B **95**, 094422 (2017).
[24] Z. L. Dun, X. Li, R. S. Freitas, E. Arrighi, C. R. Dela Cruz, M. Lee, E. S. Choi, H. B. Cao, H. J. Silverstein, C. R. Wiebe, J. G. Cheng, and H. D. Zhou, Phys. Rev. B **92**, 140407(R) (2015).
[25] A. Poole, A. S. Wills, and E. Lelievre-Berna, J. Phys.: Condens. Matter **19**, 452201 (2007).
[26] A. M. Hallas, J. Gaudet, N. P. Butch, G. Xu, M. Tachibana, C. R. Wiebe, G. M. Luke, and B. D. Gaulin, Phys. Rev. Lett. **119**, 187201 (2017).
[27] S. Petit, E. Lhotel, F. Damay, P. Boutrouille, A. Forget, and D. Colson, Phys. Rev. Lett. **119**, 187202 (2017).
[28] S. E. Palmer and J. T. Chalker, Phys. Rev. B **62**, 488 (2000).
[29] S. Guitteny, S. Petit, E. Lhotel, J. Robert, P. Bonville, A. Forget, and I. Mirebeau, Phys. Rev. B **88**, 134408 (2013).
[30] M. Blume, A. Freeman, and R. Watson, Phys. Rev. **134**, A320 (1964).
[31] A. J. Princep, D. Prabhakaran, A. T. Boothroyd, and D. T. Adroja, Phys. Rev. B **88**, 104421 (2013).
[32] M. Hutchings, in *Solid State Physics*, edited by F. Seitz and D. Turnbull (Academic, New York, 1964), Vol. 16, pp. 227–273
[33] J. L. Prather, *Atomic Energy Levels in Crystals*, NBS monograph 19 (National Bureau of Standards, Washington, DC, 1961).
[34] A. J. Freeman and R. E. Watson, Phys. Rev. **127**, 2058 (1962).
[35] U. Walter, J. Phys. Chem. Solids **45**, 401 (1984).
[36] K. W. H. Stevens, Proc. Phys. Soc. London, Sect. A **65**, 209 (1952).
[37] A. Freeman and J. Desclaux, J. Magn. Magn. Mater. **12**, 11 (1979).
[38] G. Squires, *Introduction to the Theory of Thermal Neutron Scattering* (Cambridge University Press, Cambridge, UK, 1978).
[39] A. Bertin, Y. Chapuis, P. D. de Réotier, and A. Yaouanc, J. Phys.: Condens. Matter **24**, 256003 (2012).
[40] M. A. Subramanian, G. Aravamudan, and G. V. S. Rao, Prog. Solid. State. Chem. **15**, 55 (1983).
[41] A. M. Hallas, J. Gaudet, M. N. Wilson, T. J. Munsie, A. A. Aczel, M. B. Stone, R. S. Freitas, A. M. Arevalo-Lopez, J. P. Attfield, M. Tachibana, C. R. Wiebe, G. M. Luke, and B. D. Gaulin, Phys. Rev. B **93**, 104405 (2016).
[42] A. M. Hallas, A. Z. Sharma, Y. Cai, T. J. Munsie, M. N. Wilson, M. Tachibana, C. R. Wiebe, and G. M. Luke, Phys. Rev. B **94**, 134417 (2016).
[43] A. Huq, J. P. Hodges, O. Gourdon, and L. Heroux, Z. Kristallogr. Proc. EPDIC, 127 (2010).
[44] J. Rodriguez-Carvajal, Physica B **192**, 55 (1993).
[45] G. E. Granroth, A. I. Kolesnikov, T. E. Sherline, J. P. Clancy, K. A. Ross, J. P. C. Ruff, B. D. Gaulin, and S. E. Nagler, J. Phys.: Conf. Ser. **251**, 012058 (2010).
[46] O. Arnold, J. Bilheux, J. Borreguero, A. Buts, S. Campbell, L. Chapon, M. Doucet, N. Draper, R. Leal, M. Gigg *et al.*, Nucl. Instrum. Methods Phys. Res., Sect. A **764**, 156 (2014).
[47] R. T. Azuah, L. R. Kneller, Y. Qiu, C. M. Brown, J. R. D. Copley, R. M. Dimeo, and P. L. W. Tregenna-Piggott, J. Res. Natl. Inst. Stan. Technol. **114**, 341 (2009).
[48] H. Cao, A. Gukasov, I. Mirebeau, P. Bonville, C. Decorse, and G. Dhalenne, Phys. Rev. Lett. **103**, 056402 (2009).
[49] J. Gaudet, D. D. Maharaj, G. Sala, E. Kermarrec, K. A. Ross, H. A. Dabkowska, A. I. Kolesnikov, G. E. Granroth, and B. D. Gaulin, Phys. Rev. B **92**, 134420 (2015).
[50] J. S. Gardner, S. R. Dunsiger, B. D. Gaulin, M. J. P. Gingras, J. E. Greedan, R. F. Kiefl, M. D. Lumsden, W. A. MacFarlane, N. P. Raju, J. E. Sonier, I. Swainson, and Z. Tun, Phys. Rev. Lett. **82**, 1012 (1999).
[51] M. J. P. Gingras, B. C. den Hertog, M. Faucher, J. S. Gardner, S. R. Dunsiger, L. J. Chang, B. D. Gaulin, N. P. Raju, and J. E. Greedan, Phys. Rev. B **62**, 6496 (2000).

[52] A. W. C. Wong, Z. Hao, and M. J. P. Gingras, Phys. Rev. B **88**, 144402 (2013).

[53] Q. Li, L. Xu, C. Fan, F. Zhang, Y. Lv, B. Ni, Z. Zhao, and X. Sun, J. Cryst. Growth **377**, 96 (2013).

[54] S. Rosenkranz, A. P. Ramirez, A. Hayashi, R. J. Cava, R. Siddharthan, and B. S. Shastry, J. Appl. Phys. **87**, 5914 (2000).

[55] M. Ruminy, E. Pomjakushina, K. Iida, K. Kamazawa, D. T. Adroja, U. Stuhr, and T. Fennell, Phys. Rev. B **94**, 024430 (2016).

[56] G. Lau, B. Muegge, T. McQueen, E. Duncan, and R. Cava, J. Solid State Chem. **179**, 3126 (2006).

[57] J. Zhang, K. Fritsch, Z. Hao, B. V. Bagheri, M. J. P. Gingras, G. E. Granroth, P. Jiramongkolchai, R. J. Cava, and B. D. Gaulin, Phys. Rev. B **89**, 134410 (2014).

[58] A. J. Princep, H. C. Walker, D. T. Adroja, D. Prabhakaran, and A. T. Boothroyd, Phys. Rev. B **91**, 224430 (2015).

Chapter 4

Conclusions and Future Directions

This thesis is a study of the effect of various perturbations on the magnetism of the XY pyrochlores $Yb_2Ti_2O_7$ and $Er_2Ti_2O_7$. In Chapter 2, we focused on the magnetic ground state properties of $Yb_2Ti_2O_7$. Publication I contains a characterization of the single-ion properties of $Yb_2Ti_2O_7$, which was achieved by measuring the CEF excitations with inelastic neutron scattering. Local XY anisotropy has been refined for the CEF ground state of $Yb_2Ti_2O_7$ with a dominant $|J = 7/2, m_J = \pm 1/2\rangle$ contribution, which favors quantum fluctuations. Publication II revealed that the magnetic ground state of our polycrystalline sample of $Yb_2Ti_2O_7$ has ferromagnetic Bragg peaks whose intensities correlate with the broad anomaly in its specific heat and are insensitive to its sharp specific heat anomaly at 265 mK. At low temperature, the low energy inelastic neutron scattering spectra of $Yb_2Ti_2O_7$ consists of a continuum of gapless spin excitations, which also develop concomitantly with the broad specific heat anomaly. Finally, Publication III used neutron diffraction and μSR spectroscopy techniques to probe the magnetic ground state of $Yb_2Ti_2O_7$ under hydrostatic pressure. A quantum phase transition from a spin liquid state at ambient pressure to a long-range ferromagnetic state at 11 kbar has been observed highlighting the fragility of its magnetic state.

In Chapter 3, we investigated the magnetic ground state properties of $Er_2Ti_2O_7$ when perturbed by dilution of spins, applied magnetic field, and chemical pressure. In Publication IV, we demonstrated that the ψ_2 ground state of $Er_2Ti_2O_7$ is unstable towards magnetic dilution. Indeed, a mosaic of ψ_2 and ψ_3 states is stabilized in a 20%-Y diluted $Er_2Ti_2O_7$. Such a mosaic of ψ_2 and ψ_3 states was not predicted by theory where both bond randomness and site dilution were predicted to stabilize a pure ψ_3 state [94, 95]. However, recently, new theoretical work has shown that a mosaic of ψ_2 and ψ_3 is obtained when the effect of random transverse fields due to bond randomness and site dilution are properly taken into account [97]. These random transverse fields have been shown to destabilize long-range order and hence, explain our observation in Publication IV. Publication V focused on the domain reorientations and redistributions occurring in $Er_2Ti_2O_7$ under a magnetic field applied along the high symmetry crystallographic directions. As it was theoretically predicted, the Zeeman coupling arising in a small applied field can be well described using a conventional clock, where the 12 hours are represented by the 12 ψ_2-ψ_3 states. Finally, Publication VI focuses on the single-ion properties of $Er_2Ti_2O_7$ and its chemical pressure analogs. We found that the magnetic ground states of the erbium pyrochlores correlate well with the strength of their local spin anisotropy where weak XY anisotropy leads to a Γ_5 phase and strong XY anisotropy leads to a Γ_7 phase.

In conclusion, the results presented in this thesis unambiguously reveal that the magnetic ground states of XY pyrochlores are fragile. This fragility in the magnetism of XY pyrochlores is naturally explained by the intrinsic multiphase competition existing in rare earth XY pyrochlores [48, 49]. From the results presented in this thesis, we conclude that the spin liquid state of $Yb_2Ti_2O_7$ is driven by phase competition between a ferromagnetic Γ_9 phase and an antiferromagnetic Γ_5 phase. However, the exact nature of the quantum excitations arising from this state is still unknown and represents an interesting puzzle for future theoretical works. Finally, multiphase competition also promotes order-by-disorder effects [48, 49]. From the results obtained in Chapter 3, it is tempting to conclude that order-by-disorder drives the magnetism in the erbium pyrochlores, but a direct proof of this phenomenology is still missing. As proposed in a recent theoretical work, an experiment that could provide unambiguous evidence for order-by-disorder is the characterization of $Er_2Ti_2O_7$'s spin dynamics in a pulsed magnetic field. [98].

Bibliography

[1] J Gaudet, DD Maharaj, G Sala, E Kermarrec, KA Ross, HA Dabkowska, AI Kolesnikov, GE Granroth, and BD Gaulin. Neutron spectroscopic study of crystalline electric field excitations in stoichiometric and lightly stuffed $Yb_2Ti_2O_7$. *Physical Review B*, 92(13):134420, 2015.

[2] J Gaudet, KA Ross, E Kermarrec, NP Butch, G Ehlers, HA Dabkowska, and BD Gaulin. Gapless quantum excitations from an icelike splayed ferromagnetic ground state in stoichiometric $Yb_2Ti_2O_7$. *Physical Review B*, 93(6):064406, 2016.

[3] E Kermarrec, J Gaudet, K Fritsch, R Khasanov, Z Guguchia, C Ritter, K A Ross, Dabkowska H A, and Gaulin B D. Ground state selection under pressure in the quantum pyrochlore magnet $Yb_2Ti_2O_7$. *Nature Communications*, 8:14810, 2017.

[4] J Gaudet, AM Hallas, DD Maharaj, CRC Buhariwalla, E Kermarrec, NP Butch, TJS Munsie, HA Dabkowska, GM Luke, and BD Gaulin. Magnetic dilution and domain selection in the XY pyrochlore antiferromagnet $Er_2Ti_2O_7$. *Physical Review B*, 94(6):060407, 2016.

[5] J Gaudet, AM Hallas, J Thibault, NP Butch, HA Dabkowska, and BD Gaulin. Experimental evidence for field-induced emergent clock anisotropies in the XY pyrochlore $Er_2Ti_2O_7$. *Physical Review B*, 95(5):054407, 2017.

[6] J Gaudet, AM Hallas, AI Kolesnikov, and BD Gaulin. Effect of chemical pressure on the crystal electric field states of erbium pyrochlore magnets. *Physical Review B*, 97:024415, 2018.

[7] AM Hallas, J Gaudet, MN Wilson, TJ Munsie, AA Aczel, MB Stone, RS Freitas, AM Arevalo-Lopez, JP Attfield, M Tachibana, CR Wiebe, GM Luke, and BD Gaulin. XY antiferro-

magnetic ground state in the effective S = 1/2 pyrochlore $Yb_2Ge_2O_7$. *Physical Review B*, 93(10):104405, 2016.

[8] AM Hallas, J Gaudet, NP Butch, M Tachibana, RS Freitas, GM Luke, CR Wiebe, and BD Gaulin. Universal dynamic magnetism in Yb pyrochlores with disparate ground states. *Physical Review B*, 93(10):100403, 2016.

[9] AM Hallas, J Gaudet, NP Butch, G Xu, M Tachibana, CR Wiebe, GM Luke, and BD Gaulin. Phase competition in the Palmer-Chalker XY pyrochlore $Er_2Pt_2O_7$. *Physical Review Letters*, 119:187201, 2017.

[10] AM Hallas, J Gaudet, and BD Gaulin. Experimental insights into ground-state selection of quantum XY pyrochlores. *Annual Review of Condensed Matter Physics*, 9(1), 2018.

[11] L Balents. Spin liquids in frustrated magnets. *Nature*, 464(7286):199–208, 2010.

[12] JS Gardner, MJP Gingras, and JE Greedan. Magnetic pyrochlore oxides. *Reviews of Modern Physics*, 82(1):53, 2010.

[13] A Bertin, Y Chapuis, P Dalmas de Réotier, and A Yaouanc. Crystal electric field in the $R_2Ti_2O_7$ pyrochlore compounds. *Journal of Physics: Condensed Matter*, 24(25):256003, 2012.

[14] MJ Harris, ST Bramwell, DF McMorrow, TH Zeiske, and KW Godfrey. Geometrical frustration in the ferromagnetic pyrochlore $Ho_2Ti_2O_7$. *Physical Review Letters*, 79(13):2554, 1997.

[15] ST Bramwell and MJ Harris. Frustration in Ising-type spin models on the pyrochlore lattice. *Journal of Physics: Condensed Matter*, 10(14):L215, 1998.

[16] S T Bramwell and M J P Gingras. Spin ice state in frustrated magnetic pyrochlore materials. *Science*, 294(5546):1495–1501, 2001.

[17] T Fennell, PP Deen, AR Wildes, K Schmalzl, D Prabhakaran, AT Boothroyd, RJ Aldus, DF McMorrow, and ST Bramwell. Magnetic Coulomb phase in the spin ice $Ho_2Ti_2O_7$. *Science*, 326(5951):415–417, 2009.

[18] AP Ramirez, A Hayashi, RJ Cava, R Siddharthan, and BS Shastry. Zero-point entropy in 'spin ice'. *Nature*, 399(6734):333–335, 1999.

[19] C Castelnovo, R Moessner, and SL Sondhi. Magnetic monopoles in spin ice. *Nature*, 451(7174):42–45, 2008.

[20] DJP Morris, DA Tennant, SA Grigera, B Klemke, C Castelnovo, R Moessner, C Czternasty, M Meissner, KC Rule, JU Hoffmann, Kiefer K, Gerischer S, Slobinsky D, and Perry RS. Dirac strings and magnetic monopoles in the spin ice $Dy_2Ti_2O_7$. *Science*, 326(5951):411–414, 2009.

[21] M Hermele, MPA Fisher, and L Balents. Pyrochlore photons: The U(1) spin liquid in a S= 1/2 three-dimensional frustrated magnet. *Physical Review B*, 69(6):064404, 2004.

[22] A Banerjee, SV Isakov, K Damle, and YB Kim. Unusual liquid state of hard-core bosons on the pyrochlore lattice. *Physical Review Letters*, 100(4):047208, 2008.

[23] N Shannon, O Sikora, F Pollmann, K Penc, and P Fulde. Quantum ice: a quantum Monte Carlo study. *Physical Review Letters*, 108(6):067204, 2012.

[24] L Savary and L Balents. Coulombic quantum liquids in spin-1/2 pyrochlores. *Physical Review Letters*, 108(3):037202, 2012.

[25] O Benton, O Sikora, and N Shannon. Seeing the light: experimental signatures of emergent electromagnetism in a quantum spin ice. *Physical Review B*, 86(7):075154, 2012.

[26] SB Lee, S Onoda, and L Balents. Generic quantum spin ice. *Physical Review B*, 86(10):104412, 2012.

[27] L Savary and L Balents. Spin liquid regimes at nonzero temperature in quantum spin ice. *Physical Review B*, 87(20):205130, 2013.

[28] MJP Gingras and PA McClarty. Quantum spin ice: A search for gapless quantum spin liquids in pyrochlore magnets. *Reports on Progress in Physics*, 77(5):056501, 2014.

[29] J Villain, R Bidaux, J-P Carton, and R Conte. Order as an effect of disorder. *Journal de Physique*, 41(11):1263–1272, 1980.

[30] JR Tessman. Magnetic anisotropy at 0° K. *Physical Review*, 96(5):1192, 1954.

[31] H Cao, A Gukasov, I Mirebeau, P Bonville, C Decorse, and G Dhalenne. Ising versus XY anisotropy in frustrated $R_2Ti_2O_7$ compounds as "seen" by polarized neutrons. *Physical Review Letters*, 103(5):056402, 2009.

[32] JA Hodges, P Bonville, A Forget, M Rams, K Królas, and G Dhalenne. The crystal field and exchange interactions in $Yb_2Ti_2O_7$. *Journal of Physics: Condensed Matter*, 13(41):9301, 2001.

[33] BZ Malkin, AR Zakirov, MN Popova, SA Klimin, EP Chukalina, E Antic-Fidancev, PH Goldner, P Aschehoug, and G Dhalenne. Optical spectroscopy of $Yb_2Ti_2O_7$ and $Y_2Ti_2O_7$: Yb^{3+} and crystal-field parameters in rare-earth titanate pyrochlores. *Physical Review B*, 70(7):075112, 2004.

[34] ST Bramwell, MN Field, MJ Harris, and IP Parkin. Bulk magnetization of the heavy rare earth titanate pyrochlores-a series of model frustrated magnets. *Journal of Physics: Condensed Matter*, 12(4):483, 2000.

[35] KA Ross, L Savary, BD Gaulin, and L Balents. Quantum excitations in quantum spin ice. *Physical Review X*, 1(2):021002, 2011.

[36] JD Thompson, PA McClarty, D Prabhakaran, I Cabrera, T Guidi, and R Coldea. Quasiparticle breakdown and spin hamiltonian of the frustrated quantum pyrochlore $Yb_2Ti_2O_7$ in a magnetic field. *Physical Review Letters*, 119:057203, 2017.

[37] LD Pan, SK Kim, A Ghosh, CM Morris, KA Ross, E Kermarrec, BD Gaulin, SM Koohpayeh, O Tchernyshyov, and NP Armitage. Low-energy electrodynamics of novel spin excitations in the quantum spin ice $Yb_2Ti_2O_7$. *Nature Communications*, 5:4970, 2014.

[38] R Applegate, NR Hayre, RRP Singh, T Lin, AGR Day, and MJP Gingras. Vindication of $Yb_2Ti_2O_7$ as a model exchange quantum spin ice. *Physical Review Letters*, 109(9):097205, 2012.

[39] NR Hayre, KA Ross, R Applegate, T Lin, RRP Singh, BD Gaulin, and MJP Gingras. Thermodynamic properties of $Yb_2Ti_2O_7$ pyrochlore as a function of temperature and magnetic field: validation of a quantum spin ice exchange Hamiltonian. *Physical Review B*, 87(18):184423, 2013.

[40] LJ Chang, MR Lees, I Watanabe, AD Hillier, Y Yasui, and S Onoda. Static magnetic moments revealed by muon spin relaxation and thermodynamic measurements in the quantum spin ice $Yb_2Ti_2O_7$. *Physical Review B*, 89(18):184416, 2014.

[41] JDM Champion, MJ Harris, PCW Holdsworth, AS Wills, G Balakrishnan, ST Bramwell, E Čižmár, T Fennell, JS Gardner, J Lago, DF McMorrow, M Orendac, O Orendacova,

D McK Paul, RI Smith, MTF Telling, and A Wildes. $Er_2Ti_2O_7$: Evidence of quantum order by disorder in a frustrated antiferromagnet. *Physical Review B*, 68(2):020401, 2003.

[42] L Savary, KA Ross, BD Gaulin, JPC Ruff, and L Balents. Order by quantum disorder in $Er_2Ti_2O_7$. *Physical Review Letters*, 109(16):167201, 2012.

[43] ME Zhitomirsky, MV Gvozdikova, PCW Holdsworth, and R Moessner. Quantum order by disorder and accidental soft mode in $Er_2Ti_2O_7$. *Physical Review Letters*, 109(7):077204, 2012.

[44] AWC Wong, Z Hao, and MJP Gingras. Ground state phase diagram of generic XY pyrochlore magnets with quantum fluctuations. *Physical Review B*, 88(14):144402, 2013.

[45] ME Zhitomirsky, PCW Holdsworth, and R Moessner. Nature of finite-temperature transition in anisotropic pyrochlore $Er_2Ti_2O_7$. *Physical Review B*, 89(14):140403, 2014.

[46] J Oitmaa, RRP Singh, B Javanparast, AGR Day, BV Bagheri, and MJP Gingras. Phase transition and thermal order-by-disorder in the pyrochlore antiferromagnet $Er_2Ti_2O_7$: A high-temperature series expansion study. *Physical Review B*, 88(22):220404, 2013.

[47] B Javanparast, AGR Day, Z Hao, and MJP Gingras. Order-by-disorder near criticality in XY pyrochlore magnets. *Physical Review B*, 91(17):174424, 2015.

[48] LDC Jaubert, O Benton, JG Rau, J Oitmaa, RRP Singh, N Shannon, and MJP Gingras. Are multiphase competition and order by disorder the keys to understanding $Yb_2Ti_2O_7$? *Physical Review Letters*, 115(26):267208, 2015.

[49] H Yan, O Benton, L Jaubert, and N Shannon. Theory of multiple-phase competition in pyrochlore magnets with anisotropic exchange with application to $Yb_2Ti_2O_7$, $Er_2Ti_2O_7$, and $Er_2Sn_2O_7$. *Physical Review B*, 95(9):094422, 2017.

[50] AJ Freeman and RE Watson. Theoretical investigation of some magnetic and spectroscopic properties of rare-earth ions. *Physical Review*, 127(6):2058, 1962.

[51] KWH Stevens. Matrix elements and operator equivalents connected with the magnetic properties of rare earth ions. *Proceedings of the Physical Society. Section A*, 65(3):209, 1952.

[52] U Walter. Treating crystal field parameters in lower than cubic symmetries. *Journal of Physics and Chemistry of Solids*, 45(4):401–408, 1984.

[53] MT Hutchings. Point-charge calculations of energy levels of magnetic ions in crystalline electric fields. *Solid State Phys.*, 16:227–273, 1964.

[54] S Rosenkranz, AP Ramirez, A Hayashi, RJ Cava, R Siddharthan, and BS Shastry. Crystal-field interaction in the pyrochlore magnet $Ho_2Ti_2O_7$. *Journal of Applied Physics*, 87(9):5914–5916, 2000.

[55] SH Curnoe. Quantum spin configurations in $Tb_2Ti_2O_7$. *Physical Review B*, 75(21):212404, 2007.

[56] Shigeki Onoda. Effective quantum pseudospin-1/2 model for Yb pyrochlore oxides. In *Journal of Physics: Conference Series*, volume 320, page 012065. IOP Publishing, 2011.

[57] BC den Hertog and MJP Gingras. Dipolar interactions and origin of spin ice in Ising pyrochlore magnets. *Physical Review Letters*, 84(15):3430, 2000.

[58] ST Bramwell, MJ Harris, BC Den Hertog, MJP Gingras, JS Gardner, DF McMorrow, AR Wildes, AL Cornelius, JDM Champion, RG Melko, and T Fennel. Spin correlations in $Ho_2Ti_2O_7$: a dipolar spin ice system. *Physical Review Letters*, 87(4):047205, 2001.

[59] Taras Yavors'kii, Tom Fennell, Michel JP Gingras, and Steven T Bramwell. $Dy_2Ti_2O_7$spin ice: a test case for emergent clusters in a frustrated magnet. *Physical Review Letters*, 101(3):037204, 2008.

[60] Sergei V Isakov, R Moessner, and SL Sondhi. Why spin ice obeys the ice rules. *Physical Review Letters*, 95(21):217201, 2005.

[61] M Ruminy, E Pomjakushina, K Iida, K Kamazawa, D T Adroja, U Stuhr, and T Fennell. Crystal-field parameters of the rare-earth pyrochlores $R_2Ti_2O_7$ (R= Tb, Dy, and Ho). *Physical Review B*, 94(2):024430, 2016.

[62] YM Jana, A Sengupta, and D Ghosh. Estimation of single ion anisotropy in pyrochlore $Dy_2Ti_2O_7$, a geometrically frustrated system, using crystal field theory. *Journal of Magnetism and Magnetic Materials*, 248(1):7–18, 2002.

[63] S Guitteny, J Robert, P Bonville, J Ollivier, C Decorse, P Steffens, M Boehm, H Mutka, I Mirebeau, and S Petit. Anisotropic propagating excitations and quadrupolar effects in $Tb_2Ti_2O_7$. *Physical Review Letters*, 111(8):087201, 2013.

[64] J Robert, E Lhotel, G Remenyi, S Sahling, I Mirebeau, C Decorse, B Canals, and S Petit. Spin dynamics in the presence of competing ferromagnetic and antiferromagnetic correlations in $Yb_2Ti_2O_7$. *Physical Review B*, 92(6):064425, 2015.

[65] S Petit, E Lhotel, F Damay, P Boutrouille, A Forget, and D Colson. Long-range order in the dipolar XY antiferromagnet $Er_2Sn_2O_7$. *Physical Review Letters*, 119:187202, 2017.

[66] SE Palmer and JT Chalker. Order induced by dipolar interactions in a geometrically frustrated antiferromagnet. *Physical Review B*, 62(1):488, 2000.

[67] X Li, WM Li, K Matsubayashi, Y Sato, CQ Jin, Y Uwatoko, T Kawae, AM Hallas, CR Wiebe, AM Arevalo-Lopez, JP Attfield, JS Gardner, RS Freitas, HD Zhou, and JG Cheng. Long-range antiferromagnetic order in the frustrated XY pyrochlore antiferromagnet $Er_2Ge_2O_7$. *Physical Review B*, 89(6):064409, 2014.

[68] ZL Dun, X Li, RS Freitas, E Arrighi, CR Delacruz, Minseong Lee, Eun Sang Choi, HB Cao, HJ Silverstein, CR Wiebe, JG Cheng, and HD Zhou. Antiferromagnetic order in the pyrochlores $R_2Ge_2O_7$ (R = Er, Yb). *Physical Review B*, 92(14):140407, 2015.

[69] ZL Dun, M Lee, ES Choi, AM Hallas, CR Wiebe, JS Gardner, E Arrighi, RS Freitas, AM Arevalo-Lopez, JP Attfield, HD Zhou, and JG Cheng. Chemical pressure effects on magnetism in the quantum spin liquid candidates $Yb_2X_2O_7$ (X = Sn, Ti, Ge). *Physical Review B*, 89(6):064401, 2014.

[70] A Poole, AS Wills, and E Lelievre-Berna. Magnetic ordering in the XY pyrochlore antiferromagnet $Er_2Ti_2O_7$: A spherical neutron polarimetry study. *Journal of Physics: Condensed Matter*, 19(45):452201, 2007.

[71] KA Ross, Th Proffen, HA Dabkowska, JA Quilliam, LR Yaraskavitch, JB Kycia, and BD Gaulin. Lightly stuffed pyrochlore structure of single-crystalline $Yb_2Ti_2O_7$ grown by the optical floating zone technique. *Physical Review B*, 86(17):174424, 2012.

[72] A Yaouanc, P Dalmas de Réotier, C Marin, and V Glazkov. Single-crystal versus polycrystalline samples of magnetically frustrated $Yb_2Ti_2O_7$: specific heat results. *Physical Review B*, 84(17):172408, 2011.

[73] G.L. Squires. Introduction to thermal neutron scattering. *Cambridge University Press, Cambridge, UK*, 1978.

[74] KA Ross, JPC Ruff, CP Adams, JS Gardner, HA Dabkowska, Y Qiu, JRD Copley, and BD Gaulin. Two-dimensional Kagome correlations and field induced order in the ferromagnetic XY pyrochlore $Yb_2Ti_2O_7$. *Physical Review Letters*, 103(22):227202, 2009.

[75] KA Ross, LR Yaraskavitch, M Laver, JS Gardner, JA Quilliam, S Meng, JB Kycia, DK Singh, Th Proffen, HA Dabkowska, and BD Gaulin. Dimensional evolution of spin correlations in the magnetic pyrochlore $Yb_2Ti_2O_7$. *Physical Review B*, 84(17):174442, 2011.

[76] LJ Chang, S Onoda, Y Su, YJ Kao, KD Tsuei, Y Yasui, K Kakurai, and MR Lees. Higgs transition from a magnetic Coulomb liquid to a ferromagnet in $Yb_2Ti_2O_7$. *Nature Communications*, 3:992, 2012.

[77] RM D'Ortenzio, HA Dabkowska, SR Dunsiger, BD Gaulin, MJP Gingras, T Goko, JB Kycia, L Liu, T Medina, TJ Munsie, . Pomaranski, KA Ross, YJ Uemura, TJ Williams, and GM Luke. Unconventional magnetic ground state in $Yb_2Ti_2O_7$. *Physical Review B*, 88(13):134428, 2013.

[78] KE Arpino, BA Trump, AO Scheie, TM McQueen, and SM Koohpayeh. Impact of stoichiometry of $Yb_2Ti_2O_7$ on its physical properties. *Physical Review B*, 95(9):094407, 2017.

[79] GC Lau, RS Freitas, BG Ueland, P Schiffer, and RJ Cava. Geometrical magnetic frustration in rare-earth chalcogenide spinels. *Physical Review B*, 72(5):054411, 2005.

[80] GC Lau, BD Muegge, TM McQueen, EL Duncan, and RJ Cava. Stuffed rare earth pyrochlore solid solutions. *Journal de Physique Solid State Chemistry*, 179(10):3126–3135, 2006.

[81] Y Yasui, M Soda, S Iikubo, M Ito, M Sato, N Hamaguchi, T Matsushita, N Wada, T Takeuchi, N Aso, and K Kakurai. Ferromagnetic transition of pyrochlore compound $Yb_2Ti_2O_7$. *Journal of the Physical Society of Japan*, 72(11):3014–3015, 2003.

[82] A Scheie, J Kindervater, S Säubert, C Duvinage, C Pfleiderer, HJ Changlani, S Zhang, L Harriger, K Arpino, SM Koohpayeh, O Tchernyshyov, and C Broholm. Reentrant phase diagram of $Yb_2Ti_2O_7$ in a $\langle 111 \rangle$ magnetic field. *Physical Review Letters*, 119(12):127201, 2017.

[83] A Yaouanc, P Dalmas de Réotier, L Keller, B Roessli, and A Forget. A novel type of splayed ferromagnetic order observed in $Yb_2Ti_2O_7$. *Journal of Physics: Condensed Matter*, 28(42):426002, 2016.

[84] V Peçanha-Antonio, E Feng, Y Su, V Pomjakushin, F Demmel, LJ Chang, RJ Aldus, Y Xiao, MR Lees, and T Brückel. Magnetic excitations in the ground state of $Yb_2Ti_2O_7$. *Physical Review B*, 96(21):214415, 2017.

[85] A Yaouanc, P Dalmas de Réotier, P Bonville, JA Hodges, V Glazkov, L Keller, V Sikolenko, M Bartkowiak, A Amato, C Baines, PJC King, PCM Gubbens, and A Forget. Dynamical splayed ferromagnetic ground state in the quantum spin ice $Yb_2Sn_2O_7$. *Physical Review Letters*, 110(12):127207, 2013.

[86] JA Hodges, P Bonville, A Forget, and G André. First-order transition in frustrated $Yb_2Ti_2O_7$ without long-range order. *Canadian Journal of Physics*, 79(11-12):1373–1380, 2001.

[87] JS Gardner, G Ehlers, N Rosov, RW Erwin, and C Petrovic. Spin-spin correlations in $Yb_2Ti_2O_7$: A polarized neutron scattering study. *Physical Review B*, 70:180404, Nov 2004.

[88] K Baroudi, BD Gaulin, SH Lapidus, J Gaudet, and RJ Cava. Symmetry and light stuffing of $Ho_2Ti_2O_7$, $Er_2Ti_2O_7$, and $Yb_2Ti_2O_7$ characterized by synchrotron x-ray diffraction. *Physical Review B*, 92(2):024110, 2015.

[89] G Sala, MJ Gutmann, D Prabhakaran, D Pomaranski, C Mitchelitis, JB Kycia, DG Porter, C Castelnovo, and JP Goff. Vacancy defects and monopole dynamics in oxygen-deficient pyrochlores. *Nature Materials*, 13(5):488–493, 2014.

[90] A Mostaed, G Balakrishnan, MR Lees, Y Yasui, LJ Chang, and R Beanland. Atomic structure study of the pyrochlore $Yb_2Ti_2O_7$ and its relationship with low-temperature magnetic order. *Physical Review B*, 95(9):094431, 2017.

[91] PA McClarty, SH Curnoe, and MJP Gingras. Energetic selection of ordered states in a model of the $Er_2Ti_2O_7$ frustrated pyrochlore XY antiferromagnet. *Journal of Physics: Conference Series*, 145(1):012032, 2009.

[92] S Petit, J Robert, S Guitteny, P Bonville, C Decorse, J Ollivier, H Mutka, MJP Gingras, and I Mirebeau. Order by disorder or energetic selection of the ground state in the XY pyrochlore antiferromagnet $Er_2Ti_2O_7$: An inelastic neutron scattering study. *Physical Review B*, 90(6):060410, 2014.

[93] JG Rau, S Petit, and MJP Gingras. Order by virtual crystal field fluctuations in pyrochlore XY antiferromagnets. *Physical Review B*, 93(18):184408, 2016.

[94] VS Maryasin and ME Zhitomirsky. Order from structural disorder in the XY pyrochlore antiferromagnet $Er_2Ti_2O_7$. *Physical Review B*, 90(9):094412, 2014.

[95] A Andreanov and PA McClarty. Order induced by dilution in pyrochlore XY antiferromagnets. *Physical Review B*, 91(6):064401, 2015.

[96] VS Maryasin, ME Zhitomirsky, and R Moessner. Low-field behavior of an XY pyrochlore antiferromagnet: Emergent clock anisotropies. *Physical Review B*, 93(10):100406, 2016.

[97] EC Andrade, JA Hoyos, S Rachel, and M Vojta. Cluster-glass phase in pyrochlore XY antiferromagnets with quenched disorder. *arXiv preprint arXiv:1710.06658*, 2017.

[98] Y Wan and R Moessner. Control of the effective free-energy landscape in a frustrated magnet by a field pulse. *Physical Review Letters*, 119(16):167203, 2017.